Fatigue Behaviour of CFRP Strengthened Reinforced Concrete Beams

Theoretical and Experimental Investigation

Valontino Ruwhellon James

Fatigue Behaviour of CFRP Strengthened Reinforced Concrete Beams

Prepared by: Valontino Ruwhellon James (JMSVAL001)
Supervisor: Professor Pilate Moyo
Submission Date: 28 February 2020

This dissertation has been submitted to the Department of Civil Engineering, Faculty of Engineering and the Built Environment, University of Cape Town, in partial fulfilment of the requirements for a Master of Science degree in Structural Engineering.

AUTHENTICITY DECLARATION

I, Valontino James, hereby declare that this dissertation is my own, unaided work. I know the meaning of plagiarism and declare that all the work in the document, save for that which is properly acknowledged, is my own. This thesis/dissertation has been submitted to the Turnitin module and I confirm that my supervisor has seen my report and any concerns revealed by such have been resolved with my supervisor. It is being submitted for the degree of Master of Science in Engineering in the University of Cape Town and has not been submitted before for any degree or examination in any other University.

Signed by candidate

Valontino Ruwhellon James
February 2020

ABSTRACT

The performance of reinforced concrete (RC) structures, such as bridges in the heavy haul industry, may be severely impacted by fatigue when subjected to repeated cyclic loading. Fatigue not only reduces load carrying capacity and serviceability limit states (SLS), but it can cause structural failure even when the components are subjected to low stress range cyclic loading. Corrosion damage exacerbates fatigue related problems as chloride induced pitting corrosion facilitates the formation and gradual propagation of cracks under cyclic loading. A common rehabilitation and retrofitting approach that involves patch repairing and fibre reinforced polymer (FRP) strengthening has proven effective to not only restore structural capacity, but also to enhance infrastructure service life.

The structural repair process involves the replacement of deteriorated cover concrete with a less permeable patch repair mortar. The patch repair only restores durability of the structure; to restore or enhance structural capacity the repair process further involves bonding of FRP laminates. Particularly in the case of FRP's with a low elastic modulus, the design is often guided by serviceability limit states as opposed to ultimate limit states (ULS), resulting in an over-reinforced structural member. In addition, the reinforcement area of commercially available FRP strengthening may exceed the design requirements, especially at low levels of corrosion damage. In both the abovementioned considerations the design may result in an over-reinforced section. At the time when this researched was proposed, the effect of increasing damage extent on fatigue behaviour of over-reinforced RC beams was not clear and merited further investigation.

A scientific experimental approach was developed to investigate the long-term performance of fifteen (15) full-scale 40MPa RC beams with dimensions 155x254x2000mm and ultimate capacity of 62.3kNm. Accelerated corrosion damage was induced in varied extents which included 450mm, 800mm, 1300mm and 1800mm length to a constant degree of 10% on all specimens. Specimens from each damage extent were patch repaired using SikaCrete214 and subsequently strengthened with externally bonded with SikaCarboDurS512 carbon fibre reinforced polymer (CFRP) laminates.

Four-point bending monotonic loading tests were conducted on one (1) specimen from each damage extent. The results obtained from the quasi-static tests were used to determine two (2) cyclic loading stress ranges at which the remaining 2 specimens from each damage extent would be tested under. Under the 40% and 60% stress ranges four-point bending cyclic loading tests were carried out at a test frequency of 4Hz. Information was acquired on key performance indicators that included fatigue life, crack development, failure mode and stiffness degradation, where stiffness was assessed in terms of midspan deflection, composite material strains and neutral axis shift. Information on these parameters were collected using strain gauges, linear variable differential transducers (LVDT), DEMEC strain targets and digital image correlation (DIC).

Ultimate failure loads under monotonic loading showed that despite having the highest degree of corrosion, the 450mm damage extent specimen had the highest failure load of 325kN. The failure load gradually reduced to 290kN as the damage extent was increased to 1800mm and the 0mm (control) specimen failed at the lowest load of 274kN. In contrast to the static behaviour, the specimen fatigue life enhanced by 106.3% as the damage extent was increased from 450mm to 1800mm. As expected, the 40% stress range tests yielded much longer fatigue lives than their 60% stress range counterparts. Furthermore, the experimentally obtained fatigue lives were compared to three fatigue life prediction models and the Helgason and Hanson model yielded the closest correlation with the experimental results.

Crack densities were found to increase with a longer fatigue life. An increase in damage extent was found to positively affect crack development and overall stiffness of the specimen during long-term fatigue testing. This finding was further substantiated by an assessment of midspan deflection, compression concrete strain and carbon fibre strain results, which all suggested a lower neutral axis and a lower stiffness reduction rate under fatigue loading as the damage extent was increased from 450mm to 1800mm. Furthermore, the tension concrete cracks propagated gradually during longer fatigue tests periods, while the tension steel and carbon fibre were comparably less affected by the resultant internal forces. Unfortunately, the neutral axis strain measurements using DEMEC targets were unable to assess the relative effect of an increase in damage extent as well as the compression concrete and carbon fibre strains were able to.

During this experimental period, it was established that the laboratory layout was not conducive for carrying out the DIC process of long-term cyclic loading tests. The area in which testing took place did not adequately protect the camera against the environment and therefore required daily storage of the equipment. Regular movement of the camera for storage purposes introduced measurement inaccuracies which accumulated over longer test periods of up 20 days. However, for the short-term tests that did not require movement of the camera, the DIC process yielded favourable results. It was possible to capture the crack patterns early in the test period when the crack growth rate and development of new cracks was high using DIC. It was found that the high strain cracks coincided with the points of maximum vertical deflection (obtained through DIC) and eventual failure location of the specimen. The points of maximum deflection obtained from the DIC process were often not at midspan, which in the absence of the DIC process, would not have been possible to predict accurately.

The results have shown that the specimens with the longer damage extents exhibit improved fatigue performance than their shorter counterparts. This revealed a stark contrast to their monotonic loading performance which favoured shorter damage extents. Furthermore, DIC holds potential to predict failure location more accurately than conventional approaches used for structural health monitoring (SHS).

ACKNOWLEDGEMENTS

I would like to express my sincerest gratitude to the following people who have contributed to and assisted my research in various ways.

To my supervisor, Professor Pilate Moyo, thank you for stimulating higher level thought and independent research. Every time you challenged my proposed methods, critical assessment was required and that ultimately resulted in deeper comprehension of structural behaviour.

Thank you Concrete Materials and Structural Integrity Research Unit (CoMSIRU) for funding my research and for providing an environment that allowed me to explore various other research fields, apart from my own, through regular seminars and industry work opportunities.

To all the laboratory staff: Christopher Ceasar, Charles May, Charles Nicholas, Elvino Witbooi, Leonard Adams, Nooredien Hassen and Tahir Mukaddam, thank you for all your help, I could not have done this without you.

To the postgraduate students Brian Abala, Haris Sohawon, Bukhosi Nyoni, Dr. Philemon Arito and especially Dr. Kabani Matongo, thank you for offering your valuable time to critique my research.

Dr. Richard Curry and Sherlyn Gabriel of the UCT Mechanical Engineering Department, thank you for your assistance and guidance on digital image correlation processing.

To Kevin Kimbrey at Sika, thank you for all the materials that you have generously donated to my research.

Ashley Mc Nab, my partner and muse, thank you for all the sandwiches, curries and patience throughout my research.

Finally, and most importantly my family, especially my grandparents, Eduard and Wilhelmina James, for raising me, loving me and supporting me throughout my journey both spiritually and financially. I dedicate this thesis to you!

TABLE OF CONTENTS

LIST OF FIGURES

LIST OF TABLES

GLOSSARY

RC	-	Reinforced Concrete
FRP	-	Fibre Reinforced Polymer
DIC	-	Digital Image Correlation
ULS	-	Ultimate Limit State
SLS	-	Serviceability Limit State
LVDT	-	Linear Variable Differential Transducer
HDPE	-	High-density Polyethylene
SANS	-	South African National Standard
kN	-	Kilonewtons
kNm	-	Kilonewton Meters
FEM	-	Finite Element Model
FEA	-	Finite Element Analysis
NDT	-	Non-destructive Test
ITZ	-	Interfacial Transition Zone
pH	-	Potential of Hydrogen
NA	-	Neutral Axis
DC	-	Direct Current
2-D	-	Two Dimensional
3-D	-	Three Dimensional
NaCl	-	Sodium Chloride
A	-	Ampere
MP	-	Megapixel
FPS	-	Frames Per Second
PMC	-	Polymer Modified Cementitious
SHM	-	Structural Health Monitoring
EBR	-	Externally Bonded Reinforcement
NSM	-	Near Surface Mounted
FRC	-	Fibre Reinforced Concrete
CDM	-	Continuum Damage Mechanics
BFRP	-	Basalt Fibre Reinforced Polymer
CCD	-	Charge-coupled Device
SENB	-	Single Edged Notched Beam

1. INTRODUCTION

1.1 Background and significance of study

Infrastructure deterioration is a growing global concern, whether premature failure is due to substandard durability design or because structural capacity has been exceeded. For example in the heavy haul railway industry there has been an international drive for higher axle loads and longer trains, than what infrastructure had initially been designed for, in an attempt to increase haul capacity (Busatta & Moyo, 2017). Chloride and carbon dioxide rich environments have proven to significantly exacerbate infrastructure deterioration, especially where cover concrete design had been inadequate (Ballim et al., 2009). Due to the considerable cost associated with infrastructure development, investors and infrastructure managers are commonly interested in residual life of existing infrastructure and how service life could be extended. A comprehensive understanding of infrastructure condition as well as its behaviour is required to make informed predictions.

Corrosion damage is a twofold problem that causes deterioration of both reinforcing steel and cover concrete (Ballim et al., 2009). Reinforcement corrosion primarily reduces steel cross-section either by uniform or pitting corrosion, where the latter is more critical as is it characterized by larger, localized cross-section loss. Moreover, corrosion damage degrades cover concrete due to the corrosion reaction products that occupy a larger volume than the original steel. The corrosion products exert tensile forces on cover concrete that progressively results in cracking, delamination and eventually spalling of concrete from the structure.

Reinforced concrete (RC) infrastructure is susceptible to fatigue failure when subjected to cyclic loading. Fatigue is characterized by micro-cracking, cracks that propagate as the structure experiences an increasing number of fatigue cycles until eventual rupture of one of its components. Although each component of the composite structure is susceptible to fatigue failure, fatigue of tensile steel commonly governs fatigue life of the entire structural component (Mahal, 2015). This type of failure is accelerated by prior corrosion damage (Ma et al., 2014). Pitting corrosion reduces steel cross-section and provides an ideal location for crack formation. This combined effect of corrosion damage and fatigue behaviour may be more detrimental than the sum of their individual effects (Song & Yu, 2015).

The most common approach to repair corrosion damaged RC structures involves the removal of damaged concrete and corrosion products, followed by treating corroded steel and ultimately applying a concrete repair mortar. These repairs restore serviceability of concrete elements, without increasing structural capacity. The success of the patch repairs relies on its compatibility with the concrete substrate. Differential expansion between the two components could lead to excessive cracking of the repair concrete, exposing reinforcement to further corrosion (Beushausen, 2015).

Fibre reinforced polymer (FRP) strengthening has become a favourable structural strengthening method, given its high strength-to-weight ratio as well as its ease of application (Qeshta et al., 2016). Moreover, it has a been proven to be effective in not only restoring, but enhancing structural performance of corrosion damaged structures in terms of immediate ultimate limit state (ULS) capacity as well as long-term serviceability limit state (SLS) fatigue performance (Dong et al., 2012). The increased performance can be attributed to the redistribution of stresses between the reinforcing steel and FRP laminates (Ferrier et al., 2011).

The challenge with corrosion damaged, patch repaired and FRP strengthened RC structures is the inherent complex behaviour of composite multi-layered structures (Grant & Rousseau, 2008). Predicting the failure mode becomes challenging, because each one of the four interfaces is likely to fail (Ferrier et al., 2011). These four interfaces include the interface between concrete substrate and

patch repair mortar; one between the repair mortar and reinforcing steel; one between the repair mortar and FRP epoxy and lastly one between the epoxy and FRP laminate. Furthermore, in the case of FRP's with a low elastic modulus, the design is often guided by serviceability limit states as opposed to ultimate limit states (ULS), resulting in an over-reinforced structural member. In addition, the reinforcement area of commercially available FRP strengthening may exceed the design requirements, especially at low levels of corrosion damage. In both the abovementioned considerations the design may result in an over-reinforced section.

While fatigue behaviour of FRP strengthened RC structures has been reported in literature, there is a dearth of information on the fatigue behaviour of RC elements that have been patch repaired and over-reinforced with FRP strengthening.

1.2 Problem statement

Corrosion damage causes substantial service life loss of RC structures and compromises structural integrity. Although patch repairing and FRP strengthening have been proven to effectively restore durability and structural capacity, respectively, in terms of short-term mechanical properties, they come with their own set of challenges. Patch repairs are often associated with shrinkage cracks (Beushausen, 2015) that gradually propagate and form an ideal location for FRP laminates to start debonding.

With respect to long-term behaviour some research has been carried out on the fatigue behaviour of FRP strengthened beams, which includes research by Mahal (2015) who considered the effect of both externally bonded reinforcement (EBR) and near surface mounted (NSM) reinforcement. The study found that although EBR specimens performed better under cyclic loading than NSM reinforced specimens, both FRP strengthening methods improved the fatigue performance of RC beams. Song & Yu (2015) considered the long-term behaviour of strengthened RC beams that have corrosion damage and found that fatigue life was reduced by an increase in the degree of corrosion. However, neither of the aforementioned studies considered the effect of the patch repair component. Gregan (2012) did consider this combined effect, however the damage extent was not varied in his research. Dladla (2014) and Mundeli (2014), considered the effect of varying damage extent, but only reviewed its performance under static loading. Furthermore Habimana (2017) studied the behaviour of patch repaired beams with varying damage lengths under impact loading. The proposed research forms on the fatigue behaviour of corrosion damaged, patch repaired and over-reinforced with FRP strengthened RC beams with varying damage extents.

1.3 Research objectives

The main objective of this research was to design and conduct an experiment that would evaluate the effect of increasing the length of corrosion damage, patch repair and CFRP strengthening on the fatigue life of corrosion damaged RC beams that have been FRP strengthened. Specific aims of the study were to:

- Investigate the mode of failure of the composite system, considering the behavior of all materials and their interfaces
- Examine the effect of increasing damage length on the fatigue performance in terms of fatigue life, midspan deflection, neutral axis migration, material strains and crack behavior
- Monitor predetermined performance parameters using various data acquisition techniques that includes the use of strain gauges, linear variable differential transducer's (LVDT) and Demec targets
- Analyze the fatigue behaviour of the beams under cyclic loading with the aid of digital image correlation (DIC) in terms of crack behavior and midspan deflection. DIC will be assessed

during the first load cycle at various load intervals as well as during fatigue tests at a sample rate that is high enough to detect any structural behavior changes

- Compare failure modes to those obtained under static and impact loading

1.4 Scope and limitations of this research

This research endeavoured to investigate the research objectives set out in **Section 1.3** of this chapter. The research focus was on long-term behaviour of RC beams that have been corrosion damaged, patch repaired and over-reinforced with FRP strengthened in the context of the conceptual framework outlined in **Figure 1.1**. The conceptual framework outlined below categorizes parameters that affect structural performance, highlighting the focal areas of this research. These factors are not exhaustive, but were limited for the purpose of this research topic.

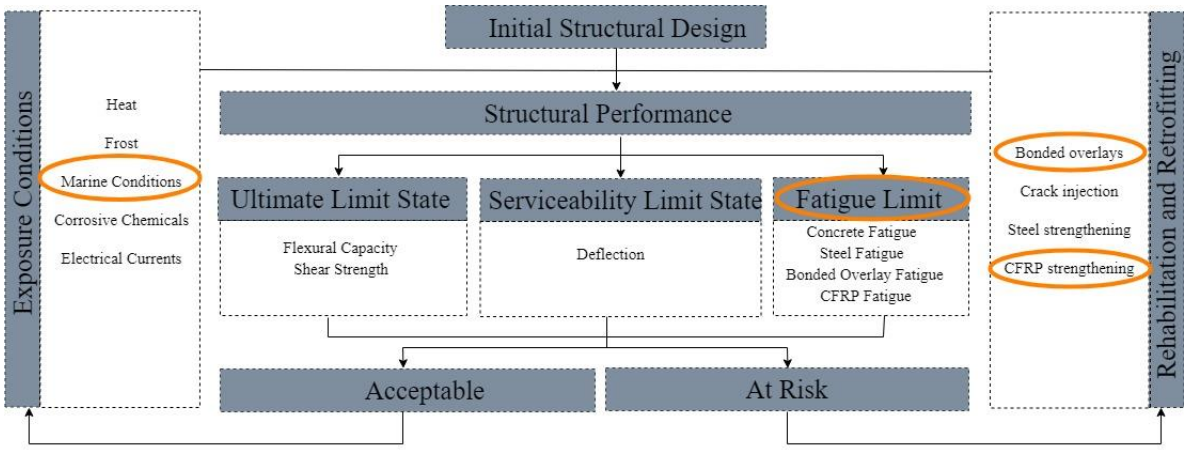

Figure 1.1 Research Conceptual Framework

Although the literature review covers the following list of parameters, they were kept constant during the experimental investigation:

- Various degrees of corrosion damage
- Different types of patch repair mortars
- Assorted classes of FRP strengthening

1.5 Thesis guide

This dissertation comprises seven main chapters that make up the body. Other headings that include the abstract, acknowledgements, list of figures, list of tables, list of abbreviations and appendices all serve to assist the reader in navigating and understanding the documented research.

***Chapter 1**: Introduction*

The first chapter sets out to introduce the research, giving a brief background of the topic while providing justification for the research. The chapter also lists research objectives and the scope of the research.

***Chapter 2**: Corrosion damaged reinforced concrete*

The second chapter serves as a foundation for this research study. It provides a thorough critical discussion of corrosion damaged reinforced concrete by considering the various processes and damage mechanisms associated with this composite section, in order to extract informed inferences from experimental data. These inferences are based on the fundamental behaviour of the individual materials involved, their combined performance, suitable performance indicators and the techniques used to assess them. The following topics are discussed in this chapter.

- RC corrosion
- Repair and strengthening of corrosion damaged RC
- Behaviour of corrosion damaged strengthened RC elements

***Chapter 3**: Fatigue of reinforced concrete*

Chapter 3 builds on the previous chapter as it narrows the literature study to fatigue behaviour. It discusses fatigue behaviour in general before considering the behaviour of the various composite materials under cyclic loading. A study of the various performance indicators builds on the performance indicators were introduced in the previous chapter that could be used to evaluate and understand the failure modes exhibited during fatigue testing specifically. Lastly the section considers various experimental techniques that aided in the design of the experiment in the subsequent chapter.

***Chapter 4**: Experimental methodology*

This chapter provides a detailed description of the experimental methodology employed to investigate the research objectives. The experimental methodology can be disintegrated into 5 main chronological steps as follows:

1. Design and casting of specimens
2. Accelerated corrosion
3. Patch repairing
4. FRP strengthening
5. Static and fatigue testing

***Chapter 5**: Results and discussions*

Chapter 5 presents experimental results of the specimens in terms of their performance indicators and are discussed in relation to ultimate research objectives.

***Chapter 6**: Conclusions and recommendations*

Concluding remarks and potential future undertakings are discussed.

***Chapter 7**: References*

References used in this research are listed in chapter 7 to substantiate documented findings.

2. CORROSION DAMAGED REINFORCED CONCRETE

The immoderate effects of steel corrosion on reinforced concrete (RC) civil engineering infrastructure, especially in terms of structural performance, have facilitated the need for this and similar studies for the primary purpose of understanding its damage mechanisms and how to improve both the immediate as well as long-term performance of structures affected by it. This chapter discusses its effects and potential mitigation measures against the backdrop of ultimate and serviceability limit states as contextualized in the research conceptual framework presented **Chapter 1**.

2.1 Reinforcement corrosion

Steel corrosion diminishes structural capacity of RC infrastructure due to a reduction of the steel cross-section. Reduced structural capacity, triggered by corrosion initiation, consequently shortens the anticipated service life of a structure as illustrated in **Figure 2.1**.

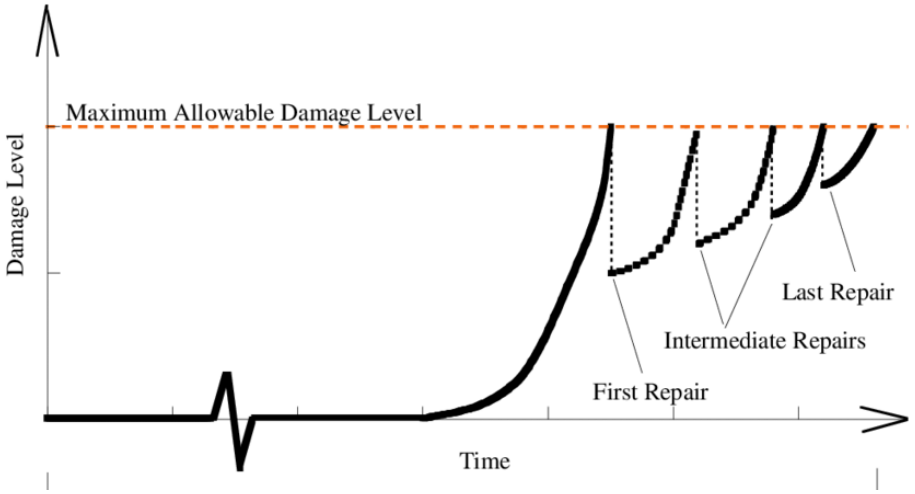

Figure 2.1 Infrastructure quality deterioration trajectories affected by corrosion (Sangoju et al., 2015)

Exposed steel undergoes a chemical reaction, generally known as corrosion and the reaction produces iron oxide. Corrosion of RC structures occurs at the interface between reinforcing bar and surrounding concrete, when an electrochemical cell is activated (Otieno et al., 2014). The interface, characterized by a passivating film, is inherently unreactive when encased in concrete, due to the relatively high hydrogen potential (pH) of concrete which is between 12.5-13.5 (Holmberg, 2010). The electrochemical cell on the reinforcement surface consists of two half cells, namely the anode and the cathode, which are represented by **Equations 2.1** and **2.2**. These equations govern corrosion of a divalent metal.

At the anode: $$Fe = Fe^{++} + 2e^{-} \quad (2.1)$$

At the cathode: $$\frac{1}{2}O_2 + H_2O + 2e^{-} = 2OH^{-} \quad (2.2)$$

Corrosion is initiated when electrochemical equilibrium between the two half cells is disturbed. There are two essential requirements to activate an electrochemical cell on the reinforcement surface. First, the passivating film should be destroyed (Owens, 2013). This is possible when the pH of the surrounding concrete is reduced sufficiently by carbonation or through the ingress of chlorides. Moreover, a potential difference is required between the concrete-steel system. This requirement can be fulfilled when sufficient moisture and oxygen accumulates at the interface, as it facilitates the electrolyte required for the electrochemical cell to be activated (Alhozaimy et al., 2014). When these two requirements are met, the corrosion process as shown in **Figure 2.2**, is initiated.

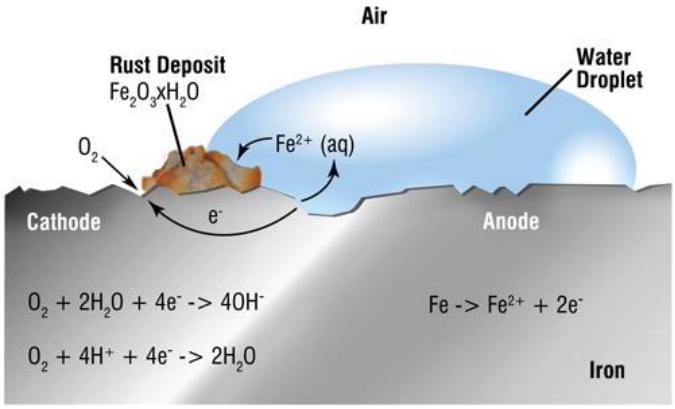

Figure 2.2 Electrochemical cell formed on reinforcement surface (Hydropars, 2020)

2.1.1 Damage progression

As documented by Otieno (2008) RC corrosion occurs in three distinct phases, namely:

- Initiation phase
- Propagation phase
- Acceleration phase

Requirements for initiation have been detailed in the previous paragraph. The propagation phase is dependent on the corrosion thermodynamics, which is best explained through the Pourbaix diagram of steel as shown in **Figure 2.3**. The diagram establishes possible stable phases of an aqueous electrochemical system (Alhozaimy et al., 2014; Arito, 2012). There are certain ideal conditions under which the corrosion process will thrive; that is a low pH and high potential difference.

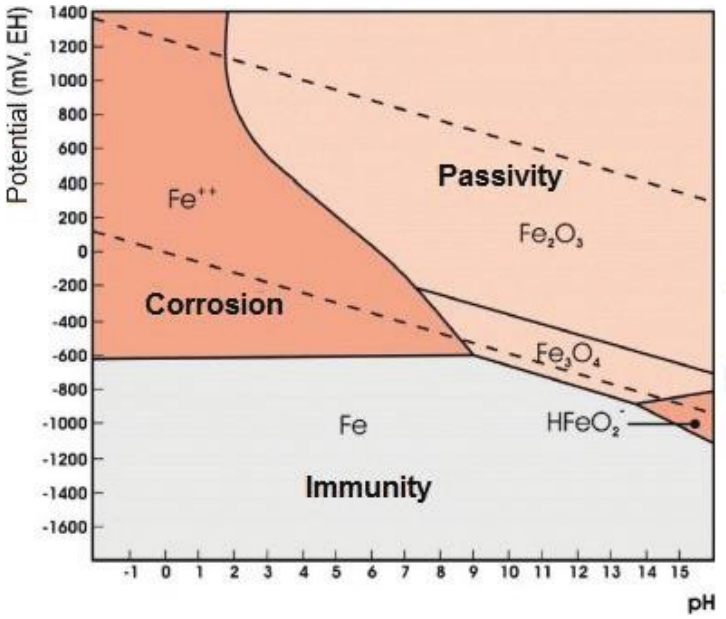

Figure 2.3 Pourbiax diagram illustrating ideal conditions to induce corrosion (Rivetti et al.,2018)

As depicted in **Figure 2.2**, corrosion products are formed at a different position from where the reaction takes place. These products, commonly known as rust, occupy a larger volume than the original steel and exert tensile forces on cover concrete (Owens, 2013). When sufficient rust accumulates the tensile forces will cause cracking, delamination and eventually spalling of cover concrete. Cracking can be considered the start of the acceleration phase of corrosion. When cracking occurs, a direct path to the

steel is availed for chlorides to de-passivate the protective film, as opposed to diffusing through the concrete pore structure (Otieno et al., 2010).

2.1.2 Durability of RC structures

Uncracked dense cover concrete provides a barrier against corrosion enabling environments (Otieno, 2008). However, once that barrier is conquered, carbon dioxide and or chlorides de-passivate the protective layer around steel and activates the chemical reaction.

Durability studies of RC structures constructed during the last few centuries have revealed a reduction in quality of cover concrete, compared to ancient Roman structures. Prescriptive design approaches, as opposed to performance based design have contributed to cover concrete that is more penetrable and permeable (Ballim & Alexander, 2009). Another contributing factor is that earlier cements used in the construction of ancient Roman structures, such as cathedrals and coliseums, either incorporated pozzolanic binders or they were made from inherently durable cements (Ballim et al., 2009); unfortunately, natural resources are depleted over time and those binders and cements are no longer available.

The environment that structures are exposed to is equally important and must be considered carefully. Steel may be exposed to the environment and still yield the same service life that it would have achieved had the corrosion initiation requirements not been met. Conversely, there are some environments that are highly conducive to reinforcement corrosion. Haque & Al-Khaiat (1997) found that buildings in coastal environments experienced a higher annual carbonation rate than in hot dry environments. Furthermore, Al-Negheimish & Alhozaimy (2008) documented that extremely hot weather affects concrete workability through increased slump which augments plastic shrinkage problems synonymous with hot environments. Therefore, in these two environments, reinforcement corrosion is more likely to occur if cover concrete is not adequately designed for. Performance-based design and service life models that have been validated with field observations have been argued as the most suitable engineering tool for durability design (Alexander & Beushausen, 2019).

2.2 Repair and strengthening of corrosion damaged RC

Premature deterioration may require rehabilitation and retrofitting to restore structural capacity as well as durability. As documented by Tilly & Jacobs (2007), there are various repair options available to stop or mitigate the effects of the corrosion reaction (options 1 to 4) and to enhance structural capacity (options 5-8).

1. Crack injection
2. Hydrophobic coating
3. Sprayed concrete
4. Cathodic protection
5. Fibre reinforced polymer (FRP) strengthening
6. U-jacketing (structural enlargement)
7. External post tensioning
8. Bonded steel strengthening

Each of the abovementioned repair options are associated with their own set of advantages and challenges, however, patch repairs or bonded overlays have prevailed as a commonly used technique (Beushausen, 2015). This may be due to its ability to restore and enhance durability of cover concrete if it is effective. Depending on how far the corrosion damage has progressed, structural strengthening techniques, such as FRP strengthening, may be considered to either restore or increase structural capacity, however FRP laminate debonding has been identified as a common cause of failure for RC

elements repaired using this method, despite it high strength-to-weight ratio and ease of installation (Gregan, 2012).

The repair and strengthening approach considered in this research involves three stages. It commences with the removal of damaged concrete, followed by application of a suitable patch repair mortar and ultimately the installation of an FRP laminate. This approach has been found effective in restoring durability and structural capacity of corrosion damage structures from a short-term ULS and SLS perspective (Dladla, 2014; Habimana, 2017; Malumbela et al., 2011; Mundeli, 2014; Tigeli, 2014).

2.2.1 Patch repair

The patch repair process as described above restores the alkaline protective film inherent of the concrete-steel interface (Ballim & Alexander, 2009). Effective patch repairs are ideally less penetrable than the original concrete structure, therefore improving durability of the structure (Eldho & Jones, 2016). Whilst popular, patch repairs are not immune to failure. In the discussion of effectiveness of patch repairs it is important to consider the various patch repair mortars available. **Table 2.1** shows the mechanical properties of the various patch repair mortars.

Table 2.1 Mechanical properties of various bonded overlays (Morgan et al., 1996)

Property	Resin Mortar	PMC Mortar	Plain Cementitious Mortar
Compressive strength (MPa)	50 - 100	30 - 60	20 - 50
Tensile strength (MPa)	10 - 15	5 - 10	2- 5
Modulus of elasticity in compression (GPa)	10 - 20	15 - 25	20 – 30
Thermal expansion coefficient (per °C)	25 - 30 x 10^{-6}	10 - 20 x10^{-6}	10 x10^{-6}
Water absorption (% by mass)	1 - 2	0.1 - 0.5	5 - 15
Maximum Service temperature (°C)	40 - 80	100 - 300	300

As shown in **Table 2.1**, patch repair mortars can be classified into three main categories (Gregan, 2012), which include:

1. Resin mortar
2. Polymer modified cementitious mortar
3. Plain cementitious mortar

The effectiveness of the patch repair is heavily reliant on compatibility between the patch repair mortar and the substrate concrete (Dladla, 2014; Gregan, 2012). That is compatibility in terms of strength, thermal expansion coefficients as well as material composition or microstructure. Hassan & Brooks (2001) found polymer modified cementitious (PMC) repair mortars to be most appropriate for patch repairs given their dimensional stability as well as similar elastic modulus and low shrinkage strains in relation to substrate concrete. In addition, from a structural performance viewpoint, their results showed that a mismatch in modulus of elasticity lead to a reduction in load carrying capacity. Although patch repairs are commonly used to restore durability of RC structures, studies conducted by Tigeli (2014) and Malumbela (2010) have shown that patch repairs may also improve stiffness by as much as 10%.

2.2.1.1 Failure mechanisms

The problems associated with patch repairs are most commonly related to restrained shrinkage and debonding of the patch repair mortar (Beushausen, 2015; Beushausen & Chilwesa, 2013). Both problems are due to incompatibility of the two materials.

Cracking occurs because of differential shrinkage when mortar closest to the surface loses moisture faster than internal mortar. The relative contraction between surface and internal material induces tensile forces which lead to cracking (Ballim & Alexander, 2009).

Bond strength between the substrate concrete and patch repair mortar plays a crucial role in ensuring compatibility. If the applied loads induce stresses that exceed the bond slip stress, delamination of the patch repair is likely to occur. To that end Courard et al.(2014) showed the importance of substrate preparation in yielding high bond strength. In addition to substrate preparation, a performance-based design approach may be useful to improve compatibility. This can be done by preparing various mix designs and conducting laboratory tests such as shrinkage tests, tensile strength and compressive strength tests, as well as pull-off tests on field concrete core samples to assess their mechanical properties (Beushausen & Alexander, 2006; Dladla, 2014). Ring tests assess restrained shrinkage performance of the bonded overlay, where bridging fibres have shown to reduce shrinkage cracking (K. Kim et al., 2017) and pull-off tests assess bond strength between the two materials.

2.2.2 Fibre reinforced polymer strengthening

The application of fibre reinforced polymers (FRPs) in civil engineering started in the 1980s and has since been proven quite effective in restoring as well as enhancing structural capacity of deteriorating structures (Aravind et al., 2013; Chen & Qiao, 2009). Compared to other structural strengthening methods such as external post-tensioning, structural enlargement or micro-reinforcement concrete systems, FRP strengthening has been a more favourable option. This may be attributed to its high strength-to-weight ratio and ease of installation (Dladla, 2014; Gregan, 2012; Mahal, 2015). Furthermore, FRPs require little to no additional space, as shown in **Figure 2.4,** in relation to other techniques and especially for retrofitting purposes where clearance height is limited this property is highly beneficial.

Figure 2.4 FRP strengthening application (structuraltechnologies, 2018)

Due to the high cost associated with structural strengthening and FRP strengthening in particular, literature recommends a thorough investigation and analysis of the existing structure prior to any structural strengthening (Abdelrahman & El-Hacha, 2014; Täljsten, 2006). Wipf et al.(1987) evaluated the cost-effectiveness of two structural strengthening methods on existing bridges in comparison with an option of replacing the bridge altogether. Their strengthening options included strengthening the bridge with steel stringers (method 1) and adding a pier at midspan (method 2); it was found that both strengthening options would cost less than the replacement alternative with method 1 costing 28.01% lower than the replacement option and method 2 costing 1.64% lower. Seixas & Costa (2013) analysed the costs associated with three strengthening methods used for building, which included CFRP laminates, CFRP sheets and externally bonded steel plate strengthening. They found that CFRP

strengthening using sheets was 16.28% more expensive than steel plate strengthening. In relation with the study by Wipf et al.(1987) the cost of CFRP strengthening would only be 11.73% lower than the replacement option. If one considers the cost of bridge construction in South Africa can be as high as R3.9 billion, a cost saving 28.01% in comparison with 11.73% can be quite significant.

While material properties may be established through the use of various non-destructive test (NDT) methods, the employment of structural health monitoring (SHM) may provide an indication of the actual structural performance (Busatta & Moyo, 2017; Xu & Brownjohn, 2018). Once existing properties and structural behaviour is known, an informed performance-based design can be carried out. FRPs are available in various materials. Aravind et al. (2013) and Täljsten (2006) have documented the different types of FRPs in much detail. The mechanical properties of various types of FRPs are presented in **Table 2.2**.

Table 2.2 Mechanical properties of various FRPs (Täljsten, 2006)

Fibre	Elastic Modulus (GPa)	Tensile Strength (MPa)	Ultimate Tensile Strain (%)
Glass			
E	72-77	2000-3700	3,0-4,5
S	80-90	3500-4900	4,2-5,4
AR	71-74	3000-3300	3,0-4,3
Aramid			
Low modulus	70-80	3500-4100	4,3-5,0
High modulus	115-130	3500-4000	2,5-3,5
Carbon			
PAN	230-600	2500-6000	0,9-2,0
Pitch	200-800	2100-3100	0,2-0,9

These FRPs are available in various forms as well, which may include laminates, sheets (wrap) and near surface mounted rods (NSMR). Sheets can be used for strengthening columns, as shown in **Figure 2.4**, to resist bursting forces. They can also be used on RC beams to enhance shear strength, as showed by Dong et al. (2012). Laminates and NSMR are generally used for strengthening RC slabs or beams to resist flexural stresses. Mahal et al., (2015) found externally bonded specimens to be appreciably stiffer than NSMR specimens in terms of deflection, crack distribution and crack height when subjected to fatigue behaviour. In contrast Ceroni (2010) found NSMR to outperform externally bonded laminates when the specimens were strengthened to a higher degree. In terms of failure mode Ceroni (2010) found that NSMR failed by crushing of compression concrete, whereas externally bonded specimens exhibited brittle failure due to end debonding of the laminates. It was however noted that end debonding failure could be ameliorated using U-shaped FRP strips. Nonetheless, both research studies demonstrated that strengthened beams outperformed their un-strengthened counterparts.

Various types of FRPs can be considered during the design phase. Each of these are associated with their own advantages and drawbacks with respect to mechanical properties, fire resistance, cost, sustainability and durability (Täljsten, 2006). **Table 2.2** shows the difference in mechanical properties of three types of FRPs, however carbon fibre reinforced polymers (CRFP) have been shown to be most suitable for RC structures (Kim et al., 2017). FRP design is informed and guided by potential failure modes, therefore it is important to consider the various failure modes prior carrying out any designs.

2.2.2.1 Failure mode of FRP strengthened beams

FRPs can be either isotropic or anisotropic materials that exhibit multiple failure modes if considered in isolation (Täljsten, 2006). These failure modes include:

- Matrix failure
- Fibre failure

- Adhesion failure
- Delamination

If considered as part of a RC composite system the FRP laminate, rod or sheet forms part of an intricate composite system, where breakdown of the entire composite section is more likely to occur before the FRP fails (Täljsten, 2006). RC beams that have been patch repaired and FRP strengthened consist of multiple layers and their adjoining interfaces. This repair approach considered involves four interfaces, which include:

1. Interface 1 between concrete substrate and patch repair
2. Interface 2 between reinforcement and patch repair
3. Interface 3 between patch repair and epoxy adhesive
4. Interface 4 between epoxy adhesive and FRP laminate

Figure 2.5 depicts all the forces on a finite element of an RC beam strengthened with FRP. This figure serves to depict the complexity of such a system. Depending on the imposed loads, any one of the interfaces are subject to failure if their design capacities are exceeded.

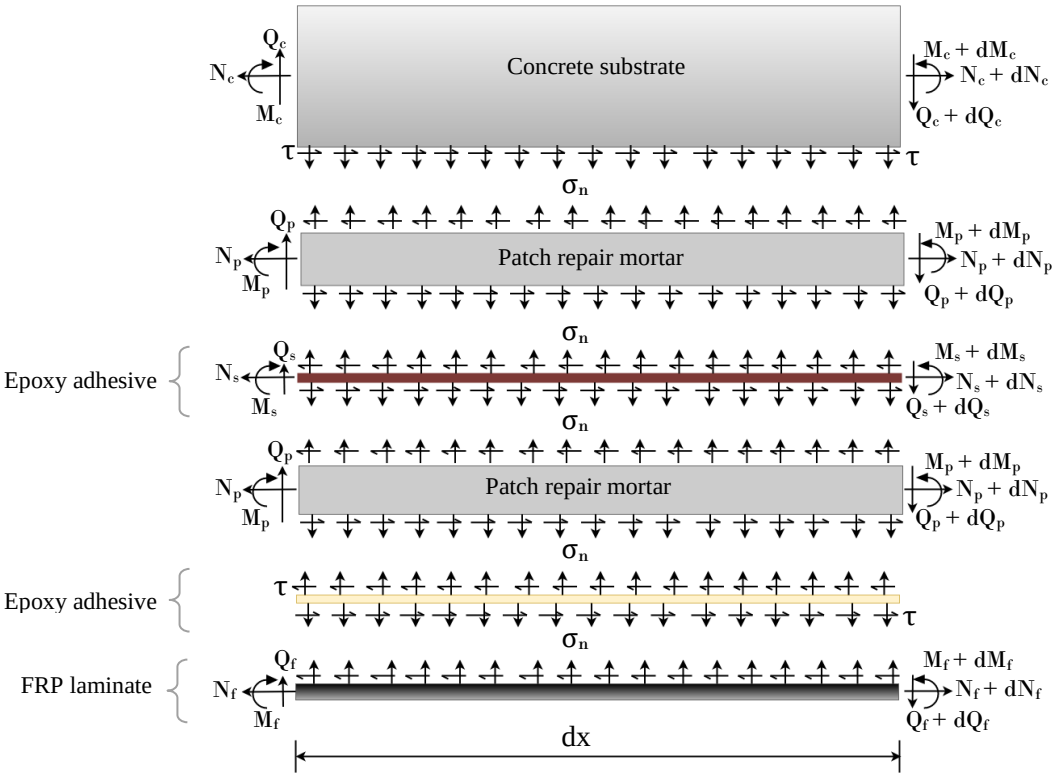

Figure 2.5 Forces at various interfaces of composite system

Effective redistribution of applied stresses requires a strong bond between the concrete substrate and FRP. Once tension steel has ruptured or yielded, much of the strain is assumed by the FRP causing the bond between the FRP and substrate concrete to be the source of failure (Ceroni, 2010; Dladla, 2014). A good epoxy adhesive ensures the desired compatibility that provides structural force equilibrium between the compressive concrete, tensile steel and the FRP (Malumbela, 2010). To that end quality control is essential, to ensure that there are no unbonded areas between the FRP laminate and concrete substrate, as these areas have shown to increase the likelihood of FRP delamination. Dladla (2014) documented the potential that infrared thermography holds in identifying areas of delamination, despite it not being as useful in his research study as he may have liked.

The primary failure mechanism associated with layered systems is bond stress slip (Dladla, 2014; Song & Hou, 2017; Song & Yu, 2015; Zhang, Teng, & Yu, 2013). A significant reduction of bond shear stress that causes slippage has been identified with layered systems, especially if the concrete does not contain any bridging materials such as steel fibres (K. Kim et al., 2017). When slip occurs, the entire bonded overlay or parts of it may delaminate and peel off.

Using **Equations 2.3** and **2.4**, or adaptions thereof accommodate various types of materials, it is possible to determine the principle stresses at each interface due to imposed loads (Dladla, 2014).

$$\sigma_x = \frac{N}{A} - \frac{M_z y}{I_{zz}} + \frac{M_y z}{I_{yy}} \tag{2.3}$$

$$\tau_{xy} = \frac{QAy}{Ib} \tag{2.4}$$

Where:

σ	=	normal stress in a certain direction
τ	=	shear stress
M	=	moment about a certain direction
A	=	area
I	=	second moment of inertia
Q	=	shear force
b	=	section breadth
z	=	unit measurement in z-direction
y	=	unit measurement in y-direction

FRP strengthened RC beams may exhibit multiple modes of failure, as shown in **Figure 2.6**, which are related to either an under-reinforced or over-reinforced section (Täljsten, 2006).

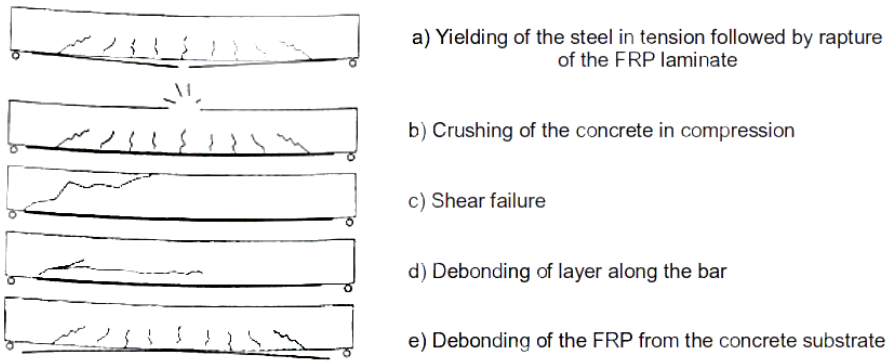

Figure 2.6 Failure modes of FRP strengthened RC beams (Radyab, 2018)

A good FRP design considers bending, shear, torsion as well as fatigue behaviour (Täljsten, 2006), however, *fib* (2001) recommends a safety concept with respect to ULS design, which suggests that the governing failure mode of a flexural member shall be of a nature that brittle failure, associated with shear and torsion, are excluded. Therefore, the desired failure would be yielding of tension steel or crushing of compression concrete prior to debonding or rupturing of the FRP. For this reason, only the flexural design will be considered in this discussion.

2.2.2.2 Design for strengthening

Over-reinforced sections are undesirable due to the brittle failure modes associated with them; however, they are often unavoidable for two main reasons. Firstly, the modulus of elasticity ***E*** of non-carbon FRP reinforcement is often lower than that of steel as shown in **Table 2.2**, in which case the serviceability limit state (SLS) design will govern the design check as opposed to ultimate limit state (ULS) design (Spadea, Orr, & Nanni, 2016). Furthermore, the reinforcement area $\boldsymbol{A_s}$ of commercially available FRP strengthening may exceed the design requirements, especially at low levels of corrosion damage. In both the abovementioned considerations the design may result in an over-reinforced section. This illuminates the likelihood of a substantial number of flexural members that have been over-reinforced using FRP to limit deflection and are therefore likely to exhibit a brittle failure mode as opposed to the ductile failure recommended in the *fib* Bulletin 14 (2001). There is a dearth in research that considers the performance of over-reinforced concrete beams, therefore this section will focus on the design of over-reinforced sections.

The design for FRP strengthening follows the same limit state design principles used in RC design which considers the horizontal internal force equilibrium. **Figure 2.7** shows the internal forces on an FRP strengthened RC beam.

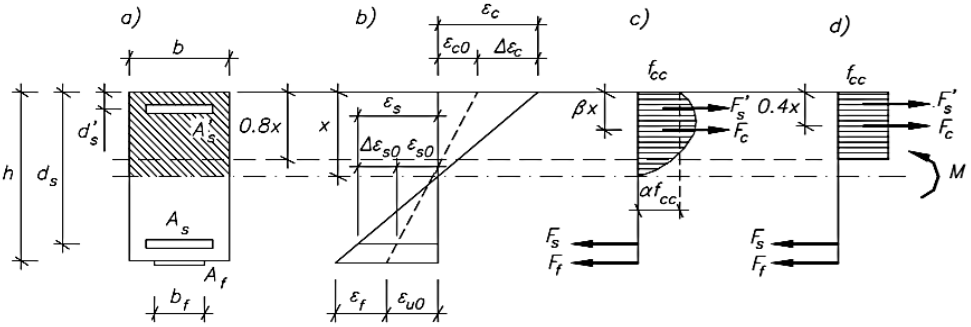

Figure 2.7 Stress-strain relationship in FRP strengthened RC beams (Täljsten, 2006)

There are two main design categories to consider when analysing FRP strengthened sections at ULS (*fib*, 2001), which are:

1. Full composite action
2. Loss of composite action

Full composite action contemplates two predominant failure modes, which include (a) steel yielding followed by concrete crushing and (b) steel yielding followed by FRP fracture. Loss of composite action deals with (a) peeling-off caused at shear cracks, (b) Peeling-off at the end anchorage and at flexural cracks, (c) end shear failure and (d) peeling-off caused by the unevenness of the concrete surface (*fib*, 2001). Täljsten (2006) makes a further distinction among the failure modes of section for full composite action analysis as listed I to IV below. It is possible to design for one of these failure modes to control the behaviour of the structure when it fails by adjusting the reinforcement ratio (Täljsten, 2006).

I. Failure in laminate with yielding in the compression steel reinforcement
II. Failure in laminate without yielding in the compression steel reinforcement
III. Crushing of concrete as well as yielding in the compression steel reinforcement
IV. Crushing of concrete without yielding in the compression steel reinforcement

When commencing with an FRP strengthening design, in the case of a corrosion damaged section, the amount of FRP strengthening can initially be estimated by the change in moment due to the loss of cross-section using **Equation 2.5**.

$$A_{FRP} = \frac{\Delta M}{0.9\, h \varepsilon_f E_f} \tag{2.5}$$

Where:

ΔM	=	difference in ULS moment to be carried by FRP
h	=	beam depth
ε_f	=	FRP strain as provided by supplier
E_f	=	FRP elastic modulus as provided by supplier

Once the amount of FRP strengthening has been estimated the four failure modes, associated with full composite action behaviour, can be considered for flexural design. The failure modes are dependent on strengthening ratios, where the ratios represent the amount of actual reinforcement relative to a normally-reinforced section. The four possible failure modes for double reinforced beams are paired with the strengthening ratio conditions as follows:

I. Failure in laminate with yielding in the compression steel reinforcement

$$\rho_{fu} \leq \rho_{f1} \leq \rho_{fn} \tag{2.6}$$

II. Failure in laminate without yielding in the compression steel reinforcement

$$\rho_{f2} \leq \rho_{fu}\,, \rho_{fn} \tag{2.7}$$

III. Crushing of concrete as well as yielding in the compression steel reinforcement

$$\rho_{f1} \geq \rho_{fn}\,, \rho_{f0} \tag{2.8}$$

IV. Crushing of concrete without yielding in the compression steel reinforcement

$$\rho_{fn} \leq \rho_{f2} \leq \rho_{f0} \tag{2.9}$$

Parameter ρ_f is a strengthening ratio which represents the strain condition in the compression steel reinforcement. ρ_{f1} and ρ_{f2} indicate whether the steel has yielded or not, respectively. ρ_{fu} , ρ_{fn} and ρ_{fo} evaluate either normally-reinforced, balanced or over-reinforced strengthened cross-sections, respectively. Depending on the desired outcome, the amount of strengthening can be adjusted.

The moment capacity of the strengthened section will depend on the desired failure type. In the case of an over-reinforced section the element will exhibit failure mode IV. For that failure mode the neutral axis depth and moment capacity is calculated from **Equations 2.10** and **2.11**, respectively, below.

$$\alpha f_{cc} b x + \left(\frac{x - d'_s}{x}\right) A'_s E_s = A_s f_y + \left(\frac{h-x}{x}\varepsilon_{cu} - \varepsilon_{u0}\right) E_f A_f \tag{2.10}$$

$$M_{capacity} = \left(\frac{x-d'_s}{x}\varepsilon_{cu}\right) A'_s E_s (\beta x - d'_s) + A_s f_y (d_s - \beta x) + \left(\frac{h-x}{x}\varepsilon_{cu} - \varepsilon_{u0}\right) E_f A_f (h - \beta x) \tag{2.11}$$

Where:

$M_{capacity}$ = moment capacity of strengthened RC beam
α = proportionality factor for concrete
f_{cc} = concrete compression strength
x = inner lever arm
d_s = effective height to tensile reinforcement
d'_s = effective height to compression reinforcement
ε_{cu} = compressive strain in concrete
ε_{u0} = strain in underside concrete remaining load
A'_s = compression reinforcement area
A_s = tensile reinforcement area
A_f = cross-sectional area of composite
E_s = modulus of elasticity of steel
E_f = modulus of elasticity for composite
β = proportionality factor for concrete
f_y = yield stress in tensile reinforcement
h = section height

Täljsten (2006) and *fib* (2001) present various permutations of **Equations 2.10** and **2.11** depending on the failure mode; due to the specific interest in over-reinforced sections they will not be presented in this section.

2.3 Behaviour of corrosion damaged strengthened RC elements

The method of enhancing structural performance of corrosion damaged RC structures described in this chapter, by patch repairing and strengthening using FRP laminates, constitutes a composite structure with complex failure mechanisms as evident by the literature reviewed in the sections above. During the last decade research by Malumbela (2010), Gregan (2012), Tigeli (2014), Mundeli (2014), Dladla (2014) and Habimana (2017) have illuminated some interesting parametric correlations of specimens repaired using this method. There are five main performance parameters which were deemed relevant and useful to the topic of this research; these parameters are:

- Flexural capacity
- Fatigue life
- Development of cracks
- Ductility
- Stiffness

At this point it may be convenient to make a clear distinction between static and dynamic structural performance. The nature of discourse for the above listed performance parameters will differ depending on the type of performance under consideration. Some parameters will only be applicable to static performance such as ductility, where the transition between the elastic and plastic regime is considered (Dladla, 2014). Other parameters such as fatigue life are specific to long-term dynamic behaviour (Gregan, 2012).

To derive a holistic comprehension of these parameters, they will be discussed both in terms of their static performance as well as long-term dynamic performance. This section will only focus on their static performance. Chapter 3, which narrows the focus of the study to fatigue behaviour, will discuss these parameters in the context of long-term dynamic behaviour.

2.3.1 Flexural capacity

Reinforcement corrosion, especially in the accelerated phase, leads to rapid loss of steel cross-section that reduces structural load carrying capacity (Lee et al., 1999). Malumbela et al., (2011) studied 20 quasi-full-scale patch repaired and FRP strengthened RC beams that were corrosion damaged to various degrees, tested under sustained loading. Their results found that a 1% mass loss in steel diminishes load carrying capacity by 0.8%. They further found that FRP strengthening was able to significantly increase the flexural capacity to 50% more than the uncorroded specimens, as shown in **Figure 2.8**. Although their findings showed that the patch repair contributed insignificantly to increasing flexural capacity compared to FRP strengthening, more importantly it showed that the rate of load bearing capacity reduction was reduced after patch repairing and FRP strengthening.

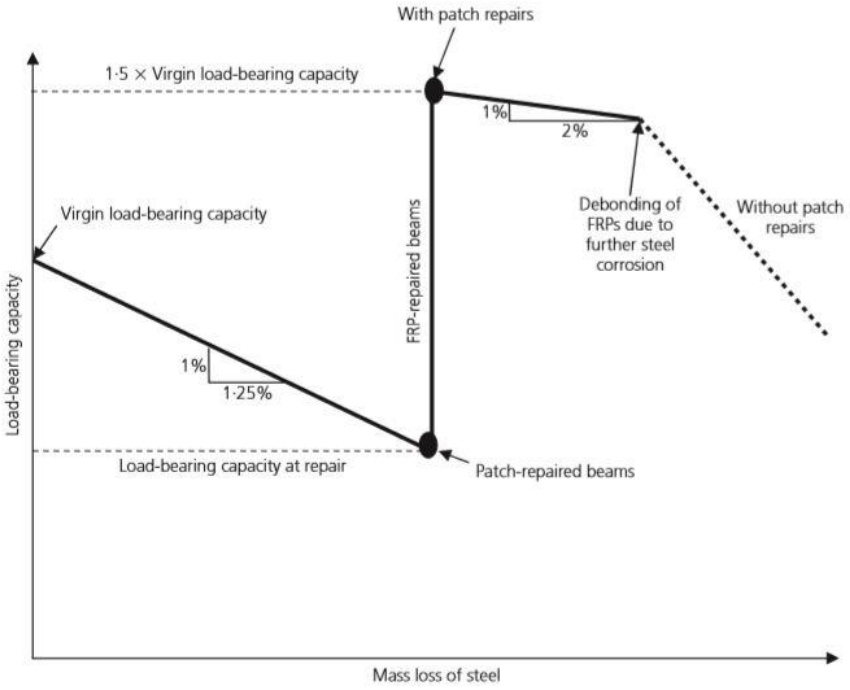

Figure 2.8 Effect of FRP strengthening and patch repairs on corrosion damaged RC beams (Malumbela et al., 2011)

Malumbela's (2010) findings were quite similar to predictions made by Ting & Nowak (1991) who carried out a finite element analysis (FEA) of a typical concrete bridge T-beam. In their finite element model (FEM) they considered various degrees of corrosion and their analysis showed that a 1% steel mass loss resulted in 0.7% reduction in load carrying capacity, in the absence of patch repairs and FRP strengthening. Azad et al. (2007) also documented correlations of a 1.4% reduction in load carrying capacity due to 1% mass loss, which may entertain the idea of an even linear relationship between steel mass loss and residual structural capacity. However, Azad et al. (2007) as well as Mangat & Elgarf (1999) agree that at higher degrees of mass loss the relationship gradient varies considerably as Mangat & Elgarf (1999) recorded a 78% reduction in load carrying capacity due to a 20% steel mass loss.

Dladla (2014) also investigated the flexural capacity of quasi-full-scale corrosion damaged, patch repaired and FRP strengthened RC beams, under sustained loading. However, instead of varying the degrees of corrosion, he opted for a uniform degree of corrosion of 5% area loss and rather varied the length of damage on the specimen between 0mm, 450mm, 800mm, 1300mm and 1800mm. Results from this study showed that specimens with a corrosion and patch repair length of 1800mm had a 6% higher flexural capacity than those with 450mm corrosion and patch repair length.

These studies show that flexural performance of RC specimens is sensitive to not only the degree of corrosion, but also the length of the corrosion damage; an increase in the degree of corrosion may reduce the load carrying capacity whereas an increase in the length of corrosion damage increases the flexural capacity if these specimens are patch repaired to the equivalent length as the corrosion damage and subsequently FRP strengthened. Furthermore, they show that FRPs assist a great deal in restoring structural capacity. This may be attributed to the FRP's role in assuming the tensile forces that were initially solely carried by tensile steel and concrete as shown in horizontal force equilibrium diagram in **Figure 2.7**.

2.3.2 Development of cracks

Cracking in RC structures may occur for various reasons. It may be due to either one or a combination of the causes listed below:

- Shrinkage cracking
- Plastic settlement cracking
- Thermal expansion and contraction cracking
- Corrosion cracking
- Structural cracking

The cracks may start off as micro-cracks and gradually widen as the structure experiences cyclic loading (Gregan, 2012; Kumar, Gardoni, & Sanchez-Silva, 2009; Mahal, 2015). For infrastructure management and SHM purposes, it is essential to identify the location of these cracks and monitor their progression. In their review of externally bonded RC beams Qeshta et al. (2016) made a strong argument for externally bonded FRPs, reporting that they improve cracking behaviour of RC beams. Their findings were augmented by Elghazy et al., (2018) who evaluated the performance of corrosion damaged specimens, patch repaired and strengthened with externally bonded FRPs. Their study showed that corroded un-strengthened specimens exhibited crack patterns that were denser, deeper and wider than those specimens that were patch repaired and strengthened, as shown in **Figure 2.9**.

Qeshta et al. (2016) also reported that externally bonded RC beams required a higher applied load to induce cracking than un-strengthened beams. The study conducted by (Dladla, 2014) extended the findings put forth by Qeshta et al. (2016) by showing that, for the same degree of corrosion, the load required to cause initial cracking reduced as the damage extent increase from 450mm to 1800mm.

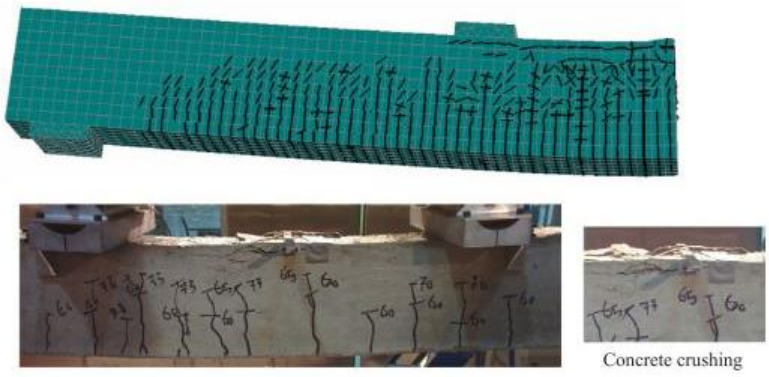

(a)

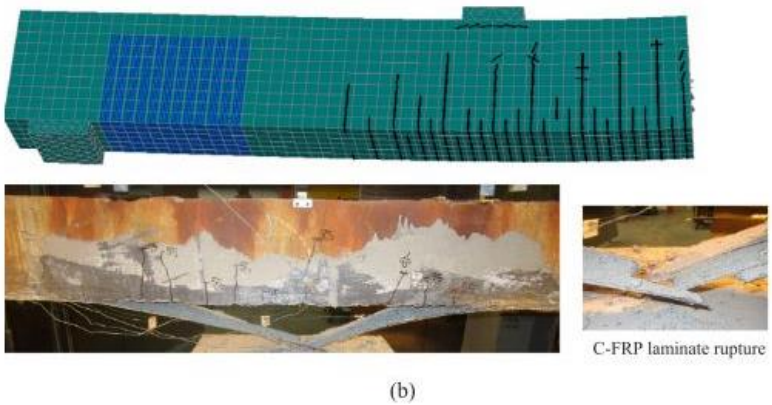

Figure 2.9 Effect of FRP strengthening on crack behaviour (Elghazy et al., 2018)

2.3.3 Ductility

A material experiences the transition between elastic and plastic regimes if it has ductile qualities. This transition or ductile zone serves two main function. Primarily, to alert structural engineers of impending structural failure. This is a desirable quality and is recommended in terms of the design for FRP (*fib*, 2001), as it allows for plans to salvage the structure, as opposed to sudden brittle failure (Täljsten, 2006). Secondly, during this phase redistribution of stresses occurs. When redistribution occurs, excessive cracking may be observed. Corrosion tends to reduce ductility of RC beams (Yi et al., 2011) while FRPs have been shown to enhance ductility of RC beams (Maranan et al., 2015), it would therefore be interesting to investigate the effect that a patch repair has on ductility.

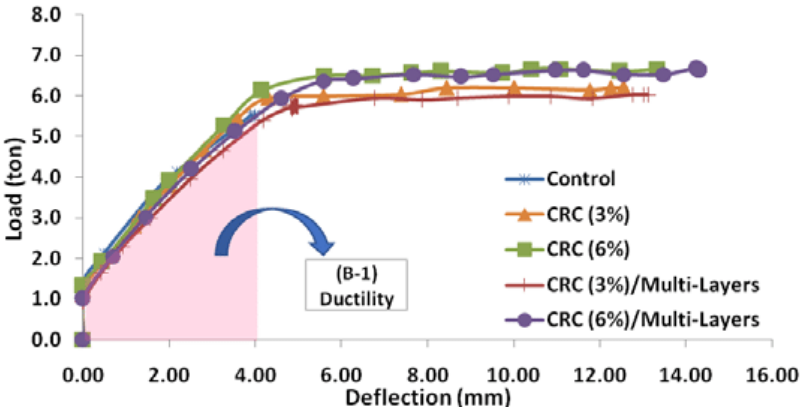

Figure 2.10 RC beam transition into ductile regime (Emam & Yehia, 2018)

Although ductility is useful when discussing static behaviour, it is not a parameter synonymous with fatigue, and even less so with over-reinforced concrete sections. This is because fatigue problems commonly occur at low operational stresses before any yielding has occurred (Mahal, 2015). Though it is a very useful concept to keep in mind when discussing stiffness, especially with regard to redistribution of stresses.

2.3.4 Stiffness degradation

There are multiple ways in which stiffness can be assessed. Although this section will document three different methods, only two of them will be discussed in depth as the third one, namely its assessment using natural frequency, falls outside the scope of this research.

2.3.4.1 Deflection resistance

Flexural stiffness can be defined as a resistance to deformation (Dladla, 2014). It is a system parameter determined by deflection and applied load. Stiffness can be calculated using **Equation 2.12**:

$$k = \frac{P}{\delta} \tag{2.12}$$

Where:

k	=	stiffness
P	=	applied load
δ	=	deflection

Stiffness or load deflection behaviour consists of three main stages: pre-cracking, post-cracking and post yielding (Qeshta et al., 2016). These three stages may be used to establish a framework for the discussion as it immediately highlights two other performance parameters that are closely linked to each of these stages, which are crack behaviour and ductility (Dladla, 2014). Another crucial parameter in the discussion of stiffness is stress redistribution.

If one considers the main stages of stiffness, most beams under service loads are in the post-cracking stage. In fact, ULS design assumes a cracked section which renders tensile concrete ineffective; as shown in **Figure 2.11** there is no contribution from the tension concrete (Malumbela et al., 2011). In the absence of FRP, the internal forces responsible for resisting externally applied forces are the compression steel, compression concrete and tension steel, they are essentially responsible for the stiffness of the structure. However, if one adds the FRP force the internal force diagram, it will aid the stiffness of the section, assuming all bonds between materials are perfect and robust.

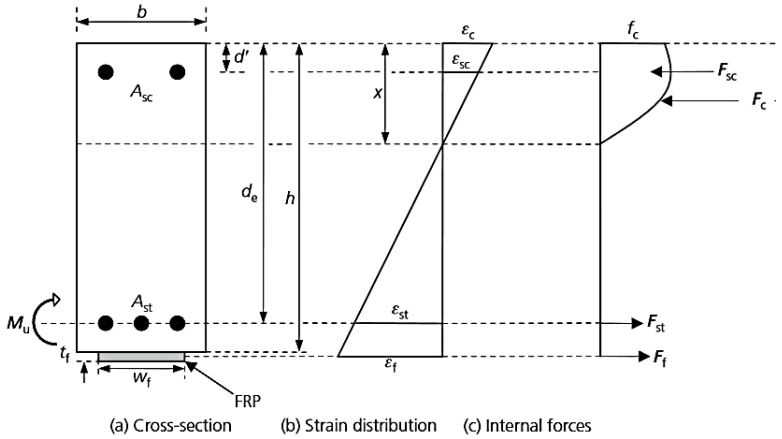

Figure 2.11 Internal force and strain distribution of an FRP strengthened RC beam (Malumbela et al., 2011)

The concept described in the previous paragraph forms the basis of many research studies that have shown how FRP strengthening improves the stiffness of corrosion damaged element. Some of these studies include those by Lee et al. (1999) and Qeshta et al. (2016). As discussed in the section on crack behaviour, FRPs reduce the crack behaviour. One would therefore also need to consider the contribution of the tension concrete to the internal forces, and in the case of a patch repaired section, the contribution of the patch repair as described by Malumbela et al. (2011). If one were to incorporate the internal force contribution of the tensile concrete as well as the patch repair mortar, it may be useful to make use of the elastic theory of SLS design to quantify the net moment resistance (Kong & Evans, 1987), which assesses the in-service behaviour of specimens prior to yielding of tension steel.

If one looks at the post yielding stage of load-deflection, one can interpret the behaviour of RC sections with stress redistribution in mind. In the absence of FRP, when the tension steel yields and is no longer able to resist the applied load, the section will in attempt to establish internal equilibrium by redistributing the internal stresses amongst the various materials. As this happens the neutral axis

migrates downwards, causing an increase in strain in the compression concrete. As this happens, the section experiences increased deflection and crack behaviour as it transitions through its ductile phase (Kong & Evans, 1987). Various studies have shown that when yielding occurs, the tensile stressed are assumed by the FRP for a certain period, essentially improving the ductility of the section. The behaviour described in this paragraph is associated with under-reinforced sections. With over-reinforced sections the tension steel is designed not to exhibit this failure mode (Täljsten, 2006).

2.3.4.2 Neutral axis migration

The depth of the neutral axis from the compression surface is another useful way of assessing the stiffness of a flexural member. Various studies have done this by tracking the relative movement of Demec targets at midspan on one or more surfaces of a specimen (Dladla, 2014; Gregan, 2012; Tigeli, 2014).

Considering the various internal forces of a section shown in **Figure 2.11**, Hollaway (1999) and Dladla (2014) describe a downward shift of the neutral axis as it operates in the elastic regime, but once the tension concrete is fully cracked and the FRP is fully engaged there is a transient stiffening of the section characterized by an upward shift of the neutral axis. This phenomenon known is as post-cracking stiffness and occurs fairly early in the service life of FRP strengthened specimen. The study by Dladla (2014) showed that as the sustained load is increased, there is a further upward shift of the neutral axis. In addition, the study revealed that as the corrosion damage length was increased, the neutral axis tended to shift downward; the neutral axis for the 1800mm specimen shifted by 6.86mm further down than for the 800mm specimen. In addition**, Figure 2.11** shows how a significant portion of strain is assumed by the tensile steel and FRP, resulting in a relatively high neutral axis. This provides some insight as to why FRP strengthening has been found effective in controlling crack behaviour, which directly affects structural durability and stiffness (Dong et al., 2012).

The method of tracking neutral axis migration described in this section, is not always reliable. Dladla, (2014) reported that strain measurements were disrupted as the cracks in the tension concrete propagated and only the targets closest to the compression face could be used. This latter statement brings into question the usefulness of this method in tracking the migration of the neutral axis.

2.3.4.3 Natural frequency

Natural frequency is an essential parameter in the analysis of dynamic behaviour of structures, where it resists externally applied loads together with inertial and damping forces (Chopra, 2012). It also provides another possible parameter to monitor structural stiffness. If the structural system undergoes change, such as cracking, reduction in strength due to fire damage or when structural strengthening is carried out, there will be a change in the natural frequency (Dladla, 2014). A change in natural frequency may be detected by a change in the elastic modulus if all the other system parameters remain unchanged. Natural frequency is calculated using **Equation 2.13**:

$$\omega_i = \frac{{\lambda_i}^2}{2\pi L}\sqrt{\frac{EI}{m}} \tag{2.13}$$

Where:

ω_i = natural frequency
λ_i = dimensionless parameter which is a function of the boundary conditions
L = beam span
E = elastic modulus
I = second moment of inertia

2.4 Chapter summary

The literature reviewed in this chapter considered various factors that form part of the research objectives and more specifically the conceptual framework outlined in **Figure 1.1**. The section on corrosion damaged RC beams discusses the damage mechanisms and the effect that corrosion has on structural performance. The literature review highlighted the importance of durable cover concrete in preventing the effects of corrosion damage and the critical influence that performance-based concrete design could have in the prevention attempt. The section further considered common approaches used to restore structural durability and capacity, with specific emphasis on patch repairs and FRP strengthening. The importance of compatibility between the substrate concrete and patch repair was emphasized not only in terms of chemical composition, but mechanical properties as well. Moreover, FRP strengthening was discussed in terms of design approach and how over-reinforced sections are a common occurrence despite *fib* (2010) recommendations advising against it. The chapter finally identifies parameters that can be used to evaluate structural performance of this complex composite section, focussing specifically on static behaviour. Although performance parameters ductility and natural frequency as a measure of stiffness degradation were discussed given their relevance to structural performance, they are not synonymous with fatigue behaviour and will therefore not form part of the experimental study.

3. FATIGUE OF REINFORCED CONCRETE

3.1 General fatigue behaviour

Fatigue is characterized by microcracking of a material, cracks that propagate under cyclic loading until eventual rupture (Mahal, 2015). Fatigue behaviour of corrosion damaged RC beams is not an entirely new phenomenon, given that Hoeppner (1979) already made significant research contributions a few decades ago, when he proposed a model for prediction of fatigue life through the use of an empirical pitting rate curve together with crack growth data. The fatigue behaviour of RC structures has been a subject of study owing to its ability to cause structural failure at stresses well below ULS design stresses.

Although each one of the composite materials of corrosion damaged, patched repaired and FRP strengthened RC beams are subject to fatigue failure, the fatigue life of a strengthened beam is based on the fatigue life of the component that fails first (El Refai, 2007). Rupturing of tensile reinforcement has been shown to be the predominant failure mode for RC structures in fatigue (Täljsten 2006; Mahal, 2015)

Due to the brittle failure mode associated with over-reinforced structures, they are commonly undesirable and are advised to be avoided from a safety viewpoint (*fib*, 2001). Notwithstanding the above reasoning, when one considers FRP strengthened RC elements over-reinforced sections have become more common, as its design is often guided by SLS design checks due to the low elastic modulus of FRPs which may result in more reinforcement being used, to limit deflection, than what the ULS design requires (Spadea et al., 2016). Extensive research has been carried out on factors that affect fatigue of tensile reinforcement, such as corrosion of normally reinforced sections (Dong et al., 2012; D. Li, Huang, Qin, Zheng, & Guo, 2017; Peng, Zhang, Shang, Liu, & Cai, 2016; Tong, Liu, & Zhao, 2017; Yi et al., 2011), whereas similar studies for over-reinforced sections are scarce.

To gain a better understanding of failure mechanisms associated with fatigue of RC structures the following section will consider fatigue behaviour of each material component.

3.2 Fatigue behaviour of constituent materials

3.2.1 Plain concrete

Fatigue is commonly associated with steel construction where cyclic loading may be experienced possibly due to vibrating machinery, however concrete structures also exhibit fatigue when subjected to repeated cyclic loading. The heterogenous nature of plain concrete makes it inherently full of defects. As concrete sets and hardens, its microstructure is filled with voids and pores that are caused by numerous factors. As concrete undergoes the hydration reaction, moisture is lost and voids or capillaries form in its micro-structure which is best explained using Powers' model for hydration (Igarashi, Kawamura, & Watanabe, 2004). Voids may also form at the interfacial transition zone (ITZ) between the hardened concrete paste and the coarse aggregate if concrete bleeding occurs (Ballim et al., 2009). The last major type of void or openings in the concrete pore structure is caused by restrained shrinkage as discussed in **Section 2.2.1**. Under cyclic loading these micro-cracks link other voids in the pore structure as shown in **Figure 3.1**.

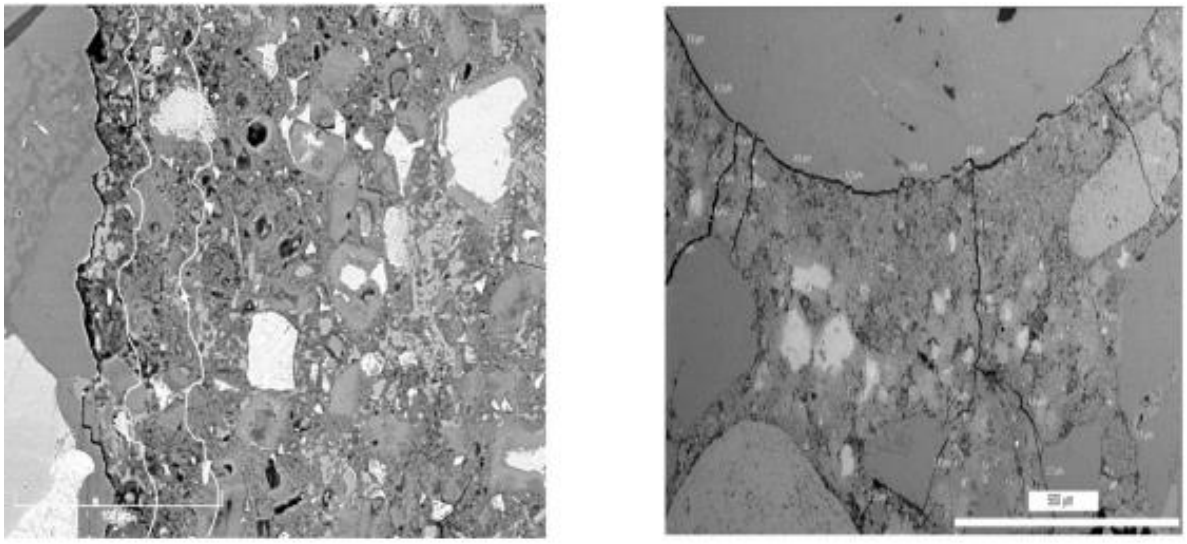

Figure 3.1 Concrete micro-cracks in pore structure (Wu, 2014)

The fatigue failure of concrete is not yet well established, but various studies have proposed hypotheses related to crack initiation and propagation, suggesting that it occurs in three distinct phases under cyclic loading(Ahsan, 2014; Amesu, 2016; M. K. Lee & Barr, 2002). These phases include: flaw initiation, microcracking and eventual macrocracking. The first stage involves the initiation of the micro-cracks in the pore structure, which creates weak regions within the concrete. The second stage involves the propagation of these micro-cracks, a process which links the various voids within the cement matrix and aggregate interface. The third and final stage involves the development of these micro-cracks into macro-cracks which percolate through the cross-section until failure. Furthermore, fatigue crack growth occurs in two distinct stage, namely the deceleration phase and acceleration phase (Ahsan, 2014). During the first stage, the rate of crack growth decreases as the cracks grow. During the acceleration phase the cracks grow at a steady rate right up to failure.

As plain concrete experiences repeated cyclic loading, various studies have observed a reduction in material mechanical properties and ultimately the performance of the structure (Ahsan, 2014; Amesu, 2016; Gylltoft, 1984; Van Ornum, 1907). Van Ornum conducted compression tests in two separate studies in 1903 and 1907 on concrete cubes and prisms, after subjecting the specimens to cyclic loading at test frequencies ranging between 2 and 4Hz. Although he considered various aging periods in his experimental research, as shown in **Figure 3.2**, the results showed a consistent reduction in fatigue strength.

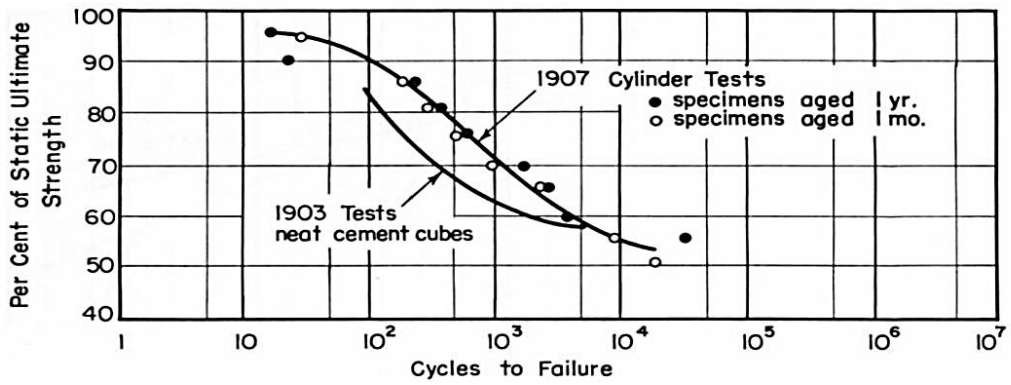

Figure 3.2 S-N curves for concrete subjected to repeated axial compression loading; based on Van Ornum (Ahsan, 2014)

The main performance indicators identified in literature have been fatigue strength, tension strain, stiffness and modulus of elasticity (Ahsan, 2014; M. K. Lee & Barr, 2002). Experimentally obtained fatigue strengths are commonly compared to static strengths measured for equivalent concrete structures; the fatigue strength is then expressed as a fraction of the static strength for a given number of cycles as shown in **Figure 3.2** (Ahsan, 2014; Van Ornum, 1903, 1907). The results presented in the **Figure 3.2** show a fatigue strength of 55% of the static strength after 7000 load cycles. In addition to a reduction in fatigue strength, concrete also experiences an increase in strain under fatigue loading conditions, similar to the behaviour of concrete under sustained loading (Mahal, 2015). Concrete softening is observed as a result of the change in stress-strain behaviour of concrete under repeated loading, which characterized by change in the stress-strain curve slope or alternatively described as a reduction in the material modulus of elasticity (M. K. Lee & Barr, 2002). Furthermore, the increase in strain coupled with the cyclic loading crack propagation culminate in an overall stiffness reduction.

There are various factors that influence the failure mechanisms and performance of plain concrete under fatigue loading. Some of these factors are listed below:

- Load regime
- Load frequency
- Matrix composition
- Stress level
- Stress ratio
- Boundary conditions
- Number of cycles
- Age of concrete and curing regime
- Water-to-cement ratio
- Cement content

The loading cycle regime directly influences the failure mechanism. **Table 3.1** presents the various loading regimes, where low-cycle fatigue presents itself in the form of high stress ranges with a low number of cycles, whereas high-cycle fatigue is characterized by a significantly larger number of load cycles at low stress ranges (Mahal, 2015). The fatigue loading regimes presented in the **Table 3.1** can further be discussed in terms of load intensity and load frequency (Ahsan, 2014; Mahal, 2015). Low-cycle fatigue is identified by high intensity loads with low frequencies, whereas high-cycle fatigue can be distinguished by low intensity loads at high frequencies. According to Ahsan (2014) the dominant failure mechanism for low-cycle fatigue is the formation of cracks in the mortar that lead to continuous cracked networks, whereas for high-cycle fatigue on the other hand, bond cracks are encountered.

Table 3.1 Classes of fatigue loading regimes (Lee & Barr, 2004)

Low-cycle fatigue			High-cycle fatigue				Super-high cycle fatigue		
1	10^1	10^2	10^3	10^4	10^5	10^6	10^7	10^8	10^9
Structures subjected to earthquake			Airport pavements and bridges		Highway and railway bridges, highway pavements		Mass rapid transit structures		Sea structures

The modulus of elasticity of concrete has been found to be sensitively influenced by the load intensity and fatigue life has been found to be primarily determined by stress range and test frequency to which concrete specimens are subjected to (Van Ornum, 1903, 1907). However, the loading frequency only influences the fatigue strength noticeably at low stress ranges; at high stress levels of up to 75% of the static strength, increasing the loading frequency from 1 to 15Hz had no significant effect on the fatigue strength of concrete (Mahal, 2015).

Concrete matrix composition is another major consideration in the discussion of fatigue performance. A rich dense high strength concrete material has shown to exhibit a greater resistance to fatigue. Concrete with high cement content, low water-to-cement ratio and that had been adequately cured and aged displays a greater resistance to fatigue; Van Ornum (1903, 1907) documented a 33% to 64% variation in fatigue resistance depending on moisture, aggregate and curing regimes. As shown in **Figure 3.2**, the concrete that had aged for a year showed a slightly higher resistance to fatigue. In addition, fibre reinforced concrete (FRC) has also shown to benefit the fatigue performance of concrete structures (M. K. Lee & Barr, 2002).

The hydration reaction of concrete, that was briefly discussed at the start of this section, may provide some insight as to why the parameters discussed in this paragraph contribute to a material that exhibits a higher resistance to fatigue. Concrete with high cement content, low water-to-cement ratio and that had been adequately cured and aged is likely to be highly impermeable (H. Beushausen et al., 2019). That is permeability in terms porosity of concrete as well presence of shrinkage crack. With that in mind, a concrete matrix with a lower density of voids and openings will require more energy, in the form of applied load, to induce cracks that can then propagate under repeated cyclic loading. Moreover, if enough energy is induced in the material to cause fracturing, the presence of fibrous material in the material matrix may prolong the deceleration phase of fatigue crack growth (K. Kim et al., 2017). Bridging materials such as steel fibres or fibrous fly ash have been shown to reduce the effects of shrinkage cracking (Shetty, Venkataramana, & Narayan, 2014) and may therefore influence the fatigue of both concrete and patch repair mortars.

Although the above discussed parameters are important, many of them have not been have not been agreed upon in literature, nor incorporated in fatigue life prediction models. The two most important parameters are ultimately the stress range and concrete strength as Gylltoft (1984) proposed. His model for estimating the fatigue life of plain concrete in tension is presented by **Equation 3.1**. His study investigated the fracture mechanics of plain concrete where he compared the results of a proposed FEM models to those obtained through experimental testing.

$$\log(N) = \left(\frac{1}{0.043}\right)\left(0.93 - \frac{\sigma_{max}}{f_c}\right) \tag{3.1}$$

Where:

N = number of fatigue cycles
σ_{max} = maximus stress on the specimen
f_c = concrete compressive strength

The study by Gylltoft (1984) highlighted the significance of concrete strength in the prediction of fatigue life. If one considers this fatigue prediction model for plain concrete by Gylltoft (1984) together with the S-N relationships for concrete by Van Ornum (1903, 1907) in **Figure 3.2** it is evident that concrete fatigue becomes a compounded problem, where cyclic loading reduces the fatigue strength of concrete, which in turn reduces its fatigue life. In addition to the complexity of plain concrete fatigue behaviour highlighted above, it should be noted that none of the literature studies have found a fatigue limit for concrete. In other words, no stress range has been identified, below which the fatigue life of the specimen becomes infinite (M. K. Lee & Barr, 2002).

3.2.2 Patch repair mortars

Patch repair mortars exhibit similar failure mechanisms to that of concrete discussed in **Section 3.2.1**, given their resemblance in chemical composition, pore structure, mechanical properties and

susceptibility to shrinkage cracking. A major difference is that patch repair mortars generally make use of smaller coarse aggregate than concrete and therefore have a relatively smaller amount of interfacial voids (National Concrete Pavement Tehnology Center, 2007). In addition, low drying shrinkage patch repair mortars with less micro cracks may extend not only the material fatigue life, but the entire structure's flexural strength (Pattnaik, 2017). The latter statement was foreseeable considering Gylltoft's (1984) fatigue prediction model in **Equation 3.1**, where materials with a higher flexural strength will endure a larger number of fatigue cycles.

3.2.3 Tension steel

Fatigue failure of metal structures is a well-known technical problem and although metal fatigue has been studied for more than 160 years, many problems remain unsolved. Structural failure by fatigue of tension steel is often described as brittle and without warning, which makes it especially hazardous (Täljsten, 2006). In the 19th century metal fatigue was thought to be a mysterious phenomenon in the material, because damage could not be seen (Sharif, 2014). This was especially concerning as these failures occurred at stresses far below the static strength of the structure. Noteworthy research on fatigue, including work by Wöhler (1860), has been able to dispel the mystery surrounding metal fatigue failure and to describe its failure mechanisms more accurately.

3.2.3.1 Crack progression

There is a noticeable similarity in the fatigue failure mechanism of steel when compared to plain concrete fatigue. Steel also experiences three stages of cracking, as shown in **Figure 3.3**, when subjected to repeated cyclic loading. These three stages include crack initiation, crack growth and final fracture.

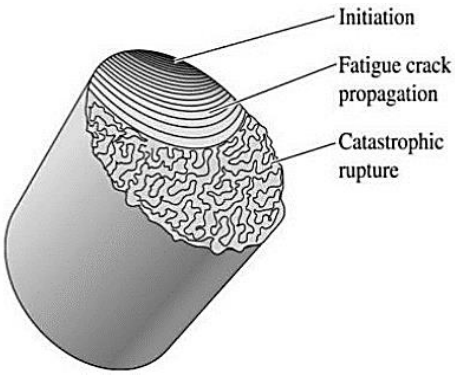

Figure 3.3 Fatigue Crack propagation through reinforcing steel (Thornton, 2015)

Crack initiation

Crack initiation can further be subdivided into three processes as shown in **Figure 3.4**, which includes cycle slip, cycle nucleation and micro crack growth.

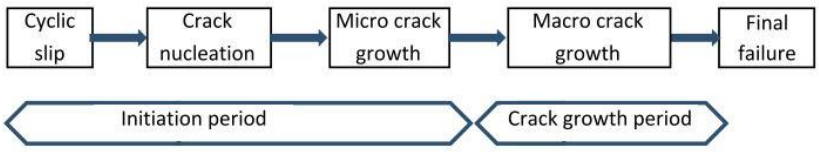

Figure 3.4 Steel fatigue cracking phases and relevant factors (Sharif, 2014)

When subjected to cyclic loading, especially at low stress cycles, slippage may occur on a microscopic level at the material grain surfaces due to lower constraint on slip (Sharif, 2014). When granular slip occurs slip lines are formed. As shown on **Figure 3.5**, when a fresh new material rim is exposed to the environment it is immediately covered by an oxide layer which is not easily removed. As the metal

experiences these back and forth cycles, the monolayers repeatedly form ultimately creating a slip band. During this plastic deformation process, strain hardening occurs in the slip band.

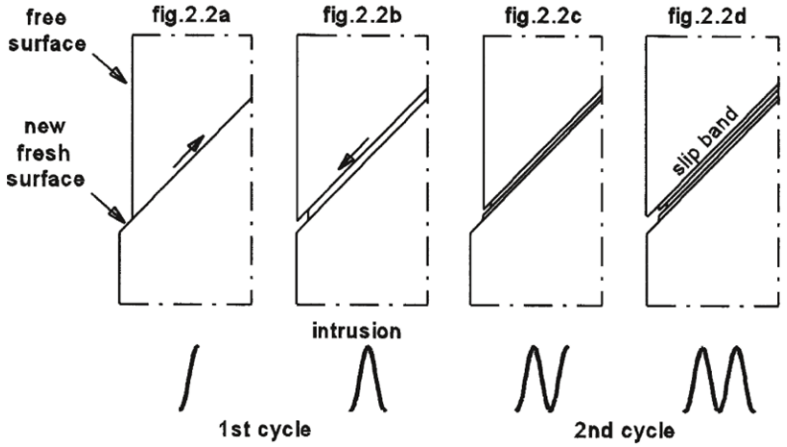

Figure 3.5 Cycle slip and crack nucleation illustration

According to Sharif (2014) not all fatigue cracks nucleate along slip bands, but they have been shown to cause microcracking at least indirectly. Fatigue cracks have been shown to nucleate at or near discontinuities, where discontinuities may include: inclusions, second-phase particles, corrosion pits, grain boundaries, twin boundaries, pores, voids and also slip bands. Corrosion pits are of particular interest for this research. Pitting corrosion damage, in particular, has two effects on tension steel. First of all, it causes localized reduction in cross-section, which increases the stress experienced by steel. This has more of an effect on the flexural capacity, as fatigue failure generally occurs at much lower stresses (Mahal, 2015). Apart from localised cross-section reduction pitting corrosion provides an ideal location for micro-crack formation, which further reduces reinforcement cross-section as the crack propagates; the cross-section reduction is depicted in **Figure 3.3**.

Crack growth

The crack initiation period described in the previous section forms part of Stage I, illustrated in **Figure 3.6**. For as long as the microcrack size is still in the order of the grain size it will not grow, as it remains part of an elastic anisometric material with a crystalline structure and various slip systems (Sharif, 2014). At the tip of this microcrack there is a stress concentration making it likely to activate one of the other slip systems. If the crack does however grow into an adjacent grain, there will be increased restraint on slip displacement due to the presence of neighbouring grains. For the microcrack to grow effectively, it will require numerous slip planes, as it is difficult to accommodate increasing slip displacements from just one slip plane.

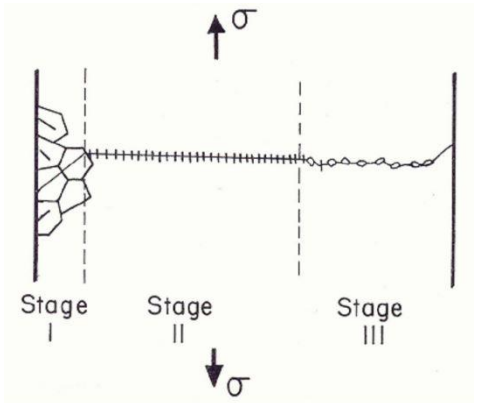

Figure 3.6 Fatigue crack propagation schematic drawing

If slip displacements do occur and the microcracks grow, there is a tendency for the crack to change direction, turning from the direction of the of the slip band crack to perpendicular to the loading direction as shown in the **Figures 3.7(a)** and (**b)**.

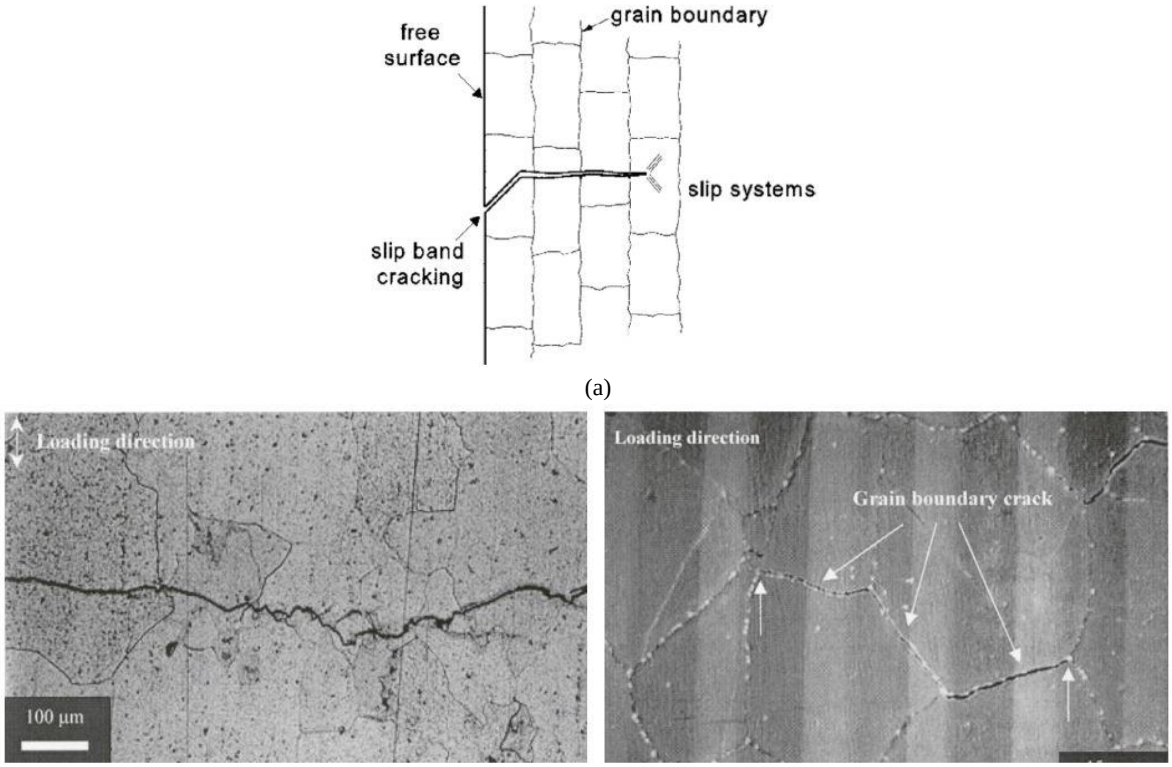

(a)

(b)

Figure 3.7 Fatigue crack propagation perpendicular to load direction in variable direction from slip planes (Sharif, 2014)

During microcracking the crack growth rate is still low, and it may progress for more than 90% of the structures fatigue life as shown in **Figure 3.8**. The figure below shows how well manufactured, smoothly polished steel surfaces are characterized by non-propagating cracks, which allow for a possibly infinite fatigue life, whereas surfaces with defects such as corrosion pits have a definite fatigue life as it already starts in the macrocracking phase.

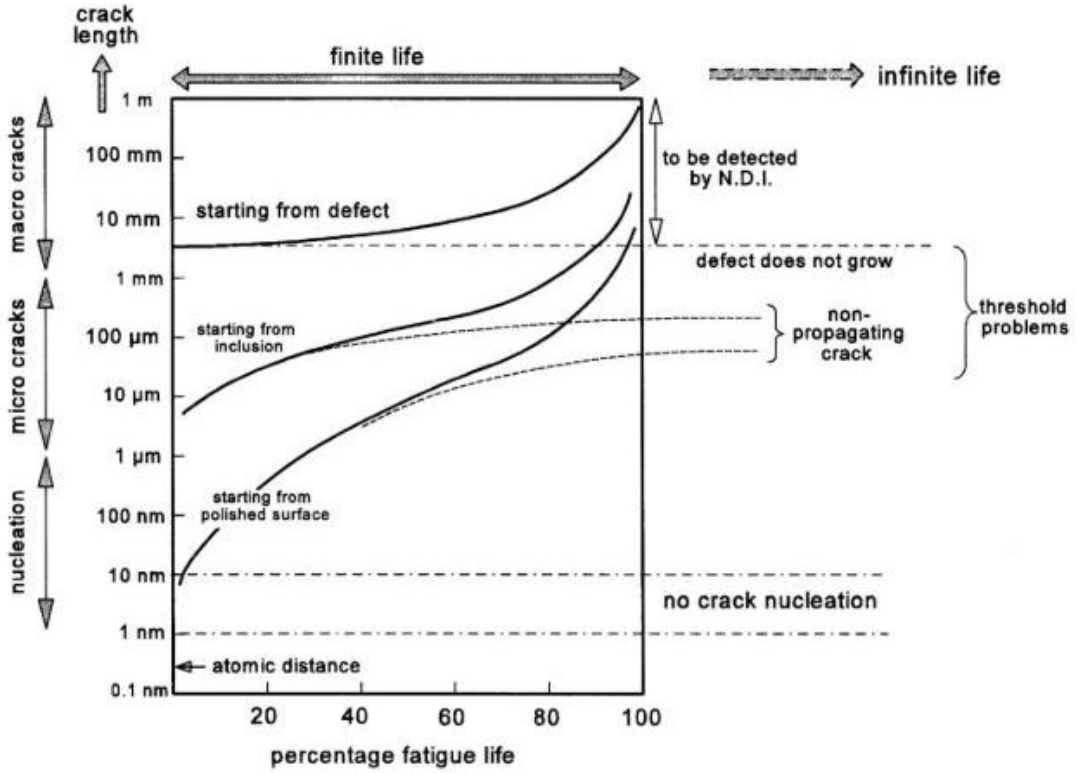

Figure 3.8 Fatigue crack propagation for steel with various material defects (Sharif, 2014)

This microcracking phase has been shown to cause a gradual stiffness reduction characterized by a upward shift in the section neutral axis as the microcracks propagate and ultimately reduce fatigue life.

Final fracture

The microcracks will continue to grow incrementally in Stage II until the crack becomes so big that that sudden failure occurs. According to Sharif (2014) Stage III or more commonly referred to as final fracture occurs when fracture toughness of the material $\mathbf{K_{ic}}$ is the same as or more than the stress intensity factor $\mathbf{K_t}$. When this point is reached the crack propagates uncontrollably through the remaining cross-section, causing abrupt failure.

3.2.3.2 Fatigue life prediction models

Many experiments have shown that reinforcing steel has a fatigue limit (Basquin, 1910; Mason & Hirschberg, 1964; Fatemi & Yang, 1998), i.e. a threshold below which no fatigue occurs. In contrast, concrete has no such limiting value. This difference is clearly depicted in **Figure 3.9**. This difference exists because steel is a strain hardening material whereas concrete is a strain softening material. Various fatigue life models for RC are based on the stress in the tension steel (fib, 2013; Mahal, 2015; Zorn, 2006) . This shows that fatigue of RC structures is heavily reliant on fatigue of the tension steel (Täljsten, 2006).

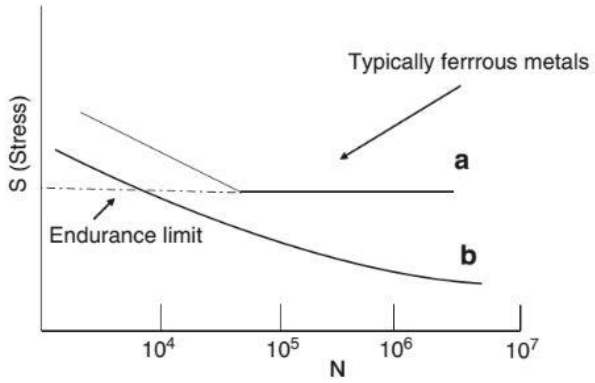

Figure 3.9 Fatigue behaviour of concrete versus fatigue (Sharif, 2014)

An increase static strength of steel reinforcement does not mean that the fatigue strength increases correspondingly. Sharif (2014) documented the most important factors for fatigue resistance to be geometry, possible defects, load range, environment, stress and strain.

There are five main models used to predict the fatigue of steel, but in the past and currently the most common approach is the stress-based approach. The five main approaches are listed below.

- Stress-based approach
- Strain-based life-times approach
- Energy based approach
- Continuum damage mechanics approach
- Paris-Erdogan law approach

Stress-based approach

The ability of a structural element to accommodate continuous vibrational or cyclic loading may be tested by subjecting it to loading in a wave form that matches its intended purpose. There are various sinusoidal wave forms that can be considered for testing as shown in **Figure 3.10**. During testing various information can be recorded such as stress, strain, number of cycles and deflection.

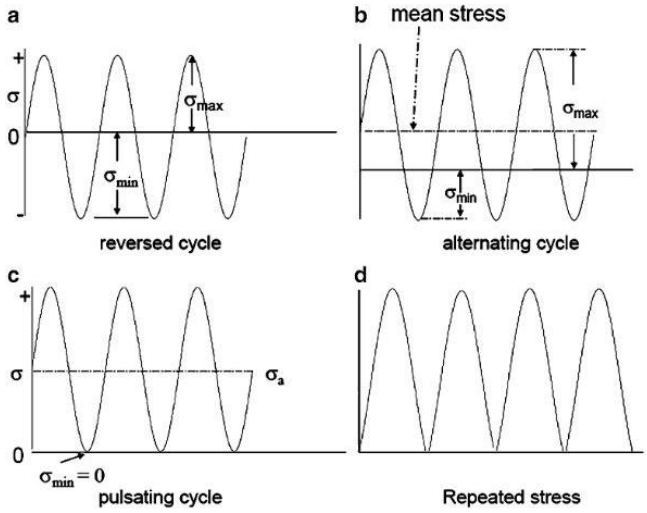

Figure 3.10 Typical cyclic loading wave forms (Sharif, 2014)

In the stress-based approach fatigue life, represented by the number of cycles ***N***, can be related to stress amplitude σ_a. In general, when this relationship is plotted for a metal, a curve of the Basquin (1910) form is obtained, which is governed by the **Equation 3.2**:

$$\sigma_a = \frac{E\Delta\varepsilon_e}{2} = \sigma'_f(2N)^b \tag{3.2}$$

Where:

N	=	number of cycles to failure
E	=	modulus of elasticity for steel
$\Delta\varepsilon_e$	=	change in elastic strain
σ'_f	=	fatigue strength coefficient
b	=	fatigue strength exponent (negative sign)
$2N$	=	number of load reversals to failure
σ_a	=	stress amplitude

The plots of these results are referred to as S-N curves, where ***S*** is the stress range and ***N*** is the number of cycles. **Figure 3.11** shows a typical S-N for a low-alloy steel fatigue test.

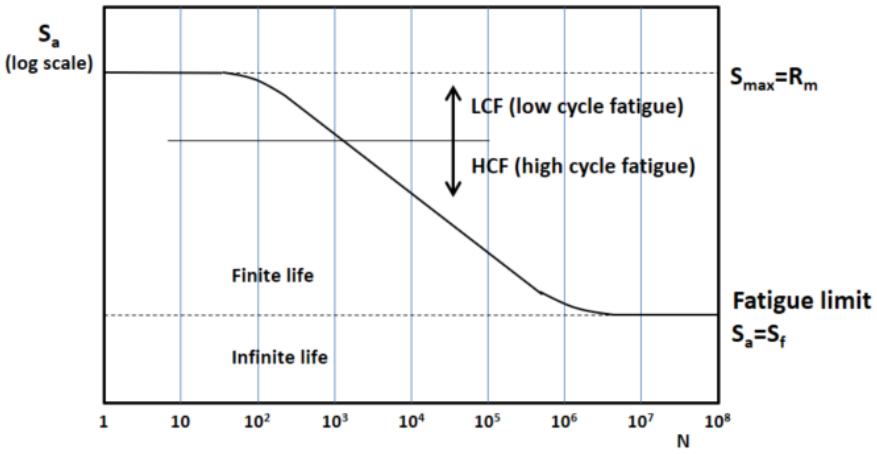

Figure 3.11 Fatigue test results of a low-alloy steel

Strain-based life-times approach

In steel fatigue design there may be situations where the structural element is notched, in which case plastic strains are imposed by the surrounding elastic material. In addition, where a structure encounters extremely high load levels at low cycle intervals the applied strain is likely to have a high plastic component. These cases are strain controlled, making the strain-based life-times approach more applicable as it accounts for both elastic and plastic strains. **Equation 3.3** was developed by Mason & Hirschberg (1964) and shows how both the elastic and plastic components are covered.

$$\frac{\Delta\varepsilon_T}{2} = \varepsilon_a = \frac{\Delta\varepsilon_e}{2} + \frac{\Delta\varepsilon_p}{2} = \frac{\sigma'_f}{E}(2N)^b + \varepsilon'_f(2N)^c \tag{3.3}$$

Where:

E	=	modulus of elasticity for steel
$\Delta\varepsilon_T$	=	total change in strain
$\Delta\varepsilon_e$	=	change in elastic strain
$\Delta\varepsilon_p$	=	change in plastic strain
σ'_f	=	fatigue strength coefficient
ε'_f	=	fatigue ductility coefficient
b	=	fatigue strength exponent (negative sign)

c = fatigue ductility component (negative sign)
$2N$ = number of load reversals to failure
ε_a = strain amplitude

According to Sharif (2014) the total-strain life curve approaches the plastic-strain life curve in the low cycle region and the stress life curve in the high cycle region, which makes it possible to plot a curve with strong accuracy for both low and high cycle fatigue.

Energy based approach

Between the early 1970s and early 1990s several researchers reviewed cumulative fatigue damage models, more specifically related to energy-based damage. According to Fatemi & Yang (1998) it was realized that an energy-based damage parameter can unify the damage caused by different types of loading such as thermal cycling, creep, and fatigue. Sharif (2014) documented that by using Glinka's rule, together with the recently proposed fatigue strain energy density parameter ***W****, for the critical plane, as presented in **Equations 3.4, 3.5** and **3.6,** it is possible to predict the fatigue life of various materials under multi-axial loading. Furthermore, it is possible to analyse the damage accumulation of notched specimens or components by the energy approach.

$$W^* = \frac{\Delta\sigma_{12}}{2}\frac{\Delta\gamma_{12}}{2} + K_1 K_2 \frac{\Delta\varepsilon_{22}}{2}\frac{\Delta\sigma_{22}}{2} \tag{3.4}$$

$$K_1 = \frac{\gamma'_{f'}}{\varepsilon'_{f'}} \tag{3.5}$$

$$K_2 = \frac{\sigma'_f}{\tau'_f} \tag{3.6}$$

Where:

W^* = fatigue strain energy density
$\Delta\sigma_{12}$ = shear stress range in the critical plane
$\Delta\gamma_{12}$ = shear strain ranges in the critical plane
$\Delta\varepsilon_{22}$ = normal strain ranges in the critical plane
$\Delta\sigma_{22}$ = normal stress range in the critical plane
$\gamma'_{f'}$ = torsional fatigue ductility coefficient
$\varepsilon'_{f'}$ = fatigue ductility coefficient
σ'_f = fatigue strength coefficient
τ'_f = torsional fatigue strength coefficient

The challenge with this approach is that it does not quantify the exact number of cycles a steel structure can endure. Nevertheless, it is a useful fatigue performance measure.

Continuum damage mechanics approach

The study that deals with mechanical behaviour of a deteriorating medium at continuum level is a relatively new subject in engineering mechanics. A nonlinear damage evolution has been formulated for the fatigue behaviour of steel, as presented in **Equation 3.7**, by measuring changes in tensile load carrying capacity and making use of the effective stress concept.

$$D = 1 - \left[1 - r^{1/1-\alpha}\right]^{1/1+\beta} \tag{3.7}$$

Where:

D = nonlinear damage evolution
r = damage state
α = function of the stress state
β = material constant

According to Sharif (2014) these continuum damage mechanics (CDM) models were developed for uniaxial loading and were proven to effectively account for the mean stress effect. However, when this model was extended to multiaxial bending, inaccuracies started to arise, possibly due to the complexity of non-proportional multiaxial fatigue problems. For that reason, a three-dimensional (3-D) anisotropic CDM model does not yet exist.

Paris-Erdogan law approach

Deformed reinforcing bars have a better adherence to concrete. Some deformations may include the ridges on the bars, manufacturing dents or corrosion pits. These deformations create localized stress concentrations that will shorten the fatigue life of the reinforcing bars under cyclic loading (Täljsten, 2006). The bar diameter also contributes to a lower fatigue strength.

The Paris-Erdogan's law theorizes that the rate of crack growth for an isotropic material at a constant load amplitude can be expressed as an increase of crack depth per load interval ***da/dN***, as shown in **Equation 3.8**, where ***C*** and ***m*** are two constants related to the specimen microstructure, frequency, environment, temperature and tension factor $R(R=\sigma_{min}/\sigma_{max})$:

$$\frac{da}{dN} = C(\Delta K)^m \tag{3.8}$$

Where:

da = change in crack depth
dN = change in fatigue cycles

According to the Paris-Erdogan law the stress intensity factor ***R*** is described to be the steering factor for fatigue crack growth. One drawback with the Paris-Erdogan law is that the accurate prediction of fatigue lifetime under certain conditions requires the position and size of initial crack, which is not always practically obtainable.

3.2.4 Fibre reinforced polymers

FRPs can be either isotropic or anisotropic materials that exhibit multiple failure modes if considered in isolation (Täljsten, 2006). Although fatigue of isotropic materials is well apprehended, the fatigue of composite materials is very complex and not easily predictable. For long FRP composite materials have been regarded insensitive to fatigue. If considered as part of a RC composite system, fatigue will most likely cause a breakdown of the entire composite before the FRP fails (Täljsten, 2006). However, many new composite materials, such as the carbon fibre reinforced polymers (CFRP), which were designed to have a higher failure strain with sustained strength under higher temperatures, unfortunately exhibit unfavourable fatigue conditions.

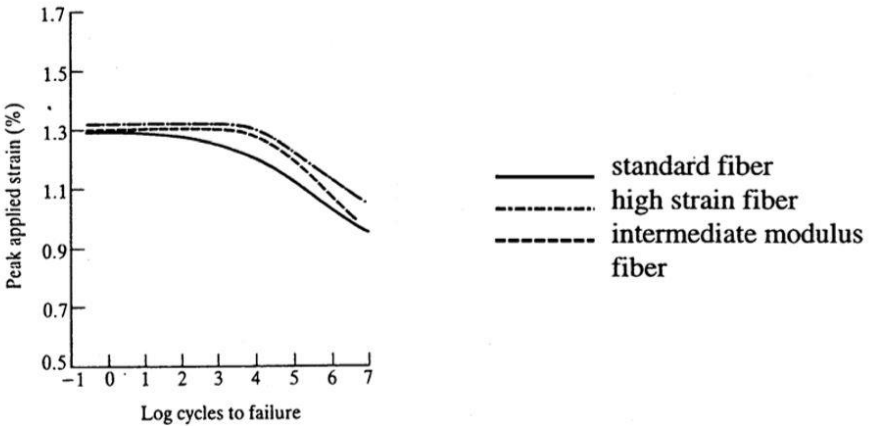

Figure 3.12 S-N curves for various types of FRP materials (Täljsten, 2006)

Despite commendable effort by manufacturers to double tensile strength and increase the elasticity module by 40%, the new more ductile materials are shown to be more prone to fatigue failure (Täljsten, 2006), as evident with their steeper S-N curves in **Figure 3.12**. Under cyclic loading conditions these fatigue failure modes may be encountered, sometimes more than one simultaneously:

(a) Matrix failure (failure within a laminate)
(b) Fibre failure
(c) Adhesion failure (failure in the boundary between fibre and matrix)
(d) Delamination (separation between different composite layers)

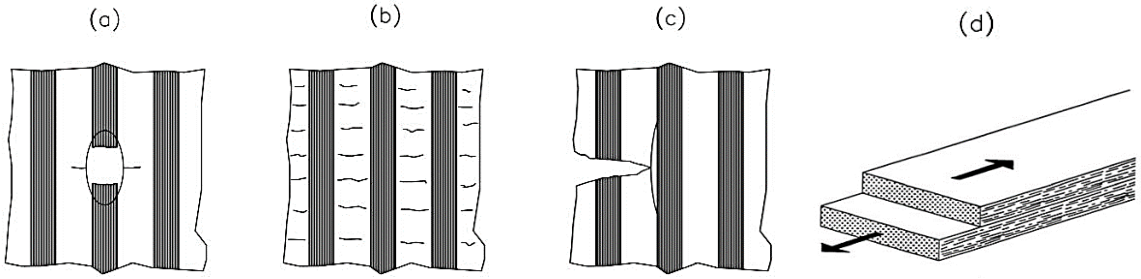

Figure 3.13 Failure modes of FRP materials (Täljsten, 2006)

During the design process, to avoid some of these failures certain checks can be done. To avoid end delamination, it is possible to adjust the width/thickness ratio be 30 or greater to reduce the inter-laminar tensions, which are critical for end-delamination, to near zero (*fib*, 2001).

3.2.4.1 Fatigue life prediction models

Regardless the type of fatigue failure mode that may be encountered, there are 6 fatigue prediction models that are commonly used for FRP materials (Mahal, 2015). These models listed and discussed below:

- Stress ratio approach
- Stress frequency approach
- Temperature approach
- Matrix approach
- Fibre type approach
- Fibre load angle approach

Stress ratio approach

The stress ratio approach is a commonly used model that relates the fatigue strength of a material, in this case carbon fibre, to its stress ratio ***R*** (ratio of the minimum stress to the maximum stress). Test results using this method have shown that fatigue life of the material is increased when the stress amplitude is decreased, and the stress ratio is increased. Using the model by Toutanji et al. (2006) in **Equation 3.9** it is possible to evaluate the effects of stress ratio and stress range on fatigue life.

$$S = \frac{\sigma_{max}}{f_{fu}} = 1 - \alpha(1 - R)\log(N) \tag{3.9}$$

Where:

σ_{max}	=	maximum applied stress
S	=	applied cyclic stress level
N	=	number of cycles to failure
R	=	stress ratio
f_{fu}	=	ultimate strength
α	=	experimentally determined constants

Stress frequency approach

Hwang & Su (2006) theorized that at higher test frequencies the maximum applied strains and stresses are reduced. This results in an increase in the specimen's fatigue life. Conversely, at lower frequencies the maximum strain is reached faster. Using the Epaarchchi & Clausen (2003) model in **Equation 3.10**, which relates stress ratio, stress frequency and maximum applied frequency it is possible to evaluate the number of fatigue cycles to failure.

$$\sigma_u - \sigma_{max} = \alpha\sigma_u^{1-\gamma}\sigma_{max}^{\gamma}(1 - R)^{\gamma}\frac{1}{f^{\beta}}(N^{\beta} - 1) \tag{3.10}$$

Where:

σ_{max}	=	maximum applied stress
σ_u	=	ultimate static stress
α	=	constant determined experimentally
f	=	frequency
γ, β	=	material constants

Temperature approach

Increased temperature was found to significantly affect the fatigue life of polymer matrix composites (Kawai & Taniguchi, 2006). It was found that heat changed the composite matrix, thereby weakening the bond performance of the material. This not only affects the fatigue life of the specimen, but also other mechanical properties such as modulus of elasticity and ultimate strength of the material. The Mivehchi & Vervani-Farahani (2010) model presented in **Equations 3.11** and **3.12** considers temperature in the evaluation of FRP fatigue life.

$$\sigma_{max} = A(T_0)\left[1 - \frac{\left(\frac{A(0)}{A(T_0)} - 1\right)}{ln\left(1 - \frac{T_0}{T_m}\right)} ln\left(\frac{\left(1 - \frac{T_0}{T_m}\right)}{\left(1 - \frac{T_0}{T_m}\right)}\right)\right]\left(N_f(T)\right) \tag{3.11}$$

$$m(T_0)\frac{ln\left(1 - \frac{T}{T_m}\right)}{ln\left(1 - \frac{T}{T_m}\right)} \tag{3.12}$$

Where:

σ_{max}	=	maximum applied stress
A(T)	=	curve characteristic
m(T)	=	curve characteristic
N_f	=	fatigue life
T_o	=	room temperature (Kelvin)
T_m	=	polymer melting temperature (Kelvin)
T	=	temperature (Kelvin)

Matrix approach

Newaz (1985) carried out fatigue testing on composite fibres of the same E-Glass fibre, but with two different matrix materials. Papakonstantinou & Balaguru (2007) also carried out fatigue tests on carbon fibre with geopolymer resin matrix. In both studies it was agreed that the type of matrix influenced the fatigue life of the specimen, owing to its ability to resist cracks and fibre matrix debonding. The S-N model represented by **Equations 3.13** and **3.14** were derived through the experimental work conducted by Papakonstantinou & Balaguru (2007).

$$\frac{S_{max}}{S_{ult}} = 1.1055 - 0.046903 Log\ N \tag{3.13}$$

$$\frac{S_{max}}{S_{ult}} = 0.8227 - 0.0519 Log\ N \tag{3.14}$$

Where:

S_{max}	=	maximum applied load
S_{ult}	=	average of the monotonic load-carrying capacity
N	=	fatigue life

Fibre type approach

Similar to the work that had been done with the various types of matrices, Wu et al. (2010) compared various fibre types. These included carbon fibre (CFRP), E-glass fibre (GFRP), basalt fibres (BFRP) and a hybrid FRP carbon/E-glass fibre (C1G1) with the same epoxy matrix. The carbon fibre and polyparaphenylene FRP sheets showed favourable results in terms of tensile modulus of elasticity and fatigue resistance, compared to the other test specimens. The model in **Equation 3.15** together with information provided on **Table 3.2** provides the S-N relationship for the fatigue performance of various types of fibres.

$$\frac{P_{max}}{P_{av}} = A - \alpha Log\ N \tag{3.15}$$

Where:

P_{max}	=	maximum applied load
P_{av}	=	average of the monotonic load-carrying capacity
N	=	fatigue life
A	=	constants as shown in **Table 3.2**

Table 3.2 Fatigue constants for the S-N model of fibre types and material constants (Mahal, 2015)

Fiber Type	A	α	Tensile modulus (GPa)	Tensile strength (MPa)	Ultimate Strain (%)
CFRP	1.001	0.020	230	3400	1.48
GFRP	1.004	0.062	73	1500	2.05
C1G1	1.015	0.069	152	2242	1.48
BRRP	0.997	0.071	91	2100	2.31

Fibre load angle approach

The results from tests that had been done on GFRP and CFRP, respectively by Hashin & Rotem (1973) as well as by Awerbuch & Hahn (1981) showed that fatigue life is strongly related to fibre load angle. The specimens that were loaded at a wide fibre angle tended to exhibit a lower fatigue life. Using the model presented in **Equation 3.16** together with the information on **Tables 3.3** and **3.4** it is possible to evaluate the fatigue life of FRPs loaded at various fibre angles.

$$S_{max} = A - \alpha Log\ N \tag{3.16}$$

Where:

S_{max} = maximum applied stress (MPa)
N = fatigue life
A = constants as shown in **Table 3.3** and **Table 3.4**
α = constants as shown in **Table 3.3** and **Table 3.4**

Table 3.3 Fatigue constants for the S-N model for CFRP load angle (Mahal, 2015)

Fibre angle (degree)	A	α
10º	427.9	40.1
20º	191.4	13.2
45º	89.5	7.3
60º	57	1.4

Table 3.4 Fatigue constants for the S-N model for GFRP load angle (Mahal, 2015)

Fibre angle (degree)	A	α
10º	151.4	9.7
20º	95.9	9.1
45º	73.4	7.3
60º	29.8	1.1

Depending on the environment to which the material is subjected, whether it may be a high frequency, high stress or high temperature environment, any of these fatigue life prediction models may be applicable.

3.3 Fatigue behaviour of corrosion damaged strengthened RC elements

Apart from Malumbela et al. (2011), Dladla (2014) and Gregan (2012) most of the available research and design guidelines on structural strengthening using FRP do not consider the effect of using bonded overlays. This may be attributed to the assumption of cracked tension concrete or patch repair mortar when designing for ULS. When evaluating fatigue behaviour though, the internal force due to the patch repair becomes important. When testing at low stress cycles, the section can be considered partially cracked; it is therefore governed by elastic theory and its behaviour should be interpreted as such (Kong & Evans, 1987). With the that in mind, the behaviour of structures repaired in this way is not yet fully understood.

Similar to the discussion in the previous chapter about performance parameters related corrosion damaged, patch repaired and FRP strengthened RC beams under sustained loading, this section will

extend that discussion to incorporate dynamic loading. In this section the 3 performance parameters related to fatigue behaviour will be discussed.

3.3.1 Fatigue life

Fatigue life of a specimen can be defined as the number of load cycles it can endure before it fails. Flexural capacity is a useful parameter when discussing static behaviour of a structure, but not as much when considering fatigue behaviour. In the study of fatigue, the stress range to which tensile steel is subjected to as well as crack initiation become far more critical. Stress ranges of as low as 45% of the yield stress can cause failure under cyclic loading conditions once a crack has initiated (Mahal, 2015). However, the discussion of fatigue cannot be uncoupled from that of flexural capacity. Studies by life Hoeppner (1979) and Ma et al. (2014) have shown that a reduction in flexural capacity due to corrosion results in a shorter fatigue. As corrosion reduces the steel cross-section it effectively increases the tension steel stress range and provides an ideal location for crack formation, which ultimately leads to reduced fatigue life of the structure. The effect of stress range on fatigue life can be illustrated by stress-cycle graphs such as the one shown in **Figure 3.14**, where the lower the stress amplitude the longer the fatigue life.

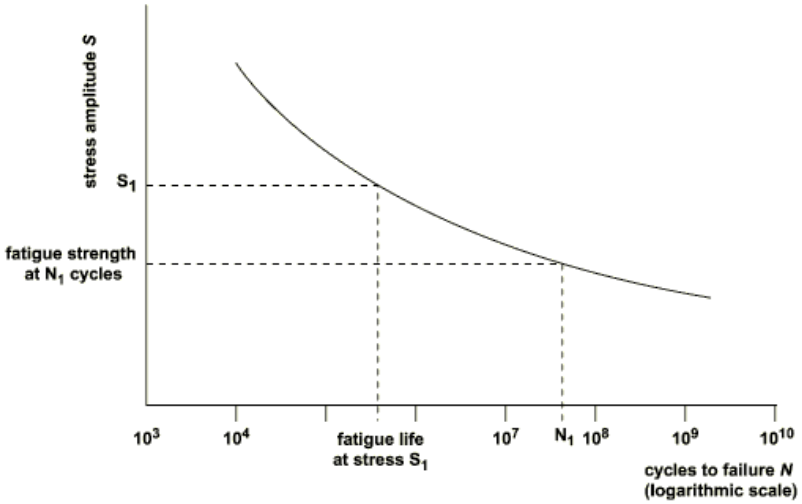

Figure 3.14 RC beam S-N curve (Noël & Soudki, 2018)

3.3.1.1 Fatigue life prediction models

There are numerous fatigue prediction models to quantify fatigue life of an RC member (Barnes & Mays, 1999; Breña et al., 2005; Dong et al., 2011; Heffernan & Erki ,2004; Papakonstantinou et al., 2001; Yu et al., 2011; Quattlebaum et al., 2005; Badawi, 2007; Wahab, 2011; Gussenhoven & Breña, 2005; Ma et al., 2007; Aidoo et al., 2004; Derkowski, 2006 and Harries et al., 2007), but they all seem to be some variation of **Equation 3.17**.

$$\log(N) = a - b \log(\sigma_r) \tag{3.17}$$

Where:

N = number of fatigue cycles
σ_r = fatigue stress range
a,b = model dependant constants

The fatigue of steel is commonly lower than that of CFRP composites, which justifies the use of current fatigue life prediction models of RC beams regardless of it being strengthened or un-strengthened, if the structure is under-reinforced. The fatigue life of a strengthened beam is dependent on the rupture of

the steel bar if no delamination has occurred before fatigue fracture. Furthermore, crack initiation in the tension steel bar is critical to the fatigue life of the RC beam.

Even though there are many fatigue life models available in literature, as mentioned at the start of this section, perhaps the four most established models are listed below, and they all describe the relationship between tension steel reinforcing stress range ***Sr*** and the number of cycles to failure ***Nf***.

- Mallet model
- Tilly and Moss model
- CEB/FIB Model code model
- Helgason and Hanson model

Mallet model

The Mallet (1991) model is suitable for uncorroded steel reinforcement that is embedded in concrete and is governed by **Equation 3.18**.

$$S_r{}^9 N_f = 1.539 \times 10^{27} \tag{3.18}$$

Where:

N_f = number of fatigue cycles
S_r = fatigue stress range (MPa)

Tilly and Moss model

The Tilly and Moss (1982) model presented in **Equation 3.19** is commonly also referred to as the Barnes and Mays' model. This model was derived empirically and is suitable for steel reinforcing bars with a diameter of 16mm or smaller that is embedded in concrete.

$$S_r{}^9 N_f = 3.09 \times 10^{27} \tag{3.19}$$

Where:

N_f = number of fatigue cycles
S_r = fatigue stress range (MPa)

CEB/fib Model code model

Similar to the Tilly & Moss (1982) model, the 2010 *fib* Model code model is also limited to 16mm diameter bars embedded in concrete, but it is further limited operating stress ranges that result in a fatigue life of less than 1 000 000 cycles. The 2010 *fib* Model code model is governed by **Equation 3.20**.

$$S_r{}^5 N_f = 4.0841 \times 10^{17} \tag{3.20}$$

Where:

N_f = number of fatigue cycles
S_r = fatigue stress range (MPa)

Helgason and Hanson model

The Helgason and Hanson model (1974) based on the performance of steel under direct tension in air under cyclic loading. This model, as presented in **Equation 3.21**, has been considered to produce more lower bound stress cycle behaviour compared to the Tilly and Moss (1982) and the *fib* Model code

(2010) models, which have been found to exhibit more upper bound stress cycle behaviour (Zorn, 2004). This upper and lower bound stress cycle behaviour was further verified by (Mahal, 2015).

$$\log(N_f) = 6.969 - 0.00555S_r \tag{3.21}$$

Where:

N_f = number of fatigue cycles
S_r = fatigue stress range (MPa)

Based on the models presented above, it can be gathered that the selection of a suitable fatigue life prediction model will depend on the reinforcement diameter, stress range as well as the anticipated number of fatigue cycles. Stress-cycle (S-N) curves, such as the one in **Figure 3.14**, derived from fatigue prediction models, can be used to estimate the fatigue limit for a given structure. For a low stress ranges the structure can sustain a larger number of fatigue cycles. Fatigue stress range may be estimated from the ULS design strength of the beam, where low amplitudes can range between 20% and 60% of ultimate strength and high load amplitude may range between 20% and 80% of the ultimate strength (Gregan, 2012). However, the stress range is one of the most varied parameters as Charalambidi et al. (2016) comprehensively documented.

The Helgason and Hanson model has been shown to be predict the fatigue life FRP strengthened RC beams reasonably well. Mahal (2015) and Aidoo et al. (2004) both compared experimentally obtained fatigue life results to three of the fatigue life prediction models presented above, namely: the Helgason & Hanson model, CEB/*fib* Model code model and the Tilly & Moss model. Mahal (2015) found that the best model for estimating the fatigue life of CFRP strengthened RC beams was the Helgason & Hanson model. Aidoo et al. (2004) who studied the fatigue behaviour of CFRP strengthened RC bridge girders found that the CEB/*fib* model represents a lower bound as it is intended to be used as a design relationship. This seems to contradict Zorn's (2004) report that the *fib* model was found to exhibit more upper bound stress-cycle behaviour. Aidoo et al. (2004) did however note that their results may reflect a scale effect, given that the *fib* model is more suitable for smaller diameter bars (16mm diameter or less) and that they had used larger diameter bars. Moreover, Aidoo et al. (2004) reported that the Tilly and Moss model represented a mean stress-cycle relationship for steel embedded in concrete and that the Helgason and Hanson model appeared to provide a reasonable fatigue life prediction of the specimens used in their study.

In their review paper of the fatigue behaviour of RC beams strengthened in flexure with FRP laminates, Charalambidi et al. (2016) seem to advise against the use of all three models discussed in the previous paragraph. Their evaluation of the experimental investigation by Gussenhoven et al. (2005), Wang et al. (2007) and Heffernan et al. (2004) showed that these test specimens failed at a number of cycles lower than what had been predicted by the Helgason & Hanson, CEB/*fib* Model code and the Tilly & Moss models. This report by Charalambidi et al. (2016) is in stark contrast to what had been documented by Mahal (2015) and Aidoo et al. (2004). Closer examination of the experimental studies conducted by Gussenhoven et al. (2005), Wang et al. (2007) and Heffernan et al. (2004), suggested that the reason for the opposing views might be related to the stress ranges at which experiments were conducted. Gussenhoven et al. (2005) tested relatively small-scale specimens 102x102x914mm specimens under 3 different fatigue loads and FRP areas. These peak fatigue loads included loads that were 60%, 70% and 80% of the yield stress $\boldsymbol{f_y}$. Wang et al. (2007) tested 150x500x5000mm specimens at a stress range with a peak load of 87.5% of the yield stress. Heffernan et al. (2004) tested 150x300x3000mm and 300x500x5000mm specimens at a stress range with peak loads of 87.5% of the yield stress. All three of these studies were conducted under high stress ranges fatigue testing, whereas Mahal (2015) tested at a low fatigue stress range with a peak stress of 44.6% of the yield stress. This

may suggest that the Helgason & Hanson, CEB/*fib* Model code and the Tilly & Moss models are not able to predict the fatigue life of the FRP strengthened RC beam if tests are conducted at high stress ranges. However, Aidoo et al. (2004) conducted fatigue testing at both low and high stress ranges, but still managed to agree with Mahal (2015) regarding the appropriateness of the Helgason & Hanson model to predict the fatigue behaviour of FRP strengthened RC beams.

3.3.2 Development of cracks

Crack behaviour is an important performance parameter, especially in long-term SHM. From a durability perspective, considering that prevalence of cracking increases the permeability of cover concrete, it therefore makes the structural element susceptible further to corrosion damage. Furthermore, in terms of the scope of this research, crack behaviour is an indication of structural performance. In the field of SHM cracks and crack patterns are used to gauge the condition of a structure. It is essential to be able to identify different types of cracks, such a shrinkage cracks or shear cracks for example.

As discussed in the previous section, cracks weaken composite material bonds (Lindorf & Curbach, 2010). That can be the bond between the concrete and reinforcing steel, or in the case of FRP strengthened specimens, the bond between the FRP and the tension concrete or patch repair mortar. Regardless of the failure sequence, whether it is one of the methods listed in **Section 2.2.2.1** or even reinforcing steel rupturing before concrete crushing and then laminate debonding, what often happens is that debonding of the laminate begins at one of the cracks (Malumbela et al. 2011).

The study by Dladla (2014) that considered the effect of damage length on corrosion damaged, strengthened RC beams under static loading, showed that longer patch repaired sections improved crack behaviour in terms of average crack spacing as well as the loads at which first cracks appear. This is an indication that the longer patch repaired sections showed improved stiffness, as a higher load was required to overcome the internal patch repair tensile force. Both Gregan (2012) and Mahal (2015) found that the rate of crack growth was high during the first load cycle, without any significant change until rupture of the steel.

3.3.3 Stiffness degradation

In the context of static loading the stiffness of RC beams remains constant prior to yielding of tension steel (Kong & Evans, 1987). The stiffness reduction occurs after yielding as the section experiences ductile behaviour, characterized by an increase in crack growth rate. During this phase the deformations experienced by the section become permanent or irreversible, in other words it experiences plastic deformation. However, under fatigue loads, which generally induce a fraction of the steel yield stress, stiffness reduction occurs during the elastic regime.

3.3.3.1 Deflection resistance

In the comparative fatigue behaviour study of RC beams strengthened in flexure by Charalambidi et al. (2016) seven different studies were reviewed and discussed. In six of those studies the specimens were tested at a stress range with a maximum stress of between $0.54\boldsymbol{f_y}$ and $0.89\boldsymbol{f_y}$, only one test considered an upper maximum stress equal to the yield stress.

Mahal (2015) studied the fatigue behaviour of CFRP strengthened RC beams at a stress range with a maximum stress of $0.45\boldsymbol{f_y}$. The study investigated the behaviour of externally bonded near surface mounted CFRP as well as the influence of pre-cracking prior to strengthening. The study revealed that all the specimens experienced a stiffness reduction in the order of 10% during their fatigue lives, but that the specimens that were strengthened with an FRP that had a higher elastic modulus exhibited higher stiffness and also had a longer fatigue life. In addition, it was found that the specimens that were pre-cracked, prior to strengthening with the CFRP with the higher elastic modulus not only had a higher

stiffness, but also a longer fatigue life than both the uncracked samples. The exact stiffness reduction, in terms of a percentage was not explicitly reported by Mahal (2015), these observations and stiffness reduction estimations were interpreted by a study of Mahal's (2015) experimental result plots.

A study by Gregan (2012) of fatigue behaviour of FRP strengthened RC beams considered the effect of corrosion damage. Fatigue tests were carried out under 3 different stress ranges with maximum loads of 45%, 55% and 67% of ultimate failure loads, where the different loads represented low, medium and high stress, respectively. Results from the study revealed that the high stress test (67% stress range) not only had a substantially shorter fatigue life of 11.8% compared to the low stress test (45% stress range), as expected, but its rate of stiffness reduction was also higher. The high stress test had a stiffness reduction rate of 0.003mm/cycle whereas the low stress fatigue exhibited a stiffness reduction of 0.0000003mm/cycle which shows a substantial difference between the two stress ranges.

3.3.3.2 Neutral axis shift

A study by Song & Yu (2015) investigated the fatigue behaviour of corrosion damaged FRP strengthened RC beams. They specifically looked at the effect of an increase in degree of corrosion damage from 0% to 16.7%. Their study showed that as the corrosion extent increased, both the stiffness and the fatigue life reduced. The fatigue life reduces by more than 85% as the degree of corrosion increased from 8.3% to 16.7%. During fatigue testing period they tracked the strains in the section which revealed that the compression concrete remained relatively unchanged while the FRP strain increased, as shown in **Figure 3.15**. This increase in FRP strain caused a gradual upward shift in the neutral axis, essentially reducing the stiffness of the section during its fatigue life.

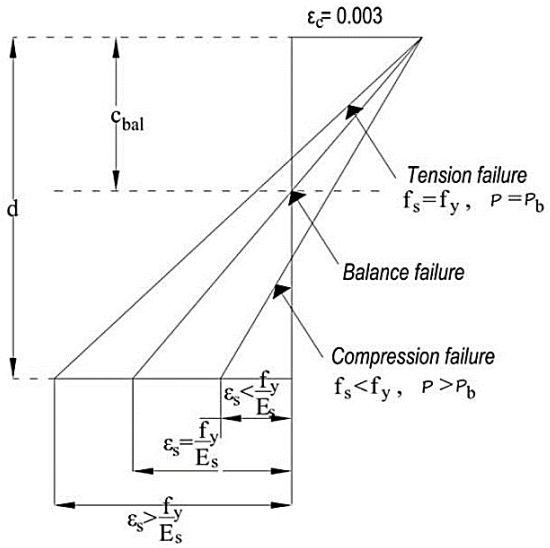

Figure 3.15 Internal force and strain diagram depicting shift in neutral axis (Priastiwi et al., 2014)

The study further found that FRP strengthening was able to not only increase the initial stiffness of the specimens, similar to what Mahal (2015) had established, but that it was able to reduce the stiffness degradation rates. It was reported that one layer of CFRP strengthening was able to increase initial stiffness of a 5% corrosion damaged specimen by 10% and reduce the stiffness degradation rate by a factor of 1.14. Two layers of CFRP strengthening was able to increase initial stiffness of a 10% corrosion damaged specimen by 16% and reduce the stiffness degradation rate by a factor of 3.75.

3.3.4 Failure modes

The design guideline for FRP strengthening of existing concrete structures by Täljsten(2006) as well as various FRP strengthening design codes such as *fib* (2001) recommend a ductile structural failure for

bending at ULS. This is a safety approach to ensure that whoever occupies or uses the structure has enough time to vacate it, but often with structures affected by fatigue behaviour, such as bridges, stadia and concert halls, catastrophic brittle failure is observed., which was the case when the Mianus bridge collapsed in 1987.

Literature on fatigue behaviour, especially on corrosion damaged RC structures, indicates that a rupture of tension steel causes another increase in crack growth rate (Charalambidi et al., 2016; Gregan, 2012; Mahal, 2015; Song & Yu, 2015), leading to either an immediate crushing of compression concrete and eventual debonding of FRP strengthening or, as was the case with Gregan (2012), the section is still able to experience a significant number of fatigue cycles until FRP debonding. This is shown on **Figure 3.16**.

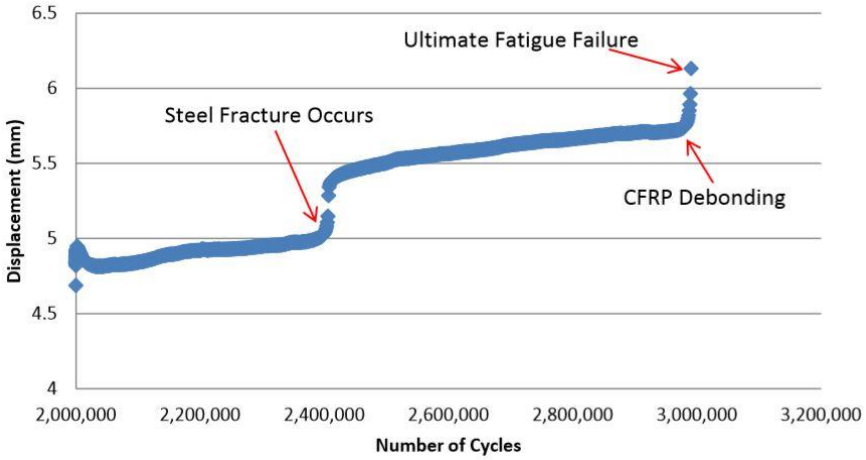

Figure 3.16 Displacement-cycle number locating potential steel rupture (Gregan, 2012)

This post-fatigue behaviour could be interpreted as a rather strong FRP-tension concrete bond. Another possible explanation is that at this point (2 400 000 cycles as shown in **Figure 3.16**) only one of the two bars fractured. This is what Mahal (2015) had encountered in his study of fatigue behaviour of RC beams strengthened with CFRP. The study by Charalambidi et al. (2016) noted that although the ultimate failure of the FRP ended up being debonding, the critical component which triggered the fatigue of the entire composite was cracking in the tension steel. In all the fatigue life prediction models discussed by Charalambidi et al., (2016), the steel stress range is the only input, which reinforces its significance.

3.4 Experimental techniques

3.4.1 Fatigue testing of RC beams

3.4.1.1 Test configuration

Various methods exist for testing fatigue behaviour of RC beams. The two common methods used for flexural testing are 3-point and 4-point bending tests. The FRP strengthened specimens considered by Qeshta et al. (2016) in their review of flexural behaviour of externally bonded RC beams, 79% of the specimens were tested under 4-point bending and the rest under 3-point bending.

3.4.1.2 Load application

It is possible to conduct fatigue testing under either load(stress)-controlled or displacement(strain)-controlled modes. For materials like rubbers and plastics, displacement-controlled testing has been reported more suitable as certain global deformation parameters, such as grip displacement and rotational angle, are usually kept constant with these materials. For reinforced concrete (RC) though, researchers and designers are more interested in stiffness degradation, specifically an increase in

deflection, because span deflection is a critical service life design criterion (*fib*, 2013). If deflection is experienced in excess, a structure may exhibit undesirable cracking, which may then also become a durability concern.

Displacement control

In displacement-controlled tests a specimen is loaded at certain displacement increments, while strain measurements are obtained. This control mode was used by Cachin et al. (2002) when they tested the fatigue behaviour of fiber-reinforcement plain concrete in compression. Prior to fatigue testing they loaded their specimens monotonically to maximum stress level using displacement control, as shown in **Figure 3.17**, at a rate of 50μm/s.

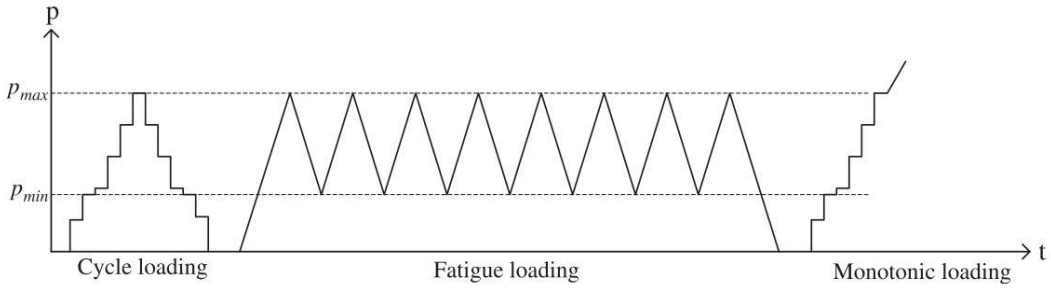

Figure 3.17 Typical fatigue testing regime using multiple load application modes (Cachin et al., 2002)

Baluch et al. (1987) made use of displacement control mode to investigate single edged notch beam (SENB) plain concrete specimens in a three-point bending set up to establish the applicability of Paris' law of crack propagation to plain concrete. Their research yielded positive results using this control method. Castro & Sanchez (2007) also used displacement-control in a three-point bending configuration to develop a damage-based model for plain asphalt concrete. Mundeli (2014) on the other hand used displacement control in a numerical study to assess the static behaviour of patch repaired and strengthened RC beams using FRP composites. It was found that displacement control failed to adequately represent the crack patterns, however it accurately captured the failure characteristics of monotonically loaded RC beams.

Load control

In load or stress-controlled tests a specimen is loaded at predetermined load increments while displacement is measured. Mundeli's (2014) numerical study on the monotonic behaviour of FRP strengthened RC beams also included load-control testing and it was found that although this type of control mode was not good for capturing failure mechanisms, it was able to provide a proper representation of crack patterns.

Both Gregan (2012) and Aidoo et al. (2004) used load control successfully to assess fatigue behaviour of CFRP strengthened RC elements. Aidoo et al. (2004) considered 508mm deep and 5.6m long RC T-beam bridge girders, whereas Gregan (2012) further considered the effect of steel corrosion damage and patch repairing on 150x250x3000mm specimens, to test the fatigue behaviour using load control. Gregan (2012) noted that load control was not effective during monotonic loading prior to cyclic load testing as it was difficult to control specimen failure; for that function displacement control was more suitable. This agreed with the findings expressed by Mundeli (2014) regarding the efficacy of displacement control to capture failure characteristics.

From the above discussion regarding load versus displacement control it can be inferred that the selection of load application mode will depend on the type of testing to be conducted as well as the specimen type (reinforced or plain concrete). The use of displacement control has been effective in

testing fatigue of plain (unreinforced) concrete as well as for static load testing. Furthermore, for monotonic load testing in both three- and four-point configurations, displacement control has proven to be more appropriate in establishing damage mechanisms as well as damage-based models than load control modes. Despite its deficiency with respect to damage mechanisms, load control has been advantageous for investigating crack behaviour as well as for the study of fatigue behaviour of RC elements.

3.4.1.3 Stress range

It is important to identify the stress range at which RC beam samples will be tested. As shown in **Equation 3.17** stress range directly influences fatigue life. The stress range during fatigue testing as shown in **Figure 3.18** refers specifically to the stress in the tensile steel reinforcement (Mahal, 2015).

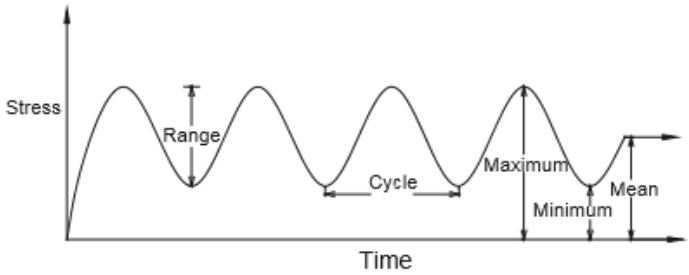

Figure 3.18 Terminology used in fatigue testing (Mahal, 2015)

Charalambidi et al. (2016) conducted an analysis of fatigue tests in 7 different studies. All the studies considered specimens that were FRP strengthened. Charalambidi et al., (2016) reported that most of the studies were carried out at peak stresses of between 60% and 80% of the steel yield stress. These were all high stress range tests, only one study considered low stress range of between 15% and 35% of the yield stress. The tests with the low stress ranges were terminated after up to 6 000 000 cycles. This emphasizes the time-consuming nature of fatigue testing, which may shed some light as to why many of the studies opted for high stress range testing. Mahal, (2015) tested both low and high stress ranges, but for a relatively short period. All the tests specimens that did not fatigue after 600 000 cycles were terminated. Depending on the type of structure under consideration a fatigue life can be estimated from **Table 3.1** in **Section 3.2.1** in order to have an estimation of the duration of the test.

3.4.1.4 Test frequency

It is essential to consider fatigue cycles against the backdrop of load frequency (Li et al., 2017; Mahal, 2015; Song & Yu, 2015), as it could significantly diminish the service life of any structure. Frequency, measured in hertz (Hz), is the number of cycles a specimen experiences per second; this will also vary depending on the type of load the structure experiences. Mass rapid transit structures for example experience low operational loads at a high frequency, compared to railway bridges that experience a lower frequency of loading, but the operational loads may be higher.

For test purposes frequencies can be increased to reduce the testing period. Test frequencies ranging between 1-10Hz have been documented in various research, which is quite a wide range (Charalambidi et al., 2016; Gregan, 2012; Mahal, 2015; Qin, Huang, Zhou, Guo, & Zheng, 2016). Within one experiment for example Qin et al., (2016) considered two frequencies of 2Hz and 10Hz, where they assessed fatigue and durability behaviour of RC beams strengthened with CFRP in hot-wet environments, whereas (Mahal et al., 2015) tested at a low 1.7Hz frequency. In crack growth research test frequencies have been as high as 30Hz (Hoeppner, 1979), however this is uncommon for fatigue testing of RC specimens.

3.4.2 Accelerated corrosion

Reinforcement corrosion may take years to initiate, depending on the quality of cover concrete as well as the likelihood of the other conditions required to induce corrosion being fulfilled (Gregan, 2012; Malumbela et al., 2011; Tigeli, 2014). For research purposes, it may be required to reduce steel diameter to simulate corrosion. This may be done be grinding off a portion of the steel cross-section (Dladla, 2014) or corrosion can be induced in a controlled environment at a higher reaction rate than it would naturally occur (Gregan, 2012). With accelerated corrosion the equivalent structural damage achieved during a year with a corrosion current of 3 μA/cm^2 could be achieved within 2 hours by applying a corrosion current of 10 400 μA/cm^2 (Malumbela, 2010).

Accelerated corrosion entails allowing chloride ions to penetrate cover concrete by means of a sodium chloride (NaCl) solution to de-passivate the protective film at the concrete-steel interface by reducing its pH. The concentration of this solution has been varied from 1% (Mangat & Elgarf ,1999) to 5% (El Maaddawy & Soudki. 2003) by weight of cement, where the higher concentration allows for the critical chloride threshold (0.4% at the steel surface) required for corrosion to occur, to be reached faster. Furthermore, Malumbela (2010) documented that much larger steel mass loss is achieved with long wetting and drying periods of the NaCl solution. This process allows sufficient time for oxygen to reach the concrete-steel interface to stimulate the electrochemical cell.

In addition to the sodium chloride solution, the accelerated corrosion process further requires an electrical current in terms of the Pourbaix diagram shown in **Figure 2.4**. This can be done by connecting RC beam specimens in an electrical series circuit that is powered by a direct current (DC) power supply. A series circuit allows for equal distribution of current between all the specimens (Gregan, 2012). Malumbela (2010) discussed that at high corrosion rates undesirable pitting corrosion may occur, therefore this should be considered when calculating corrosion current. However, as discussed in **Section 3.2.3**, pitting corrosion provides ideal locations for fatigue cracks to form and propagate, therefore in the context of this research, pitting may not be undesired. Corrosion current and mass loss are interlinked by Faraday's law which can be used to determine the mass loss of reinforcement over a certain period as shown in **Equation 3.22** for a predetermined current or vice versa.

$$I_{corr} = \frac{\Delta m F z}{M t} \tag{3.22}$$

Where:

I_{corr}	=	Corrosion current
Δm	=	mass loss in grams
F	=	Faraday's constant
z	=	Ionic charge
M	=	Atomic weight of steel
t	=	Time in seconds

To simulate in service conditions of structures under stress, accelerated reinforcement corrosion is often carried out under sustained load (Gregan, 2012; Malumbela et al., 2011). Some research such as that conducted by Vidal et al. (2007) considered sustained loads of up to 80% of ultimate capacity. The amount of sustained load can be selected as a percentage of the cracking moment of the specimen (Ye et al., 2018). In the case of a RC beam the cracking moment may be calculated using **Equation 3.23** from the South African Standard (SANS 10100-1: 2000):

$$M_{cr} = \frac{f_r I_g}{\gamma_t} \tag{3.23}$$

Where:

M_{cr} = Beam cracking moment
F_r = Modulus of rupture
γ_t = Distance from neutral axis to tension face
I_g = Second moment of inertia

3.4.3 Digital image correlation

Common practice in civil engineering research makes use of strain gauges and strain targets to measure bending or axial strain at predetermined points (Busatta & Moyo, 2017; Dladla, 2014; Malumbela, 2010). LVDT's as well as deflection gauges are used to measure vertical displacement. Cracks are often visually monitored and measured using crack width gauges or Vernier callipers. These measuring devices may be accurate for specific locations on a structure, but do not necessarily provide information about a specific mechanical property of a structure over a larger surface area, such as strain or crack patterns, to the extent that digital image correlation (DIC) enables (Mahal, 2015).

DIC is an optical non-contact tracking and image registration method that is synonymous with the aerospace, mechanical, electronics and automotive industries. More recently it has demonstrated usefulness in structural engineering to measure displacement, strain and crack behaviour. Using DIC it is possible to visualize strain and deflection on the entire surface of a material. The process involves the comparison of a series of images that are captured successively using a high-resolution charge-coupled device (CCD) monochrome camera. The shutter speed of these cameras may be varied between 0.1ms and 2**s** and have resolutions of 2024x2024 pixels. This enables the capturing of high-quality images of high frequency activities, such as bomb blasts, in order to detect phenomena occurring on the material surface that would normally be nearly impossible to detect using traditional techniques. An example of material surface activities may include micro-crack formation as shown in **Figure 3.19**.

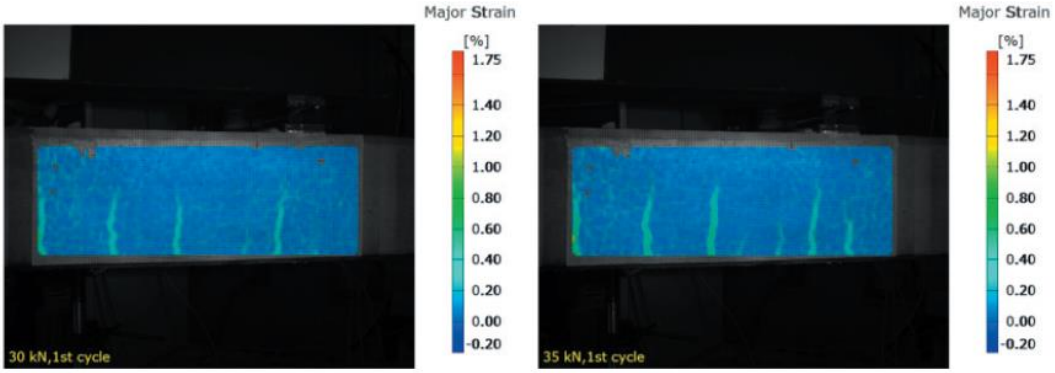

Figure 3.19 DIC images showing crack patterns and crack development (Mahal, 2015)

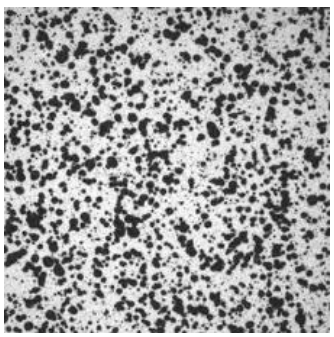

Figure 3.20 Speckle pattern on the surface of a DIC test specimen

To track the strain and deformation on the material surface requires a random speckle pattern to be sprayed onto the surface to be measured, as shown in **Figure 3.20**. An optical strain measuring system, which may include commercially available software such as ARAMIS or Dantec, converts the monochrome images that are captured with the high-resolution camera into distributions of grey scale values. It is possible to evaluate the transformation or deformation of the grey scale values in successive images by comparing it to an original untransformed image that has been calibrated within a predetermined area of interest. The initial grey scale distribution for any pixel area, represented by a function ***g(x,y)*** is related to the transformed image function ***g(x_t,y_t)*** by the expression in **Equation 3.24**.

$$g(x, y) = g(x_t, y_t) \tag{3.24}$$

Where:

x	-	centre x-coordinate of pixel centre
y	-	centre y-coordinate of pixel centre
x_t	-	transposed centre x-coordinate of pixel centre
y_t	-	transposed centre y-coordinate of pixel centre

The original image is converted into the transformed image using the **Equations 3.25** and **3.26**.

$$x_t = a_1 + a_2 x + a_3 y + a_4 xy \tag{3.25}$$

$$y_t = a_5 + a_6 x + a_7 y + a_8 xy \tag{3.26}$$

Where:

a_1 and a_5	=	describe the translation of the pixel's centre
a_2, a_3, a_4, a_6, a_7 and a_8	=	describe the rotation and deformation of the pixel's centre

The above described process characterized the deformation on a two-dimensional (2D) surface, however, it is possible to enable three-dimensional (3D) DIC capabilities by capturing two sets of images using two cameras that have been calibrated to define the 3D space in which the object is being tested.

The application of DIC may vary from microstructural observation, such as research by Li, Gua, Yu, & Fu (2017) on mechanical behaviour of ceramic-metal joints to macrostructural behaviour observations by Karaiskos et al. (2016) on autonomously healed concrete performance as well as Amirshayan et al. (2017) who investigated fatigue of fibreglass reinforced beams. Perhaps the topic that is most related to this research, is work by Mahal (2015) who considered the fatigue performance of FRP strengthened RC beams. Even though the effect of corrosion and patch repairing was disregarded by Mahal (2015) **Figure 3.19** demonstrates how crack pattern development can be monitored over a large surface area, using DIC to measure strain and it is further complimented by the its capability to measure displacement to a high degree of accuracy as shown in **Figure 3.21**.

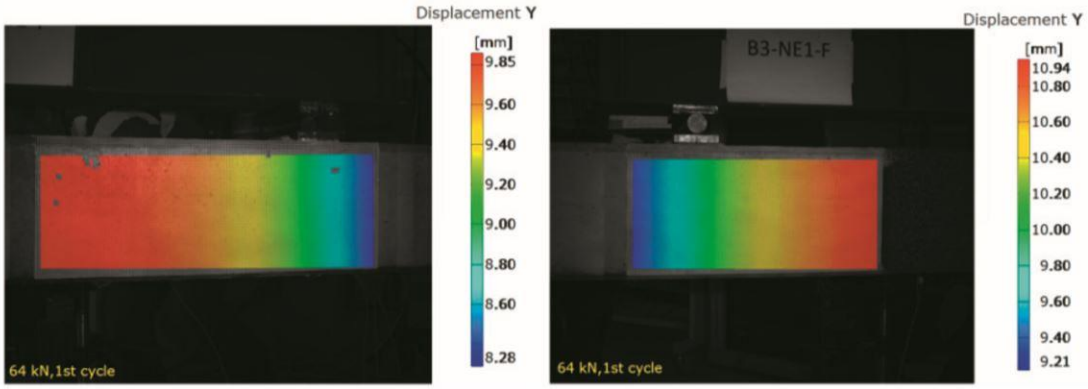

Figure 3.21 DIC images showing crack patterns and crack development (Mahal, 2015)

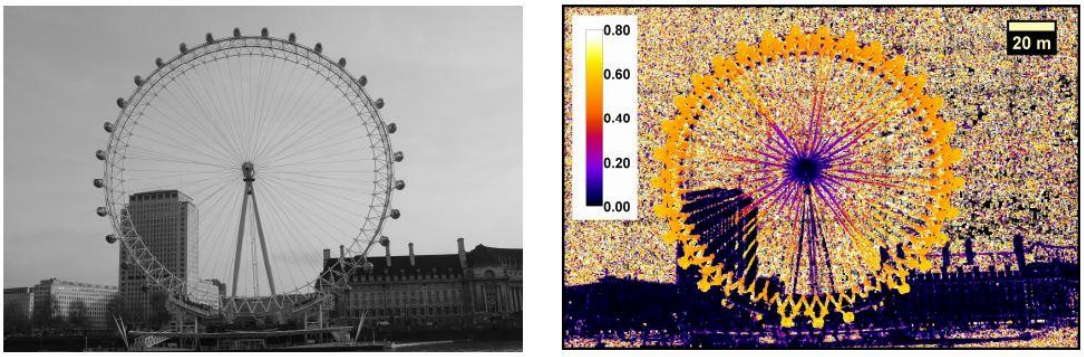

Figure 3.22 The application of DIC on the London Eye from a 20m distance

Mahal (2015) demonstrated the effectiveness of DIC on quite a small test surface of 750mmx300mm from a distance of 1m away, but its application is not limited to such a confined space. Other practical in-situ applications of DIC on civil engineering infrastructure include the monitoring of a railway bridge from about 10m way as demonstrated by Koltsida et al. (2013) as well as the monitoring of the London Eye by McCormick and Lord (2010) from 20m away as shown in **Figure 3.22**. The accuracy of the measurements from further distances will depend on the type of camera lens used to capture the images for processing, as not all lenses are suitable for all structural health monitoring (SHM) applications.

Despite the advantages that vision-based SHM systems (DIC in particular) have over traditional displacement measurement systems, which may include lower instrumentation cost, installation efforts and measurement capacity, they are accompanied by their own set of limitations and challenges. In their review paper of machine-vision based methodologies for displacement measurement in civil structures, Xu & Brownjohn (2018) critically discussed vision-based systems as a three-component framework listing camera calibration, target tracking and structural displacement calculation as the main compartments. According to their review, the factors that influenced the success of these components included:

- Camera and support motion induced by wind may lead to error, possibly affecting the calibration of the camera.
- The camera lens exposure may be affected by variation in lighting and background. This could potentially affect the greyscale values of successively captured images.
- Atmospheric refraction and turbulence of optical light propagating through air, with greyscale values in mind, could induce errors in mathematical models used in vision-based models.
- Short-term tests (less than 12hours) were not as susceptible to the influence of temperature variation on measurement accuracy as long-term tests, with a duration of a few months.

Interpretation of DIC measurement results, especially field application on civil engineering infrastructure, should therefore bear in mind the above listed limitations. Some of the above listed influencing factors may be eliminated where tests are conducted in controlled laboratory environments (Mahal et al., 2015; Ramos et al., 2015; Sadek et al., 2003) through the implementation of artificial lighting and ground vibration control (conducting experiments on a strong floor).

3.5 Chapter summary

This chapter narrowed the research focus on fatigue behaviour of corrosion damaged reinforced concrete. It especially considered how corrosion damage affects structural performance of specimens subjected to fatigue loading. The fatigue behaviour of each constituent material of FRP strengthened RC beams was reviewed critically, before considering the combined behaviour of the composite section.

It was observed that both plain concrete and steel experience 3 stages of cracking, which included crack initiation, crack growth and final rupture, if considered in isolation. It was also found that pitting corrosion may provide an ideal location for crack nucleation to commence on the steel surface. Furthermore, it was reported that FRP composites subjected to fatigue loading are sensitive to: stress ratio, stress frequency, temperature, matrix composition, fibre type and fibre loading angle, but despite these frailties of FRP materials in their own right, fatigue failure of FRP strengthened sections is likely to be caused by rupturing of tension steel before the FRP laminate fails. The Helgason & Hanson (1974) model for steel under direct tension in air under cyclic loading, was found to be the most appropriate fatigue life prediction model for FRP strengthened RC beams, when compared to the Mallet (1991), Tilly & Moss (1982) and the CEB/fib Model code (2010) models. The benefits of using patch repairs and FRP strengthening were considered on the backdrop of the performance parameters introduced at the end of **Chapter 2**. The literature review highlighted the interlude in research that considers the effect of patch repairing on the fatigue behaviour of corrosion damaged and FRP strengthened RC beams, especially where the patch repair extent was varied.

The chapter further discussed various test methods used for fatigue behaviour assessment, considering possible test-set ups, load application methods, stress range selection, suitable test frequencies as well as induction of accelerated corrosion. The review highlighted that four-point bending configurations and load displacement control are more common approaches in fatigue testing than three-point bending configurations and displacement control, respectively. Inducing accelerated corrosion and the use of higher test frequencies were discussed in terms of the benefits they hold for reducing lengthy experimental programmes. Lastly, this chapter considered the potential of DIC as a data acquisition technique when monitoring performance indicators, by discussing how the procedure works as well as its benefits compared to conventional methods used in structural engineering research.

A thorough review of the factors that influence the conceptual design has highlighted some important considerations that were critical in designing the experimental methodology to follow. The experimental methodology design was guided not only by the objectives set out in **Chapter 1**, but more importantly by the selection of appropriate experimental techniques that would assist in achieving the research objectives.

4. EXPERIMENTAL METHODOLOGY

4.1 Introduction

The overall experimental methodology was designed to mimic in-service conditions that structural components are exposed to; more specifically those components that are susceptible to cyclic loading.

The experimental programme comprised fifteen (15) full-scale 155x254x2000mm RC beams with tensile reinforcement that either remained uncorroded or was subjected to accelerated corrosion, and subsequently patch repaired. As shown on **Table 4.1**, 3 beams were left uncorroded (control beams), 3 beams were corrosion damaged over a 450mm length, 3 beams were corrosion damaged over an 800mm length, 3 beams were corrosion damaged over a 1300mm length and the last 3 beams were corroded over a 1800mm length. All 15 RC beams were strengthened with CFRP.

Table 4.1 Test specimen notation

Sample	Identity	Description	Patch Repair Length	FRP strengthening	Test Regime
1	S_CNTRL 1	no corrosion	No patch repair	Strengthened	Monotonic testing
2	S_CNTRL 2	no corrosion	No patch repair	Strengthened	Fatigue 40% stress range
3	S_CNTRL 3	no corrosion	No patch repair	Strengthened	Fatigue 60% stress range
4	S_450mm 1	10% corrosion	450mm	Strengthened	Monotonic testing
5	S_450mm 2	10% corrosion	450mm	Strengthened	Fatigue 40% stress range
6	S_450mm 3	10% corrosion	450mm	Strengthened	Fatigue 60% stress range
7	S_800mm 1	10% corrosion	800mm	Strengthened	Monotonic testing
8	S_800mm 2	10% corrosion	800mm	Strengthened	Fatigue 40% stress range
9	S_800mm 3	10% corrosion	800mm	Strengthened	Fatigue 60% stress range
10	S_1300mm 1	10% corrosion	1300mm	Strengthened	Monotonic testing
11	S_1300mm 2	10% corrosion	1300mm	Strengthened	Fatigue 40% stress range
12	S_1300mm 3	10% corrosion	1300mm	Strengthened	Fatigue 60% stress range
13	S_1800mm 1	10% corrosion	1800mm	Strengthened	Monotonic testing
14	S_1800mm 2	10% corrosion	1800mm	Strengthened	Fatigue 40% stress range
15	S_1800mm 3	10% corrosion	1800mm	Strengthened	Fatigue 60% stress range

4.2 Assumptions

Where possible all material specifications were verified through experimental testing, however where laboratory equipment, time and budget constraints were encountered, assumptions were made. The following assumptions were made during the experimental research:

- All materials specifications and properties provided by material suppliers were correct. These materials included cement, superplasticizer, CFRP laminates, steel reinforcement, strain gauges, sodium chloride and epoxy adhesives.
- Although concrete compressive strength tests showed varying results, all beams were assumed to have the same concrete strength.
- There was perfect bonding between the concrete substrate and the bonded overlay, as well as between the bonded overlay and CFRP laminates.
- Concrete stress-strain behaviour used in the analysis represents conventional stress-strain models.

4.3 Experimental procedure

Various sequential procedures were carried out to prepare the RC beam specimens listed on **Table 4.1** for fatigue testing; section will present details all those procedures.

4.3.1 Structural design and details of RC beams

The RC beams were designed in accordance with SANS 10100-1 to resist a ULS moment of 62.3kNm. This design moment was chosen to sustain the beam own weight as well as a maximum assumed imposed load of 90kN at midspan in a four-point bending configuration. Furthermore, the designed failure mechanism was crushing of compressive concrete and yielding of tension steel. Design calculations for the RC beam specimen are detailed in **Appendix A**. The design moment used in this experiment was higher than that used by Dladla (2014) and Habimana (2017), they had a design moment of 44kNm, therefore the amount of steel reinforcement in this experiment was more than what they had used in their experiments.

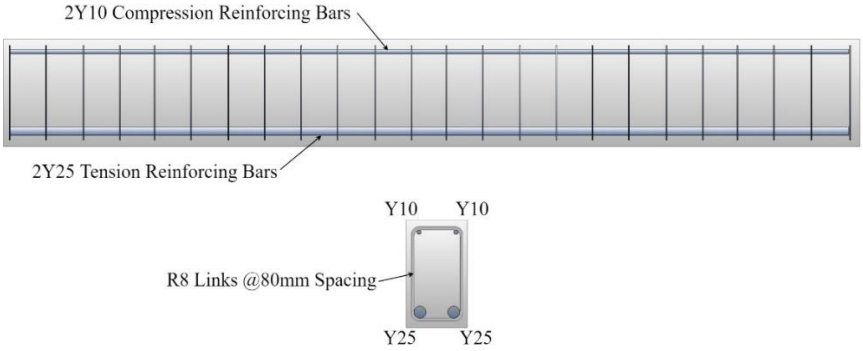

Figure 4.1 Beam specimen reinforcement layout

As depicted in **Figure 4.1**, the design required 2Y25 bars in tension and 2Y10 bars in compression. R8 shear links were placed at 80mm along the beam length. **Table 4.2** provides the steel reinforcement mechanical properties as provided by the local supplier.

Table 4.2 Reinforcing steel mechanical properties

Reinforcement Diameter (mm)	Yield Strength (MPa)	Ultimate Strength (MPa)
10	531	644
25	550	693

All 15 beams were cast using 40MPa concrete, where cover was maintained at 25mm throughout. The concrete strength was lower than the 50MPa concrete used by Dladla (2014) and Habimana (2017). The 40MPa concrete mix was designed in accordance with the 9th edition of Fulton's Concrete Technology which yielded the constituent mix quantities shown in **Table 4.3**.

Table 4.3 Concrete mix constituent quantities

Binder Type	W/C ratio	Water (l/m^3)	Binder (kg/m^3)	Coarse Aggregate(kg/m^3)	Fine Aggregate(kg/m^3)
CEMI 52.5N	0.55	195	355	1007	840
For 1.5m^3		292.5	532.5	1510.5	1260
Concrete volume required – 1.1811 m^3 (mix 1.5m^3 to account for testing)					

Due to the limited number of beam moulds available in the concrete laboratory, four concrete batches were mixed. Four beams were cast with each batch using the moulds shown in **Figure 4.2**.

Figure 4.2 Steel moulds for beam specimens

For quality control purposes six (6) 100x100x100mm concrete cube samples, 6 dog bone samples and 6 100x200mm cylindrical prism samples were collected from each batch for compressive strength, tensile and elastic modulus testing, respectively. Three samples were tested at 7 and 28 days, respectively, for each of these mechanical properties. All concrete samples were water-cured at a temperature of 24ºC. Concrete mechanical property results are summarized on **Table 4.4**; the results presented in **Table 4.4** are averages of the four batch mixes. Chryso Premia 310 super plasticizer was added to the freshly mixed concrete to adjust workability. Concrete slumps were taken to gauge workability where slump was maintained to 120±20mm.

Table 4.4 Concrete 40MPa mix material properties

	7 days	Standard Deviation	28 days	Standard Deviation
Compressive Strength (Mpa)	36.5	± 1.9	43.5	± 1.1
Tensile Strength (Mpa)	2.3	± 0.04	2.7	± 0.2
Modulus of Elasticity (Gpa)	34.5	± 3.9	39.6	± 1.2

24 hours after concrete casting each batch of beams was demoulded and cured using damp Hessian cloth for 28 days as shown in **Figure 4.3**, to achieve maximum concrete strength.

Figure 4.3 Beam specimen wrapped in hessian cloth during curing phase

4.3.2 Accelerated corrosion

Reinforcement corrosion was induced electrochemically in a controlled environment through acceleration corrosion. The corrosion extent was varied to obtain damage lengths of 450mm, 800mm, 1300mm and 1800mm. However, over each damage extent a uniform 10% degree of corrosion was maintained for each damage length. This equates to 5% corrosion per tensile reinforcing bar, as 5% has been shown to yield the maximum bond strength between reinforcing steel and surrounding concrete (Almusalla et al., 1996).

Figure 4.4 Electrical wiring taped to reinforcement prior to soldering

Corrosion was induced by creating an electrochemical cell, where tensile steel reinforcement served as anode and 12mm stainless-steel rods served as cathode. Copper electrical wires were soldered to tensile reinforcement prior to casting concrete as **Figure 4.4** depicts. These wires were also soldered to the stainless-steel rods. The soldered connections were covered with shrink tubing to prevent moisture intrusion. To achieve uniform corrosion damage, the electrical wiring from 12 beams were connected in parallel to supply the same current from a DC power supply to all specimens. A corrosion pond containing 5% sodium chloride solution was assembled on the beam tensile face using HDPE strips as shown in **Figure 4.5(d)**.

The time required to induce 10% corrosion in the RC beams was calculated in **Appendix B.2** using Faraday's law as shown in **Equation 4.1**. For a corrosion current of 1 ampere (A), the desired degree of corrosion can be obtained in approximately 30.8 days. The current supplied for the DC power supply was continuously monitored. Where fluctuations were encountered, the current was adjusted to the desired current.

$$I_{corr} = \frac{\Delta m F z}{M t} \tag{4.1}$$

Where:

I_{corr}	=	Corrosion current
Δm	=	mass loss in grams
F	=	Faraday's constant
z	=	Ionic charge
M	=	Atomic weight of steel
t	=	Time in seconds

All 12 beams were corroded under sustained static loading. Dead load was applied onto the beams through an inverse 4-point bending system where the loads applied at the beam ends, as shown in **Figure 4.5(a)**, induced a bending moment on the beam tensile surface equivalent to 60% of the beam cracking moment. The beam's cracking moment was calculated using **Equation 4.2** below as detailed in **Appendix B.3**.

$$M_{cr} = \frac{f_r I_g}{\gamma_t} \tag{4.2}$$

Where:

M_{cr}	=	Beam cracking moment
F_r	=	Modulus of rupture
γ_t	=	Distance from neutral axis to tension face
I_g	=	Second moment of inertia

Pinned supports were created at the loading points using mild steel round bars, as shown in **Figure 4.5(c)**, to allow the beams to deflect during corrosion. Deflection during corrosion was measured using dial gauges, however no deflection of more than 0.2mm was observed.

(a) (b)

(c) (d)

Figure 4.5 Sustained static load beams setup to induce partial cracking moment

4.3.3 Patch repair

The patch repair process commenced with removal of damaged cover concrete in the tension region in varying lengths of either 450mm, 800mm, 1300mm or 1800mm. Concrete was removed using jack hammers to a depth of at least 20mm below the corroded reinforcement and 50mm beyond the damage extent as shown in **Figure 4.6**. Concrete removal was carried out carefully to avoid damaging the rest

of the beam. Exposed steel surfaces were then sufficiently cleaned using compressed air and any remaining rust was removed from corroded steel using hand operated mechanical rotary steel brush.

Figure 4.6 Exposed RC beam after removal of damaged cover concrete in the tension region

After removal of damage cover concrete strain gauges were installed on the corroded steel bar; the gauges were protected with aluminium angles and sealed with a waterproof silicone sealant. The purpose of the strain gauges will be discussed under **Section 4.3.5.2** of this chapter. Before applying the patch repair mortar, the corrosion damaged steel bars were treated with SikaTop-Armatec110 EpoCem, a locally available anti-corrosion coating, to reinstate the passive protective layer inherent of the steel-concrete interface. Lastly, SikaTop-Armatec110 EpoCem was applied to the concrete substrate as a bonding agent prior to patch repairing.

Locally sourced Sikacrete 214 was used as the patch repair mortar in this experiment. It was chosen due to its cementitious chemical base that provides compatibility with the concrete substrate, as well as its high tensile bond strength, low shrinkage and rapid strength development characteristics.

Table 4.5 Sika 214 mortar material properties

	7 days	Standard Deviation	28 days	Standard Deviation
Compressive Strength (MPa)	64.2	± 1.9	79.2	± 1.2
Tensile Strength (MPa)	1.9	± 0.9	2.8	± 0.4
Modulus of Elasticity (GPa)	28.9	± 1.2	35.6	± 2.6
Tensile bond strength (MPa)	2.3	± 0.2	2.5	± 0.5

During application of patch repair mortar six (6) 100x100x100mm concrete cube samples, 6 dog bone samples and 6 100x200mm cylindrical prism samples were collected from each batch for compressive strength, tensile and elastic modulus testing, respectively, at 7 and 28 days. In additionally, six (6) 150x150x75mm half cubes, made from the concrete beam mixes, were patch repaired with Sikacrete 214 in order test for tensile bond strength at 7 and 28 days. All mortar samples were water-cured at a temperature of 24ºC. Material strength results are documented in **Table 4.5**. Considering that the patch repair product is a free-flowing mortar, no slump measurements were taken. The patch repaired areas were demoulded after 24 hours and cured for 7 days by covering with damp Hessian cloth as shown in **Figure 4.7**. Due to the drying shrinkage problems associated with patch repair mortars (PRMs), the desire to yield high early-age strength, commercially available PRMs tend to have high mechanical properties. Ideally it is preferred for the PRM to match substrate concrete, but with locally available

products it was not possible. The high strength PRMs used in this research is likely to cause an increase in stiffness of the test specimens.

Figure 4.7 Patch repaired RC beams covered with damp Hessian cloth

4.3.4 Design and details of CFRP strengthening

The RC beam FRP strengthening was designed for flexure in accordance with Täljsten (2006), as they were intended for four-point bending cyclic load testing. As detailed in **Section 4.3.1** the RC beams were initially designed to resist a ULS capacity of 62.3kNm; this capacity was reduced 10% by accelerated corrosion. The difference in performance capacity was used to calculate the amount of FRP strengthening required using **Equation 4.3**.

$$A_{FRP} = \frac{\Delta M}{0.9\, h \varepsilon_f E_f} \tag{4.3}$$

Where:

A_{FRP}	=	amount of FRP strengthening
ΔM	=	difference in ULS moment to be carried by FRP
h	=	beam depth
ε_f	=	FRP strain as provided by supplier

Design calculations detailed in **Appendix C.1** show that the induced capacity reduction of 6.22kNm required a 9.71mm^2 of FRP reinforcing. SikaCarboDurS512 carbon fibre laminates were selected, each laminate has a cross-section of 60mm^2, 2 laminates were considered during design analysis to simulate an over-reinforced section. The flexural design considered 4 possible failure modes associated with double reinforced beams, which were:

I. Failure in laminate with yielding in the compression steel reinforcement

$$\rho_{fu} \leq \rho_{f1} \leq \rho_{fn} \tag{4.4}$$

II. Failure in laminate without yielding in the compression steel reinforcement

$$\rho_{f2} \leq \rho_{fu}\,, \rho_{fn} \tag{4.5}$$

III. Crushing of concrete as well as yielding in the compression steel reinforcement

$$\rho_{f1} \geq \rho_{fn}, \rho_{f0} \tag{4.6}$$

IV. Crushing of concrete without yielding in the compression steel reinforcement

$$\rho_{fn} \leq \rho_{f2} \leq \rho_{f0} \tag{4.7}$$

Parameter $\boldsymbol{\rho_f}$ is a strengthening ratio which represents the strain condition in the compressed steel reinforcement. $\boldsymbol{\rho_{f1}}$ and $\boldsymbol{\rho_{f2}}$ indicate whether the steel has yielded or not, respectively. $\boldsymbol{\rho_{fu}}$, $\boldsymbol{\rho_{fn}}$ and $\boldsymbol{\rho_{fo}}$ evaluate either normally-reinforced, balanced or over-reinforced strengthened cross-sections, respectively. After computing and analysing these strengthening ratios, for the selected FRP cross-sectional area, with respect to the 4 possible failure modes, it was established that failure mode IV would prevail. Based on the anticipated failure mode an updated ULS capacity of 79.3kNm was calculated in **Appendix C.1** using **Equation 4.8**.

$$M_{capacity} = \left(\frac{x-d'_s}{x}\varepsilon_{cu}\right) A'_s E_s(\beta x - d'_s) + A_s f_y(d_s - \beta x) + \left(\frac{h-x}{x}\varepsilon_{cu} - \varepsilon_{u0}\right) E_f A_f(h - \beta x) \tag{4.8}$$

Where:

$M_{capacity}$ = moment capacity of strengthened RC beam
x = inner lever arm
d_s = effective height to tensile reinforcement
d'_s = effective height to compression reinforcement
ε_{cu} = compressive strain in concrete
ε_{u0} = strain in underside concrete remaining load
A'_s = compression reinforcement area
A_s = tensile reinforcement area
A_f = cross-sectional area of composite
E_s = modulus of elasticity of steel
E_f = modulus of elasticity for composite
β = proportionality factor for concrete
f_y = yield stress in tensile reinforcement
h = section height

Locally sourced epoxy adhesive Sikadur 30 was used to bond FRP strips and the patch repair mortar or concrete surface once the substrate had reached a minimum tensile strength of 1.5MPa. The epoxy was applied uniformly to the FRP laminates using an applicator as shown in **Figure 4.8**.

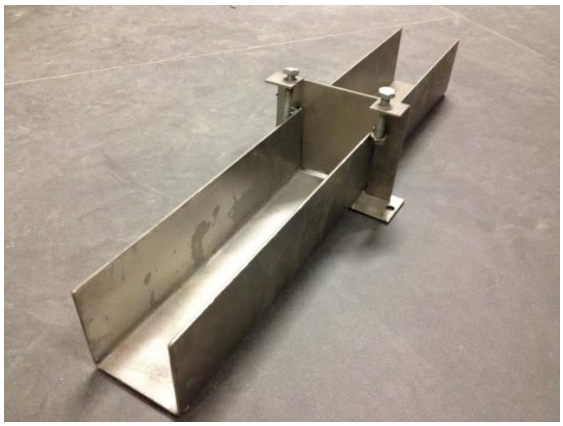

Figure 4.8 Epoxy adhesive applicator

The FRP strips were cleaned using SikaColma prior to installation. Furthermore, SikaWrap was bonded to the RC beam ends with an epoxy adhesive, SikaDur 330 to provide restraint against end-debonding of the laminates. Mechanical properties of the various FRP and epoxy materials used in this experiment are shown in **Table 4.6**.

Table 4.6 Sika CFRP structural strengthening material properties

	FRP Laminate	FRP Wrap	Epoxy resin for repair mortar	Epoxy resin for FRP laminate	Epoxy resin for FRP wrap
Compressive Strength (MPa)	-	-	60-70	70-80	-
Tensile Strength (MPa)	3100	4900	18-20	24-27	30
Modulus of Elasticity (GPa)	165	230	-	11.2	3.8
Thickness (mm)	1.2	0.127	-	2	-

4.3.5 Monotonic and dynamic testing

4.3.5.1 Test setup and equipment

Monotonic and fatigue testing were conducted under a four-point bending configuration as shown in **Figure 4.9**. Two point loads 450mm apart were applied on the compression surface using an Instron actuator through a spreader beam. During both static and fatigue testing the actuator was governed by load control, because one of the objectives of the research was to monitor stiffness through midspan deflection measurements. The reason for using load control for static testing, despite literature suggesting that displacement control would be more suitable for that purpose, was because the objective of the monotonic testing was to find the failure loads of the various specimens and to record the tensile steel strain during testing and at ultimate failure.

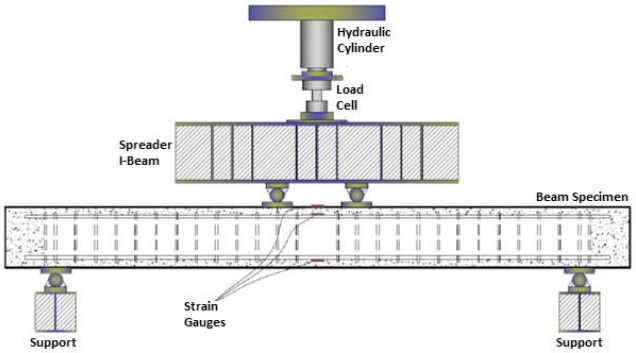

Figure 4.9 Four-point bending fatigue test set up (Maranan et al., 2015)

One specimen from each patch repair extent was tested under static loading to establish and verify ULS failure loads. Tensile steel strains were recorded during static testing and were used to gauge the stress range for cyclic load testing. **Table 4.7** presents the results from the static test results, showing that all the specimens failed at loads that were higher than they were designed for. These static test results were much higher than those obtained by Dladla (2014) and Habimana (2017), in the order of 100kN. The variation in the failure loads compared to Dladla (2014) and Habimana (2017) may be attributed to two main differences in the experimental design. The design moment and the amount of FRP reinforcement of this experiment are higher than those previously used by Dladla (2014) and Habimana (2017), ultimately resulting in the over-strengthened section considered for this research.

Table 4.7 Static loading test results

Identity	Test Type	Failure Load (kN)	Moment at Failure (kNm)	Design Moment (kNm)
S_CNTRL 1	Static	274	92.5	85.1
S_450mm 1	Static	325	109.7	79.3
S_800mm 1	Static	300	101.3	79.3
S_1300mm 1	Static	293	98.9	79.3
S_1800mm 1	Static	290	97.9	79.3

The remaining two specimens of each damage extent were subjected to cyclic loading under different stress ranges. The stress ranges were derived from the minimum and maximum applied loads, where a minimum load of 6kN was chosen to avoid impact loads and the maximum loads of either 40% or 60% of the beam ULS capacity derived from the static test results presented in **Table 4.7**. The maximum loads of 40% and 60% of ULS were used to facilitate low and high cyclic loading, respectively. The proportions ranging between 40% and 60% of ULS were selected as they represent the in-service loads experienced by structures. The stress ranges based on the static failure loads are shown in **Table 4.8**.

Table 4.8 Cyclic loading test regime

Identity	Test Type	Minimum Load (kN)	Maximum Load (kN)	Stress Range (MPa)	% of ULS	Predicted fatigue life (cycles)
S_CNTRL 2	Fatigue	6	109.6	169.4	40	$10^{6.029}$
S_CNTRL 3	Fatigue	6	164.4	265.4	60	$10^{5.496}$
S_450mm 2	Fatigue	6	130	234	40	$10^{5.670}$
S_450mm 3	Fatigue	6	195	366	60	$10^{4.938}$
S_800mm 2	Fatigue	6	120	204.2	40	$10^{5.836}$
S_800mm 3	Fatigue	6	180	219.4	60	$10^{5.197}$
S_1300mm 2	Fatigue	6	117.2	185.8	40	$10^{5.938}$
S_1300mm 3	Fatigue	6	175.8	291.8	60	$10^{5.350}$
S_1800mm 2	Fatigue	6	116	165.8	40	$10^{6.049}$
S_1800mm 3	Fatigue	6	174	261.8	60	$10^{5.516}$

The sinusoidal loads were applied at a frequency of 4Hz which is relatively high, but an acceptable test frequency for fatigue testing RC concrete. This frequency was selected to reduce the testing period. Based on the stress ranges, the anticipated number of fatigue cycles were calculated using the Helgason and Hanson model of steel under direct tension in air (Zorn, 2006) as shown in **Equation 4.9**. This model has been shown to be predict the fatigue life of CFRP strengthened RC beams reasonably well.

$$\log(N_f) = 6.969 - 0.00555S_r \tag{4.9}$$

Where:

N_f - number of fatigue cycles

S_r - tension steel stress range

The anticipated number of fatigue cycles to failure are listed in **Table 4.8**.

4.3.5.2 Data acquisition

Various methods were used to acquire the data required to assess the performance parameters. Vertical displacement measurements were collected using LVDT's at specimen midspan and supports. Strain measurements were collected using KYOWA strain gauges at four locations, namely: concrete compression surface, concrete tension surface, CFRP laminate and on tensile steel reinforcement as shown in **Figure 4.10**. **Table 4.9** provides the specifications for the strain gauges used in this experiment. Prior to patch repairing the strain gauges were protected using clay and aluminium equal angles as recommended by the supplier.

Table 4.9 Strain gauge specifications

KYOWA Strain Gauge	
Model	KFGS-5-12-C1-11
Measurement direction	Uniaxial
Resistance	120Ω
Gauge factor	2.10
Length	5mm
Leads	25mm Silver-clad copper

Figure 4.10 Strain gauge installation on tension steel reinforcement

A total of 8 Demec strain targets were placed on one side of each specimen as shown in **Figure 4.11**, to track the neutral axis migration. An extensometer was used to measure relative movement of the Demec targets, where a reduction in the distance between two targets indicated compressive strain and an increase indicated tensile stain.

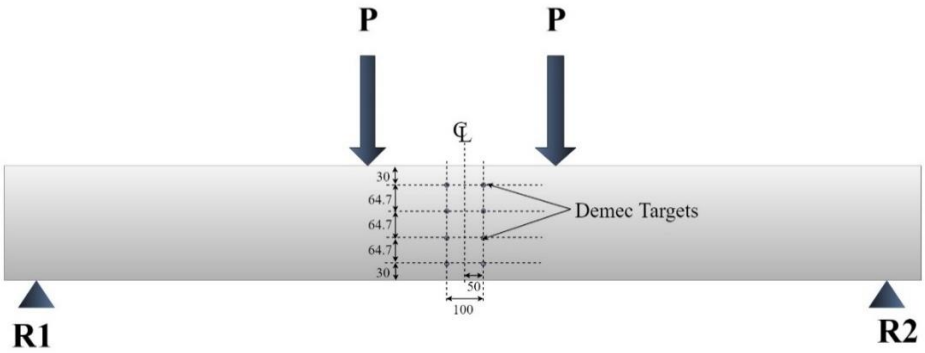

Figure 4.11 Demec strain target configuration

Crack behaviour was be monitored by using two different techniques. The first method entailed visual monitoring, where crack patterns were tracked using a permanent marker at pre-determined load

intervals. During fatigue testing crack patterns were assessed after every 20 000 load cycles. For static testing specimens were loaded at 10kN intervals, assessing crack patterns incrementally.

The second method was much more sophisticated, where material behaviour was recorded using digital image correlation (DIC). This method involved spray painting a stochastic matt black pattern on the test surface. A high-resolution 5-megapixel (MP) monochrome Basler digital camera captured the test surface through a 16mm Kowa lens 2000mm away from test specimen, as shown in **Figure 4.12(a)**, to ensure that the camera remained undisturbed for the duration testing. Artificial lighting was used to avoid possible variations in the grey scale value due to changes in natural lighting. The entire 254x2000mm surface of the beam was calibrated using a 35mm calibration target as shown in **Figure 4.12(c)**. This made it possible to evaluate strain and deflection over the surface of the beam as opposed to the localized capabilities of the LVDTs and Demec targets.

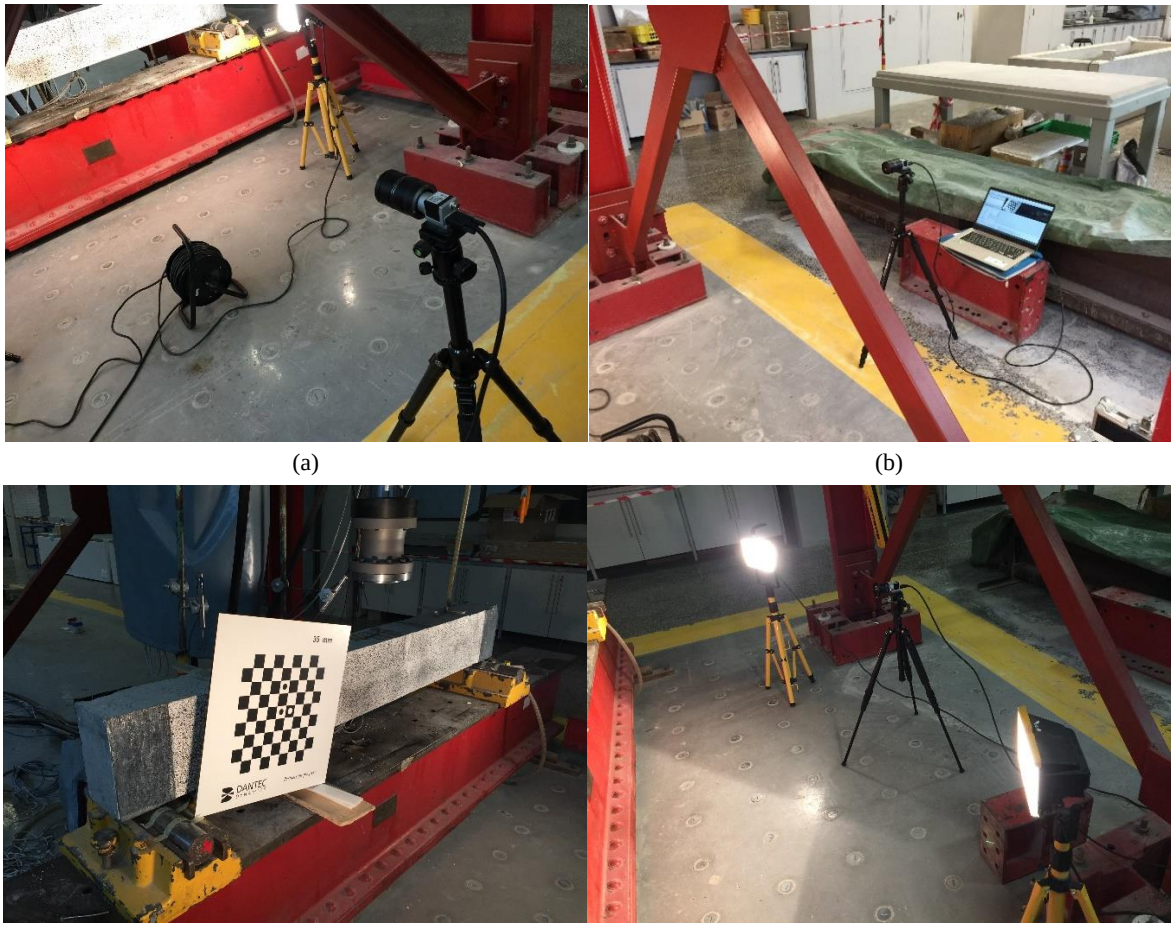

(a) (b)

(c) (d)

Figure 4.12 Digital image correlation laboratory set up

During fatigue testing the test was stopped after every 20 000 cycles and loaded to the maximum test load. At maximum load an image was captured for DIC processing. For static testing images were taken after every 10kN interval.

The images were captured using Basler's Pylon software and were then post processed using Dantec software. Dantec software tracked the surface pattern as described in **Section 3.4.3** and converted relative movement of grey scale values into displacement and strain measurements as shown in **Figure 4.12**. This second method was especially useful when monitoring micro-strains and cracks invisible to the naked eye.

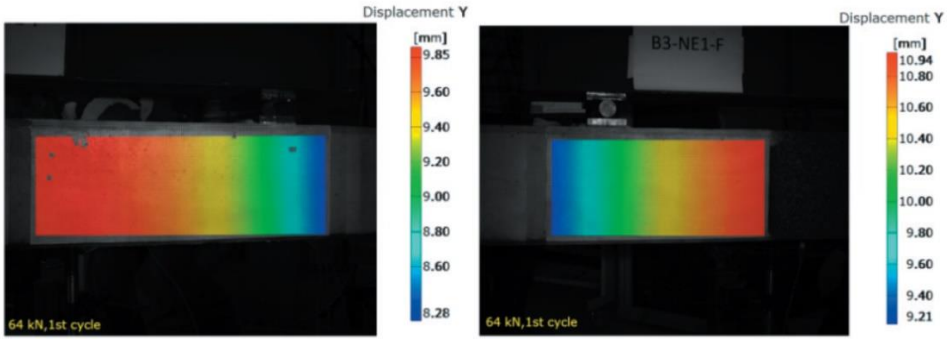

Figure 4.13 DIC image showing displacement measurements at various load cycles (Mahal, 2015)

Data acquired during the experiments, except for DIC images which was collected separately, was logged automatically by Wave Matrix computer software. This data includes strain measurements from gauges, actuator loads, displacement from LVDTs and number of fatigue cycles. All the collected data was correlated in real time, which enabled accurate analysis and post-processing of data.

4.4 Chapter summary

The research methodology described in this chapter was designed to compare the relative fatigue performance and behaviour of RC beams that have constant corrosion damage over varying patch repair lengths. RC beams were designed as over-reinforced sections as this was found to be a common occurrence in strengthened sections where the SLS design checks guide the design of the entire section. One sample of each damage extent was initially tested under monotonic loading to verify ULS capacity and to gauge cyclic loading stress ranges; the remaining two samples were used to evaluate fatigue behaviour of specimens subjected to either low or high stress range fatigue testing.

Furthermore, the methodology details various steps that were taken during the experimental programme. It commenced with the structural design of RC beams, their mix design, curing procedure as well as how their material properties were verified. The accelerated corrosion process was described, including the experimental set up, calculations of the corrosion current and the duration of the process. The methodology then proceeded to detail the patch repair process, describing the removal of damaged concrete, cleaning and application of the bonded overlay. Based on the induced corrosion the design of required FRP strengthening was outlined as well as the CFRP installation process. Lastly, the static and fatigue testing procedure was described, indicating the load application method, testing stress range, test frequency and data acquisition techniques that were employed.

5. RESULTS AND DISCUSSIONS

5.1 Introduction

This research formed part of a larger study that considered the effect of corrosion damage length on the structural performance of corrosion damaged, patch repaired and FRP strengthened RC beams. Dladla (2014) and Mundeli (2014) carried out experimental and computational mechanics studies, respectively, on the static performance of such specimens, while Habimana (2017) considered the effect of impact loading on these specimens. The aim of this research was to extend on their studies to consider the fatigue behaviour of corrosion damaged, patch repaired and FRP strengthened RC beams. To that end 15 RC beam specimens were cast and investigated considering various parameters to gauge relative performance.

The 155x254x2000mm specimens were designed according to SANS 10160-1 and cast in a controlled laboratory. After 28 days of curing, 12 of specimens were set up to induce 10% corrosion under a four-point bending sustained loading configuration. The remaining 3 specimens were left uncorroded. The 12 specimens were categorized into 4 different damage extents containing 3 samples each; these extents were 450mm, 800mm, 1300mm and 1800mm. After an accelerated corrosion period of 30.8 days, damaged concrete from the corroded specimens was removed and the specimens were patch repaired in various lengths, equal to their corrosion damage lengths. The patch repair mortar was cured for 7 days, after which all the specimens were strengthened with the same amount of CFRP laminates.

One sample of each damage extent was tested under four-point bending monotonic loading to failure. The results from the static tests were used to gauge the fatigue loading test ranges. The remaining 2 specimens from each damage extent were tested under cyclic loading where the maximum test loads were either 40% or 60% of the static failure loads. The results from the monotonic and fatigue tests are presented in **Table 5.1**.

Table 5.1 Monotonic and fatigue loading test results

Identity	Load Range (kN)	1st Cycle Dissipation Energy (Area/load)	Total No. Cycles	Ultimate Static Load (kN)	Average Steel Corrosion Mass loss (%)	Fatigue Failure Mode	Static Failure Mode	Static Load after Fatigue Testing (kN)
S_CNTRL 1	*Static*	-	-	274	0	-	CC & FD	-
S_CNTRL 2	6-109.6	0.435	$10^{6.000}$	-	0	No Fatigue Failure		276
S_CNTRL 3	6-164.4	0.458	$10^{5.408}$	-	0	SR (1 bar), FD & CC	-	-
S_450mm 1	*Static*	-	-	325	9.87	-	CC & FD	-
S_450mm 2	6-130	0.399	$10^{5.897}$	-	9.87	SR (2 bars), FD & CC		-
S_450mm 3	6-195	*IC**	$10^{5.078}$	-	9.87	SR (1 bar), FD & CC		-
S_800mm 1	*Static*	-	-	300	7.11	-	CC & FD	-
S_800mm 2	6-120	0.388	$10^{6.061}$	-	7.11	No Fatigue Failure		300
S_800mm 3	6-180	1.274	$10^{5.011}$	-	7.11	SR (1 bar), FD & CC		-
S_1300mm 1	*Static*	-	-	293	7.11	-	CC & FD	-
S_1300mm 2	6-117.2	0.557	$10^{6.035}$	-	7.11	SR (2 bars), FD & CC		-
S_1300mm 3	6-175.8	*IC*	$10^{5.304}$	-	7.11	SR (2 bars), FD & CC		-
S_1800mm 1	*Static*	-	-	290	5,68	-	CC	-
S_1800mm 2	6-116	0.622	$10^{6.301}$	-	5,68	No Fatigue, SR (1 bar)		216
S_1800mm 3	6-174	1,704	$10^{5.393}$	-	5,68	SR (2 bars), FD & CC		-

*IC= inconclusive results, CC= concrete crushing, FD= carbon fibre debonding, SR= steel rupture

During fatigue testing various data acquisition methods were employed to gather information that would allow for analysis of the performance parameters discussed in the experimental methodology. LVDTs were used to record vertical deflections. Four strain gauges were used on each specimen to track relative strain measurements on the compression concrete, tension concrete/patch repair mortar, carbon fibre

laminate as well as on the tension steel. Demec targets were used to monitor shifting of the neutral axis. Instron software recorded the number of cycles the actuator applied to each specimen. Lastly, DIC was used to track relative movement of a speckled pattern on the surface of each specimen, in order to derive deflection and strain fields across the surface. This chapter will first discuss findings from the accelerated corrosion process. The information acquired during fatigue testing will then be discussed in terms of four main performance parameters. Those performance parameters were fatigue life, stiffness, crack behaviour and failure modes.

5.2 Accelerated corrosion

After test specimens had undergone fatigue testing, they were opened once again to retrieve tension steel. The steel was wire brushed and sand blasted in order to assess the extent of corrosion damage. The exposed steel was closely examined, considering the mass loss, type of corrosion as well as the locality of the corrosion damage. **Table 5.2** presents the findings from the post-fatigue assessment of corrosion damaged tension steel. The measured mass loss presented in the table are the total amounts for both tension bars along the corrosion damaged length, whereas the equivalent uniform depth was provided for a singular bar.

Table 5.2 Accelerated corrosion results

Identity	Corrosion Type	Measured Mass Loss (g/m)*	Equivalent Uniform Depth (mm/bar)	Percentage Mass Loss (%)	Standard Deviation (%)
S_450mm 1	*Pitting*	189.96	0.31	9.87	± 0.30
S_800mm 1	*Pitting*	136.85	0.22	7.11	± 1.46
S_1300mm 1	*Pitting*	136.97	0.22	7.11	± 0.95
S_1800mm 1	*Pitting*	109.33	0.18	5,68	± 0.26

*calculated using the entire length of corroded steel

The experiment aimed to induce a combined 10% corrosion in each specimen. From the results presented in **Table 5.2** it can be seen that this aim was not possible for all the specimens. The results showed that the 450mm specimens achieved a mass loss of 9.87%, which was the closest to the desired 10%. Despite higher variability on the 800mm specimen results, the 800mm and 1300mm specimens achieved a similar mass loss of 7.11%; the 1800mm specimen had the lowest mass loss of almost half the desired mass loss, achieving only 5.68%. The reason for the reduction in mass loss with an increase in damage length is suspected to be related to the cathode-to-anode ratio, where a high cathode-to-anode ratio provides more favourable conditions for corrosion to occur. By increasing the damage length, the cathode-to-anode ratio was reduced, thus creating less favourable conditions for corrosion to occur. Another possible reason for the higher corrosion rate may be related to the fact that accelerated corrosion was carried out under sustained loading. Under sustained loading the maximum moments occur in the middle 450mm portion. At midspan the cracks tend to open more in this region allowing for a greater ingress of chlorides in this region.

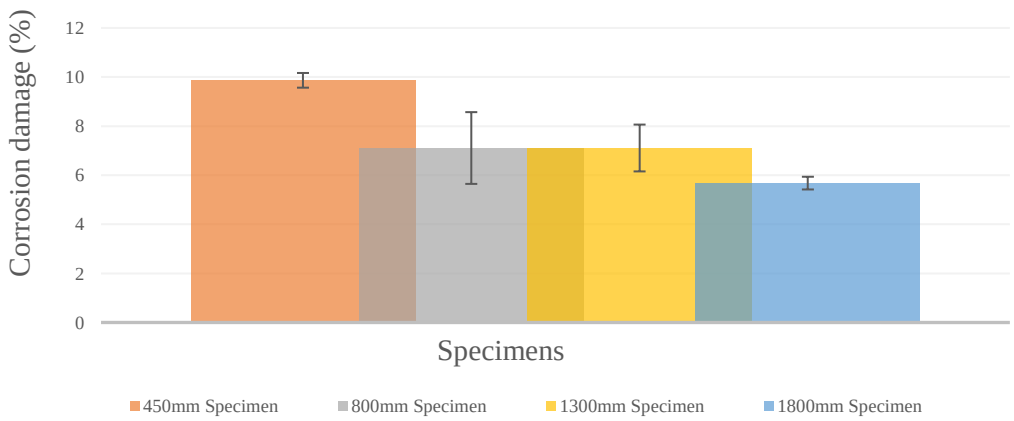

Figure 5.1 Average percentage corrosion damage due to accelerated corrosion

Findings from the corrosion damaged steel inspection revealed that the specimens with the shorter damage length experienced a higher average mass loss than the specimens with a longer damage length, as shown in **Figure 5.1**. However, regardless of the degree of corrosion, the prevailing type of corrosion was pitting corrosion as shown in **Figures 5.2** and **5.3**. This type of corrosion was expected considering that the accelerated corrosion was chloride induced, which has been commonly associated with pitting corrosion (Ballim et al., 2009).

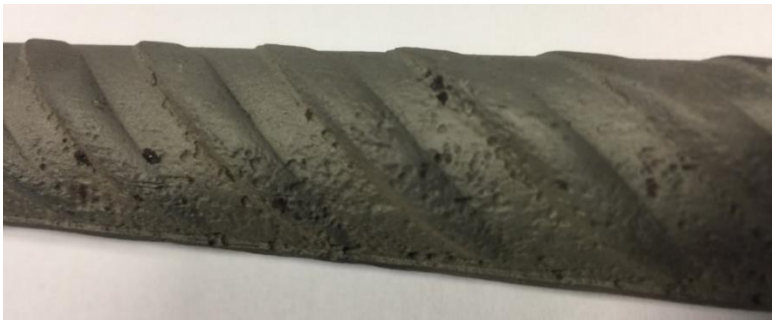

Figure 5.2 Corrosion distribution along tension reinforcement

It is evident on **Figure 5.2** that the corrosion damage was concentrated on only a portion of the steel and this portion was found to be the steel surface closest to the specimen tension surface. Therefore, although the equivalent uniform corrosion depth presented on **Table 5.2** is a reasonable representation of corrosion damage, it may be a more suitable indicator for uniform corrosion, but not so much when the corrosion is concentrated to certain areas of the reinforcing bar. The portion of steel closest to the specimen tension surface also experiences the highest tension within the steel cross section; that portion was found to be an ideal location for cracks to form and propagate from until eventual steel rupture as shown in **Figure 5.3**.

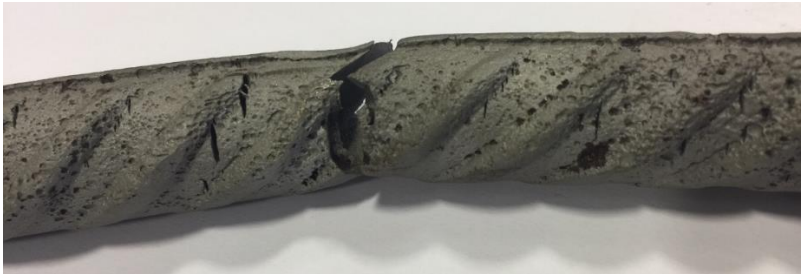

Figure 5.3 Fatigue crack propagation in relation to pitting corrosion

5.3 Performance indicators

5.3.1 Ultimate failure load & fatigue life

Monotonic loading behaviour

All 15 specimens were designed to resist an ultimate moment of 62.27kNm, as detailed in **Appendix A**. After 10% corrosion damage and FRP strengthening the moment capacity increased to 79.3kNm (i.e. maximum load 234.96kN). **Figure 5.4** shows the ultimate failure loads of the specimens with varying corrosion damage extents. The increase in ULS capacity may be attributed to higher strength materials. The steel reinforcement design strength was 450MPa, whereas the steel used in the experiment had a yield strength of 550MPa. In addition, the concrete strength of the cube samples was higher than the design strength; it was designed for 40MPa concrete, whereas the actual compressive test results yielded 43.5MPa after 28 days. A design check of the specimen capacity using the actual material strengths revealed a ULS capacity of 90.96kNm (i.e. maximum load 269.5kN). This shows a close correlation between the experimental results and moments obtained from the design check.

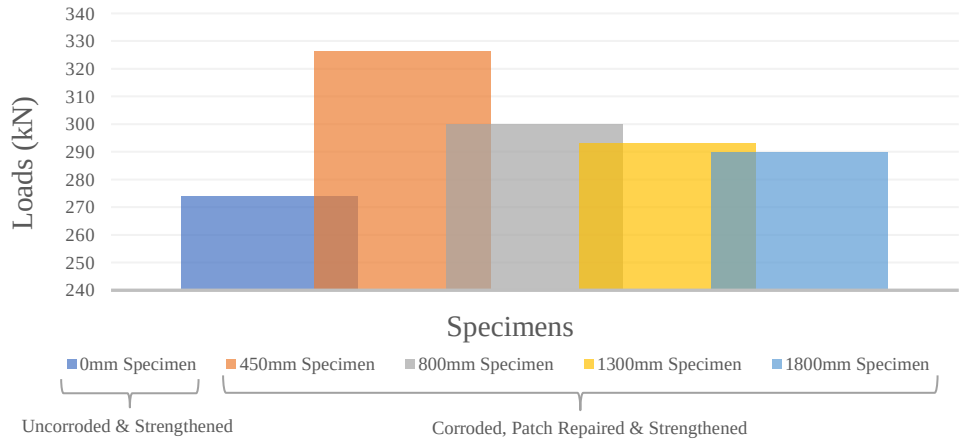

Figure 5.4 Ultimate failure load summary

The static test results shown in **Figure 5.4** indicate that the specimen with the shortest damage length outperformed the specimens with the longer damage lengths. The 450mm specimen had an 18.6% higher failure load than the control (0mm) specimen, whereas 1800mm specimen only had a 5.8% higher failure load than the control specimen. The results further show that the ULS capacity of the 450mm damage length specimen was 8.3%, 10.9% and 12.1% higher than the 800mm, 1300mm and 1800mm specimens, respectively.

Figure 5.5 presents the correlation between corrosion damage and ultimate failure load. The results show an increase in ultimate failure load as the corrosion damage increases. Initially these results may appear counterintuitive as one would expect a reduction in ultimate failure capacity with an increase in corrosion damage, but if the corrosion damage length is considered in the context of the four-point bending configuration as shown in **Figure 5.6**, then the results make more sense. The illustration provided in **Figure 5.6** shows that although the 450mm specimen experienced the highest degree of corrosion the specimen can still resist its maximum moment. When the damage extent is extended beyond the region of maximum moment, the maximum capacity becomes a function of the actual degree of corrosion.

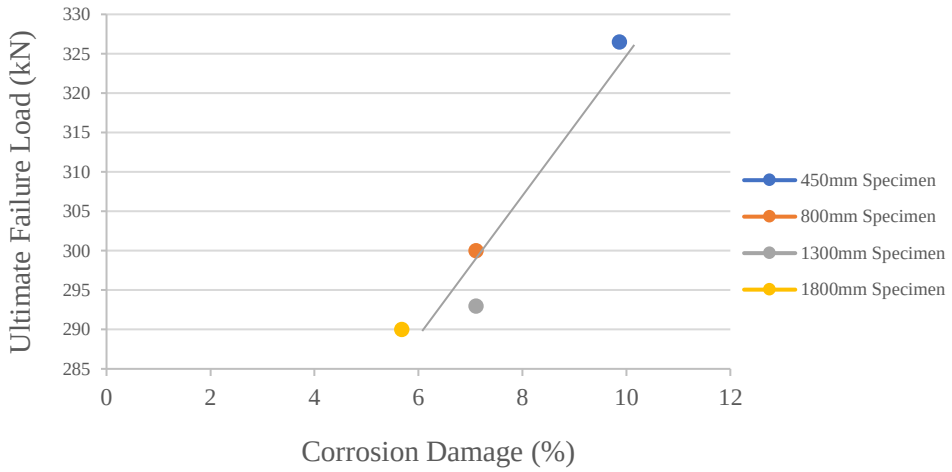

Figure 5.5 Correlation between corrosion damage and ultimate failure load

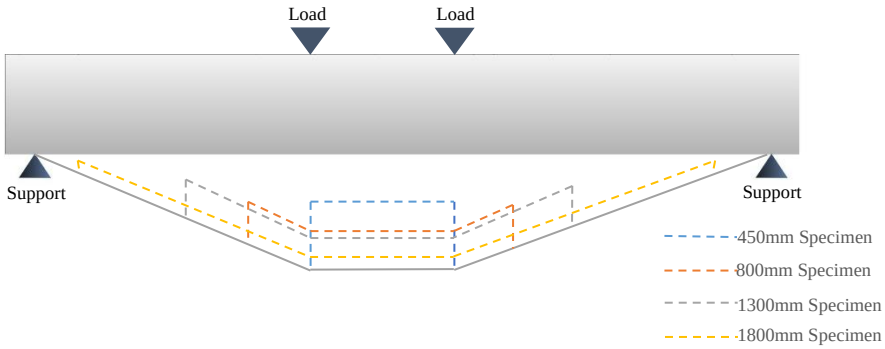

Figure 5.6 Effect of corrosion on the bending moment diagram

Although these findings agree with the hypothesis proposed by Dladla (2014), that increased corrosion damage length is likely to reduce the moment capacity of RC beams, they are also in stark contrast with the findings presented by Dladla (2014). His research revealed an increase in flexural capacity with increasing damage length. The FEM study by Mundeli (2014) which ran concurrently with the one carried out by Dladla (2014) also reported an increase in load carrying capacity with an increase in damage length. One very notable difference between this study and the ones carried out by Dladla (2014) and Mundeli (2014) is the actual degree of corrosion. Dladla (2014) made use of simulated corrosion which yields a perfect uniform degree of corrosion by grinding off a portion of the steel cross-section. Mundeli (2014) also modelled uniform corrosion in his study. In this study accelerated corrosion was used, which does not yield perfectly uniform corrosion. In fact, the accelerated corrosion results in **Section 5.2** show that all the corrosion damage presented itself in the form of pitting corrosion and that the specimens with the shorter damage length experienced a higher degree of corrosion than the specimens with a longer damage length. Notwithstanding the above differences in experimental approach, all three studies showed that corrosion damaged, patch repaired and FRP strengthened specimens achieved higher static failure loads than the uncorroded specimens. Apart from the different effect that corrosion damage length had in the 3 different studies, the failure modes were also slightly different. The specimens tested by Dladla (2014) and Mundeli (2014) were shown to have failed in a sequence characterized by excessive flexural cracking, debonding of CFRP laminate, followed by crushing of compression concrete and yielding of tension steel. The specimens tested under static loading in this experiment also experienced excessive flexural cracking, but crushing of compression concrete was encountered prior to CFRP laminate debonding.

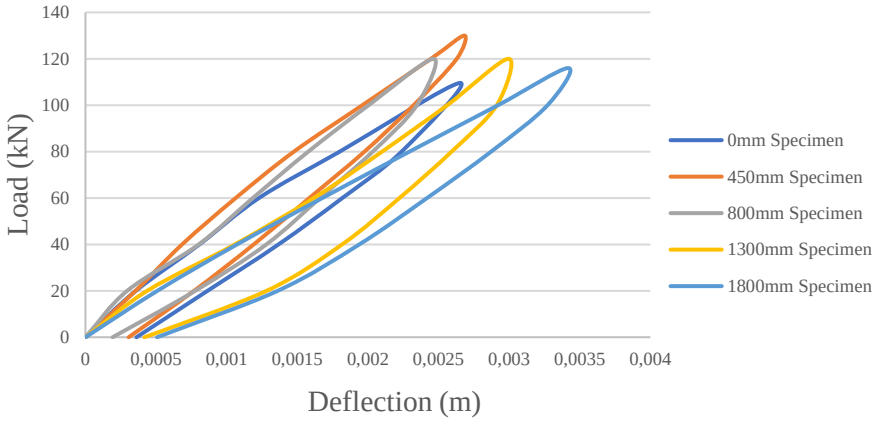

Figure 5.7 Load cycle energy dissipation of 40% stress range specimens

All specimens tested under fatigue loading were initially loaded monotonically at 20kN increments to its peak test load P_{max} and subsequently unloaded. Midspan deflection, among other parameters, were recorded during this first load cycle as shown in **Figure 5.7**. The area bound by the load-unload curve was divided by the peak load P_{max} of each specimen to obtain the rate of energy dissipation during the first load cycle of each specimen, as presented in **Table 5.1**. The area under the curve was obtained by the method of definite integration. Analysis of the energy dissipation rates of the 40% stress range specimens revealed that there is a general increase in energy dissipation rate from 0.399 to 0.622 kN.mm/kN as the corrosion and patch repair extents increase from 450mm to 1800mm, except for the 800mm specimen which yielded an energy dissipation rate of 0.388kN.mm/kN during the first load cycle. Comparison of the energy dissipation rates with the actual midspan deflection during the first load cycle show an interesting contrast. Although the energy dissipation rate of the 1800mm was the highest overall all, it did not yield the highest deflection, compared to the other specimens. In contrast, the 450mm specimen which yielded the highest overall deflection had the second lowest energy dissipation rates. The specimens loaded to 60% of the failure load showed a similar trend to those loaded to 40% of the failure load. Once again, the trend showed a general increase in energy dissipation rates from 1.274 to 1.704 kN.mm/kN as the corrosion and patch repair extents increased from 800mm to 1800mm. Unfortunately, the results from the 450mm and 1300mm energy dissipation rates were inconclusive, therefore it was not possible to identify a correlation between the two stress ranges to show that the 800mm specimen has the lowest energy dissipation rate. The results did however reveal the contrast between energy dissipation rates and the maximum deflection once again. Although the 1800mm specimen had a higher energy dissipation rate than the 800mm specimen, it had the lower maximum deflection.

Comparison of the results from the two different stress ranges, show that an increase in damage extent result in a higher energy dissipation rate. In addition, an increase in operation loads will increase the energy dissipation rate as well as the maximum deflection of all the specimens. The results from this study seem to correlate with those reported by Mundeli (2014). The FEM study by Mundeli (2014) showed that as the corrosion and patch repair extent was increased from 450mm to 1800mm the energy dissipation rate increased by 35% from 64.76 to 90.32kN/mm; results from this study as presented in **Table 5.1** show an increase of 55% and 34% as the damage extent was increased from 450mm to 1800mm for the 40% and 60% stress ranges, respectively.

Upon critical evaluation of the results, it was appreciated that energy dissipation rate and midspan deflection during the first load cycle may not be very useful in the discussion of long-term fatigue behaviour assessment, as it may take a few cycles for internal stresses to redistribute and for all the composite materials to fully engage. Nevertheless, the energy dissipation rate can be discussed in the

context on crack behaviour (Mundeli, 2014), as the fracture energy is considered to dissipate when a crack is formed (Wittmann 2002). Mahal (2014) documented that the crack growth rate is quite high during the first load cycle, after which it remains relatively low. This emphasizes the usefulness of energy dissipation rate during the 1st load cycle, especially in the context of crack behaviour. To that end the discussion on crack behaviour in **Section 5.2.3** will draw on the results from this section to understand and better interpret the results.

Fatigue loading behaviour

Fatigue life results of specimens tested under two different stress ranges are presented in this section. It should be noted that the results from the 60% stress range tests will be discussed before the 40% stress range results. This was done because some of the specimens tested under the 40% stress range did not fail due to fatigue; which introduced challenges in analysing trends with regard to fatigue life. Only 2 of 5 specimens in the 40% stress range tests failed due to fatigue, whereas all the specimens in the 60% stress range failed under fatigue conditions. **Figures 5.8** and **5.10** present the relative fatigue life cycles of specimens tested under 60% and 40% stress ranges, respectively. **Figures 5.9** and **5.11** show the predicted or anticipated fatigue life cycles based on the Helgason and Hanson model (Zorn, 2006).

Initially three different models, that were able to predict the fatigue life of RC beams, were considered. The three models are listed in **Table 5.3**:

Table 5.3 Fatigue life models (Mahal, 2015)

Model	Fatigue Life Model
RC beam, Tilly and Moss (Barnes and Mays, 1999)	$S_r^9 * N_f = 3.09 * 10^{27}$
RC Beam, Model Code (2010)	$S_r^5 * N_f = 4.0841 * 10^{17}$
Helgason and Hanson model of steel under direct tension in air (Zorn, 2006)	$log\ (N_f) = 6.969 - 0.00555 S_r$

All three models are directly reliant on the tension steel stress range and their applicability dependant on crack initiation on the tension steel. It was therefore decided to predict the fatigue life of the specimens using all three models presented in **Table 5.3** and to evaluate the correlation between these model predictions and the experimental fatigue life results.

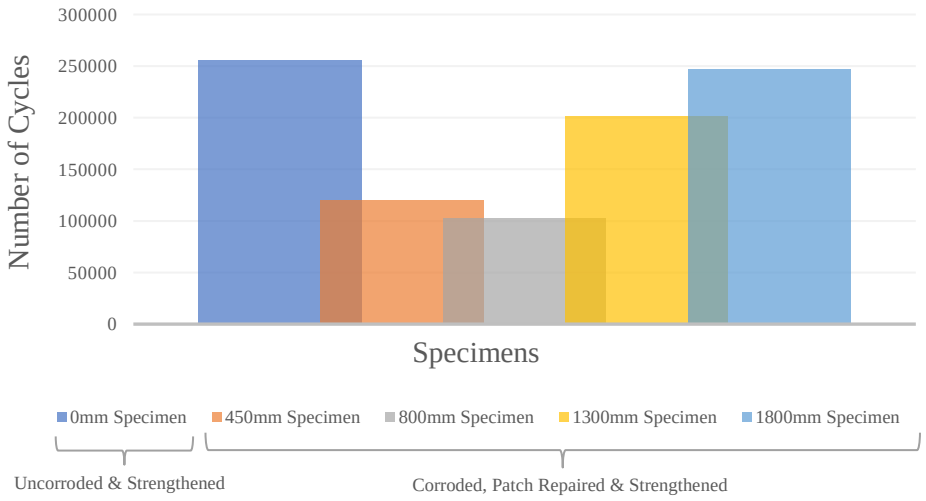

Figure 5.8 Fatigue life of 60% stress range specimens – experimental results

Results of the 60% stress range fatigue tests showed that an increase in damage length increases the amount of fatigue load cycles the specimen can sustain. With the exception of the 800mm specimen, the results indicate that as the damage extent is increased from 450mm to 1800mm there is a 106.3% increase in fatigue life of the specimen. However, for the 800mm specimen there seems to be a 16.5% reduction in fatigue cycles from the 450mm specimen. It is likely that the crack that caused fatigue failure of the 800mm specimen may have initiated from a deep corrosion pit, which caused a reduction in its fatigue life. None of the corrosion damaged and patch repaired specimens were able to sustain a larger number of fatigue cycles than the uncorroded specimens.

Table 5.4 Predicted fatigue lives using different models

Model	Specimen	Cycles
Tilly and Moss (Barnes and Mays, 1999)	*0mm Specimen*	$10^{5.675}$
	450mm Specimen	$10^{4.419}$
	800mm Specimen	$10^{4.952}$
	1300mm Specimen	$10^{5.305}$
	1800mm Specimen	$10^{5.729}$
Model Code (2010)	*0mm Specimen*	$10^{5.492}$
	450mm Specimen	$10^{4.794}$
	800mm Specimen	$10^{5.090}$
	1300mm Specimen	$10^{5.286}$
	1800mm Specimen	$10^{5.522}$
Helgason and Hanson model (Zorn, 2006)	*0mm Specimen*	$10^{5.496}$
	450mm Specimen	$10^{4.938}$
	800mm Specimen	$10^{5.197}$
	1300mm Specimen	$10^{5.350}$
	1800mm Specimen	$10^{5.516}$

Table 5.4 shows the predicted fatigue life cycles of the specimens tested at a 60% stress range. All three models presented in **Table 5.4** could have been used to predict the fatigue life of strengthened RC beams. Evaluation of the results obtained from these models show that the models produced results with a similar trend as indicated in **Figure 5.9** and that all three models produced fatigue life cycles similar to those achieved experimentally. However, the fatigue life cycles obtained from the *fib* Model Code (2010) frequently underestimated the experimental results, which seems to agree with the observations made by Gussenhoven et al. (2005), Wang et al. (2007) and Heffernan et al. (2004). In contrast the Tilly and Moss (1999) model seemed to provide more conservative upper bound fatigue life cycle predictions. The fatigue life cycles predicted by the Helgason and Hanson model (Zorn, 2006) yielded results with the closest correlation to the experimental results, it was therefore decided to use it in this research.

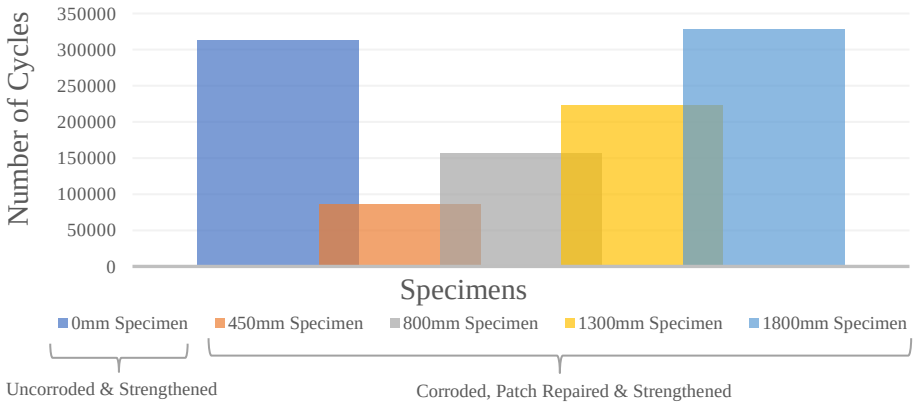

Figure 5.9 Fatigue life of 60% stress range specimens – model prediction

The predicted number of fatigue cycles of each specimen presented in **Figure 5.11** were obtained using the Helgason and Hanson model of steel under direct tension in air (Zorn, 2006). The results from the model show a similar trend to the experimental results, in that as the damage extent is increased the fatigue life of the specimen increases. The model predicts a 279.0% increase in fatigue life as the corrosion damage and patch repair extents are increased from 450mm to 1800mm. In contrast, however, the model shows that the 1800mm damage length specimen outperforms the uncorroded specimen. Another major difference between the model and experimental results is that the model does not indicate an initial reduction in fatigue as the corrosion damage and patch repair length was increased from 450mm to 800mm.

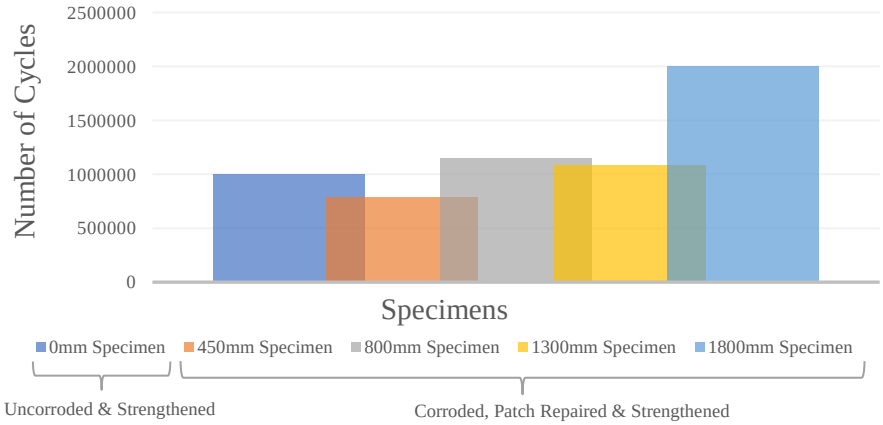

Figure 5.10 Fatigue life of 40% stress range specimens – experimental results

Figure 5.10 above presents the fatigue life results of the specimens tested under the 40% stress range load scheme. Under the lower stress range tests specimen fatigue life was much longer than for the 60% stress range tests. Due to time constraints and limitations on test parameters, such as test frequency, it was decided to stop testing samples under fatigue loading after 2 000 000 cycles and load it monotonically up to failure as shown in **Figure 3.17**. The test frequency was the biggest deterring factor with regard to test duration, where the literature reviewed revealed that fatigue testing is commonly carried out at a frequency of between 1Hz and 4Hz (Charalambidi et al., 2016; Gregan, 2012; Mahal, 2015).

Due to the constraints highlighted in the previous paragraph only two of the five specimens designated for testing under this stress range failed due to fatigue. Those were the 450mm and 1300mm specimens. From the experimental results it can be inferred that crack initiation did not occur in the

0mm, 800mm and 1800mm specimens, or that it may have taken longer to initiate. Moreover, from the two samples that failed due to fatigue, it can be noted that the specimen with the longer damage extent had a longer fatigue life. The 1300mm specimen had a 38.2% longer fatigue life than the 450mm specimen. Comparison of those two samples with the identical samples in the 60% stress range tests showed that the 1300mm specimen had a 68.3% longer fatigue life than the 450mm specimen when subjected to a higher stress range.

The fatigue life results yielded from the Helgason and Hanson model (Zorn, 2006) shown in **Figure 5.11** will first be discussed in terms of the two specimens that failed under fatigue conditions, which will be followed by a comparison to the model results from the 60% stress range tests.

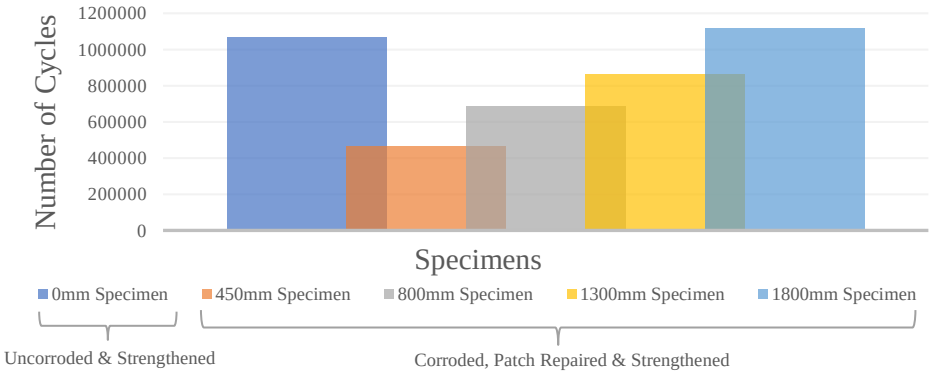

Figure 5.11 Fatigue life of 40% stress range specimens – model predictions

Similar to the finding from the experimental results, there was an increase in the fatigue life as the damage extent was increased from 450mm to 1300mm. The model results show an 85.3% increase in fatigue life as the specimen damage length was increased from 450mm to 1300mm. This indicates a lower percentage increase in the model prediction for the 40% stress range tests compared to the 60% stress range tests where a 158.3% increase was encountered as the damage length was increased from 450mm to 1300mm. In terms of the overall tends, the model results in **Figure 5.11** suggest an identical trend to that of the specimens tested under the 60% stress range, that is that the fatigue life increases as damage lengths were increased from 450mm to 1800mm. It also shows once again that the 1800mm corrosion damaged and patch repaired specimen was able to outperform the uncorroded specimen with regard to fatigue life. It was not possible to confirm this trend on the experimental results from the 40% stress range tests apart from the two specimens that failed due to fatigue. However, the 800mm specimen fatigue life seemed to challenge this trend as it was able to sustain over 1 150 000 cycles without any fatigue failure, which was more than the 1300mm specimen. Overall the experimental results suggest that as the stress range is reduced by 20% from medium cycle fatigue stress (60%) to low cycles fatigue stress (40%), the fatigue life is can be increased by 5 to 8 times. Under both stress range conditions, as the damage extent was increased from 450mm to 1800mm, the fatigue life was extended by as much as 76.7%.

The ensuing sections on specimen crack behaviour, failure modes and stiffness degradation will draw on the findings presented in this section in an attempt to thoroughly evaluate fatigue behaviour in terms of the various performance parameters.

5.3.2 Crack development and failure mode

This section considers crack behaviour and failure modes of specimens tested under fatigue loading. In addition, it assesses the evaluation of crack behaviour using DIC, especially the possibility of employing

the process to identify areas that may likely lead to structural failure. **Table 5.5** presents the relative findings of crack behaviour and failure modes of the 10 fatigue specimens.

All specimens tested under fatigue loading exhibited a similar crack propagation and failure mode. This process can be characterized by a few unique stages:

1. A crack pattern with predominantly flexural cracks as well as shear and flexural-shear cracks was clearly defined during the first load cycle up to maximum test load P_{max}. This crack pattern, as shown in **Figure 5.12**, remains relatively unchanged after first load cycle, but the crack heights and densities propagated gradually during fatigue testing.
2. Crack propagation remains low until rupture of tension steel. Rupture of tension steel causes rapid increase in crack propagation in terms of crack heights and densities. After steel rupture cracks tended to propagate in the vicinity of the ruptured steel bar.
3. If only one steel bar ruptures, it is possible that the specimen can still sustain a significant number of fatigue cycles. The post-fatigue stage can be characterized by a second phase of low crack propagation.
4. After steel rupture, CFRP laminates started to debond at the position of the main cracks. Shortly after CFRP delamination compression concrete would crush, leading to ultimate failure of the section.

Table 5.5 Crack behaviour and failure mode results

Identity	Average Crack Spacing (mm)	Average Crack Height (mm)	Predominant Crack Type	Number of Flexural Cracks	Number of Shear Cracks	Number of Flexural-shear Cracks	Fatigue Failure Mode	Failure Position
S_CNTRL 2	58.06	63.81	*flexural*	14	7	6	No Fatigue Failure	*Centre*
S_CNTRL 3	85.71	74.20	*flexural*	11	5	6	SR (1 bar), FD & CC	*Right Pin Load*
S_450mm 2	69.23	59.14	*flexural*	13	4	7	SR (2 bars), FD & CC	*Centre*
S_450mm 3	75.00	65.70	*flexural*	14	5	5	SR (1 bar), FD & CC	*Left Pin Load*
S_800mm 2	48.65	54.22	*flexural*	21	7	8	No Fatigue Failure	*Centre*
S_800mm 3	75.00	59.81	*flexural*	13	7	5	SR (1 bar), FD & CC	*Right Pin Load*
S_1300mm 2	46.15	63.66	*flexural*	22	8	8	SR (2 bars), FD & CC	*Centre*
S_1300mm 3	69.23	52.61	*flexural*	13	8	6	SR (2 bars), FD & CC	*Centre*
S_1800mm 2	45.00	75.08	*flexural*	18	8	9	No Fatigue, SR (1 bar)	*Centre*
S_1800mm 3	66.67	47.72	*flexural*	12	5	7	SR (2 bars), FD & CC	*Right Pin Load*

*IC= inconclusive results, CC= concrete crushing, FD= carbon fibre debonding, SR= steel rupture

Visual examination of the crack patterns under the two stress ranges indicated that the specimens from the 60% stress range tests had lower crack densities than the specimens tested in the 40% stress range. From this finding it was hypothesized that a longer test period leads to a higher crack density. For that reason, it was decided to discuss the tests with the shorter test period first.

5.3.2.1. 60% Stress range specimen performance evaluation

0mm Specimen

The 0mm damage extent specimen exhibited an average crack spacing of 58.06mm and an average crack height of 63.81mm. It was challenging to differentiate the flexural cracks that inclined toward the load application point from the flexural shear cracks. Though most of the cracks were flexural cracks that inclined toward to load application points. From **Figure 5.12** it can be seen the average crack spacing was higher and the crack height is lower in the region of constant moment; that is the region in between the two load application points. Moreover, the average crack spacing was lower towards the right load point and the average crack height appeared higher in that region as well. Overall there was uniform crack distribution, which indicated uniform action between the CFRP and tension concrete.

Figure 5.12(a) shows the crack pattern sketched from the actual specimen at ultimate failure as well as well as a DIC crack pattern of the specimen at the maximum load during the first load cycle. The comparison of these two different images was done intentionally for two reasons. The first reason being that it was found overall that the crack patterns did not change significantly after the first load cycle. The second reason was to evaluate the possibility of using DIC to identify possible failure locations early in the structural service life. The DIC crack patterns were obtained by plotting tangential strain in the x-direction, where positive strain concentrations indicate areas where cracks were likely to form, and conversely negative strain concentrations indicate areas where concrete crushing was likely. It must be noted that the sketched crack patterns were recorded at the back of each specimen, whereas the photos captured for DIC were taken from the front of the specimen. The cracks may not always propagate perpendicular to the surfaces, which could result in slightly different crack patterns on the front and back surfaces.

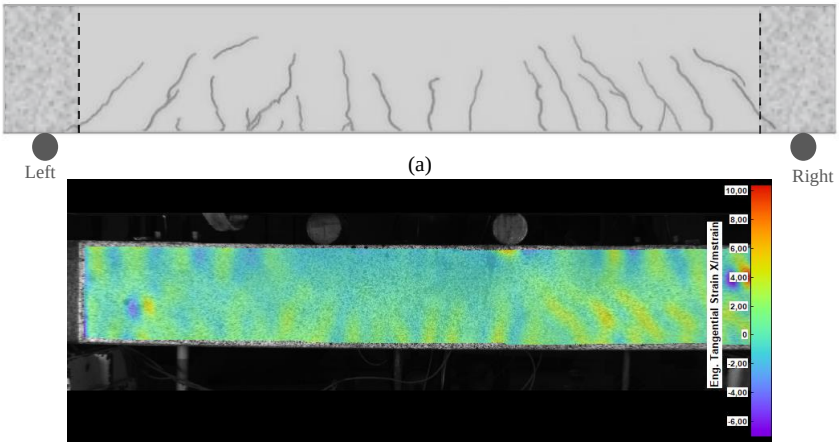

(b)

Figure 5.12 0mm specimen: Final actual crack pattern versus DIC crack pattern at 1 load cycle (60% ULS load)

The DIC image captured during the first load cycle in **Figure 5.12(b)** reveals a similar pattern to that shown in the sketch of the actual crack cracks. The crack density in the constant moment region is low compared to the areas outside of that region. Furthermore, the right side of the specimen shows a higher strain concentration than the rest of it.

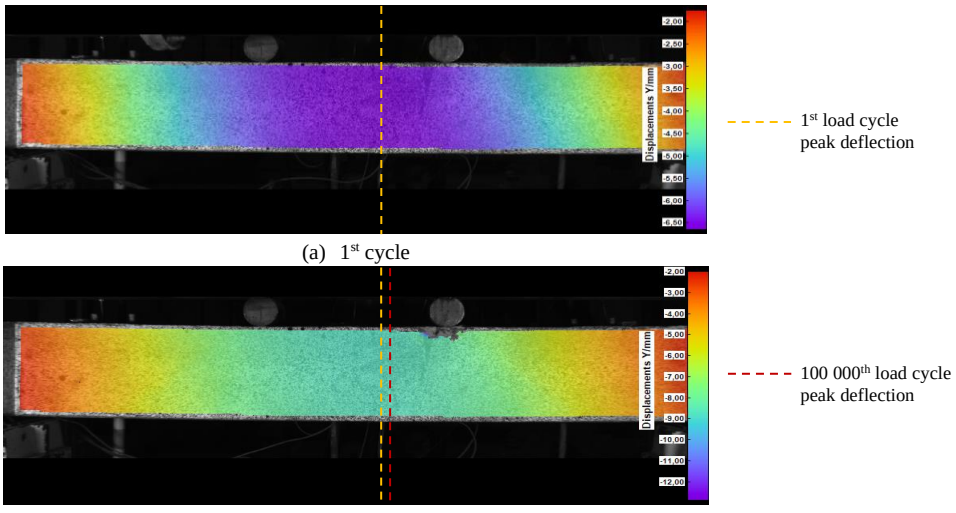

Figure 5.13 0mm specimen: Deflection fields at 1st and 100 000th cycles at 164.4kN (60% ULS load)

Although midspan deflection is a good measure of stiffness reduction, as will be discussed in **Section 5.3.3**, maximum deflection does not always occur at the centre of the specimen. Fatigue is triggered by crack initiation on the tension steel, which can happen anywhere along the steel, not necessarily at midspan. The maximum deflection trends to occur at the position where the crack has formed and propagates until eventual failure. Evidence of this is presented in **Figure 5.13** which shows points of maximum deflection, marked by red and yellow dashed lines, at various load cycle intervals. The 100 000 cycle interval was identified as a suitable interval within which all fatigue specimens could be considered at. **Figure 5.13** shows how the point of maximum deflection is already off-centre at the first load cycle and how this point shifted further toward the right pin during the first 100 000 cycles.

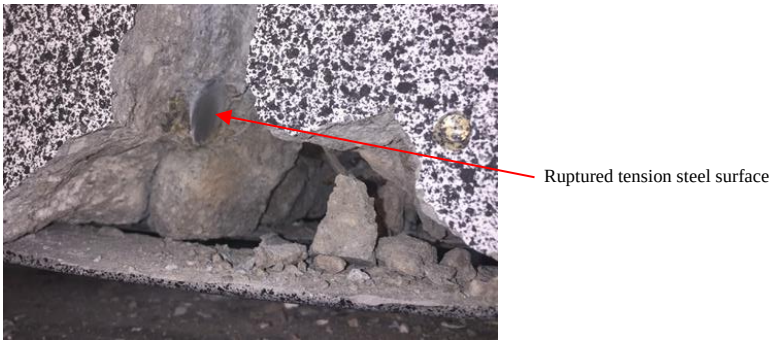

Figure 5.14 0mm specimen: steel rupture due to fatigue (60% ULS load)

The ultimate failure of the 0mm specimen was eventually caused by the rupture of 1 steel bar under the right load application point as shown in **Figure 5.14**, which led to debonding of the CFRP laminate from a major crack at that location. The position of this failure mode coincides with the crack patterns and the points of maximum deflection. The crack pattern shown in **Figure 5.12**, specifically the DIC image pattern of the 1st load cycle, shows the highest crack density in the area of the right load application point. In addition, the points of maximum deflection shown in **Figure 5.13**, also locate the point of maximum deflection closer toward the right load application point.

450mm Specimen

On the 450mm damage length specimen the difference in crack type was much more apparent. The predominant crack type was still flexural cracks with a relatively low average crack height within the constant moment region and none of those cracks propagated through the patch repair. The shear cracks had a much higher average crack height. Overall the section had an average crack height of 65.70mm. This specimen had an average crack spacing of 75.00mm and these cracks were quite evenly distributed, which again indicated uniform action between the CFRP and tension concrete. The 450mm specimen had a lower average crack spacing and height that the 0mm specimen.

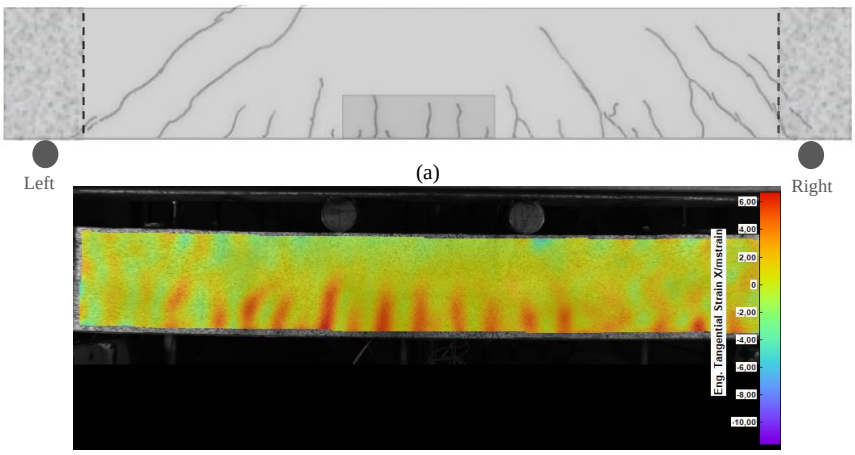

Figure 5.15 450mm specimen: Final actual crack pattern versus DIC crack pattern at 1 load cycle (60% ULS load)

The DIC crack pattern correlates with the crack pattern from the actual specimen as shown in **Figure 5.15**. It does not show the shear cracks quite as accurately as the flexural cracks; this may be due to the fact that the correlation algorithm considered only relative movement in the x-direction when it computed tangential x-strain. The shear cracks, which generally propagate at about a 45º angle would require both x-and y-direction computation. Nevertheless, the DIC crack pattern has managed to indicate a crack to the immediate left of the patch repair mortar which had the largest positive strain. This position is right below the left load application point and also the position where one of the tension steel reinforcing bars eventually ruptured, followed by CFRP debonding and crushing of compression concrete.

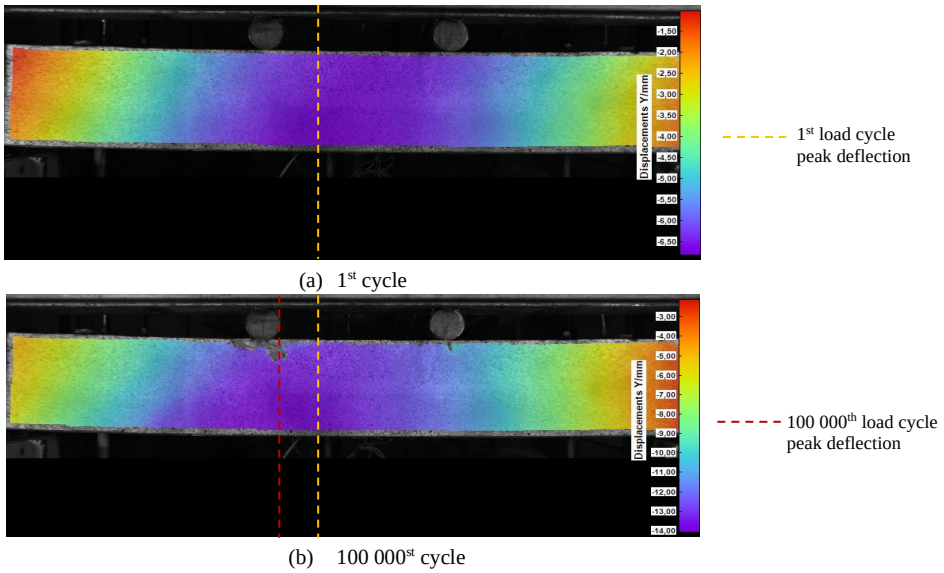

Figure 5.16 450mm specimen: Deflection fields at 1st and 100 000th cycles at 195kN (60% ULS load)

Figure 5.16 shows the position of the maximum vertical deflection at 1 and 100 000 cycles, respectively. The points of maximum deflection coincide with the position of eventual steel rupture. The DIC images above further showed how the deflection field shifts toward the left toward the point of eventual failure.

800mm Specimen

The 800m damage extent specimen had an average crack spacing of 75.00mm, which was the same as the 450mm specimen. It had a lower average crack height of 59.81mm. The flexural cracks within the

patch repaired area were quite low; none of the cracks propagated through the patch repair. Although, the cracks were generally quite evenly distributed, the flexural and shear crack densities appeared to be higher toward the right of the specimen.

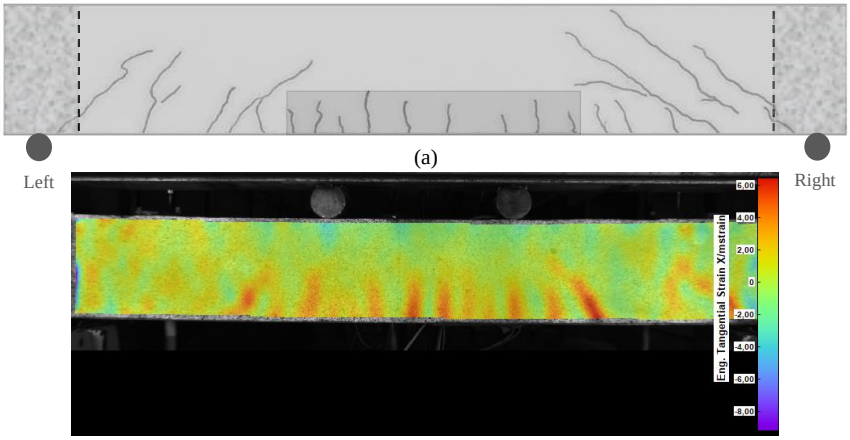

Figure 5.17 800mm specimen: Final actual crack pattern versus DIC crack pattern at 1 load cycle (60% ULS load)

The DIC crack pattern image in **Figure 5.17**, indicated a strain concentration to the right of the specimen, which again points towards the location of eventual rupture of one of the steel bars that led to ultimate failure of the section. As with the 450mm specimen, **Figure 5.17** reveals how the DIC process was not able to detect shear cracks as accurately as the flexural cracks in the centre of the specimen. Although the shear cracks may not have been as deep during the first load cycle, they were detectable during the first load cycle.

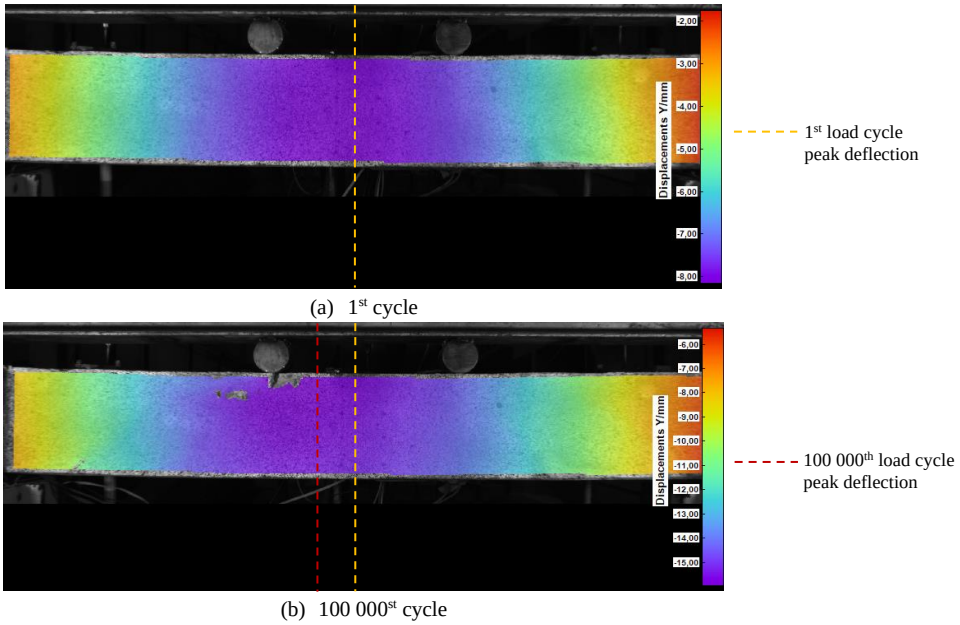

Figure 5.18 800mm specimen: Deflection fields at 1st and 100 000th cycles at 180kN (60% ULS load)

Figure 5.18 shows the points of maximum vertical deflection during the 1st and 100 000th cycles. During the first load cycle the maximum deflection coincided with the midspan of the specimen, however this point gradually shifted towards the left. In this case the point of maximum deflection did not coincide with the eventual point of failure.

1300mm Specimen

Continuing with the downward trend, the 1300mm damage extent specimen had a lower average crack spacing than the 800mm specimen of 69.23mm as well as a lower average crack height of 52.61mm. In the region of constant moment, there were only flexural cracks with a low crack height; none of those cracks propagated past the patch repair, in fact none of the flexural cracks throughout the section propagated passed a depth equal to that of the patch repair mortar. Only the shear cracks propagate passed this depth; the fact that they propagated through this section indicates composite behaviour between the patch repair mortar and the rest of the section. As with all the other specimens considered thus far, the uniform distribution of the cracks shows uniform action with the concrete and the CFRP.

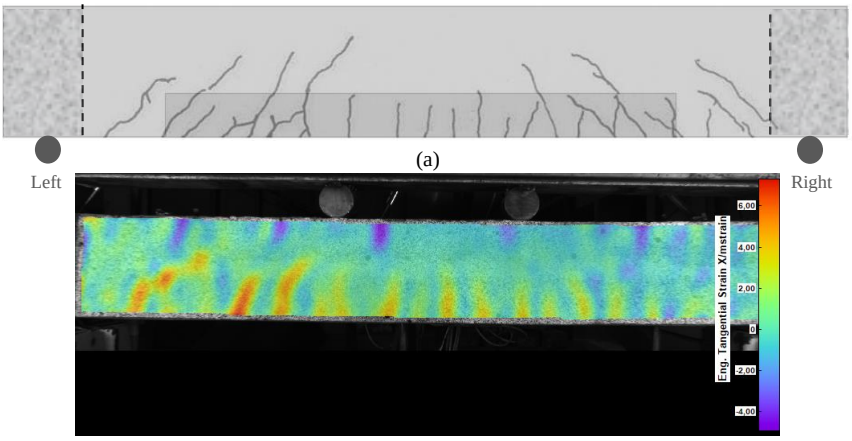

Figure 5.19 1300mm specimen: Final actual crack pattern versus DIC crack pattern at 1 load cycle (60% ULS load)

Failure of the 1300mm specimen was caused due to the rupture of both steel reinforcing bars in the centre of the beam. If one had to consider the DIC crack pattern in **Figure 5.19** and the maximum vertical deflection points at various cycle intervals in **Figure 5.20**, failure could have been predicted toward the left of the specimen. Both the sketched and DIC crack patterns indicated an increased crack pattern density towards the left of the specimen. This increased crack density is characterized not only by lower crack spacing or higher crack depths, but the strain concentration in that area is also higher than the rest of the specimen. The prediction of failure to the left would not have been unfounded, given the trend from the last three specimen failures, but it would not have been an accurate failure position prediction as the eventual failure occurred at midspan of the beam.

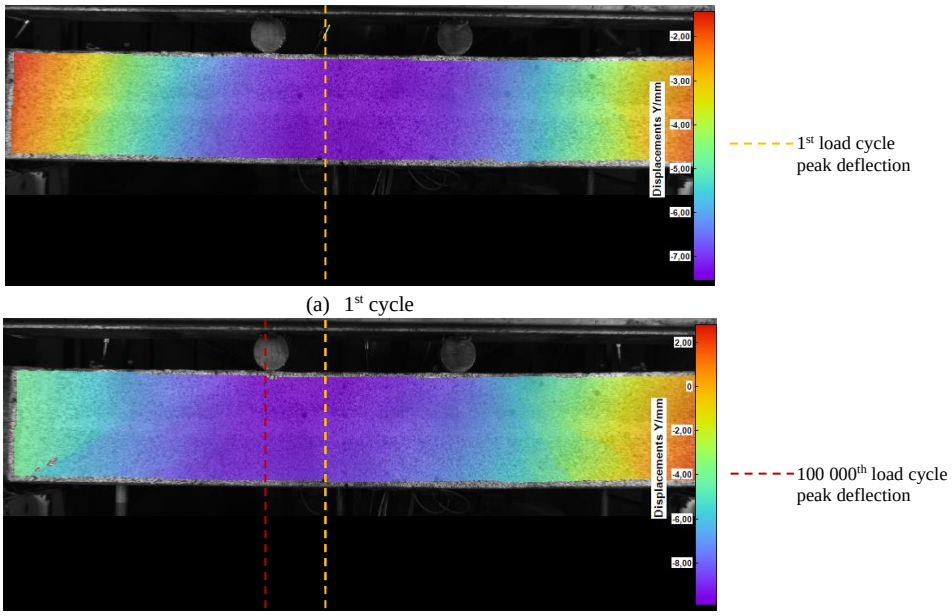

Figure 5.20 1300mm specimen: Deflection fields at 1st and 100 000th cycles at 175.8kN (60% ULS load)

1800mm Specimen

Of all the specimens in the 60% stress range, the 1800mm damage extent specimen resulted in the lowest average crack spacing of 66.67mm as well as the lowest average crack height of 47.72mm. The average crack height was low in the region of constant moment and most of all cracks did not propagate beyond the depth of the patch repair mortar. The few cracks that did propagate beyond the patch repair mortar were all outside the region of constant moment.

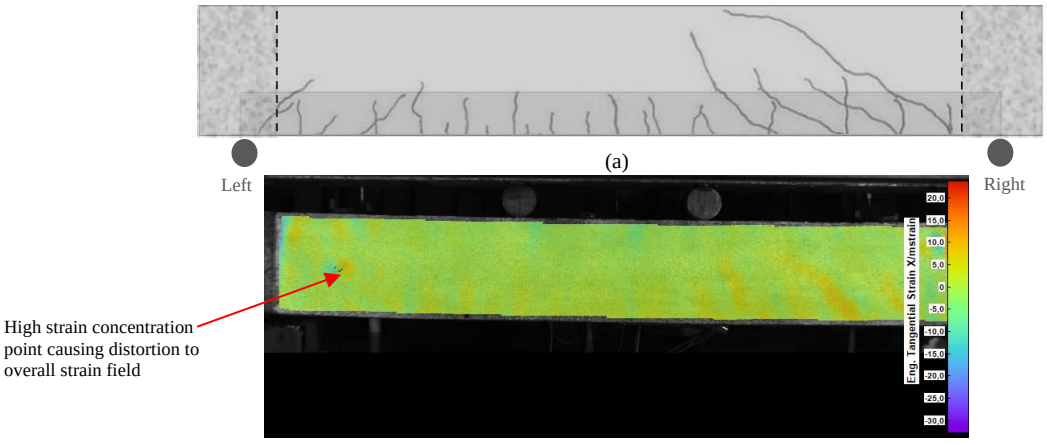

Figure 5.21 1800mm specimen: Final actual crack pattern versus DIC crack pattern at 1 load cycle (60% ULS load)

The DIC x-strain field shown in **Figure 5.21** shows a crack pattern that is not as clear as the previous specimens discussed above. Although it shows the main shear crack as well as a few flexural cracks vaguely, the overall pattern is not very clear. Upon closer assessment a point of unusually high strain was identified, as pointed out by the red arrow. This point exhibited very high positive and negative strain, which increased the strain scale almost tenfold. Therefore, the scale under consideration made it difficult for the algorithm to accurately identify crack patterns within the bandwidth of colours at its disposal. The high strain was identified as a piece of poorly concrete that had delaminated.

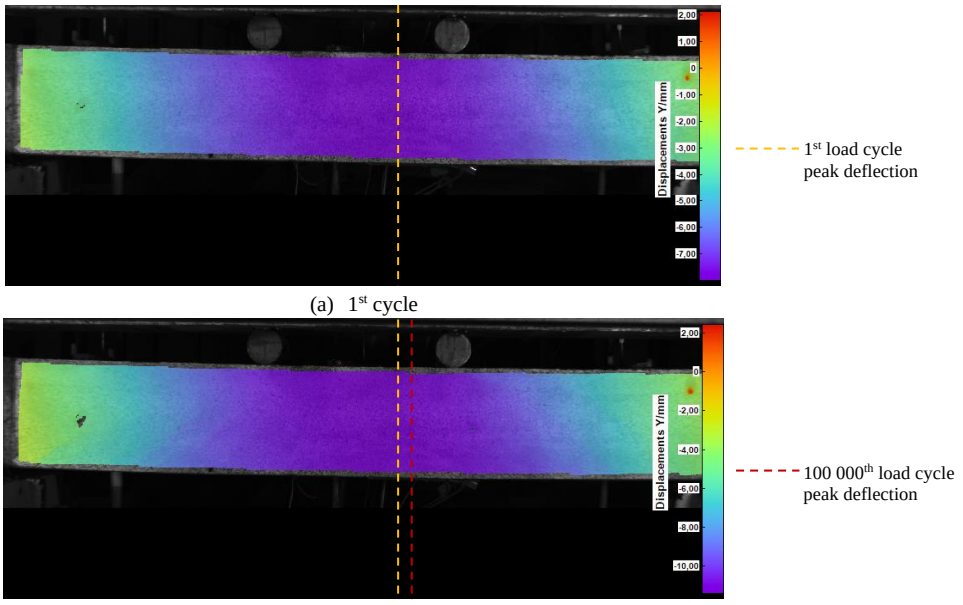

Figure 5.22 1800mm specimen: Deflection fields at 1st and 100 000th cycles at 174kN (60% ULS load)

Failure of the 1800mm specimen was eventually caused by rupturing of both reinforcing steel bars under the right loading point. The crack pattern, even though it was not very accurate, together with the point of maximum deflection shown in **Figure 5.22**, were able to provide an indication of the possible failure location.

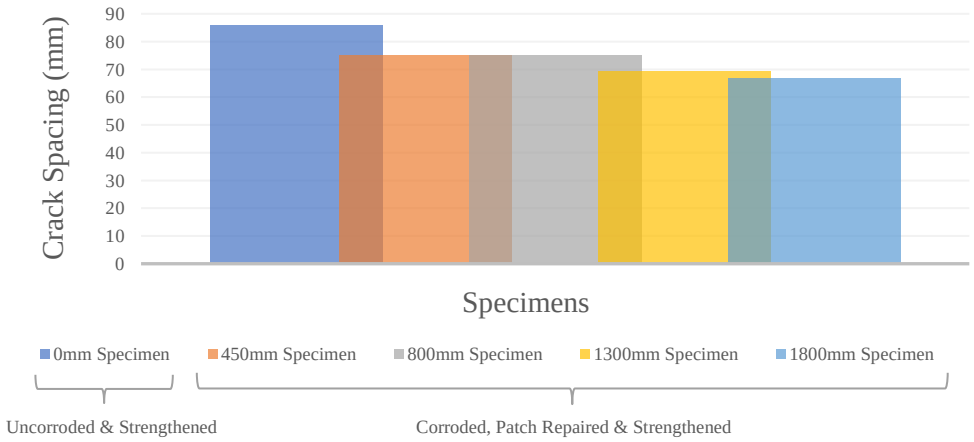

Figure 5.23 Relative average crack spacing (60% ULS load)

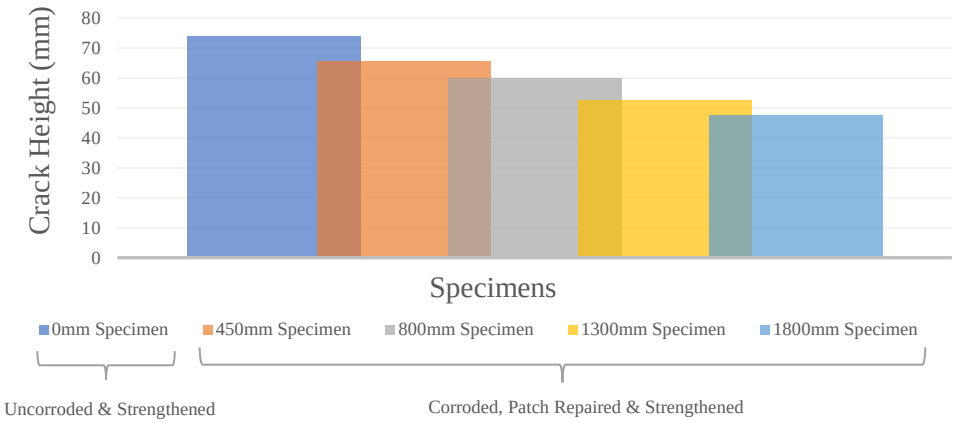

Figure 5.24 Relative average crack height (60% ULS load)

Figures 5.23 and **5.24** present the relative crack spacing and height results of specimens tested under 60% stress range fatigue tests. The average crack spacing results show that as the corrosion damage and patch repair extent is increased from 450mm to 1800 mm there is a 28.6% reduction in average crack spacing. The uncorroded and unpatched specimen had the highest crack spacing. In terms of the average crack height, the 0mm damage extent specimen, had the highest average crack height. The results indicate that as the damage extent was increased from 450mm to 1800mm there was a 55.5% reduction in average crack height. These results indicate that as the damage extent was increased, there was a subsequent increase in the number of cracks which reduce the average crack spacing, but those cracks had a lower average height. The increased crack density makes the structure less durable or more susceptible to further corrosion damage, but from a structural viewpoint the lower average crack height will improve the stiffness and capacity of the structure, because there is a larger portion of uncracked concrete under the section neutral axis, that is able to contribute to the internal force equilibrium.

The findings did not present a clear correlation between an increase in damage extent with the eventual failure mode. The 0mm, 450mm and 800mm failed due to one of the steel bars rupturing, whereas the 1300mm and 1800 specimens failed when both tension steel reinforcing bars ruptured. Furthermore, all but one of the specimens tested under the 60% stress range failed directly underneath one of the load application points. Only the 1300mm specimen failed at the centre.

5.3.2.2. 40% Stress range specimen performance evaluation

This section will analyse the crack behaviour and failure modes of the specimens tested under the 40% stress ranges. The results obtained from the specimens were also compared against those presented for the 60% stress range tests, in order to test the validity of the hypothesis that a longer test period leads to a higher crack density.

0mm Specimen

The 0mm damage extent specimen had a similar crack pattern to its counterpart that had been tested under the 60% stress range. It had the same number of shear cracks, but a larger number of flexural cracks. The average crack spacing reduced by 47.6% to 58.06mm and the average crack height reduced by 16.3% to 63.81mm, compared to the 0mm specimen tested under the 60% stress range. This indicates that the 40% stress range specimen had a larger number of cracks than the 60% stress range specimen, but those cracks had a lower average height. As with all the other specimens considered thus far, the cracks within the constant moment region were flexural cracks only, that had a lower average crack height than the cracks outside that region. In general, the cracks were uniformly spaced, indicating uniform action between the CFRP and the concrete. Furthermore, the flexural cracks tended to incline toward the load application points.

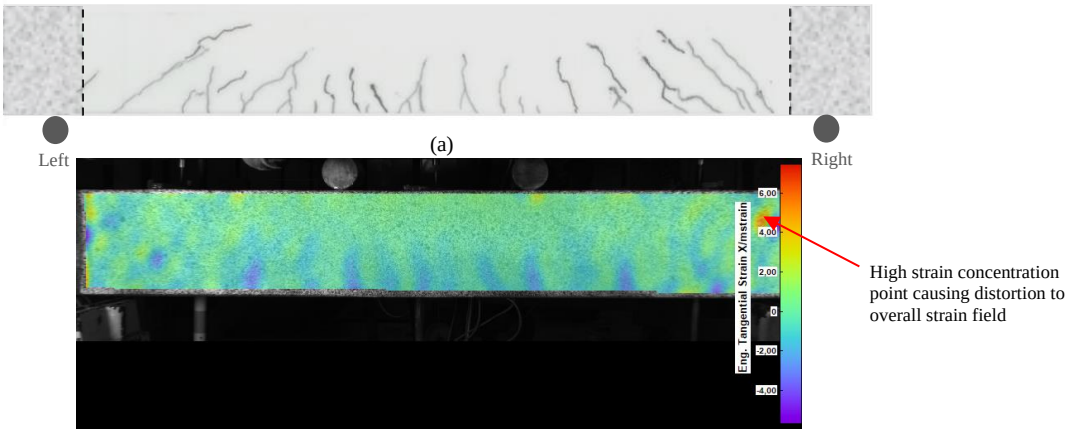

Figure 5.25 0mm specimen: Final actual crack pattern versus DIC crack pattern at 1 load cycle (40% ULS load)

The DIC crack pattern showed a fairly uniform crack pattern, with a slight reduction in average crack spacing under the left load application point. The crack strain concentrations were evenly distributed, without any specific inclination to one of the load application points. The overall crack pattern was not as clear as the first four specimens considered under the 60% stress range. Similar to the 1800mm specimen this lack in clarity may be attributed to point of high strain concentration, pointed out by the red arrow on the right, which caused distortion of the entire strain field.

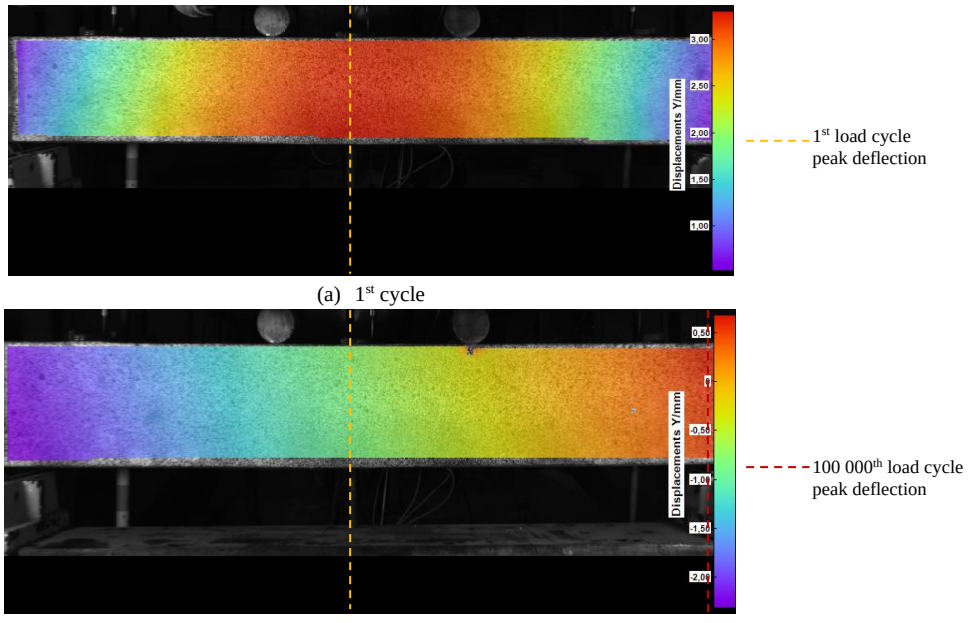

Figure 5.26 0mm specimen: Deflection fields at 1st and 100 000th cycles at 109.6kN (40% ULS load)

The 0mm specimen did not fail due to fatigue after 1 000 000 cycles. The specimen was loaded statically to failure after fatigue testing. The static failure load after fatigue testing was 276kN. This is slightly higher than the 0mm specimen tested only under static loading without any fatigue testing which failed at 274kN. The failure mode was crushing of compression concrete at midspan and subsequent debonding of FRP laminates. Inspection the tension steel revealed that there was no fracturing or yielding of the reinforcing steel.

The DIC image in **Figure 5.26** that shows the point of maximum deflection at the first load cycle, shows that the maximum deflection was close to the centre but inclined slightly to the left. This left

inclination seems to correlate with the slight increase average crack spacing toward the left, shown in **Figure 5.26(a)**. This may suggest that the if fatigue failure was to have presented itself in this specimen, it would have been to the left. However, this prediction could not be verified through the experiment. The DIC image in **Figure 5.26(b)** shows that the point of maximum deflection shifted toward the right bottom of the specimen. The right support of the specimen was a roller pin support. This roller pin was found to have shifted backwards during the test period, together with the specimen. This backward shift caused the change in the point of maximum deflection. Although it was not the desired outcome for the experiment, it showed the effectiveness of DIC in not only detecting vertical and horizontal movement, but also movement in the depth of field

450mm Specimen

The 450mm damage extent specimen tested under the 40% stress range had a higher average crack spacing than the 0mm specimen, as well as a lower average crack height. It had an average crack spacing of 69.23mm and average crack height of 59.14mm, which equated to an overall lower crack density compared to the 0mm specimen. The flexural cracks within the region of constant moment had a higher average crack spacing than the 0mm specimen above and unlike with the 60% specimens this specimen showed more flexural cracks propagating passed the depth of the patch repair mortar, which indicated composite behaviour between the patch repair and the substrate concrete. The crack spacing to the left of the specimen was generally a bit lower with a higher crack depth.

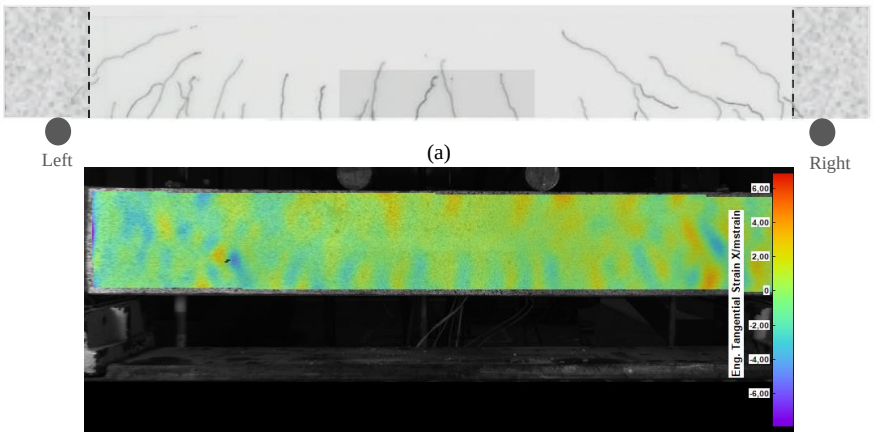

Figure 5.27 450mm specimen: Final actual crack pattern versus DIC crack pattern at 1 load cycle (40% ULS load)

The DIC crack pattern image during the first load cycle in **Figure 5.27** reflected the pattern on the back of the actual specimen quite well. It showed higher crack depths and lower crack spacing under the left of the specimen. In addition, the DIC crack pattern was able depict compression concrete strain more prominently than on the specimens discussed to this point.

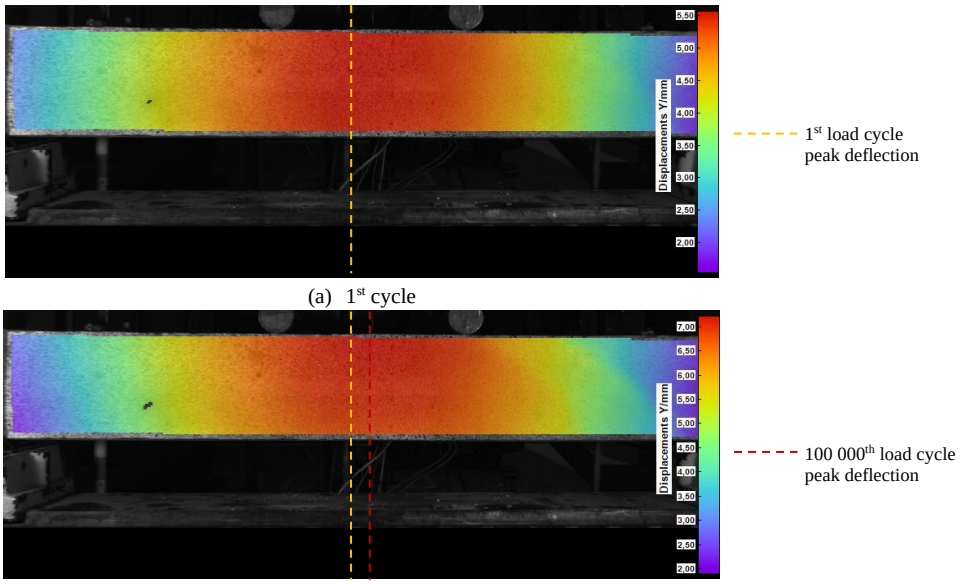

Figure 5.30 450mm specimen: Deflection fields at 1st and 100 000th cycles at 130kN (40% ULS load)

The points of maximum deflection during the 1st and 100 000th cycles, shown in **Figure 5.28**, also showed an initial left inclination where the maximum deflect was about 50mm off-centre as it coincides with the left column of Demec targets and after 100 000 cycles the maximum deflection point shifted to the centre of the beam. The eventual failure mode of the specimen was the rupture of 2 steel bars at the centre of the beam as shown in **Figure 5.29**. Even though the DIC images during the first load suggested that failure may occur toward the left load application point, the maximum deflection point at 100 000 cycles was able to predict the failure location more accurately. Furthermore, **Figure 5.29** also shows that crack density does not always provide an accurate indication of failure location.

Figure 5.28 450mm specimen: failure location (40% ULS load)

800mm Specimen

The 800mm specimen tested under the 40% stress range had a much higher crack density which resulted in a low average crack spacing of 48.65mm. However, these cracks had a low average crack height. Save for 3 cracks, all of the flexural cracks in the region of constant moment and in the wider patch repair portion, did not propagate passed the depth of the patch repair mortar. The cracks were quite uniformly spaced and from the actual crack pattern alone there was no specific indication of areas that appeared weaker than the rest. Although there was one shear crack to the right of the specimen that grazed the corner of the patch repair, which propagated the deepest into the section.

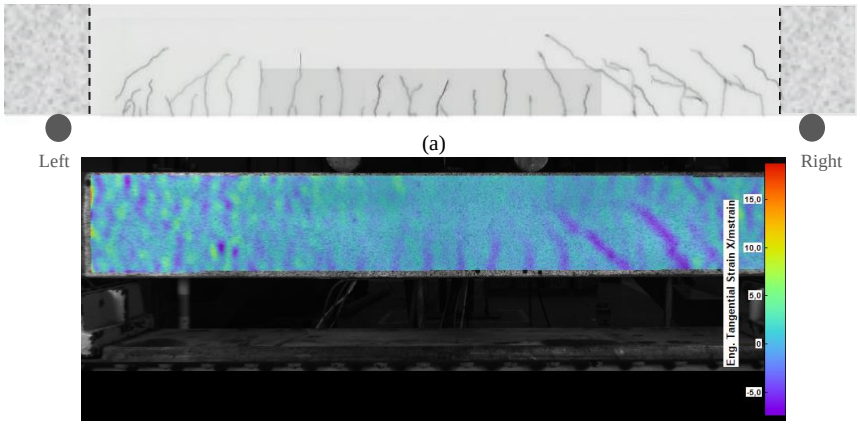

(a)

(b)

Figure 5.29 800mm specimen: Final actual crack pattern versus DIC crack pattern at 1 load cycle (40% ULS load)

The shear cracks indicated at the end of the previous paragraph was detected quite prominently by the DIC tangential x-strain field plot as shown in **Figure 5.30**. In fact, to the right of that shear crack the strain field pointed toward another area of negative strain concentration.

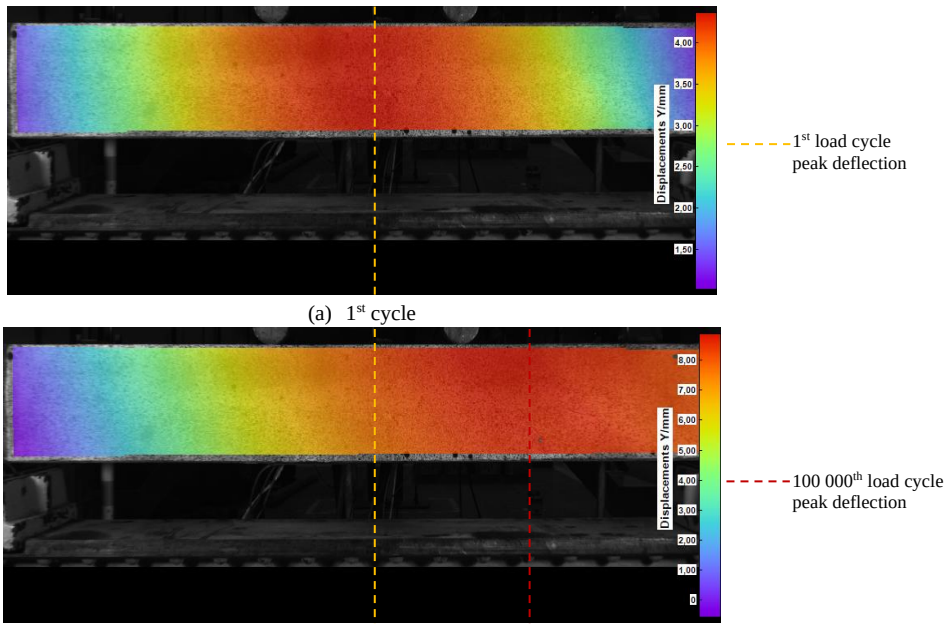

(a) 1st cycle

(b) 100 000st cycle

Figure 5.30 800mm specimen: Deflection fields at 1st and 100 000th cycles at 120kN (40% ULS load)

The points of maximum vertical deflection during the 1st and 100 000th cycles as shown in **Figure 5.31**, indicate that the maximum deflection was originally at midspan. This point gradually shifted toward the right of the specimen and at 100 000 cycles seemed to coincide with the shear cracks indicated in **Figure 5.30**. The specimen did not fail due to fatigue after 1 150 000 cycles, at which point fatigue testing was terminated due to time constraints. It was subsequently loaded statically to failure. The post-fatigue failure load was exactly that same as the failure load of 300kN of the same specimen that was not subjected to fatigue loading. The failure mode due to post-fatigue static loading was crushing in compression concrete only. The was no rupture of tension reinforcing steel.

1300mm Specimen

The crack density increased further from the 800mm to the 1300mm damage extent specimen. The 1300mm specimen had an average crack spacing of 46.15mm and average crack height of 63.66mm.

The flexural cracks within the region of constant moment were characterized by a low average crack spacing and those cracks were quite deep, propagating though the patch repair mortar. The average crack spacing reduced even further once the first steel bar rupture; this moment was characterized by a short increase in crack growth rate.

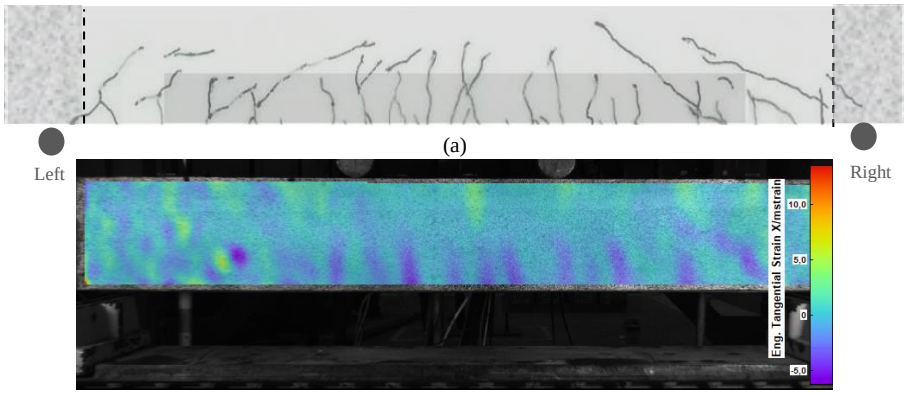

Figure 5.31 1300mm specimen: Final actual crack pattern versus DIC crack pattern at 1 load cycle (40% ULS load)

During the first load cycle the DIC crack pattern shown in **Figure 5.32** was able to reflect the high crack density at the beam midspan. The points of maximum deflection during the 1st and 100 000th cycles showed an inclination to the right load application point. The point of maximum vertical deflection at 100 000 cycles coincided with the right column of Demec strain targets.

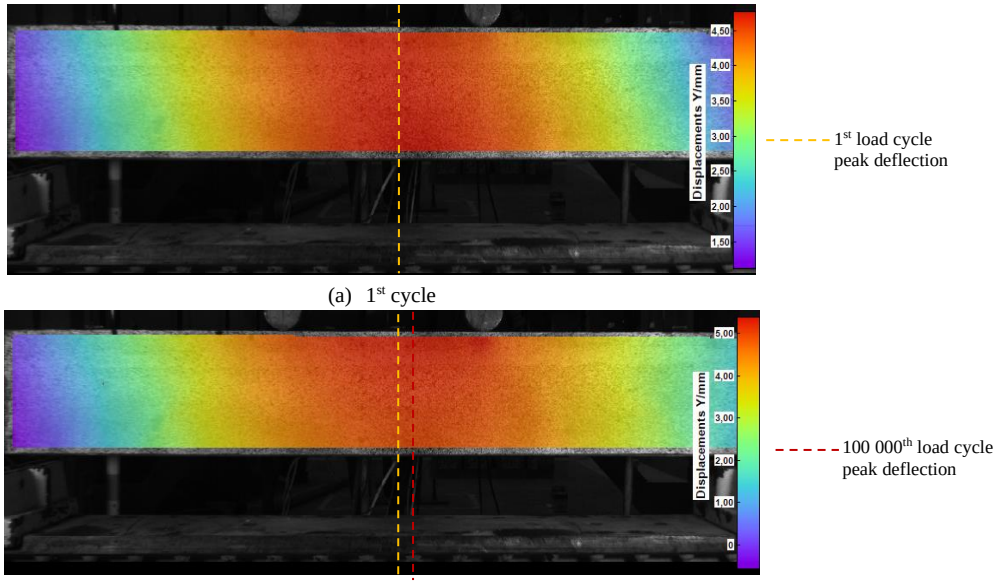

Figure 5.32 1300mm specimen: Deflection fields at 1st and 100 000th cycles at 117.2kN (40% ULS load)

The failure mode of the 1300mm specimen occurred in two stages. There was a steel rupture of one of the bars at 1 000 000 cycles, which was momentarily increased the crack growth rate at the location of steel rupture. After this point the specimen was able to sustain 83 935 cycles until the second bar ruptured. After the second bar ruptured, failure was caused by CFRP debonding and crushing of compression concrete. The location of steel rupture and subsequent CFRP debonding coincided with the point of maximum deflection indicated by the DIC deflection field captured at 100 000 cycles.

1800mm Specimen

Of all the specimens considered for both stress range tests, the 1800mm corrosion damaged and patch repaired exhibited the highest crack density. It had the lowest average crack spacing of 45.00mm and the highest relative average crack depths of 75.08mm. Even though the average crack height during the first load cycle was quite low, from the DIC crack pattern image in **Figure 5.34**, the strain field reflects the low average crack spacing exhibited by the specimen quite early on in its fatigue life.

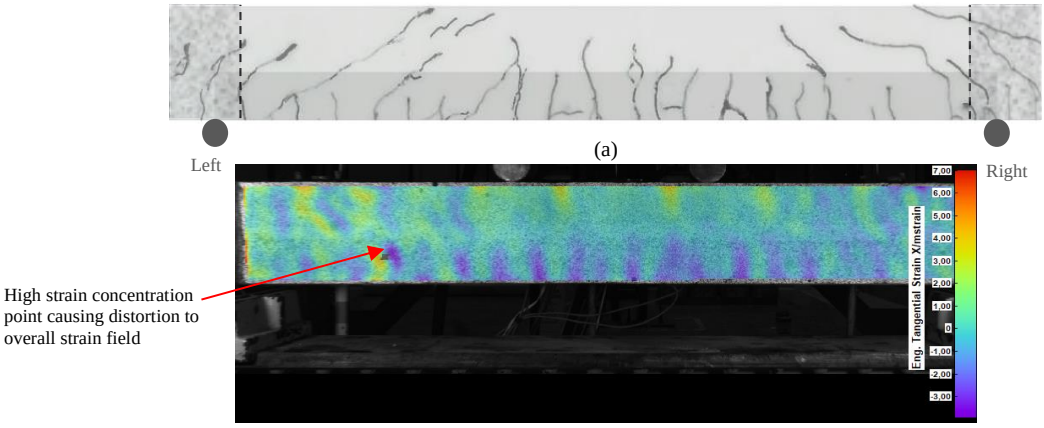

Figure 5.33 1800mm specimen: Final actual crack pattern versus DIC crack pattern at 1 load cycle (40% ULS load)

The DIC crack pattern indicates the position with the highest tangential strain the x-direction which is quite close to the midspan of the section. The point of maximum strain also coincides with the points of maximum deflection during the 1st and 100 000th cycles as shown in **Figure 5.35**.

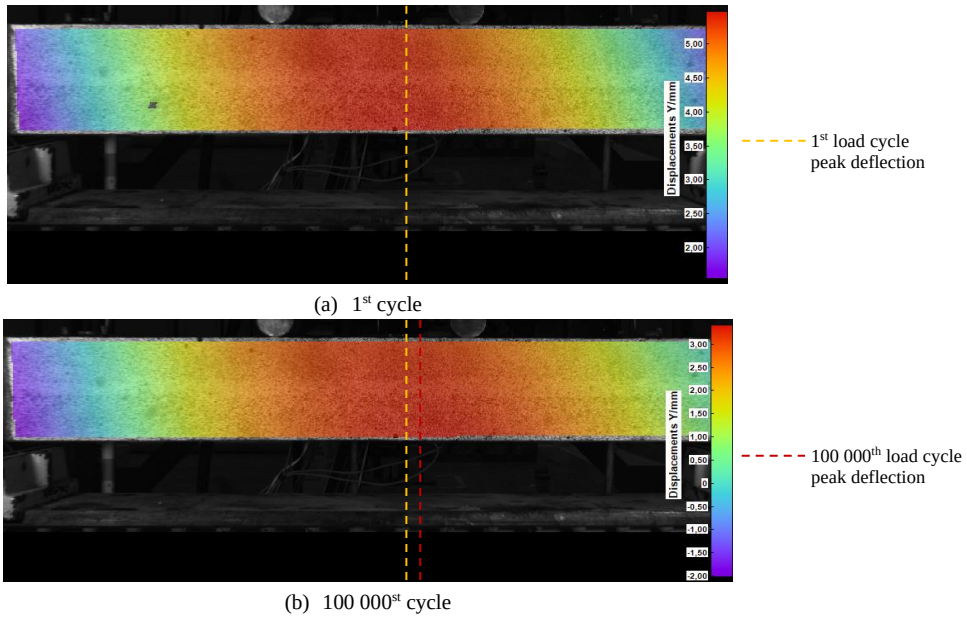

Figure 5.34 1800mm specimen: Deflection fields at 1st and 100 000th cycles at 116kN (40% ULS load)

Although one of the tension steel reinforcing bars ruptured at the centre at the point of maximum deflection, the overall specimen did not fail due to fatigue. After 2 000 000 cycles the 1800mm fatigue testing was terminated due to time constraints. The specimen was subsequently loaded to static failure which occurred at 216kN, which was 34.3% lower than the ultimate failure load of the same specimen that was not subjected to fatigue loading.

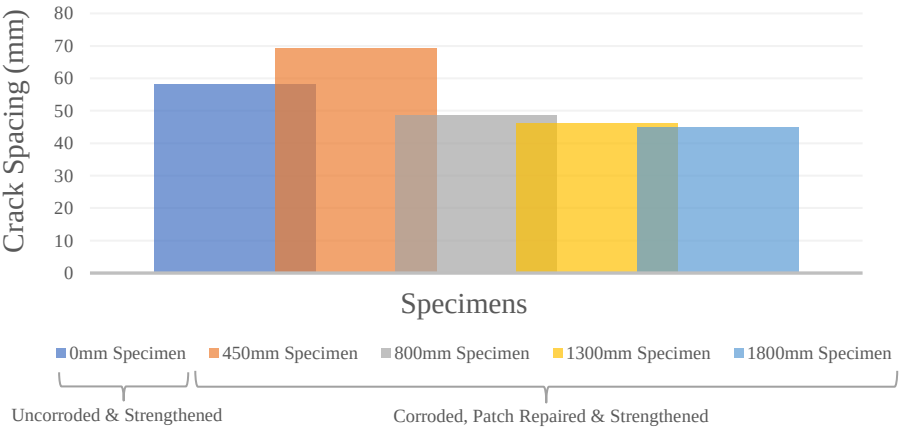

Figure 5.35 Relative average crack spacing (40% ULS load)

As shown in **Figure 5.36**, the average crack spacing of the specimens tested 40% stress range followed a similar downward trend as the specimens tested under the 60% stress range. As the damage extent was increased from 450mm to 1800mm there was a 53.9% reduction in average crack spacing. In this case though, the uncorroded unpatched specimen did not achieve the highest average crack spacing as it did during the 60% stress range tests; this may be due to the 450mm specimen that exhibited an unforeseen high average crack spacing. In comparison to the 60% stress range test specimens the 40% stress range test specimens had a 47,6% lower average crack spacing as well as a lower average crack spacing reduction as the damage extent was increased from 0mm to 1800mm. The 40% stress range specimens had an average crack spacing reduction rate of 7.25mm/m, whereas the 60% stress range specimens had a reduction rate of 10.58mm/m.

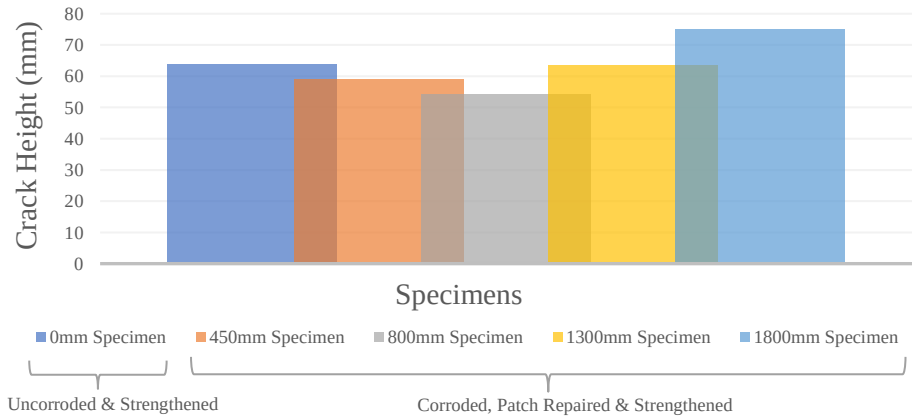

Figure 5.36 Relative average crack height (40% ULS load)

Analysis of the relative average crack height of the specimens tested under the 40% stress range regime did not reveal as clear findings, as shown in **Figure 5.37**. For the 0mm, 450mm and 800mm specimens there was a reduction in average crack height, like the specimens tested under the 60% stress range regime. However, after that the results indicated an increase in the average crack height from the 800mm to the 1800mm specimens. As the corrosion damage and patch repair extent is increased from 450mm to 800mm there is an initial 9.1% reduction in average crack height, after which the crack height increased by 38.5% from the 800mm specimen to the 1800mm specimen. The overall trajectory from 450mm to 1800mm specimens reveal a 26.95% increase in crack height.

If one considers the overall performance of the 40% stress range specimen, the reduction of average crack spacing indicates an increase in the total number of cracks as the damage extent was increased.

The increase in average crack height as the damage extent was increased indicates that there may be a stiffness reduction, as there is less uncracked concrete below the neutral axis that is able to contribute to the internal force equilibrium. Comparison of the crack height behaviour of the specimens tested under 40% and 60% stress ranges reveal a stark contrast. The results indicate that at high stress ranges, when the fatigue life is shorter, there is a reduction of the average crack height as the corrosion damage and patch repair extent is increased. However, with low stress ranges, where the fatigue life is much longer, there is an increase in average crack depth.

An overall increase in average crack depth and a reduction in average crack spacing equates to a higher crack density for the specimens tested under the 40% stress range regime, which is exacerbated by an increase in damage extent.

5.3.3 Stiffness degradation

Stiffness degradation was evaluated in terms of 3 different performance criteria, which included midspan deflection resistance, composite material strain and neutral axis shift. The relative behaviour of the corrosion damaged, patch repaired and CFRP strengthened specimens was considered for both the 40% and 60% stress range tests.

5.3.3.1. Midspan deflection

40% Stress range specimens

Deflection measurements were recorded at 20 000 cycle intervals for the 40% stress range specimens, as shown in **Figure 5.38**. The measurements were taken when specimens were loaded to the maximum load P_{max}, for a given stress range. An increase in deflection, as the maximum test load remains constant, reveals a stiffness degradation as the specimens experience cyclic loading. Investigation of midspan-deflection and composite material strain graphs enabled the identification of instances at which tension steel may have ruptured. After identifying the number of cycles at which a steel bar may have ruptured N_i, as shown in **Table 5.6**, it was possible to express the post-fatigue life (after first bar rupture) as a percentage of the overall fatigue life N_{total}.

Table 5.6 Post-fatigue behaviour of specimen tested under cyclic loading

Identity	Fatigue Life (N_{total})	Failure Mode	No. of Cycles to Rupture of 1st Steel Bar (N_1)	No. of Cycles to Rupture of 2nd Steel Bar (N_2)	Fatigue Life Remaining after First Rupture (%)
S_CNTRL 2	$10^{6.000}$	No Fatigue Failure	-	-	-
S_CNTRL 3	$10^{5.408}$	Steel rupture (1 bar)	$10^{5.342}$	-	14.1
S_450mm 2	$10^{5.897}$	Steel rupture (2 bars)	$10^{5.643}$	$10^{5.477}$	44.2
S_450mm 3	$10^{5.078}$	Steel rupture (1 bar)	$10^{4.778}$	-	49.9
S_800mm 2	$10^{6.061}$	No Fatigue Failure	-	-	-
S_800mm 3	$10^{5.011}$	Steel rupture (1 bar)	$10^{4.602}$*	-	61.1
S_1300mm 2	$10^{6.035}$	Steel rupture (2 bars)	$10^{6.000}$	$10^{4.699}$	7.7
S_1300mm 3	$10^{5.304}$	Steel rupture (2 bars)	$10^{5.255}$	$10^{4.301}$	10.7
S_1800mm 2	$10^{6.301}$	No Fatigue, Steel rupture (1 bar)	$10^{6.225}$	-	16
S_1800mm 3	$10^{5.393}$	Steel rupture (2 bars)	$10^{5.342}$	$10^{4.223}$	10.9

*LVDT reading not captured after $10^{4.602}$ cycles

0mm Specimen

The 0mm specimen, as shown in **Figure 5.38**, showed the second highest deflection during its fatigue life, despite not failing due to fatigue after 1 000 000 cycles. During the first 120 000 cycles its stiffness degradation rate was lower than the rate of the 800mm specimen, but still higher than all the other specimens. After 120 000 cycles its stiffness degradation rate was quite similar to those of the 450mm and 1300mm specimens. At 600 000 cycles there was a significant increase in deflection. This jump was thought to have been caused by the rupture of one of tension steel bars, however based on

discussions of other parameters in this chapter it is known that the eventual failure mode of the specimen was not due to fatigue, but instead crushing of compression concrete under monotonic loading. A post-failure steel inspection revealed that none of the tension steel had ruptured. It is possible that at 600 000 cycles there was a bond slip between the tension reinforcing steel and surrounding concrete, which caused internal stress redistribution that resulted in a higher portion of the applied load being carried by the carbon fibre. Assessment of composite material strains in the next section further alludes to the likelihood of an internal redistribution.

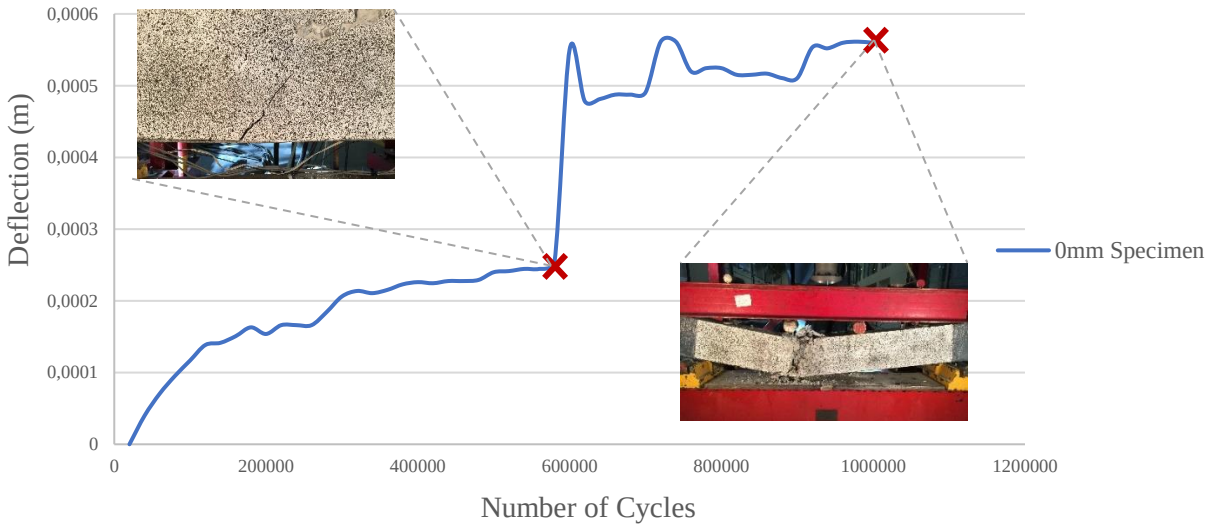

Figure 5.37 Midspan deflection of 0mm specimen during 40% stress range fatigue testing

450mm Specimen

The 450mm specimen had the second lowest initial stiffness degradation rate, of all the specimens tested under the 40% stress range, up to 140 000 cycles. After 140 000 cycles its degradation rate was comparable with the 0mm and 1300mm specimen degradation rates. After 280 000 cycles its actual deflection would eventually surpass that of the 1300mm specimen and continue to degrade at a higher rate than the 1300mm specimen until failure. From the midspan deflection and composite material strain behaviour during cyclic loading, 440 000 cycles was identified as a possible instance when one of the tension steel bars rupture, which postulates a relatively high post-fatigue life of 44.2%.

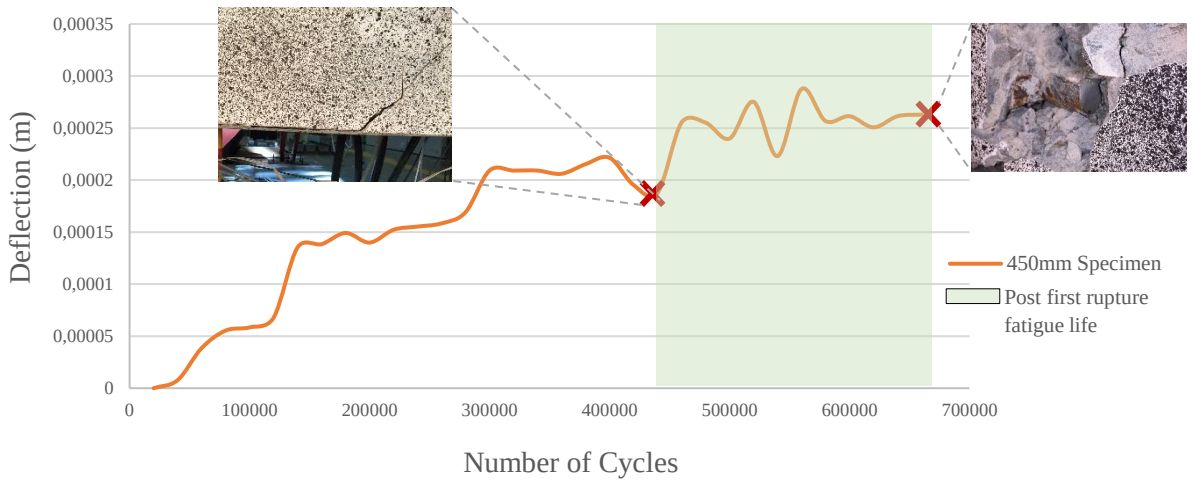

Figure 5.38 Midspan deflection of 450mm specimen during 40% stress range fatigue testing

800mm Specimen

Even though it did not have the lowest fatigue life in this stress range, the midspan deflection results on **Figure 5.40** show that the 800mm specimen exhibited the lowest stiffness of all the specimens, as it had the highest overall deflection throughout its fatigue life. The specimen showed a high stiffness degradation rate during the first 50 000 cycles, after which the stiffness degradation remained similar to the degradation rates of the 0mm, 450mm and 1300mm specimens. At 500 000 cycles there was a significant spike in midspan deflection. Once again, this spike was thought to have been caused by the rupture of one of tension steel bars, however it was found that the eventual failure mode of the specimen was not due to fatigue, but instead crushing of compression concrete under monotonic loading. Post-failure steel inspection revealed that none of the tension steel had ruptured.

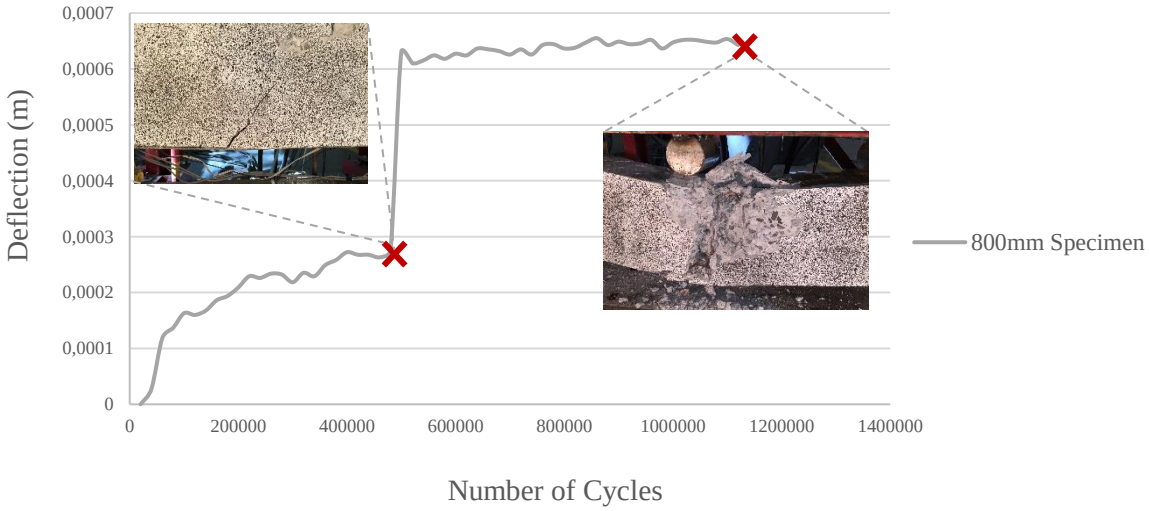

Figure 5.39 Midspan deflection of 800mm specimen during 40% stress range fatigue testing

1300mm Specimen

The 1300mm specimen experienced a stiffness degradation rate near identical to that of the 0mm specimen up to 100 000 cycles. After 100 000 cycles the degradation rate was slightly lower that of the 0mm specimen. Although its actual deflection was higher than the 450mm specimen, the degradation rate of the 1300mm was lower than the 450mm specimen, resulting in the actual deflection of the 450mm specimen surpassing it at 280 000 cycles. Furthermore, at 620 000 cycles there seems to be an infliction point for the 1300mm specimen, which marks the commencement of a slight increase in stiffness up to 1 020 000 cycles. As shown in **Figure 5.41**, at 1 020 000 cycles there was a substantial increase in midspan deflection, after which the specimen was still able to endure another 63 935 cycles (i.e. 7.7% post-fatigue life). Post-fatigue failure tension steel inspection of the specimen revealed that both tension reinforcing bars ruptured. The findings from the post failure inspection proposes the likelihood that either one or both of the steel bars ruptured at 1 020 000 cycles. If one bar were to have ruptured the remaining steel bar, together with the CFRP was able to sustain the applied loads for the remain 63 935 cycles before the second bar ruptured, leading to an abrupted ultimate failure of the section. If both bars were to have ruptured at 1 020 000 cycles, the CFRP would solely have resisted the applied loads for the remaining 63 935 cycles. The second scenario seems less likely considering that the CFRP contributes only 27.3% of the structural capacity of the section and a test load of 40% of the ultimate failure load would have exceeded that. A third scenario, which based on evaluation of the composite material strains seems more plausible, is that the second steel bar ruptured 50 000 cycles after the first bar ruptured. This was characterized by a second significant increase in midspan deflection after the first bar had ruptured, as shown in **Figure 5.41**.

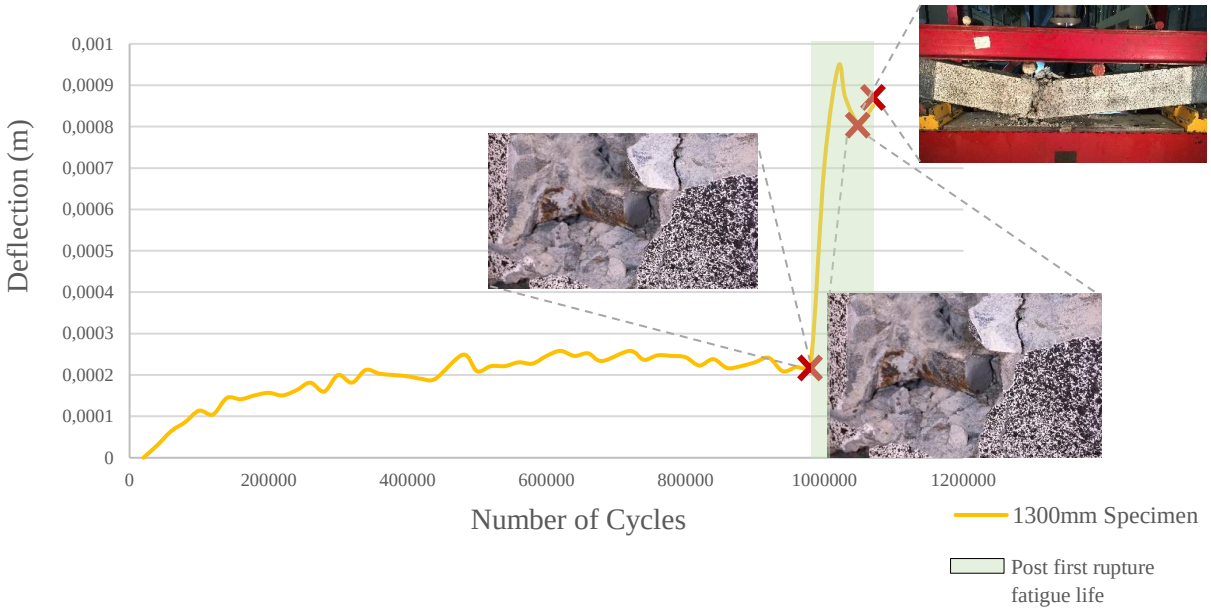

Figure 5.40 Midspan deflection of 1300mm specimen during 40% stress range fatigue testing

1800mm Specimen

The 1800mm specimen showed the highest stiffness of all the specimens tested under the 40% stress range. In contrast with the other specimens, the 1800mm specimen did not have an initial high stiffness degradation rate followed by a lower degradation rate. Its degradation rate was relatively low at the start and seemed to progressively increase during its fatigue life. At 960 000 there was a substantial increase in the midspan deflection, which suggested the possibility that one of the tension steel bars may have ruptured. The specimen did not fail due to fatigue though, after 2 000 000 cycle the specimen was loaded monotonically to failure and the post-fatigue tension steel inspection revealed that one of the tension steel bars had in fact ruptured during the course of fatigue testing. This would suggest that the other tension steel bar, together with the CFRP laminate were still able to sustain the applied cyclic loads for possibly another 1 040 000 cycles or a post-fatigue life of more than 52%, which is seems relatively high. Results from the compression concrete strain indicate that the tension steel bar may only have ruptured at 1 680 000 cycles.

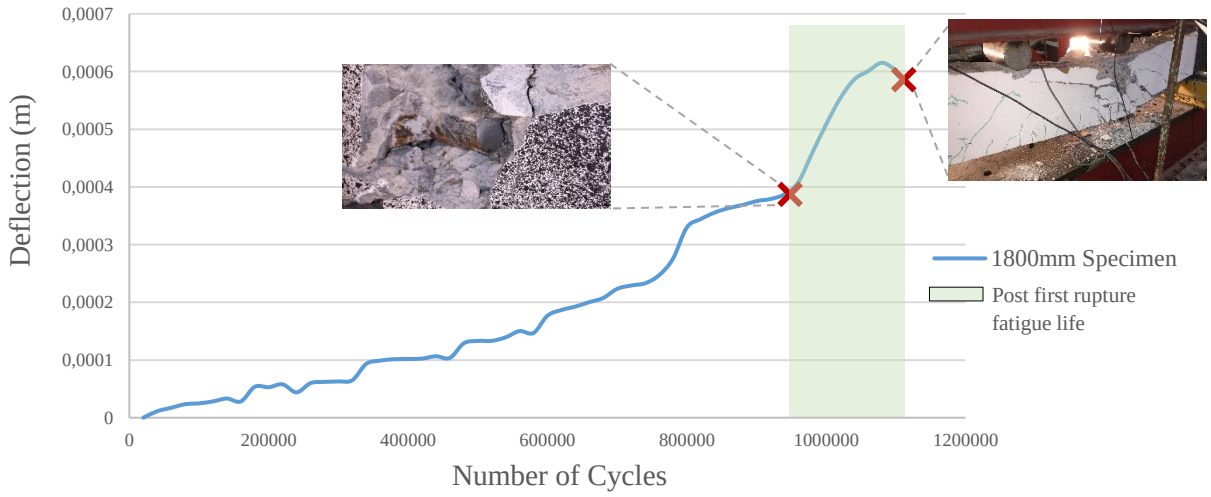

Figure 5.41 Midspan deflection of 1800mm specimen during 40% stress range fatigue testing

An overall assessment of the specimens tested under the 40% stress range show that the 800mm specimen was the least stiff, as it exhibited the highest overall deflection and highest rate of stiffness

degradation. The stiffness of the other specimens increase as the corrosion and patch repair length was increased from 0mm, 450mm, 1300mm to 1800mm specimens, respectively, where the 1800mm specimen had the highest stiffness. Correlations can be drawn from the energy dissipation during the first load cycle and the initial rate of stiffness degradation. **Table 5.1** shows that the 1800mm specimen dissipated the highest amount of energy, whereas the 800mm specimen dissipated the least amount of energy. This shows that the specimens which dissipated a large amount of energy during its first load cycle has a lower rate of stiffness degradation during the initial stages of its fatigue life and vice versa.

As mentioned earlier, the 40% stress range specimens that did not fail due to fatigue, were stopped after a certain number of cycles and subsequently tested under static loading until failure. Initially, the number of cycles used as the cut off mark was 1 000 000 cycles. This amount was gradually increased to 2 000 000 cycles, especially when the test results seemed to indicate some activity in the specimen. Some of the activity that was considered included a substantial increase in neutral axis strain, an increase in crack growth rate or a rapid increase in midspan deflection. These activities could indicate an internal stress redistribution possibly caused by steel rupture or concrete-steel bond slip.

Table 5.7 Flexural capacity of 40% stress range specimens after fatigue testing (Mahal, 2015)(Mahal, 2015)(Mahal, 2015)

	Fatigue Cycles	Virgin Specimen* Failure load	Flexural Strength After Fatigue Testing
0mm Specimen	$10^{6.000}$	*274 kN*	*276 kN*
800mm Specimen	$10^{6.061}$	*300 kN*	*300 kN*
1800mm Specimen	$10^{6.301}$	*290 kN*	*216 kN*

*Virgin specimen=subjected to no fatigue loading

Table 5.7 shows the flexural capacity of the 40% stress range specimens that did not fail during fatigue cycles and were subsequently loaded monotonically. Comparison of the flexural capacity after fatigue testing to that of the virgin specimens reveals that although the 0mm and 800mm specimens had been affected in terms of stiffness and crack behaviour (as discussed in the following sections), their flexural capacity remained relatively unchanged. The 1800mm specimen experienced a reduction in flexural capacity of 34.3% after 2 000 000 fatigue cycles. This reduction is flexural capacity may be attributed to the one tension steel bar that had ruptured during fatigue testing.

60% Stress range specimens

Deflection measurements were recorded at 10 000 cycle intervals for the specimens tested under the 60% stress range. An overall shorter fatigue life was anticipated for the 60% stress range tests, that is why the sampling rate was increased to every 10 000 cycles instead of every 20 000 cycles previously used for the 40% stress range tests. The measurements were recording when the specimens were loaded to their maximum test load $\boldsymbol{P_{max}}$.

<u>0mm Specimen</u>

In the 40% stress range regime the 0mm specimen showed the second lowest stiffness in terms of maximum midspan deflection. During the first 100 000 cycles the deflection and stiffness remained relatively unchanged and at 120 000 cycles there was a substantial increase in midspan deflection, as shown in **Figure 5.43**. This rapid increase was once again followed by a period of constant deflection up to 220 000 cycles where there was a second substantial increase in midspan deflection, which lead to the ultimate failure of the section at 256 000 cycles. Ultimate failure of the specimen was found to have been caused by rupturing of one of the tension steel reinforcing bars, which was followed by delamination of the CFRP laminates and eventually crushing of compression concrete at the right load application point. The first substantial jump at 120 000 cycles occurred quite early in the fatigue life of the specimen and a likely cause for this initial stiffness degradation was an internal stress redistribution

caused by reinforcing steel and concrete bond slippage. The second substantial stiffness reduction at 220 000 cycles was thought to have been caused by the rupturing of the tension bar. After rupturing of the steel bar, the remaining tension reinforcing bar together with the CFRP laminates were able to endure another 17 908 load cycles (i.e. post fatigue life of 14.1%) before ultimate failure.

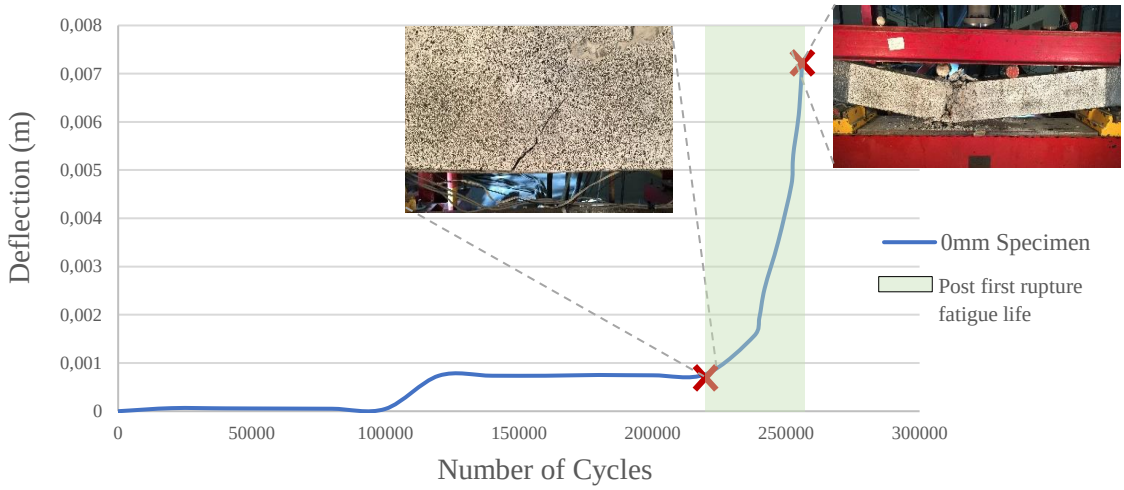

Figure 5.42 Midspan deflection of 0mm specimen during 60% stress range fatigue testing

450mm Specimen

The midspan deflection of the 450mm specimen, as presented in **Figure 5.44**, remained unchanged for a shorter period than the uncorroded unpatched specimen. After 20 000 cycles the specimen exhibited a significant increase in stiffness degradation rate for 10 000 cycles. After the 30 000 cycle interval the stiffness degradation rate reduced and remained consistent until the 60 000 cycle interval, which marked the commencement of another increase in stiffness degradation. Evaluation of the composite material strains also showed an increase in compression concrete strain at the 60 000 cycle mark, which suggested that one of the tension steel bars may have ruptures at this point. Ultimate failure of the section was caused by rupturing of the second tension steel bar leading to CFRP delamination and ultimately crushing of compression concrete under the left load application point at 119 716 cycles. This indicated a relatively high post-fatigue life of 49.9%. In terms of the overall stiffness degradation, the 450mm specimen was found to have the second lowest stiffness as well as the second lowest fatigue life, where the rapid high stiffness reduction rate during the 20 000 to 30 000 cycles period contributed significantly to the overall stiffness reduction. Given its early occurrence during the fatigue life of the specimen, this initial increase in stiffness reduction rate was attributed to likely bond slippage induced stress redistribution, after which the specimen stiffness deteriorated at a much higher rate than the other specimens tested under the 60% stress range regime.

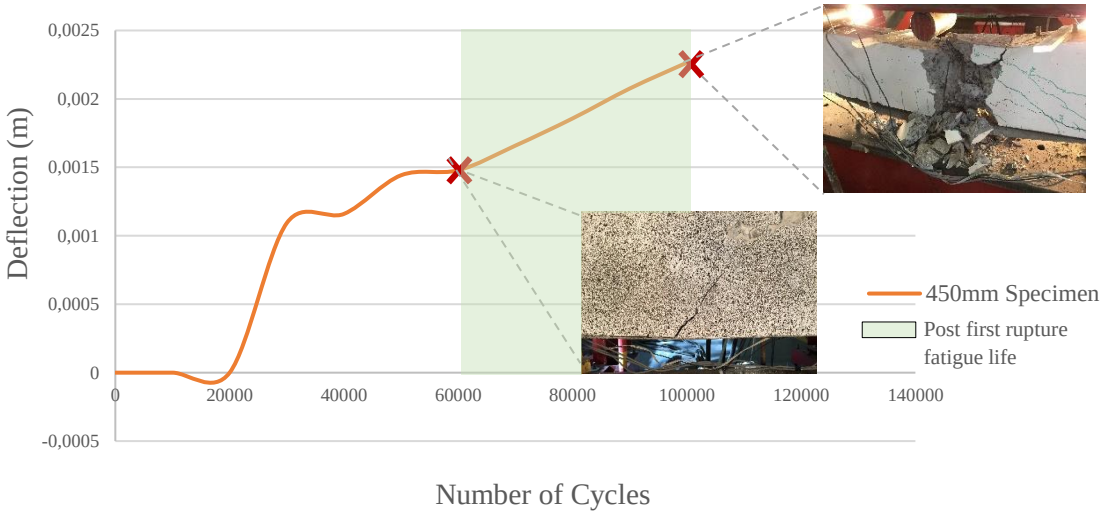

Figure 5.43 Midspan deflection of 450mm specimen during 60% stress range fatigue testing

800mm Specimen

Not only did the 800mm specimen tested under to 60% stress range have the lowest overall fatigue life of 102 750 cycles, but it also had the lowest overall stiffness of all the specimens tested under this stress range. As shown in **Figure 5.45** there was a high rate of stiffness degradation from the onset of fatigue testing up to 40 000 cycles. After 40 000 cycles the midspan deflection increased significantly more than any of the other specimens, such that the midspan deflection measurement distorted the scale of **Figure 5.45**. It was therefore decided to not display the readings beyond this point, to have a set of results that plot in a way that the results from the different specimens could be comparable. Furthermore, the results of the 800mm specimen obtained after the 50 000 cycle interval did not change at all, which indicated that the LVDT may have malfunctioned beyond this point. It was therefore not possible to identify the possible rupture of the tension steel during the fatigue life of the specimen using midspan deflection as an indicator, however evaluation of the composite material strains suggest that the tension steel bar may have ruptured that the 40 000 cycle interval.

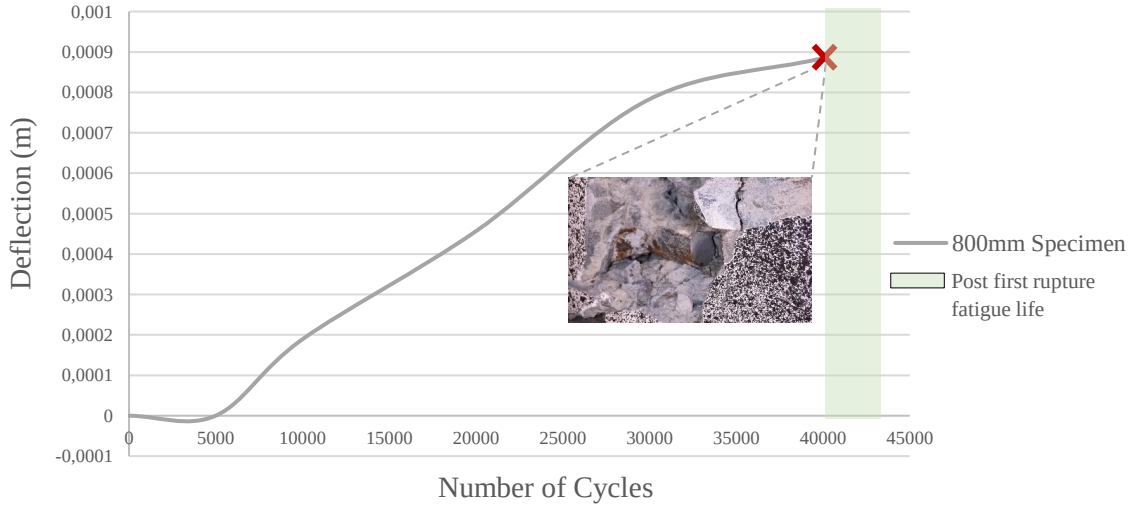

Figure 5.44 Midspan deflection of 800mm specimen during 60% stress range fatigue testing

1300mm Specimen

During its fatigue life the 1300mm specimen exhibited the highest stiffness, where its midspan deflection remained near unchanged up to 180 000 cycles, at which there was a slight increase in midspan deflection. At 200 000 cycles there was a second substantial reduction in the specimen stiffness

which rapidly led to the ultimate failure of the specimen at 201 450 cycles. Ultimate failure of the specimen was caused by rupturing of both tension reinforcing bars, debonding of CFRP laminates shortly followed by crushing of compression concrete in the centre of the specimen. The two increases in midspan deflection, which occurred in fairly quick succession of each other, could indicate the intervals during which the two reinforcing bars ruptured as shown in **Figure 5.46**, suggesting a post-fatigue life of 10.7%.

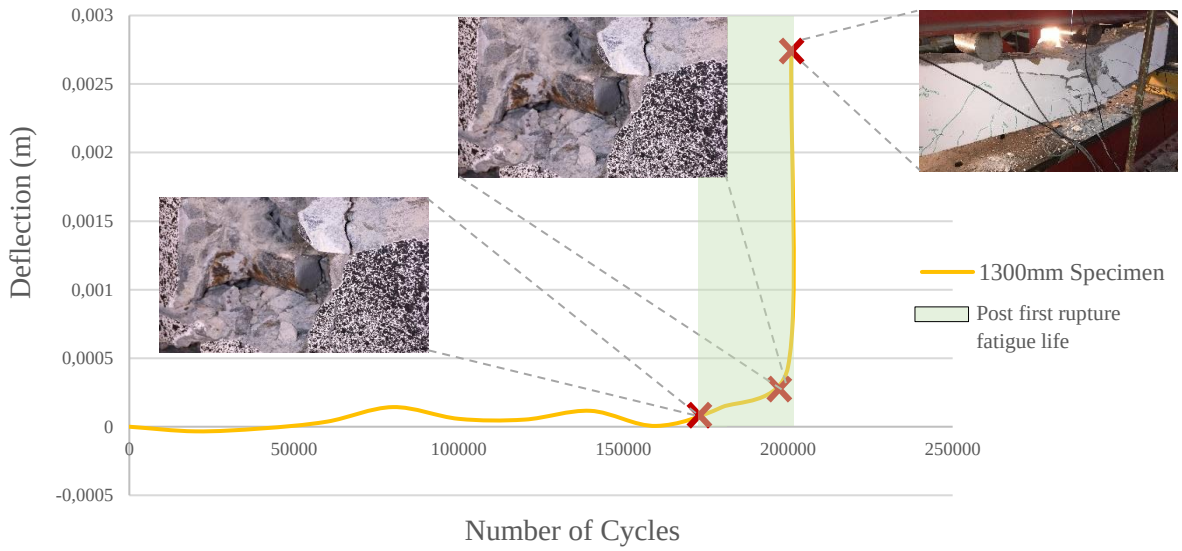

Figure 5.45 Midspan deflection of 1300mm specimen during 60% stress range fatigue testing

1800mm Specimen

The 1800mm specimen exhibited a gradual and consistent stiffness reduction during its fatigue life, as depicted in **Figure 5.47**. The specimen stiffness degradation remained constant for the first 80 000 cycles after which is seemed to plateau for a brief period up to 100 000 cycles. 120 000 cycles marked the beginning of another period of constant stiffness degradation, which once again seemed plateau from 200 000 to 220 000 cycles. From 220 000 cycles the stiffness degradation rate was much higher than the previous two periods leading to the ultimate failure of the specimen at 247 000 cycle, which was the highest overall fatigue life of the specimens tested under this stress range. The ultimate failure of the specimen was caused by the rupture of both tension steel bars, followed by the debonding of the CFRP laminates and eventual crushing of compression concrete at the right load application point. Although the 1800mm specimen yielded the highest fatigue life of specimens under the 60% stress range, it had the second highest stiffness. The major reductions in stiffness were likely caused by rupturing of the tension reinforcing bars at each one of the 220 000 and 236 720 cycle intervals, while the initial increase in stiffness degradation at 120 000 cycles may suggest an internal stress redistribution due to steel-concrete bond slippage.

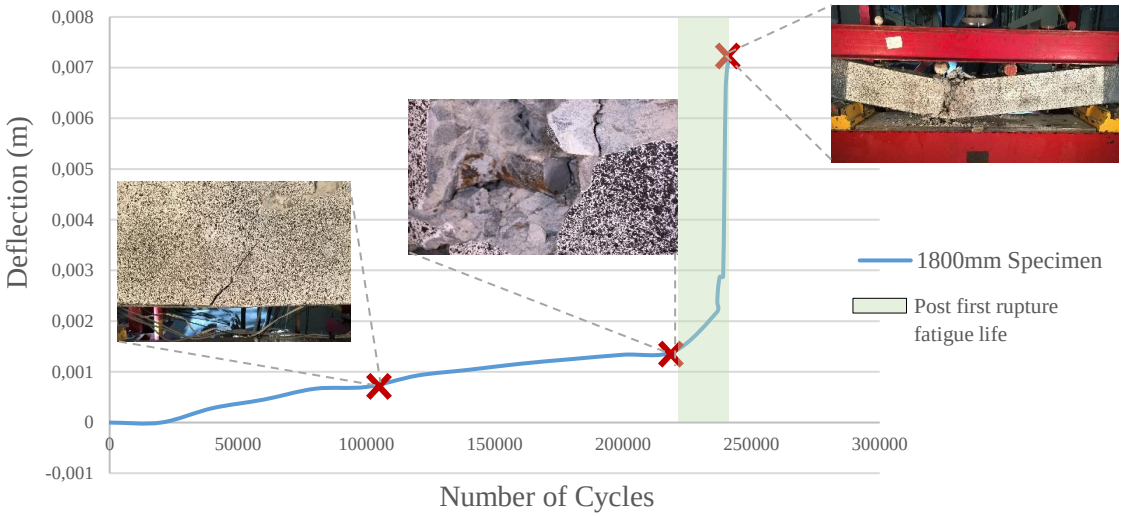

Figure 5.46 Midspan deflection of 1800mm specimen during 60% stress range fatigue testing

Assessment of the relative behaviour of all the specimens tested under the 60% stress range revealed no clear correlation between the increase in corrosion damage and patch repair extent with the stiffness performance of these specimens as it did for the specimens that were tested under the 40% stress range regime. Considering the energy dissipation rate results during the first load cycle were inconclusive for the 450mm and 1300mm specimens, it was not possible to draw accurate or comparable conclusions between the energy dissipation rate and the initial stiffness degradation rate either. Looking at a broader trend of the 60% stress range specimens indicated that the specimens with the shorter corrosion and patch repaired length, such as the 450mm and 800mm specimens, exhibited a higher initial and overall stiffness degradation than the longer specimens, such as the 1300mm and 1800mm specimens.

5.3.3.2. Digital image correlation deflection

In **Section 5.3.2** a discussion was entertained surrounding the potential usefulness of using DIC in tracking crack behaviour and identifying locations on the structure that may lead to eventual structural failure. The discussion made a compelling case for the use of DIC for two reasons. The first of which was its ability to identify crack patterns which resembled those that appeared on the specimen. If the concrete tensile strain is known, it presents the opportunity to predict the exact locations at which cracks will form. The second reason was its potential to provide a more accurate depiction of the specimen deflection field. The findings showed that very often the maximum deflection and the eventual failure mode do not occur at the specimen midspan and also that the maximum deflection is likely to coincide with the location of fatigue failure. This section will consider the correlation between the deflection results obtained from the LVDTs and the DIC images in order to explore the potential of using DIC to monitor stiffness progression. Similar to the process followed when considering crack behaviour, the maximum deflection results from the two methods will be considered at maximum load during the first load cycle and at maximum load after 100 000 cycles.

First load cycle deflections

Figure 5.48 and **5.49** show the relative maximum deflection results of the various specimens obtained from both DIC and LVDT measurements, under the 40% and 60% stress ranges, respectively. The comparative results from the 40% stress range test specimens, as shown in **Figure 5.48**, indicate that the DIC deflection measurement are consistently higher than the results obtained from the LVDTs. Under the 40% stress range the maximum deflections obtained through DIC were between 23,9% and 106.7% higher than those obtained through LVDT measurements. **Table 5.8** presents a summary of the maximum deflection results obtained from DIC, LVDT measurements and theoretical design calculations (design calculation detailed in **Appendix C.4**). Despite yielding consistent higher

deflection results that those obtained by the LVDTs, the DIC results showed a better correlation with the theoretical design values under the 40% stress range. **Figure 5.48** further shows how the results from the two different methods followed the same upward trend as the corrosion damage and patch repair extent was varied.

Table 5.8 Summary of midspan deflection results from DIC, LVDT measurements and theoretical design calculations

Identity	Maximum Test Load P_{max} (kN)	Calculated Deflection (mm)	LVDT Measurement 1st load cycle (mm)	DIC Measurement 1st load cycle (mm)	LVDT Measurement 100 000th load cycle (mm)	DIC Measurement 100 000th load cycle (mm)
S_CNTRL 2	109.6	2.57	2.65	3.29	2.77	*
S_CNTRL 3	164.4	3.86	2.41	6.63	2.46	8.41
S_450mm 2	130	6.56	2.68	5.55	2.74	7.22
S_450mm 3	195	9.84	*	6.82	2.26	14.06
S_800mm 2	120	6.06	2.47	4.35	2.58	8.88
S_800mm 3	180	9.09	7.15	8.15	7.15	15.86
S_1300mm 2	117.2	5.92	2.99	4.76	3.11	5.38
S_1300mm 3	175.8	8.87	2.36	7.54	2.42	9.93
S_1800mm 2	116	5.85	3.42	5.46	3.44	3.39
S_1800mm 3	174	8.78	7.39	7.93	8.09	11.43

* LVDT/DIC reading not captured

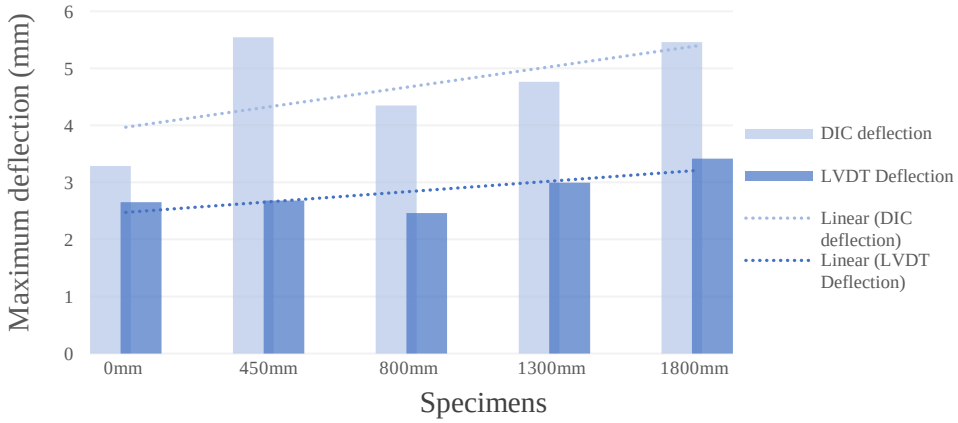

Figure 5.47 DIC versus LVDT deflection during 1st load cycle under 40% stress range test

Under 60% stress range the apparent trend, identified from the maximum deflection measurements obtained during the first load cycle, of the 2 acquisition methods was less clear. Under the 60% stress range the variability of the results increases significantly, where results obtained from the two methods varied between 7.3% to 219.2%, as shown in **Figure 5.49**. As with the 40% stress range tests, the DIC results were higher than those obtained from LVDT measurements, but once again provided better correlation with the theoretical design values. The results obtained from the LVDTs during the 60% range were not as consistent as those obtained from the 40% stress range, this was quite evident during the first load cycle deflections where 2 of the specimens yielded inconclusive energy dissipation rate results as shown in **Table 5.1**. In addition, the LVDT results from the 800mm specimen showed a substantial increase in deflection measurements at 50 000 cycles, after which no readings were obtainable even though the specimen still experienced 50 750 cycles, as shown in **Figure 5.41**.

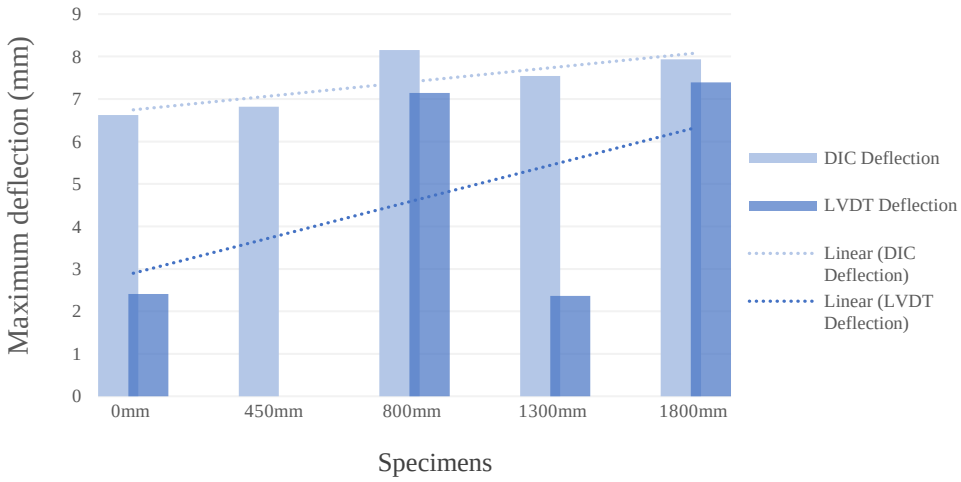

Figure 5.48 DIC versus LVDT deflection during 1st load cycle under 60% stress range test

The long-term midspan deflection results using the two different methods under both stress ranges showed very little correlation. There was no apparent trend between the results. If anything, the results contradict each other, where if one considers the results from the 40% stress range, the DIC deflection results show an increase in deflection during the first 100 000 cycles as the damage extent was increased from 0mm to 800mm whereas the LVDT results indicate a reduction in deflection. Similar contradictions can be found in the comparison of the 60% stress range deflection results.

Ideally when carrying out DIC experiments it is advised to not move the camera during the test period, after the test surface has been calibrated, especially when conducting long-term experiments such as fatigue testing (Xu & Brownjohn, 2018). The reason for that is that every time the camera is moved, the test surface has to be re-calibrated. The fatigue tests for this experiment were conducted in an open access laboratory that did not have a designated control room to house the DIC camera. For purposes of protecting the camera against dust and theft, the camera was stored away at night. Some of the specimen test periods extended as long as 20 days, which therefore required 20 test surface calibrations. This process introduces significant error into the evaluation of DIC results. With that in mind, it can be inferred that the results obtained through DIC for the long-term tests were less reliable than the LVDT deflection measurements during the same period. The DIC results captured during the first load cycles were unaffected by the re-calibration error, as all the results were obtained for one day and was not interrupted by storage.

5.3.3.3. Composite materials strain

Strain gauges were installed on the compression concrete, tension concrete, tension steel as well as the CFRP laminate surfaces. Strain measurements from these gauges were sampled at the same frequency as the midspan deflection measurements as described in **Section 5.3.3.1**. Many of the strain gauges were damaged during the fatigue testing or prior to that. Some of the strain gauges installed on the tension steel reinforcement were damaged from the onset when concrete or patch repair mortar was cast and water from the concrete mixture managed to reach the strain gauge. Other gauges were damaged as the oscillations from fatigue testing fractured the soldered connections between the strain gauge and its connecting wires. This section discusses the behaviour of the relative material strains during fatigue testing.

Compression concrete

Figures 5.50 and **5.51** show the concrete strain on all the samples under 40% and 60% stress range tests, respectively. From the 40% stress range specimen results the 1800mm specimen experienced the

least amount of compression strain as well as the lowest rate of strain increase. It experienced a rate increase of $9.35x10^{-5}$ µstrain per cycle during the first 168 000 cycles. During the discussion of midspan deflection, the LDVT measurements indicated a substantial increase at 1 120 000 cycles after which no more deflection readings were obtainable. This increase was thought to likely have been caused by rupturing of one of the tension steel bars. The 1 120 000 cycle interval was quite early in the fatigue testing period considering that the test was terminated at 2 000 000 cycles. The compression concrete results indicated that 1 120 000 cycles may have signalled a malfunction of the LVDT and the 1 680 000 cycle interval may be the actual point at which the tension steel bar ruptured.

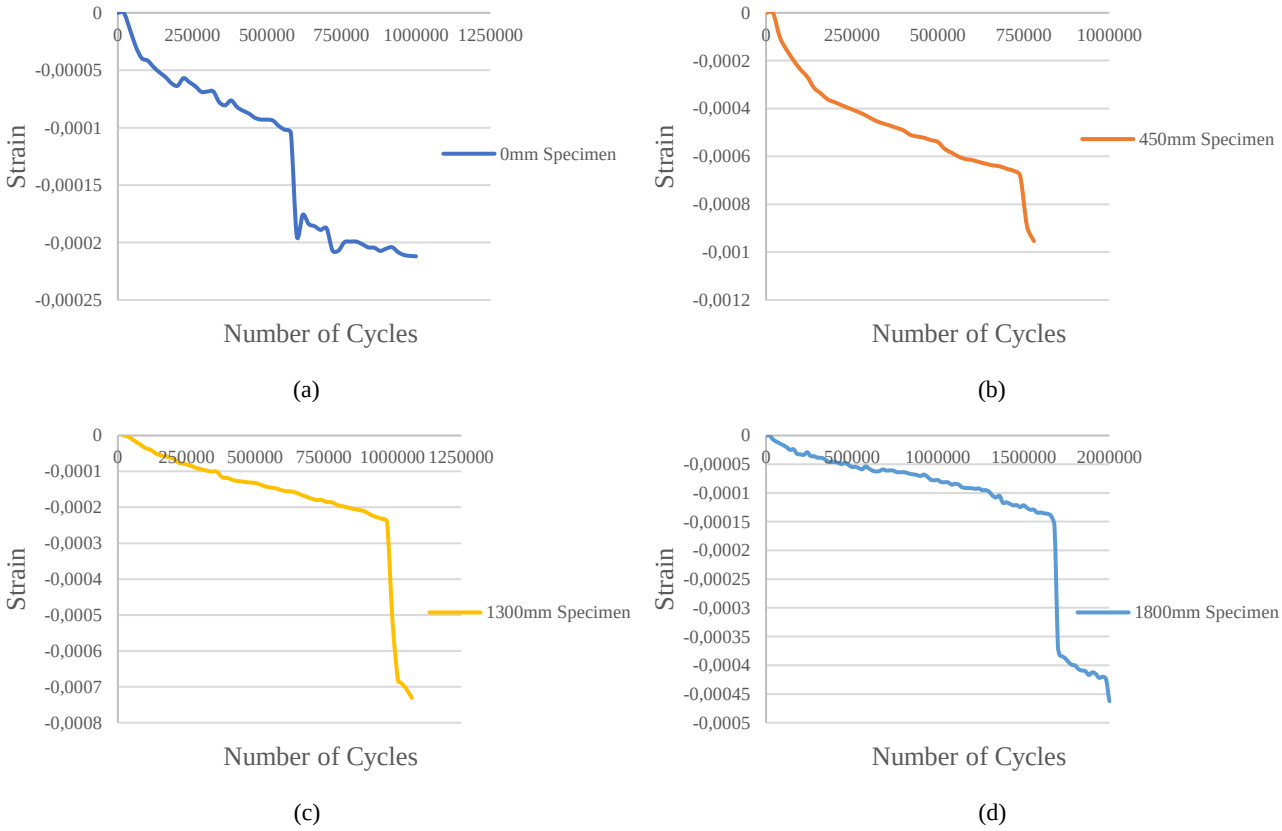

Figure 5.49 Compression concrete strain behaviour during 40% stress range test

The results further showed that as the damage extent was reduced from 1800mm to 450mm the strain at the compression concrete surface increased at a higher rate. The 1300mm specimen compression strain increased at a rate of $24.49x10^{-5}$ µstrain per cycle during the first 980 000 cycles and the 450mm specimen strain increased at a rate of $91.99x10^{-5}$ µstrain per cycle during the first 740 000 cycles. The points at which compression strain increased significantly for the 450mm and 1300mm specimens coincided with the possible rupturing of tension steel as these specimens failed shortly after these spikes in strain. The 0mm specimen compression strain increased at a rate that was in-between that of the 1800mm and the 1300mm specimens. Its compression strain increased at a rate of $17.98x10^{-5}$ µstrain per cycle during the first 580 000 cycles. The abrupt increase in compression strain at 60 000 cycles coincides with an increase midspan deflection which may be associated with a possible bond slippage which caused an internal stress redistribution, as discussed in **Section 5.3.3.1**.

Low strain in compression concrete could indicate a relative higher neutral axis position and a downward shift of the neutral axis caused by an increase in compression concrete strain indicates an increase in stiffness if the strain distribution gradient remains unchanged. With that in mind the results indicate that an increase in corrosion damage and patch repair length reduces the stiffness of a specimen,

if the specimens are subjected to low stress fatigue loading. This latter conclusion assumes a reduction in carbon fibre strain, which may not be an accurate assessment. Therefore, before drawing any conclusions regarding stiffness degradation it may be useful to consider the performance of all the composite material strains.

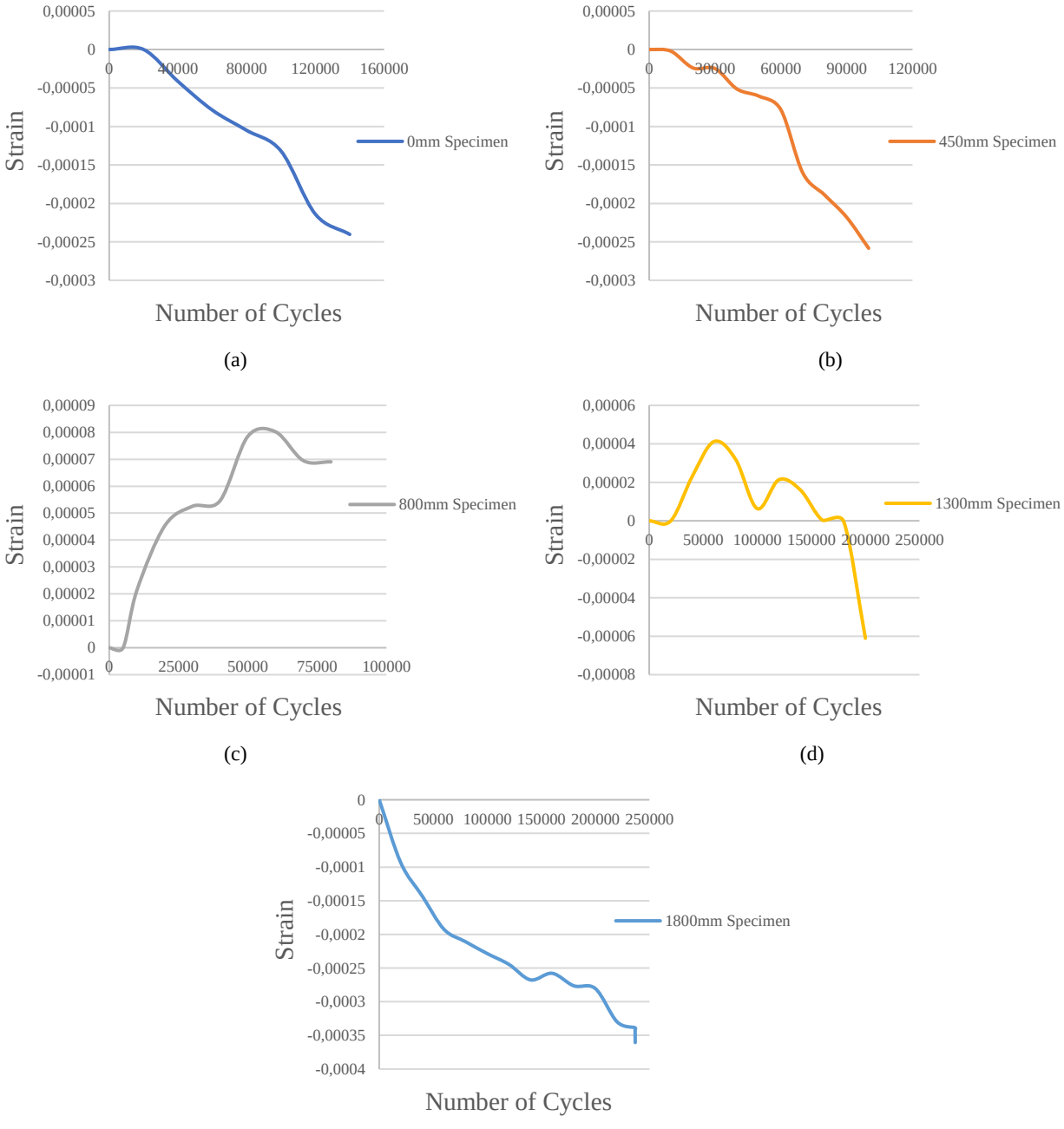

Figure 5.50 Compression concrete strain behaviour during 60% stress range test

Specimens with longer corrosion damage and patch repair extents tested under the 60% stress range regime seem to be more adversely affected that its shorter counter parts during the early stages of its fatigue life. On **Figure 5.51** it can be seen that the 1800mm specimen had the highest strain increase rate of 228.57x10^{-5} µstrain per cycle during the first 100 000 cycles. The 450mm specimen had a strain increase rate of 130.37x10^{-5} µstrain per cycle during the first 60 000 cycles, which increased significantly during the next 40 000 cycles to 450.13x10^{-5} µstrain per cycle. The 0mm specimen exhibited the lowest increase in strain during fatigue testing. During the first 20 000 cycles the

compression strain remained unchanged, after which it increased at a rate of 165.00x10^{-5} µstrain per cycle up to 100 000 cycles. The specimens with the shorter corrosion damage and patch repair extent seem to exhibit increased compression strain rates towards the end of their fatigue lives, whereas the specimens with the longer corrosion damage and patch repairs had relatively lower strain rate increases towards the end. The results from the 800mm and 1300mm specimen exhibited positive strain, which are not realistic for compression strain results and were therefore disregarded.

Tension concrete

Results from the tension concrete strain gauge measurements were dismal. For the specimens tested under the 40% stress range, three out of the four specimens where results were obtainable, yielded negative strains. Tension concrete should give positive strain measurements. The only specimen that yielded consistent positive strain results was the 1300mm specimen, however there were no other results to compare it to.

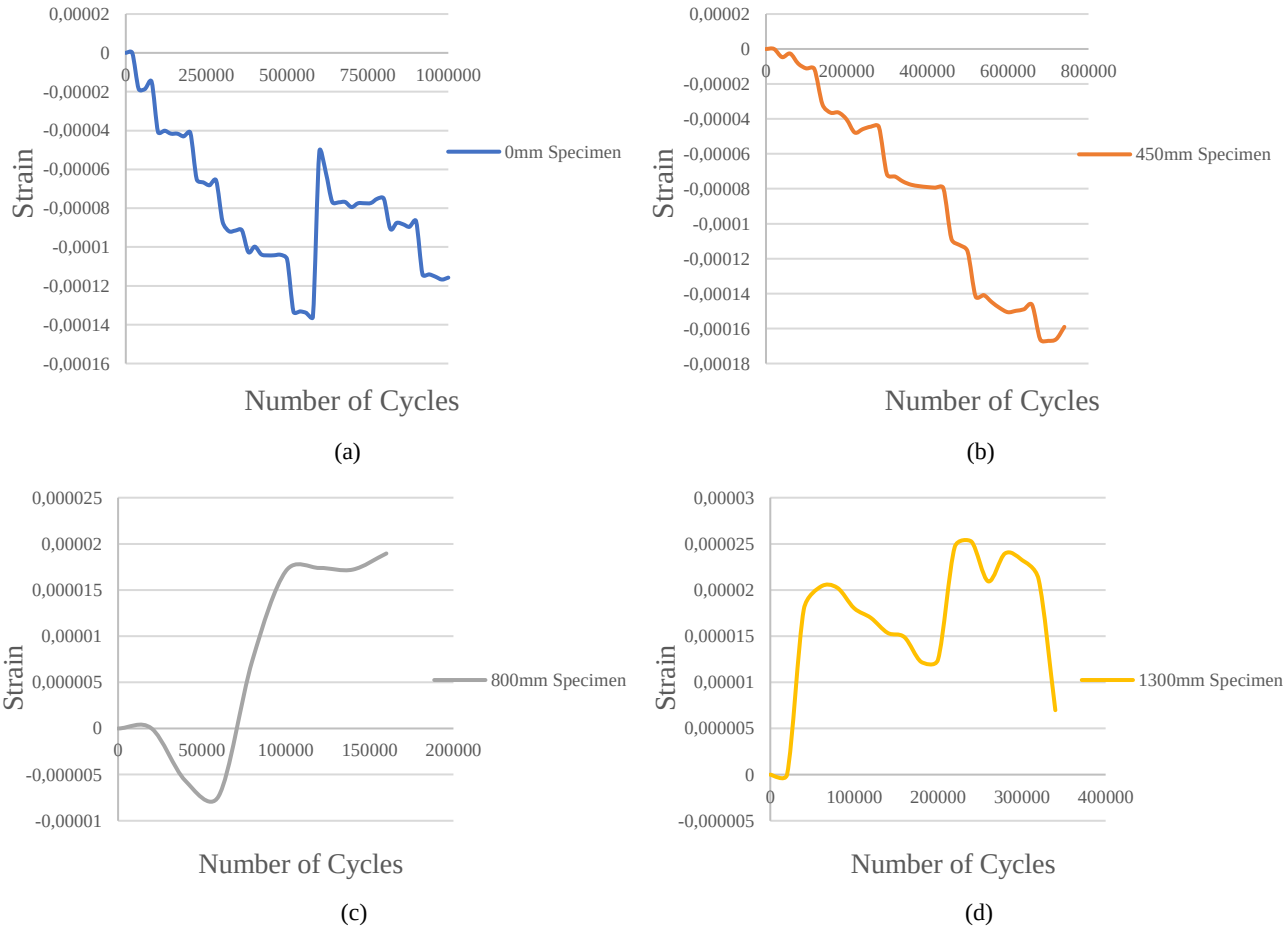

Figure 5.51 Tension concrete strain behaviour during 40% stress range test

From the 60% stress range tests two specimens yielded positive results, which were the 800mm and 1300mm specimens. The results indicate that the 800mm specimen exhibited higher strains as well as higher strain increase rates than the 1300mm specimen. The results from these two specimens seem to disagree with the results from the 60% stress range compression strains presented in **Figure 5.51**. During the initial 80 000 cycles the compression strains in the longer specimens were higher than for the specimens with the shorter damage extents. Under higher compression strains, one would expect the longer corrosion damaged specimens to have a lower tension concrete strain, which is not reflected in the tension concrete strain measurements presented in **Figure 5.53**.

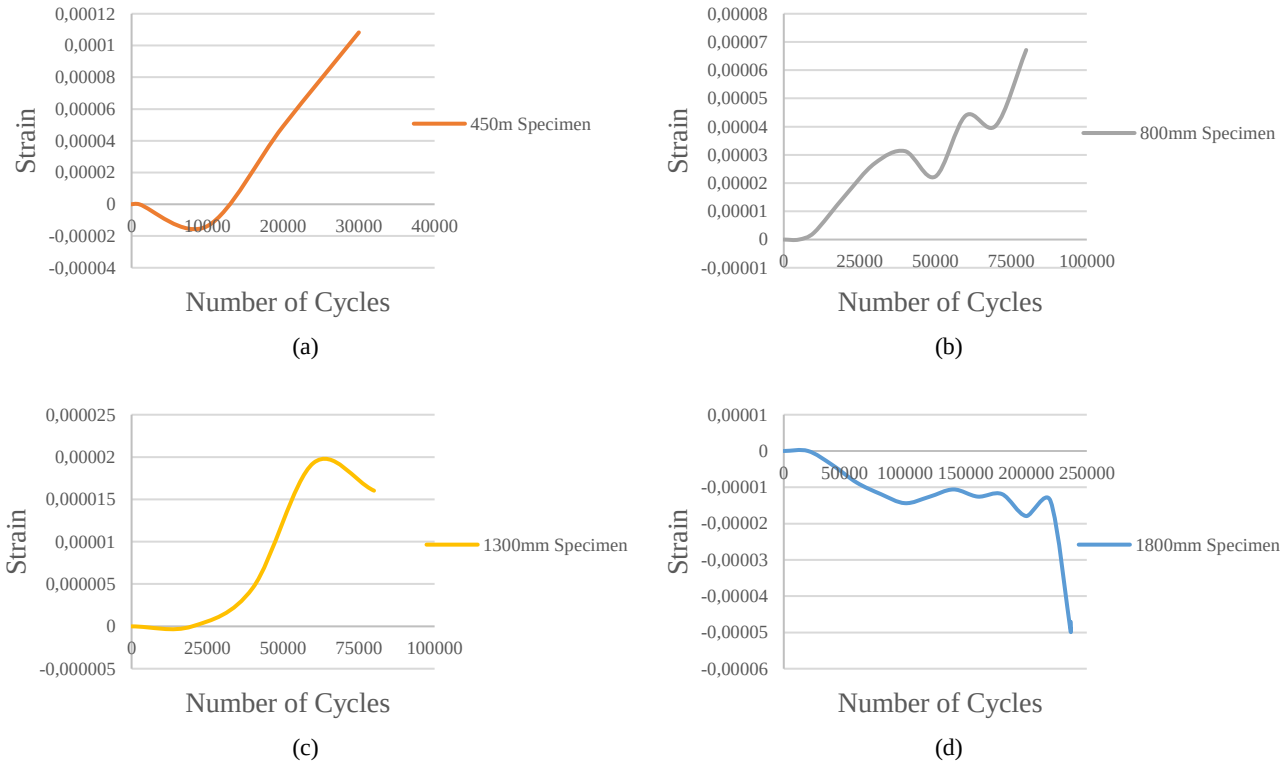

Figure 5.52 Tension concrete strain behaviour during 60% stress range test

The first load cycles under both stress ranges were characterized by a high crack growth rate as discussed in **Section 5.3.2**. The presence of cracks in the specimen tension concrete seems to have significantly affected the strain reading obtained in this area, as evidenced by the results or lack thereof in **Figures 5.52** and **5.53**.

Tension steel

The tension steel strain results were not much of an improvement from the tension concrete strain results. As shown in **Figure 5.54**, non-zero tension steel results were obtained from only three of the specimens tested under the 40% steel range regime. From the 40% tension steel strain results below, it can be seen that the 1800mm specimen is the only one that positive strain results. Both the 800mm and 1300mm specimen exhibit negative strain during the first 80 000 cycles, which seem to suggest that the tension steel is experiencing compression. This does not make sense and for that reason the results from these two specimens were disregarded. The only specimen which had positive tension strain results seems to have been damaged at 50 000 cycles when its strain increased substantially. This occurred quite early in the fatigue test of the specimen considering that this specimen was tested up to 2 000 000 cycles.

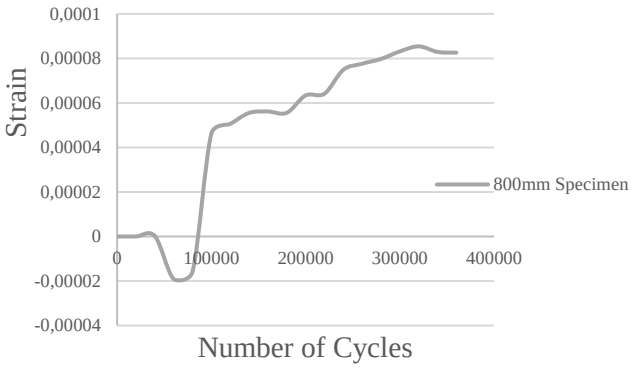

(a)

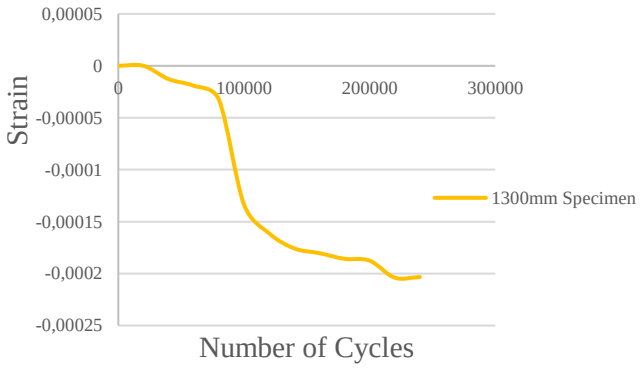

(b)

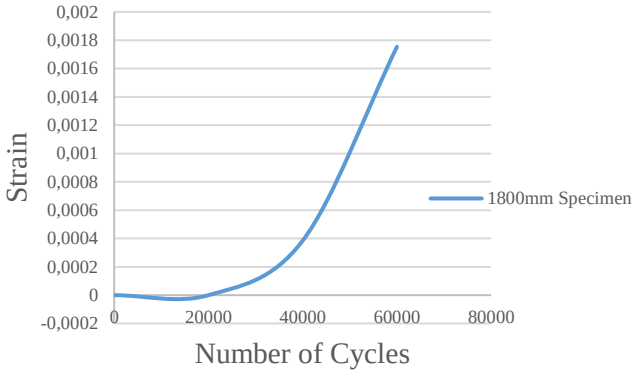

(c)

Figure 5.53 Tension steel strain behaviour during 40% stress range test

Results from the 60% stress range test specimens were slightly more fruitful. From **Figure 5.55** it is evident that only the 450mm and 1800mm specimens yielded consistent positive strain results. The 450mm corrosion damaged and patch repaired specimen experienced higher tension steel strain that the 1800mm. Unlike the tension concrete strain results, the tension steel results seem to agree with the compression concrete strain results for the 60% stress range tests shown in **Figure 5.51**. The compression concrete results showed that the shorter damage extent specimens had a lower concrete strain during the early stages of its fatigue life; as mentioned earlier if one considered the strain distribution across a RC section as shown in **Figure 3.15**, a low compression concrete strain could lead to high strain in the tension steel strain and vice versa, if the strain distribution gradient remains unchanged.

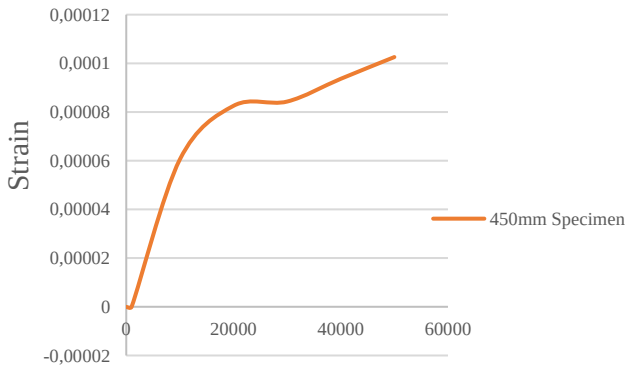

(a)

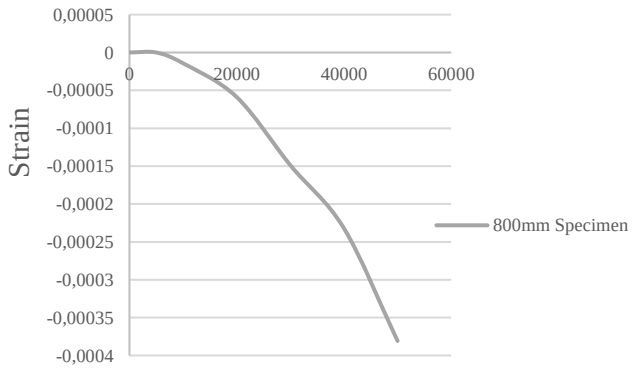

(b)

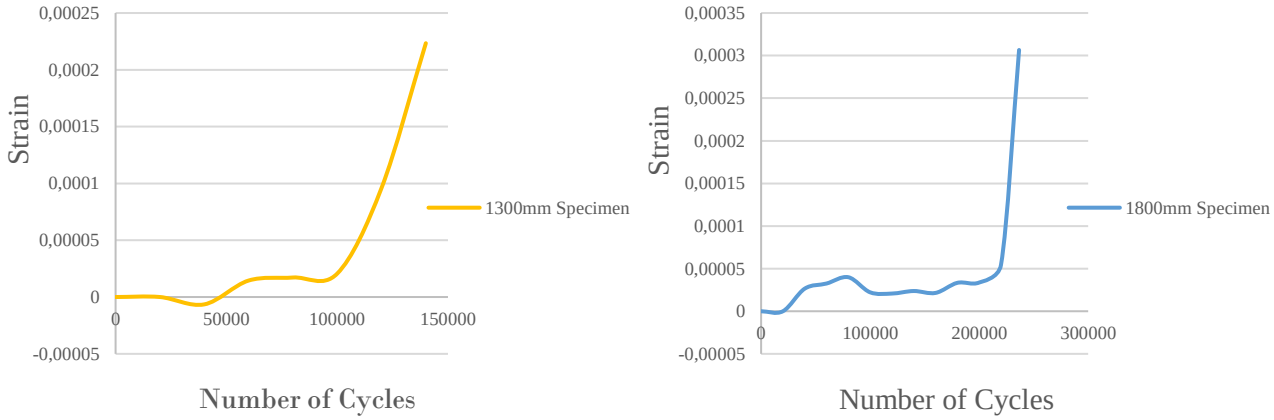

(c) (d)

Figure 5.54 Tension steel strain behaviour during 60% stress range test

Considering the combined compression concrete and tension steel strain behaviour of the specimens tested under the 60% stress range, it is evident from the results that specimens with a longer damage extent have a lower stiffness than the specimens with a shorter corrosion damage and patch repair extent. The lower stiffness was deduced from the combined assessment of the compression concrete strain and the tension steel strain.

Carbon fibre

The carbon fibre stain results of specimens tested under the 40% stress range regime are shown in **Figure 5.56**. The results show that the 1800mm damage extent specimens experienced the lowest carbon fibre strain for about 740 000 cycles, at which point the strain increase rate increased causing its strain to surpass that of the 0mm specimen at 780 000 cycles. The results for the 0mm and 1800mm specimens agree with the compression concrete strain results in **Figure 5.50** which showed that the 1800mm specimen had the lowest overall compression concrete strain which was followed by the 0mm specimen. This finding reinforced the idea that a longer damage extent specimen had a higher stiffness than an uncorroded and unpatch-repaired strengthened specimen at a low stress range.

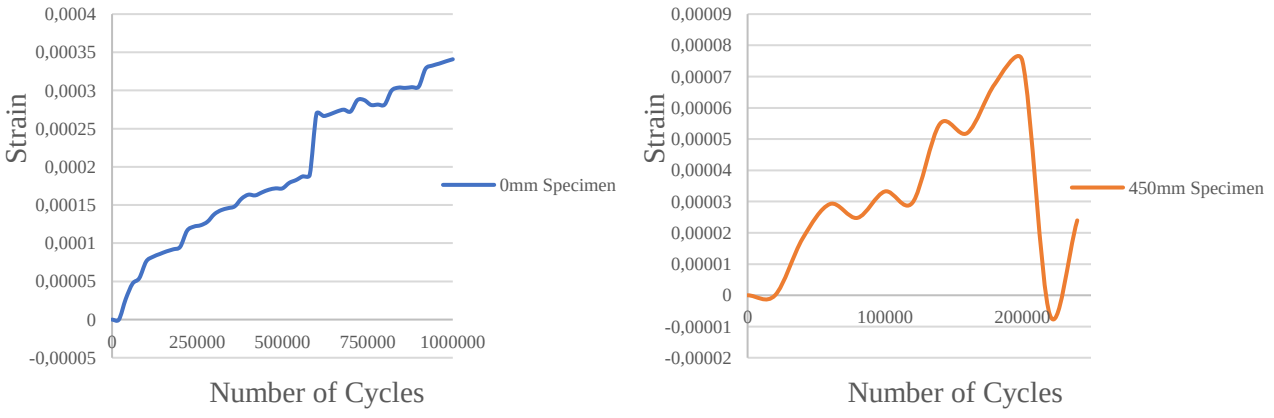

(a) (b)

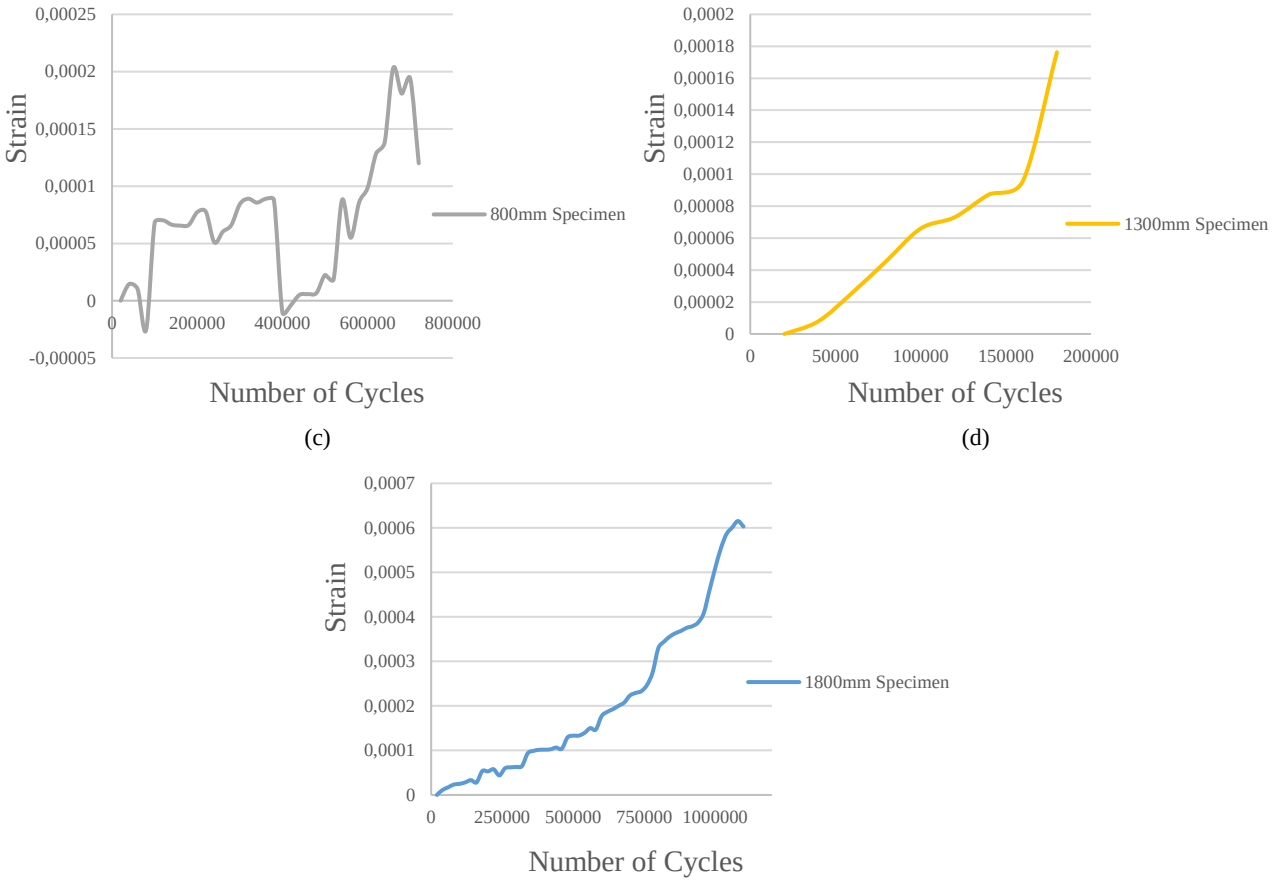

Figure 5.55 Carbon fibre strain behaviour during 40% stress range test

Another interest finding upon assessment of the 0mm specimen showed an increase in strain at 600 000 cycles. This point correlates with an increase in midspan deflection as well as an increase in compression strain at this cycle interval. Considering that this specimen did not fail due to fatigue of tension steel, the increase in carbon fibre strain seems to reiterate the possibility that bond slippage between the concrete and tension steel may have occurred, which resulted in an internal stress redistribution in the specimen. The 40% stress range results further indicated that the carbon fibre strain gauges of the 450mm and 1300mm specimens were damaged quite early in the fatigue test period, but during the period where results were obtained, the 1300mm specimen carbon fibre experience higher strain than the 450mm specimen. This once again shows higher stiffness of the specimens with a longer corrosion damage and patch repair extent. The results obtained from 800mm specimen seemed to fluctuate periodically, which provided overall inconsistent results for this specimen and for that reason its results were disregarded.

The results obtained from the 60% stress range tests during fatigue testing did not yield any comparable results. All but one of the strain gauges attached to the carbon fibre of these specimens were damaged during the first 10 000 cycles.

5.3.3.4. Neutral axis shift

Neutral axis position can be a very useful measure of stiffness. A specimen with a low neutral axis, characterized by high compression concrete strain and low strain in the tension steel, has relatively high stiffness and will therefore experience less midspan deflection. An upward migration of the neutral axis under the same applied load is likely to cause an increase tension steel, which may eventually cause the ultimate failure of the section.

The results shown in **Figures 5.57** and summarized on **Table 5.9** were obtained by taking relative strain measurements of Demec targets positioned along test specimen surfaces at midspan. **Figure 5.57** shows neutral axis movement of the 0mm specimen between 100 000 and 1 000 000 cycles under the 40% stress range. This figure shows that the neutral axis migrated upwards during fatigue testing from x_1 to x_2, signalling a reduction in stiffness of the specimen.

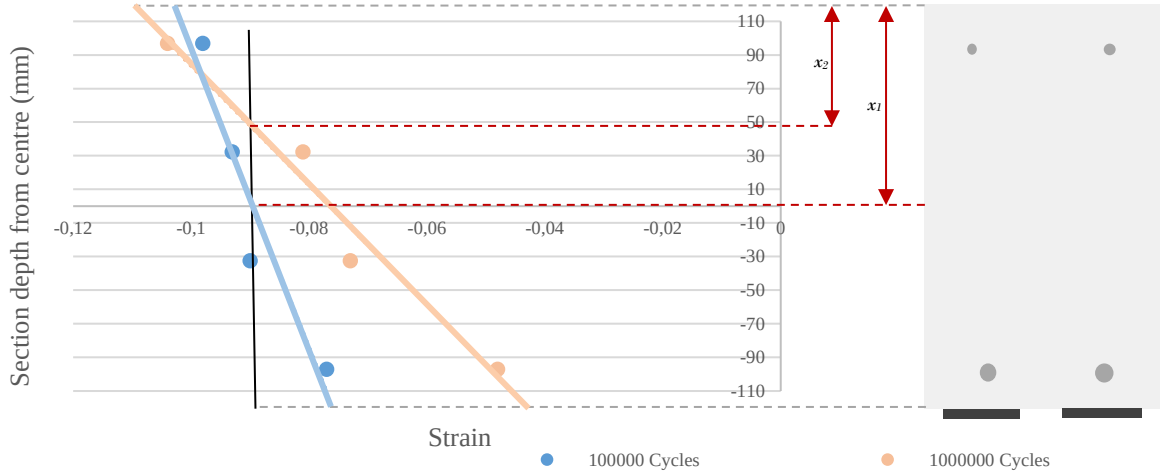

Figure 5.56 Neutral axis shift of 0mm specimen during 40% stress range test

An assessment of all the specimens such as the one shown in **Figure 5.57** was done in order to derive a comparative analysis of the specimens tested under the 40% and the 60% stress ranges. It was decided to compare the neutral axis migration of all the specimens during the first 100 000 cycles. A 100 000 cycle interval was selected, as it was considered to be a reasonable indication of the fatigue life of specimens tested under the 60% stress range. The neutral axis migration of the specimens tested under the 40% and 60% stress ranges during the first 100 000 cycles are presented in **Table 5.9**.

Table 5.9 Neutral axis shift results during fatigue testing

Identity	Neutral Axis Shift after 100 000 cycles (mm)	Neutral Axis Shift after 1 000 000 cycles (mm)	Overall Fatigue Life Neutral Axis Shift
S_CNTRL 2	-85	12	*Upward shift*
S_CNTRL 3	12	*	*Upward shift*
S_450mm 2	12	-10	*Downward shift*
S_450mm 3	-84	*	*Downward shift*
S_800mm 2	120	-35	*Downward shift*
S_800mm 3	22	*	*Upward shift*
S_1300mm 2	8	-6	*Downward shift*
S_1300mm 3	-59	*	*Downward shift*
S_1800mm 2	-1	-125	*Downward shift*
S_1800mm 3	-72	*	*Downward shift*

*fatigue life of 60% stress range specimens did not exceed 256000 cycles

Some interesting results immerged from the comparative analysis of the specimens tested under the two stress ranges during the first 100 000 cycles. Results show that under the 40% stress range the damaged specimens experienced a reduction in the stiffness characterized by an upward shift of their neutral axes, whereas the 0mm damage extent specimens experienced a downward shift of their neutral axis. The results showed that as the damage length was reduced from 1800mm to 450mm there was a relative upward shift of the neutral axis of 12mm showing that the 1800mm damage extent specimen had a relatively higher stiffness. The 800mm specimen seemed to experience the highest reduction in stiffness

during the initial 100 000 cycles, characterized by a total upward shift of 120mm. Results from the 60% stress range regime revealed a contrasting trend to that seen in the 40% stress range tests. Most of the corrosion damaged specimens, except for the 800mm specimen, experienced an increase in stiffness as their neutral axes migrated downwards. The 0mm and 800mm specimens experienced an upward shift of the neutral of 12mm and 22mm, respectively. The results did not reveal a clear correlation between an increase in damage extent and the migration of the neutral axis under the 60% stress range regime.

Results from the 60% stress range specimens during a 100 000 cycle period could be considered as a reasonable reflection of the behaviour of the neutral axis during the specimen's fatigue lives. The specimens tested under the 40% stress range 100 000 cycles is very near the start of their fatigue lives as most of them were tested beyond 1 000 000 cycles and the 1800mm specimen was even subjected to 2 000 000 cycles. With that in mind it was decided to further consider the neutral axis behaviour of the 40% stress range specimens up to 1 000 000 cycles as that would be a better reflection of the behaviour of their neutral axes during their fatigue lives. During 1 000 000 cycles the 40% stress range specimen results seemed to show a similar downward shift of the specimen neutral axes as previously found in the 60% stress range specimens. As presented in **Table 5.9,** as the damage extent was increased from 450mm to 1800mm the neutral axis shifts further down from -10mm to -125mm. The 1300mm specimen neutral axis was found to shift the least in downward direction with a total shift of only -6mm during the 1 000 000 cycles period. Once again, as with the 60% stress range tests, the 0mm specimen was found to experience an upward shirt of the neutral axis or stiffening of the specimen during a cyclic loading period of 1 000 000 cycles. Combining the overall results from the 40% it can be seen the corrosion damaged and patch repaired specimens experience an initial reduction in stiffness during the first 100 000 cycles, but an overall increase in stiffness during 1 000 000 cycles. The uncorroded specimen on the other hand seems to experience an initial increase in stiffness during the first 100 000 cycles, but an overall reduction in stiffness.

The neutral axis migration results discussed in this section seem to contradict the stiffness degradation trends suggested by the other performance parameters. The effect of the damage extent was not as distinguishable either. The reliability of the neutral axis migration results is questionable, especially considering the findings from **Section 5.3.2,** where the crack behaviour of the specimens was discussed. It was found that under the 40% stress range the average crack depth ranged between 60mm and 80mm, whereas under the 60% stress range the average crack depth was slightly lower between 40mm and 60mm. In both case there was a large portion of cracks that propagated beyond the average crack depth. Dladla (2014) suggested that crack propagation below the neutral axis influenced the strain readings obtained from the Demec targets in this region. With that in mind it is likely that the strain readings obtained from the bottom half of the section were affected by crack propagation below the neutral axis, thus bringing the reliability of these results into question.

5.4 Chapter summary

This chapter presented the experimental findings of a research study that investigated the effect of increased corrosion damage and patch repair extent on the fatigue behaviour of CFRP strengthened specimens tested under two stress ranges.

Results were first presented for the accelerated corrosion process, where it considered how the actual corrosion differed from the intended degree of corrosion. The corrosion results also considered how the damage length affected the type of corrosion that was ultimately found. It was reported that the prevailing type of corrosion was pitting corrosion and that the specimens with the shorter damage length experienced nearly double percentage mass loss (9.87%) of specimens with the longer damage lengths (5.68%). Despite the specimens with the shorter damage length almost yielding the desired corrosion

mass loss of 10%, it was found that corrosion on all the specimens was concentrated on the steel surface closest to the tension concrete surface, an ideal location for fatigue crack formation.

The chapter then discussed specimen performance in terms of the various performance indicators that included ultimate failure load, fatigue life, crack development, failure mode and stiffness degradation. The variability in performance was considered on the backdrop of increased corrosion damage and patch repair extent. Results from the static load tests showed that as the corrosion damage and patch repair length was increased from 450mm to 1800mm, the ultimate failure load reduced correspondingly, but that even the specimen with the longest damage extent was able to outperform the uncorroded strengthened specimen. In contrast, the fatigue life results showed opposing trends, where the specimens with the longer damage lengths yielded longer fatigue lives than the ones with the shorter damage extents. This trend in was verified using fatigue life prediction models that were appropriate for CFRP strengthened RC beams. In addition, fatigue failure dependence on crack initiation and stress range was emphasised, noting that 60% of the fatigue tested specimens did not fail due to fatigue under the low stress range tests, whereas the all the specimens tested under the high stress range had succumbed to fatigue failure. Moreover, it was noted that the specimens with the longer corrosion damage and patch repair extents yielded a post-fatigue life in the order of 75% lower than the specimens with the shorter damage extents.

Crack development was discussed in terms of crack density, which were specifically guided by crack spacing, crack height and crack locality. The crack locality and density were found to be closely related to the location of the eventual failure. To that end the discussion on failure mode was paralleled with that of crack development. The results indicated a reduction in crack spacing and crack height as the corrosion damage and patch repair extent was reduced from 0mm to 1800mm under the 60% stress range, indicating an increase in stiffness for the specimens with a longer damage extent, due to a lower neutral axis position. Under the 40% stress ranges tests, it was found that the longer test periods caused an increase in crack heights. Furthermore, the use of DIC was considered in the context of SHM, with specific emphasis on its ability to accurately detect crack patterns and to identify possible failure locations early in the fatigue life of a specimen. The experimental results yielded promising predictions of the failure locality early on in the fatigue tests.

Stiffness degradation was considered quite extensively in terms of three sub-parameters, which included midspan deflection, composite material strains and neutral axis migration. Midspan deflection and the composite material strains were considered in terms of not only their sensitivity to increased corrosion damage and patch repair extent, but also on the possibility of identifying critical structural damage mechanisms such as bond slippage, internal stress redistribution and or steel rupture. In terms of midspan deflection and composite material strains it was found that as the corrosion damage and patch repair extent was increased, a corresponding stiffness increase was experience by the specimens. Furthermore, the DIC deflection results were compared to the midspan deflection results obtained from LVDTs to determine whether these two methods can be used interchangeably. It was however found that although DIC results yielded highly accurate results for the short-term static tests, laboratory constraints deemed it unsuitable for long-term testing as inconsistencies in DIC results were prominent when compared to LVDT results.

6. CONCLUSIONS AND RECOMMENDATIONS

This study aimed to assess the influence of increasing corrosion damage and patch repair extent on the fatigue behaviour of RC beams that have been over-strengthened with CFRP laminates. The investigation further considered the potential of DIC as a non-contact SHM tool. The experimental results compared CFRP strengthened RC beam specimens were neither corroded nor patch repaired with specimens that were corroded and patch repaired to various damage lengths varying between 450mm, 800mm, 1300mm and 1800mm. The following sections present the main conclusions drawn from the findings discussed in **Chapter 5**. This chapter will conclude with some suggestions that may improve the outcome of this research topic and future related work.

6.1 Accelerated corrosion

The findings from the accelerated corrosion process showed that the specimens with a longer damage length experienced a lower degree of corrosion compared to the specimens with a shorter damage length. The 450mm specimens nearly achieved the desired 10% corrosion damage, as they reached 9.87% corrosion damage, but the degree of corrosion damage reduced considerably as the damage extent was increased to 1800mm where the measured degree of corrosion damage was only 5.68%. It was further found that the ultimate failure load increased as the corrosion damage increased. Although the 450mm specimen experienced the highest degree of corrosion it could still resist its maximum load capacity, because this damage was localized within the region of the maximum moment. When the damage extent was extended beyond the region of maximum moment, the maximum capacity becomes a function of the actual degree of corrosion.As expected, all the specimens experienced pitting corrosion commonly associated with chloride induced corrosion. Furthermore, the corrosion damage was concentrated to the portion of the reinforcement cross-section that was closest to the tension concrete surface.

6.2 Fatigue life

Fatigue testing of the specimens was conducted at stress ranges proportional to their static failure loads. It was found that the ultimate failure loads reduced as the damage extent of the specimen increased from 450mm to 1800mm, where the 450mm specimen failed at 325kN and the 1800mm specimen failed at 290kN. The 0mm specimen had the lowest static failure load despite it not being corrosion damaged nor patch repaired. In contrast, the fatigue lives of the specimens showed an inverse relationship to their static failure loads, where the 0mm specimen had the highest fatigue life. The results showed that as the damage extent was increased from 450mm to 1800mm the fatigue life increased by 106.3% under the 60% stress range tests. Under the 40% stress range the fatigue life increased considerably as well, though the exact increase could not be determined, because the 1800mm specimen test was terminated at 2 000 000 cycles after not failing due to fatigue. Three out of five fatigue specimens tested under the 40% stress range were terminated after not failing due to fatigue, but the two specimens that did fail showed that the specimen with a longer damage extent achieved a longer fatigue life. Furthermore, the experimentally obtained fatigue lives were compared to three fatigue life prediction models suitable for CFRP strengthened RC beams and although all three models yielded fatigue life predictions similar to the experimental results, the fatigue life cycles predicted by the Helgason and Hanson model (Zorn, 2006) yielded the closest correlation with the experimental results. Moreover, it was noted that the specimens with the longer corrosion damage and patch repair extents yielded a post-fatigue life in the order of 75% lower than the specimens with the shorter damage extents.

6.3 Crack development and failure mode

The specimens subjected to fatigue behaviour exhibited similar crack development and failure modes, where a crack pattern with predominantly flexural cracks as well as shear and flexural-shear cracks was

clearly defined during the first load cycle. This crack pattern remained relatively unchanged after first cycle, but the crack heights and densities propagated gradually during fatigue testing. Rupture of tensile steel caused a second rapid increase in crack propagation rate. After steel rupture, CFRP laminates started to debond at the position of the main cracks, which was followed by compression concrete crushing leading to ultimate failure of the section. Cracks that formed after steel rupture tended to propagate in the vicinity of the ruptured steel bar. Under the high stress range the results showed that as the damage extent was increased the average crack spacing as well as the average crack height reduced, essentially resulting in more cracks with a lower crack height. This was found to contribute to a lower neutral axis as the damage extent was increase and ultimately a stiffer section. However, under the lower stress ranges tests the crack density on the specimens increased noticeably with an increase in damage extent. In terms of the average crack spacing there was once again a reduction as the damage extent was increase, but overall the height of those cracks increased as the damage extent increased. These results from the lower stress range tests seemed to validate a hypothesis that the crack density increases with a longer fatigue life.

6.4 Stiffness degradation

Midspan deflection measurements of the 40% stress range tests showed the specimens with the longer corrosion damage and patch repair extent had a higher stiffness as they experienced the least midspan deflection increase during fatigue testing. The stiffness reduced as the damage extent was reduced, with the 800mm specimen showing the lowest stiffness. During the 60% stress range tests there was a similar trend that showed how the specimen stiffness increased as the damage extent was increase. Assessment of the accelerated corrosion results as well as the crack behaviour may provide some insight regarding this trend. The corrosion results showed that the longer damage extent experienced a lower degree of corrosion damage compared to the shorter specimens. The crack behaviour showed, especially for the 60% stress range tests, that as the damage length was increased the average crack spacing as well as the average crack heights reduced, possibly contributing to a higher specimen neutral axis and therefore a stiffer section.

The most conclusive composite material strain results were obtained from the compression strain and carbon fibre strain gauges. It is likely that crack propagation of tension concrete obstructed the strain measurements obtained in that region. Tension steel strain gauges were either damaged due to water penetration during concrete casting or very early in fatigue testing. Compression strain results concurred with the midspan deflection results, especially those obtained from the 40% stress range tests. It was found that the overall compression strain as well as the compression strain increase rate was lower for the 1800mm specimen and gradually increased as the damage length was reduced. Under the 60% stress range tests the longer damage extent specimens had an initial high compression strain increase rate, but gradually lowered allowing the compression strain of the specimens with the shorter damage extent to surpass it. The carbon fibre strain also agreed with the results from midspan deflection and compression concrete strain, showing that the specimens with the longer damage extent experience a higher strain in the carbon fibre than the specimens with the shorter damage extent. All the strain measurements obtained from the composite materials suggested that the specimens with the longer damage extent had a higher stiffness. Furthermore, from the strain and midspan deflection measurement results it was possible to identify certain structural changes that arose from possible steel rupturing or concrete-steel bond slippage that caused internal stress redistribution.

Neutral axis results obtained from the Demec targets showed an overall downward shift of the neutral axis during fatigue testing. It was not possible to gauge the effect that an increase in damage extent has on the neutral axis migration. The results from the 40% stress range tests showed that there was an initial reduction of stiffness for the corrosion damaged specimens during the first 100000 cycles,

after which a general downward shift of the neutral axis prevailed, indicating an increase in stiffness. However, this initial upward shift of the neutral axis or stiffening was not verifiable with the other performance parameters. The possible cause for not being able to assess the effect of the damage extent was attributed to the effect that extensive crack propagation in the tension concrete had on the strain measurements obtained in that area.

6.5 Digital image correlation

DIC results were evaluated for a two-dimensional surface where deflection in the y-direction and tangential strain in the x-direction were considered. The results showed that DIC was able to capture crack patterns through tangential strain contour plots. This enabled the possibility of predicting crack locations even before they form, by identifying areas of strain concentration and monitoring concrete strain approaches its tensile strength. The DIC deflection results correlated well with those obtained from the LVDTs during the first load cycle, but not so much with the long-term test results. Moreover, through the DIC process it was possible to identify the points of maximum deflection, which was shown to often coincide with the eventual failure location of the specimen. In the absence of DIC this position may not have been as accurately identifiable.

Two main drawbacks of the DIC process in this experiment were related to test surface size and movement of the camera. The camera lens used in this experiment focussed on the centre of the specimen slightly blurring out the rest of the specimen, therefore the results, especially in terms of tangential strain, were not as accurate towards the outer edges of the specimen. The second drawback was related to laboratory setup, which required the camera to be moved for storage purposes. Every time the camera was moved required the test surface to be re-calibrated and introduced error in the results. Error accumulation was evident in the long-term DIC deflection and tangential strain results.

6.6 Recommendations

Based on the findings discussed in the previous chapter as well as the conclusions drawn from them, the following recommendation are made:

- At least 3 samples should be tested for each damage extent under each stress range to verify and validate the trends obtained from the results of this experiment. With only one sample for each damage extent is was not possible assess variability and accuracy of the results.
- The use of ultimate failure load of each specimen to gauge its low and medium stress range made it difficult to ascertain whether the trends that were identified were as a result of the varied damage extent or due to the changing stress ranges. With that in mind it may be considered to apply the same test loads to all the fatigue tested specimens for a given stress range.
- Allowance must be made for a longer test period for the specimens tested under low stress fatigue, to allow the specimens to be tested to completion as opposed to terminating tests after a certain number of cycles due to time constraints.
- DIC should be carried out in a control room that does not require the camera setup to be disturbed in any way, to avoid errors introduced when moving the camera and having to re-calibrate the test surface.
- The DIC test surface could be reduced to half the 2m specimen and to introduce a second camera. A smaller test surface would increase the focus on each area and reduce the fisheye effect towards the edges of the specimen
- To improve the strain measurements obtained for the composite materials, fibre optic wires may be placed along the length of the tension steel. Fibre optic systems make use of light instead of electricity, which makes it better suited in wet environments such as freshly poured concrete. The fibre optic wires are further able to obtain information along the entire length of the reinforcing bar as opposed to at one or more predetermined locations.

- A FEM study could also be carried out to compare the results obtained from this experimental study. A FEM study affords the opportunity to consider various degrees of corrosion, CFRP strengthening as well as different stress range tests that were not considered during the experimental study.

7. REFERENCES

Abdelrahman, K., & El-Hacha, R. (2014). Cost and ductility effectiveness of concrete columns strengthened with CFRP and SFRP Sheets. *Polymers*, *6*(5), 1381–1402. https://doi.org/10.3390/polym6051381

Ahsan, R. (2014). Fatigue in Concrete Structures. In *BSRM Seminar on Fatigue Properties of Constructional Steel*. Bangladesh. Retrieved from http://scholar.google.com/scholar?hl=en&btnG=Search&q=intitle:Fatigue+in+Concrete+Structures#0%5Cnhttp://scholar.google.com/scholar?hl=en&btnG=Search&q=intitle:Fatigue+in+concrete+structures#0

Aidoo, J., Harries, K. A., & Petrou, M. F. (2004). Fatigue Behavior of Carbon Fiber Reinforced Polymer- Strengthened Reinforced Concrete Bridge Girders, *8*(December), 501–509. https://doi.org/10.1061/(ASCE)1090-0268(2004)8

Al-Negheimish, A. I., & Alhozaimy, A. M. (2008). Impact of extremely hot weather and mixing method on changes in properties of ready mixed concrete during delivery. *ACI Materials Journal*, *105*(5), 438–444.

Alexander, M., & Beushausen, H. (2019). Cement and Concrete Research Durability , service life prediction , and modelling for reinforced concrete structures – review and critique. *Cement and Concrete Research*, *122*(February), 17–29. https://doi.org/10.1016/j.cemconres.2019.04.018

Alhozaimy, A., Hussain, R. R., Al-Negheimish, A., Al-Zaid, R., & Singh, D. D. N. (2014). Effect of simulated concrete pore solution chemistry, chloride ions, and temperature on passive layer formed on steel reinforcement. *ACI Materials Journal*, *111*(4), 411–421. https://doi.org/10.14359/51686829

Almusalla, A., Al-Gahtani, A., Aziz, A. R., & Rasheeduzzafar. (1996). Effect of reinforcement corrosion on bond strength. *Construction and Building Materials*, *10*(2), 123–129.

Amesu, Y. (2016). *Identification of fatigue prone areas of the pre-stressed box-girder railway bridge support section in the transverse direction using finite element models*. University of Cape Town.

Amirshayan, S., Youngsoo, S., & Kim, R. (2017). Fatigue and fracture characterization of fiberglass grid- reinforced beam specimens using four-point bending notched beam fatigue test and digital image correlation technique. *Materials and Structures*, *50*(2), 1–13. https://doi.org/10.1617/s11527-016-0980-8

Aravind, N., Samanta, A. K., Singha Roy, D. K., & Thanikal, J. V. (2013). Retrofitting of reinforced concrete beams using fibre reinforced polymer (FRP) composites - A review. *Journal of Urban and Environmental Engineering*, *7*(1), 164–175. https://doi.org/10.4090/juee.2013.v7n1.164175

Arito, P. (2012). *Discrete Sacrificial External Anodes and Their Use in Service Life Extension of Chloride Contaminated Reinforced Concrete Structures*. University of Cape Town.

Ballim, Y., Alexander, M., & Beushausen, H. (2009a). Durability of concrete. In *Fulton's Concrete Technology* (9th ed., pp. 201–236). Midrand: Cement & Concrete Institute.

Ballim, Y., Alexander, M. G., & Beushausen, H. (2009b). Durability of Concrete. In *Fulton's Concrete Technology* (9th ed., pp. 201–236). Cement and Concrete Institue.

Beushausen, H., & Alexander, M. G. (2006). Failure mechanisms and tensile relaxation of bonded concrete overlays subjected to differential shrinkage. *Cement and Concrete Research*, *36*(10), 1908–1914. https://doi.org/10.1016/j.cemconres.2006.05.027

Beushausen, H., & Chilwesa, M. (2013). Assessment and prediction of drying shrinkage cracking in bonded mortar overlays. *Cement and Concrete Research*, *53*, 256–266. https://doi.org/10.1016/j.cemconres.2013.07.008

Beushausen, H., Otieno, M., & Alexander, M. G. (2019). Durability of concrete. In *Fulton's Concrete Technology* (10th ed.). Midrand: The Concrete Institute.

Beushausen, Hans. (2015). A parameter study on the age at cracking of bonded concrete overlays subjected to restrained shrinkage. *Materials and Structures*, *49*(5), 1905–1916. https://doi.org/10.1617/s11527-015-0622-6

Busatta, F., & Moyo, P. (2017). How testing and monitoring can support heavy haul railway bridge management: the experience gained in South Africa. In R. D. Fröhling & P. J. Gräbe (Eds.), *11th International Heavy Haul Association Conference 2017*. Cape Town.

Ceroni, F. (2010). Experimental performances of RC beams strengthened with FRP materials. *Construction and Building Materials*, *24*(9), 1547–1559. https://doi.org/10.1016/j.conbuildmat.2010.03.008

Charalambidi, B. G., Rousakis, T. C., & Karabinis, A. I. (2016). Analysis of the fatigue behavior of reinforced concrete beams strengthened in flexure with fiber reinforced polymer laminates. *Composites Part B: Engineering*, *96*, 69–78. https://doi.org/10.1016/j.compositesb.2016.04.014

Chen, F., & Qiao, P. (2009). Debonding analysis of FRP-concrete interface between two balanced adjacent flexural cracks in plated beams. *International Journal of Solids and Structures*, *46*(13), 2618–2628. https://doi.org/10.1016/j.ijsolstr.2009.02.007

Chopra, A. (2012). *Dynamics of Structures* (4th ed.). Prentice Hall.

Courard, L., Piotrowski, T., & Garbacz, A. (2014). Cement & Concrete Composites Near-to-surface properties affecting bond strength in concrete repair. *Cement & Concrete Composites*, *46*, 73–80. https://doi.org/10.1016/j.cemconcomp.2013.11.005

Dladla, T. (2014). *The behaviour of patch repaired and frp strengtheed RC beams*. University of Cape Town.

Dong, J. F., Wang, Q. Y., & Guan, Z. W. (2012). Structural behaviour of RC beams externally strengthened with FRP sheets under fatigue and monotonic loading. *Engineering Structures*, *41*, 24–33. https://doi.org/10.1016/j.engstruct.2012.03.024

El Refai, A. M. (2007). *Monotonic and fatigue flexural performance of RC beams strengthened with externally post-tensioned CFRP tendons*. University of Waterloo.

Eldho, C. A., & Jones, S. (2016). Performance of Concrete Patch Repairs : From a Durability Point of View. *5th International Conference on Durability of Concrete Structures, Jun. 30 - Jul. 1, 2016*, 66–72.

Elghazy, M., El, A., Ebead, U., & Nanni, A. (2018). Experimental results and modelling of corrosion-damaged concrete beams strengthened with externally-bonded composites. *Engineering Structures*, *172*(January), 172–186. https://doi.org/10.1016/j.engstruct.2018.06.037

Fatemi, A., & Yang, L. (1998). Cumulative fatigue damage and life prediction theories : a survey of the state of the art for homogeneous materials. *Elsevier Science Ltd*, *20*(I), 9–34.

Ferrier, E., Bigaud, D., Clément, J. C., & Hamelin, P. (2011). Fatigue-loading effect on RC beams strengthened with externally bonded FRP. *Construction and Building Materials*, *25*(2), 539–546. https://doi.org/10.1016/j.conbuildmat.2010.07.035

fib. (2001). *Externally bonded FRP reinforcement for RC structures*. *fib*. Ernst & Sohn

fib. (2013). *fib Model Code for Concrete Structures 2010*. *fib*. Ernst & Sohn.

Grant, P., & Rousseau, C. Q. (2008). *Composite Structures : Theory and Practice*. (P. Grant & C. Rousseau, Eds.). American Society for Testing and Materials.

Gregan, S. (2012). *The fatigue performance assessment of corrosion damaged RC beams, patch repaired and externally strengthened using CFRP*. University of Cape Town.

Gylltoft, K. (1984). A fracture mechanics model for fatigue in concrete. *Materials and Construction*, *17*(1), 55–58.

Habimana, P. (2017). *Behaviour of FRP Strengthened RC Beams with Patch Repairs Subjected to Impact Loading*. University of Cape Town.

Haque, M. N., & Al-Khaiat, H. (1997). Carbonation of concrete structures in hot dry coastal regions. *Cement and Concrete Composites*, *19*(2), 123–129. https://doi.org/10.1016/S0958-9465(96)00047-9

Hassan, K. E., Brooks, J. J., & Al-alawi, L. (2001). Compatibility of repair mortars with concrete in a hot-dry environment. *Cement & Concrete Composites*, *23*(2001), 93–101.

Hoeppner, D. W. (1979). Model for prediction of fatigue lives based upon a pitting corrosion fatigue process. *Fatigue Mechanisms.(A 81-10726 01-26) Philadelphia, Pa., American Society for Testing and Materials, 1979, 1979*, 841–863.

Holmberg, J. B. (2010). *Properties of Hardened Concrete Technical Reference Guide*.

Igarashi, S., Kawamura, M., & Watanabe, A. (2004). Analysis of cement pastes and mortars by a combination of backscatter-based SEM image analysis and calculations based on the Powers model. *Cement and Concrete Composites*, *26*(8), 977–985. https://doi.org/10.1016/j.cemconcomp.2004.02.031

Karaiskos, G., Tsangouri, E., Aggelis, D. G., Tittelboom, K. Van, Belie, N. De, & Hemelrijck, D. Van. (2016). Performance monitoring of large-scale autonomously healed concrete beams under four-point bending through multiple non- destructive testing methods. *Smart Materials and Structures*, *25*.

Kim, K., Park, S., Kim, W. S., Jeong, Y., & Lee, J. (2017). Evaluation of shear strength of RC beams with multiple interfaces formed before initial setting using 3D printing technology. *Materials*, *10*(12). https://doi.org/10.3390/ma10121349

Kim, M., Pokhrel, A., Jung, D., Kim, S., & Park, C. (2017). The Strengthening Effect of CFRP for Reinforced Concrete Beam. *Procedia Engineering*, *210*, 141–147. https://doi.org/10.1016/j.proeng.2017.11.059

Kong, F. K., & Evans, R. H. (1987). *Reinforced and Prestressed Concrete* (3rd ed.). London and Hong Kong: Chapman & Hall.

Kumar, R., Gardoni, P., & Sanchez-Silva, M. (2009). Effect of cumulative seismic damage and corrosion on the life-cycle cost of reinforced concrete bridges. *Earthquake Engineering and Structural Dynamics*, *38*(7), 887–905. https://doi.org/10.1002/eqe.873

Lee, H. S., Kage, T., Noguchi, T., & Tomosawa, F. (1999). The evaluation of flexural strength of RC beams damaged by rebar corrosion. *Durability of Building Materials and COmponents 8*, 320–330.

Lee, M. K., & Barr, B. I. G. (2002). An overview of the fatigue behaviour of plain and fibre reinforced concrete. *Cement & Concrete Associationnt & Concrete Composites*, *26*(2004), 299–305. https://doi.org/10.1016/S0958-9465(02)00139-7

Li, D., Huang, P., Qin, G., Zheng, X., & Guo, X. (2017). Fatigue Crack Propagation Behavior of RC Beams Strengthened with CFRP under High Temperature and High Humidity Environment, *2017*.

Li, L., Gua, W.-G., Yu, X., & Fu, D. (2017). Mechanical behavior of ceramic-metal joint under quasi-static and dynamic four point bending: Microstructures. damage and mechanisms. *Ceramics International*, *43*, 6684–6692.

Lindorf, A., & Curbach, M. (2010). S-N curves for fatigue of bond in reinforced concrete structures under transverse tension. *Engineering Structures*, *32*(10), 3068–3074. https://doi.org/10.1016/j.engstruct.2010.05.025

Ma, Y., Xiang, Y., Wang, L., Zhang, J., & Liu, Y. (2014). Fatigue life prediction for aging RC beams considering corrosive environments. *Engineering Structures*, *79*, 211–221. https://doi.org/10.1016/j.engstruct.2014.07.039

Mahal, M. (2015). *Fatigue Behaviour of RC Beams Strengthened with CFRP Sheets*. *Journal of Composites for Construction*. https://doi.org/10.1061/(ASCE)1090-0268(2001)5:4(246)

Mahal, M., Blanksvärd, T., Täljsten, B., & Sas, G. (2015). Using digital image correlation to evaluate fatigue behavior of strengthened reinforced concrete beams. *Engineering Structures*, *105*, 277–288. https://doi.org/10.1016/j.engstruct.2015.10.017

Malumbela, G. (2010). *Measurable parameters for performance of corroded and repaired rc beams under load*. University of Cape Town.

Malumbela, G., Moyo, P., & Alexander, M. (2011). Load-bearing capacity of corroded , patched and FRP-repaired RC beams. *Magazine of Concrete Research*, *63*(11), 797–812. https://doi.org/10.1680/macr.2011.63.11.797

Maranan, G. B., Manalo, A. C., Karunasena, W., Benmokrane, B., & Mendis, P. (2015). Flexural Response of GFRP-Reinforced Geopolymer Concrete Beams, (7), 287–296.

Mundeli, S. (2014). Behavior of RC beams patch repaired and strenghthened with FRP composites: a numerical study.

National Concrete Pavement Tehnology Center. (2007). *Guide to Concrete Overlay Solutions*.

Otieno, M. (2008). Corrosion propagation in cracked and uncracked concrete. *Department of Civil Engineering - University of Cape Town*.

Otieno, M., Alexander, M., & Beushausen, H. (2010). *Transport mechanisms in concrete. Corrosion of steel in concrete (initiation, propagation & factors affecting)*. *Concrete Material and Structural Intergrity Research Group*. Retrieved from http://scholar.google.com/scholar?hl=en&btnG=Search&q=intitle:Transport+mechanisms+in+concrete:+Corrosion+of+steel+in+concrete+-+Initiation,+propagation+&+factors+affecting#1

Otieno, M., Alexander, M., & Beushausen, H. (2014). *Transport Mechanisms in Concrete*.

Pattnaik, R. R. (2017). Investigation on Failures of Composite Beam and Substrate Concrete due to Drying Shrinkage Property of Repair Materials. *Journal of The Institution of Engineers (India): Series A*, *98*(1), 85–93. https://doi.org/10.1007/s40030-017-0195-1

Peng, H., Zhang, J., Shang, S., Liu, Y., & Cai, C. S. (2016). Experimental study of flexural fatigue performance of reinforced concrete beams strengthened with prestressed CFRP plates. *Engineering Structures*, *127*, 62–72. https://doi.org/10.1016/j.engstruct.2016.08.026

Priastiwi, Y. A., Imran, I., Nurojia, & Hidayat, A. (2014). Behavior of Ductile Beam with Addition Confinement in Compression Zone Behavior of ductile beam with addition confinement in compression zone. *Procedia Engineering*, *95*(December), 132–138. https://doi.org/10.1016/j.proeng.2014.12.172

Qeshta, I. M. I., Shafigh, P., & Jumaat, M. Z. (2016). Research progress on the flexural behaviour of externally bonded RC beams. *Archives of Civil and Mechanical Engineering*, *16*(4), 982–1003. https://doi.org/10.1016/j.acme.2016.07.002

Qin, G., Huang, P., Zhou, H., Guo, X., & Zheng, X. (2016). Fatigue and durability behavior of RC beams strengthened with CFRP under hot-wet environment. *Construction and Building Materials*, *111*, 735–742. https://doi.org/10.1016/j.conbuildmat.2016.02.131

Ramos, T., Furtado, A., Eslami, S., Alves, S., & Rodrigues, H. (2015). 2D and 3D Digital Image Correlation in Civil Engineering – Measurements in a Masonry Wall. *Procedia Engineering*, *114*, 215–222. https://doi.org/10.1016/j.proeng.2015.08.061

Sadek, S., Iskander, M. G., & Liu, J. (2003). Accuracy of Digital Image Correlation for Measuring, *17*(April), 88–96. https://doi.org/10.1061/(ASCE)0887-3801(2003)17

Sharif, A. (2014). Metallurgical Aspects of Fatigue Failure of Steel-Part I Metallurgical. In *BSRM Seminar on Fatigue Properties of Constructional Steel*. Bangladesh.

Shetty, A., Venkataramana, K., & Narayan, K. S. B. (2014). Effect of corrosion on flexural bond strength. *Journal of Electrochemical Science and Engineering*, *4*(3), 123–134. https://doi.org/10.5599/jese.2014.0052

Song, L., & Hou, J. (2017). Fatigue Assessment Model of Corroded RC Beams Strengthened with Prestressed CFRP Sheets. *International Journal of Concrete Structures and Materials*, *11*(2), 247–259. https://doi.org/10.1007/s40069-017-0191-x

Song, L., & Yu, Z. (2015). Fatigue performance of corroded reinforced concrete beams strengthened with CFRP sheets. *Construction and Building Materials*, *90*, 99–109. https://doi.org/10.1016/j.conbuildmat.2015.05.024

Spadea, S., Orr, J., & Nanni, A. (2016). New frontiers for the use of FRP reinforcement in geometrically complex concrete structures. *International Conference on FRP Composites in Civil Engineering*.

Tigeli, M. (2014). *Effect of structural repair and strengthening on stiffness and ultimate capacity of corrosion damaged rc beams*. University of Cape Town.

Tilly, G. P., & Jacobs, J. (2007). *Concrete Repairs - Performance in service and current practice*. (G. P. Tilly & J. Jacobs, Eds.) (1st ed.). bre press.

Ting, S.-C., & Nowak, A. S. (1991). Effect of Reinforcing Steel Area Loss on Flexural Behavior of Reinforced Concrete Beams. *American Concrete Institute*, *88*(3), 309–314.

Tong, L., Liu, B., & Zhao, X. (2017). Numerical study of fatigue behaviour of steel reinforced concrete (SRC) beams. *Engineering Fracture Mechanics*. https://doi.org/10.1016/j.engfracmech.2017.02.017

Van Ornum, J. L. (1903). Fatigue of Cement Pro-ducts. *Transactions, American Society of Civil Engineers*, 443.

Van Ornum, J. L. (1907). Fatigue of Concrete. *Transactions, American Society of Civil Engineers*, *58*, 294–320.

Wittmann, F. H. (2002). Crack formation and fracture energy of normal and high strength concrete. *Sadhana*, *27*(4), 413–423.

Wohler, A. (1860). Versucheuber die Festigkeit der Eisenbahnwagenachsen. *Engineering*, *4*, 160–161.

Xu, Y., & Brownjohn, J. (2018). Review of machine-vision based methodologies for displacement measurement in civil structures. *Journal of Civil Structural Health Monitoring*, *8*(1), 91–110. https://doi.org/10.1007/s13349-017-0261-4

Ye, H., Fu, C., Jin, N., & Jin, X. (2018). Performance of reinforced concrete beams corroded under sustained service loads : A comparative study of two accelerated corrosion techniques. *Construction and Building Materials*, *162*, 286–297. https://doi.org/10.1016/j.conbuildmat.2017.10.108

Yi, W.-J., Kunnath, S. K., Sun, X.-D., Shi, C.-J., & Tang, F.-J. (2011). Fatigue behavior of reinforced concrete beams with corroded steel reinforcement. *ACI Structural Journal*, *107*(5).

Zhang, S. S., Teng, J. G., & Yu, T. (2013). Bond-slip model for CFRP strips near-surface mounted to concrete. *Engineering Structures*, *56*(3), 945–953. https://doi.org/10.1016/j.engstruct.2013.05.032

Zorn, A. V. (2006). *Effect of Adhesive Stiffness and CFRP Geometry on Behaviour of Externally Bonded CFRP Retrofit Measures*. University of Pittsburgh.

APPENDICES

A. RC beams design calculations

The RC beam specimen used in this research was designed in accordance with SANS10100-1.

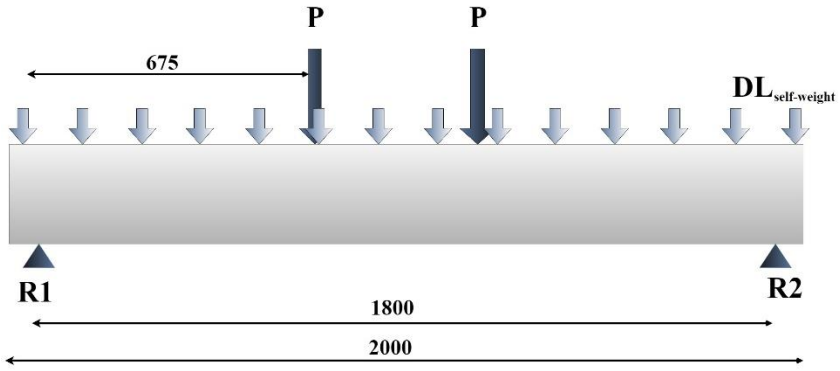

Figure A.1 RC beam specimen free body diagram

A.1. Cross-section dimensions:

Breadth (b): *155mm*
Height (h): *254mm*
Length (l): *2000mm*
Cover: *25mm*

A.2. Material properties:

Concrete unit weight (γ_{conc}): *24kN/m^3*
Concrete strength (f_{cu}): *40MPa*
Steel Yield Strength (f_y): *450MPa*

A.3. Design loading:

*Dead Load (**DL**):* $b \times h \times \gamma_{conc}$ (A.1)
$0.155 \times 0.254 \times 24$
$0.945kN/m$ *(Beam self-weight)*

*Live Load (**LL**):* *90kN (estimation)*

*Load Combination (**LC**):* $1.2DL + 1.6LL$ (A.2)
$1.2 \times 0.945 \times 2 + 1.6 \times 90$
$146.268kN$

*Reaction Force (**R**):* $R_1 = R_2 = LC \div 2 = 146.3 \div 2 = 73.134kN$ (A.3)

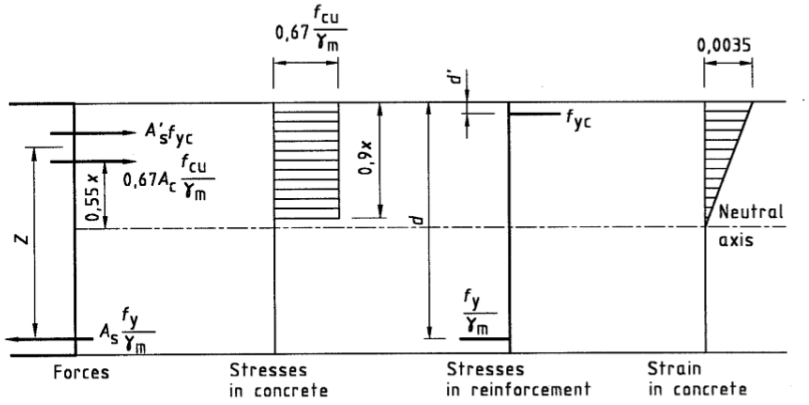

Figure A.2 Ultimate forces, stresses and strains in reinforced concrete sections at the ultimate limit state

A.4. Flexure design:

M_{max} = *0.675R₁ – 0.675×(0.675÷2)DL self-weight* (A.4)

0.675×73.134 – 0.675×(0.675÷2)×0.945

49.15kNm

K' = 0.156

d' = 25+8+(10÷2) = 38mm (A.5)

d = 254-25-8-(25÷2) = 208.5mm (A.6)

$$K = \frac{M}{bd^2 f_{cu}} = \frac{49150000}{155\times254^2\times40} = 0.183 > K'$$ (A.7)

∴ *Section doubly reinforced*

$$z = d\left[0.5 + \sqrt{0.25 - \frac{K'}{0.9}}\right] = 208.5\left[0.5 + \sqrt{0.25 - \frac{0.156}{0.9}}\right] = 161.98mm$$ (A.8)

$$x = \frac{d-z}{0.45} = \frac{208.5-161.98}{0.45} = 103.38mm$$ (A.9)

$$f_{yc} = \frac{f_y}{\gamma_m + \frac{f_y}{2000}} = \frac{450}{1.15+\frac{450}{2000}} = 327.3MPa$$ (A.10)

$\frac{d\prime}{x} = \frac{38}{103.4} = 0.368 < 0.53 = 1 - \frac{f_{yc}}{700} = 1 - \frac{327.3}{700}$ (A.11)

∴ f_{yc} *adequate*

$A_s\prime = \frac{(K-K')f_{cu}bd^2}{f_{yc}(d-d')} = \frac{(0.183-0.156)40\times155\times208.5^2}{327.3(208.5-38)} = 130.4mm^2$ (A.12)

∴ *Provide 2Y10 bars for compression reinforcement (*A_s*' provided =* $157mm^2$*)*

$A_s = \frac{K'f_{cu}bd^2}{0.85f_yz} + \frac{A_s'f_{yc}}{0.87f_y} = \frac{0.156\times40\times155\times208.5^2}{0.85\times450\times161.98} + \frac{130.4\times327.3}{0.87\times450} = 787.7mm^2$ (A.13)

∴ *Provide 2Y25 bars for tension reinforcement (*A_s *provided =* $982mm^2$*)*

∴ $M_{capacity} = 0.87A_sf_yz = 0.87\times982\times450\times161.98 = 62.27kNm$ (A.14)

A.5. Deflection assessment:

1. *Allowable deflection:*

$\frac{l}{d} = \frac{1800}{208.5} = 8.63$ (A.15)

→ *support conditions: truly simply supported* ∴ *ratio = 16*

$f_s = \frac{2}{3}f_y\frac{A_{s,req}}{A_{s,prov}} = \frac{2}{3}\times450\times\frac{787.7}{982} = 240,64$ (A.16)

$m_{ft} = 0.55 + \frac{477-f_s}{120\left(0.9+\frac{M}{bd^2}\right)} = 0.55 + \frac{477-240.64}{120\left(0.9+\frac{49150000}{155\times208.5^2}\right)} = 0.79$ (A.17)

$\frac{100A_s'}{bd} = \frac{100\times157}{155\times208.5} = 0.486$ (A.18)

∴m_{fc}*=1.136 (from Table 12, SANS10100-1, 4.3.6.3.2)*

$\frac{l}{d} = 8.63 < 14 = 16m_{ft}m_{fc} = 16\times0.7\times1.136$ ∴ *Deflection acceptable* (A.19)

2. Actual deflection:

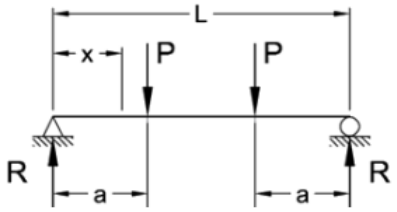

Figure A.3 Four-point configuration free body diagram

$$\alpha_e = \frac{E_s}{E_c} = \frac{200000}{30000} = 6.67 \quad \text{(A.20)}$$

$$I = \frac{bh^3}{12} + (\alpha_e - 1)(A_s + shift^2) + (\alpha_e - 1)(A'_s + shift^2) \quad \text{(A.21)}$$

$$= \frac{155 \times 254^3}{12} + (6.67 - 1)(982 + 106.1^2) + (6.67 - 1)(157 + 65.4^2)$$

$$= 211760781.3mm^4$$

For the four point configuration shown in **Figure A.3**, **Equation A.23** can be used to calculate actual beam deflection.

$$\alpha = \frac{a}{l} = \frac{675}{1800} = 0.375 \quad \text{(A.22)}$$

$$\delta_{actual} = \frac{Pl^3(3\alpha - 4\alpha^3)}{24E_c I} = \frac{45000 \times 1800^3(3 \times 0.375 - 4 \times 0.375^3)}{24 \times 30000 \times 211760781.3} = 1.57mm < 8.6 = \frac{1800}{208.5} \quad \text{(A.23)}$$

∴ *Deflection acceptable*

A.6. Shear design:

M_{max} = 49.15kNm
V = 73.134kN
f_{cu} = 40MPa
f_{yv} = 250MPa
γ_m = 1.4

$$2.5 < \frac{a_v}{d} = \frac{675}{208.5} = 3.24 < 6 \quad \text{(A.24)}$$

∴ *Flexural cracking most likely mode of shear failure*

$$v = \frac{V}{bd} = \frac{73134}{155\times208.5} = 2.263\ MPa < 4.75MPa < 0.8\sqrt{f_{cu}} = 5.06MPa \quad \text{(A.25)}$$

$$v_c = \frac{0.75}{\gamma_m}\left(\frac{f_{cu}}{25}\right)^{1/3}\left(\frac{100A_s}{bd}\right)^{1/3}\left(\frac{400}{d}\right)^{1/4} = \frac{0.75}{1.4}\left(\frac{40}{25}\right)^{1/3}\left(\frac{100\times982}{155\times208.5}\right)^{1/3}\left(\frac{400}{208.5}\right)^{1/4} = 1.069 \quad \text{(A.26)}$$

$$v_c + 0.5 = 1.569 < 2.263 = v \quad \text{(A.27)}$$

∴ Provide shear links

$$A_{sv} = \frac{b\ S_v\ (v - v_c)}{0.87\ f_{yc}} \quad \text{(A.28)}$$

→Assume A_{sv}=100.6mm^2 (R8 links)

$$S_v < \frac{100.6\times0.87\times250}{155(2.263-1.069)} = 118.23mm \quad \text{(A.29)}$$

∴Provide R8 shear links at 100mm spacing

B. Accelerated corrosion calculations

Faraday's law was used to determine the time it would take to induce 10% mass loss at a predetermined corrosion current.

B.1. Steel properties:

Density (γ_{steel}): *7860kg/m^3*

Tensile Steel diameter (D): *25mm*

Area (A_{Y25}): $\pi\left(\frac{D}{2}\right)^2 = \pi\left(\frac{25}{2}\right)^2$ = *490.87mm^2 (0.00049087m^2)* (B.1)

B.2. Faradays law:

$$I_{corr} = \frac{\Delta m F z}{M t} \quad \text{(B.2)}$$

→*Where:*

F= *96500 A/s*

z = *2*

M= *56g*

I_{corr}= *1A*

$\Delta m_{10\%}$= $2\times0.1\times A_{Y25}\times \gamma_{steel} = 2\times0.1\times$*0.00049087*$\times$*7860 = 771.65g* (B.3)

$$\therefore t = \frac{\Delta m F z}{M I_{corr}} = \frac{771.65\times96500\times2}{56\times1} = \text{2629436.6 seconds (30.8 days)}$$

B.3. Sustained loading:

Accelerated corrosion was carried out under sustained loading to ensure that tensile steel was under strain during corrosion. The four-point bending set up shown in **Figure B.1** induced a moment equivalent to 60% of the beam cracking moment (***M_{cr}***).

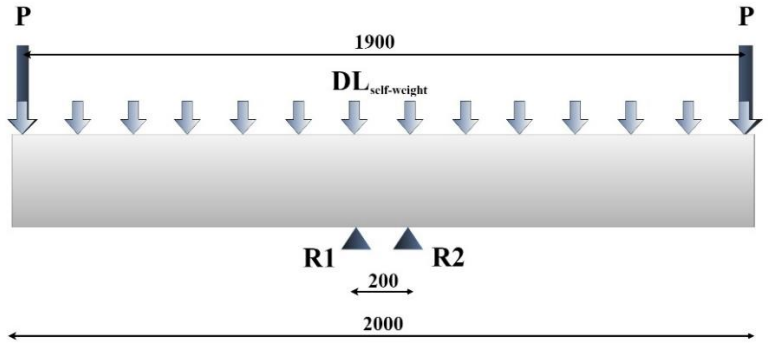

Figure B.1 Sustained load four-point bending free body diagram

$f_r = 0.65\sqrt{f_{cu}} = 0.65\sqrt{40} = 4.11MPa$ *(For unrestrained beams)* (B.4)

$$I_g = \frac{bh^3}{12} = \frac{155 \times 254^3}{12} = 211\ 666\ 243.3mm^4 \quad \text{(B.5)}$$

$$\gamma_t = h - x = h - \frac{d-z}{0.45} = 254 - \frac{208.5-161.98}{0.45} = 150.62mm \quad \text{(B.6)}$$

$$M_{cr} = \frac{f_r I_g}{\gamma_t} = \frac{4.11 \times 211666243.3}{150.62} = 5.776kNm \quad \text{(B.7)}$$

$$M_{sustained\ load} = 0.6 \times 5.776 = 3.47kNm \quad \text{(B.8)}$$

The ***P*** load, as shown in **Figure B.1**, required to induce a moment of 3.47kNm at reaction ***R1*** was calculated as follows:

$$P \times 0.85 + 0.945 \times 0.9 \times (0.9 \div 2) = 3.47kNm \quad \text{(B.9)}$$

$$\therefore P = \frac{3.47 - 0.945 \times 0.9 \times (0.9 \div 2)}{0.85} = 3.63kNm$$

It was decided to apply a dead load of 3.6kN at each end using precast concrete beams as shown on **Figure B.2**.

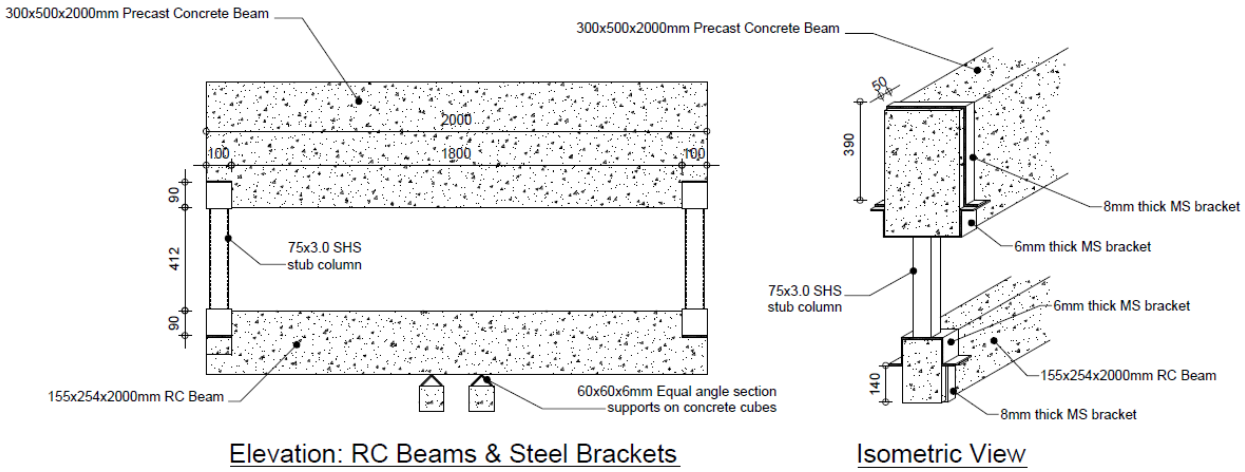

Figure B.2 Sustained load beams setup to induce partial cracking moment

C. FRP strengthening design calculations

FRP strengthening was done in accordance with Täljsten (2006), FRP Strengthening of Existing Concrete Structures: Design Guideline.

C.1. Estimated required strengthening:

$$M_{capacity} = 0.87A_sf_yz = 0.87 \times 982 \times 450 \times 161.98 = 62.27kNm \text{ (prior to corrosion)} \quad \text{(C.1)}$$

$$\Delta M_{10\%reduction} = 0.87 \times 982x0.1 \times 450 \times 161.98 = 6.227kNm \quad \text{(due to corrosion)} \quad \text{(C.2)}$$

$$A_{frp,req} = \frac{\Delta M}{0.9 \times h \times \varepsilon_f \times E_f} = \frac{6227000}{0.9 \times 254 \times 0.017 \times 165000} = 9.711mm^2 \quad \text{(C.3)}$$

$\therefore$ *Provide 2 × SikaCarboDur S512 ($A_{frp,\,prov}$= 2 ×60mm^2 = 120mm^2)*

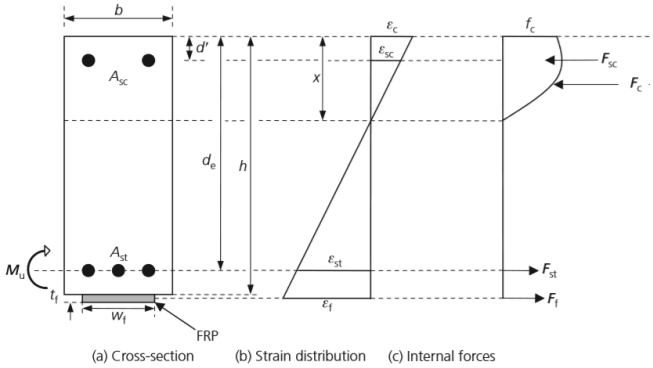

Figure C.1 Stress-strain diagram across a rectangular beam cross-section (Malumbela, 2018)

C.2. Strengthening ratio assessment:

Estimated FRP strengthening was checked against strengthening ratios to establish failure mode and possible need to increase FRP laminate area. The general compressive stress distribution shown in **Figure C.1** below, highlights the force contribution by the FRP laminates. The horizontal equilibrium equation for this cross-section was used to determine the neutral axis position $\boldsymbol{x}$. At equilibrium:

$$F_c + F'_s = F_s + F_f \quad \text{(C.4)}$$

$$\alpha f_{cc} bx + \left(\frac{x - d'_s}{x}\right) A'_s E_s = A_s f_y + \left(\frac{h-x}{x}\varepsilon_{cu} - \varepsilon_{u0}\right) E_f A_f$$

$$0.9 \times 40 \times 155x + \left(\frac{x-38}{x}\right) \times 157 \times 200000 = 883.8 \times 450 + \left(\frac{254-x}{x}\ 0.0035\right) 165000 \times 120$$

→Solving for x gives quadratic equation:

$$5580x^2 - 218510x - 21778400 = 0 \quad \text{(C.5)}$$

$\therefore x = 85.1mm$

→ Neutral axis position used to check strengthening ratios:

1. *If compression steel yields:*

$$\rho_{f1}=\frac{\alpha v_1 f_{cc}-\rho_s f_y+\rho'_s f'_s}{\left[\varepsilon_{cu}\left(\frac{h}{v_1 d_s}-1\right)-\varepsilon_{u0}\right]E_f} \quad \text{(C.6)}$$

$$v_1=\frac{x}{d_s}=\frac{85.1}{208.5}=0.408 \quad \text{(C.7)}$$

$$\therefore \rho_{f1}=\frac{0.9\times0.408\times40-\frac{883.8}{155\times208.5}450+\frac{157}{155\times208.5}250}{\left[0.0035\left(\frac{254}{0.408\times208.5}-1\right)-0\right]165000}=0.00314 \quad \text{(C.8)}$$

2. *If compression steel does not yield:*

$$\rho_{f2}=\frac{\alpha v_1 f_{cc}-\rho_s f_y+\rho'_s \varepsilon_{cu}\left(1-\frac{d'_s}{v_1 d_s}\right)E_s}{\left[\varepsilon_{cu}\left(\frac{h}{v_1 d_s}-1\right)-\varepsilon_{u0}\right]E_f} \quad \text{(C.9)}$$

$$\therefore \rho_{f2}=\frac{0.9\times0.408\times40-\frac{883.8}{155\times208.5}450+\frac{157}{155\times208.5}0.0035\left(1-\frac{38}{0.408\times208.5}\right)200000}{\left[0.0035\left(\frac{254}{0.408\times208.5}-1\right)-0\right]165000}=0.00372$$

3. *Normally-reinforced strengthened cross-section:*

$$\rho_{fu}=\frac{\alpha v_1 f_{cc}-\rho_s f_y+\rho'_s \varepsilon_{cu}\left(\frac{x-d'_s}{h-d'_s}\right)\varepsilon_f}{\varepsilon_f E_f} \quad \text{(C.10)}$$

$$\therefore \rho_{fu}=\frac{0.9\times0.408\times40-\frac{883.8}{155\times208.5}450+\frac{157}{155\times208.5}0.0035\left(\frac{85.1-38}{254-38}\right)0.017}{0.017\times165000}=0.00085$$

4. *Balanced strengthened cross-section:*

$$\rho_{fn}=\frac{\alpha f_{cc} v_2\frac{h}{d_s}-\rho_s f_y+\rho'_s \varepsilon_{cu}\left(1-\frac{d'_s}{v_2 h}\right)E_s}{\varepsilon_f E_f} \quad \text{(C.11)}$$

$$v_2=\frac{x}{h}=\frac{85.1}{254}=0.335 \quad \text{(C.12)}$$

$$\therefore \rho_{fn}=\frac{0.9\times40\times0.335\times\frac{254}{208.5}-\frac{883.8}{155\times208.5}450+\frac{157}{155\times208.5}0.0035\left(1-\frac{38}{0.335\times254}\right)200000}{0.017\times165000}=0.00169$$

5. *Over-reinforced cross-section*

$$\rho_{f0}=\frac{\alpha f_{cc} v_3 \frac{d'_s}{d_s}-\rho_s f_y+\rho'_s \varepsilon_{cu}\left(1-\frac{1}{v_3}\right)E_s}{\left[\varepsilon_{cu}\left(\frac{h}{d'_s v_3}-1\right)-\varepsilon_{u0}\right]E_f} \quad \text{(C.13)}$$

$$v_3 = \frac{x}{d'_s} = \frac{85.1}{38} = 2.24 \quad \text{(C.14)}$$

$$\therefore \rho_{fo} = \frac{0.9\times40\times2.24\times\frac{38}{208.5}-\frac{883.8}{155\times208.5}450+\frac{157}{155\times208.5}0.0035\left(1-\frac{1}{2.24}\right)200000}{\left[0.0035\left(\frac{254}{2.24\times38}-1\right)-0\right]165000} = 0.00373$$

Analysis of the strengthening ratios show that the cross-section is over-reinforced and is likely to exhibit failure mode IV, which is crushing of compression concrete without yielding of compression reinforcement, given that:

$$\rho_{fn} \leq \rho_{f2} \leq \rho_{fo} \quad \text{(C.15)}$$

With that in mind the moment capacity of the strengthened specimen for the given failure mode was calculated as follows:

$$M_{capacity} = \left(\frac{x-d'_s}{x}\varepsilon_{cu}\right)A'_s E_s(\beta x - d'_s) + A_s f_y(d_s - \beta x) + \left(\frac{h-x}{x}\varepsilon_{cu} - \varepsilon_{u0}\right)E_f A_f(h-\beta x) \quad \text{(C.16)}$$

$$= \left(\frac{85.1-38}{85.1}0.0035\right)157\times200000(0.9\times85.1-38) + 883.8\times450(208.5-0.9\times85.1) + \left(\frac{254-85.1}{85.1}0.0035-0\right)165000\times120(254-0.9\times85.1)$$

=79.3kNm

C.3. Stresses and strains at ULS:

$$v_1 = \frac{x}{d_s} = \frac{\varepsilon_{cu}}{\varepsilon_{cu}-\varepsilon_s} \quad \text{(C.17)}$$

$$0.408 = \frac{85.1}{208.5} = \frac{0.0035}{0.0035-\varepsilon_s}$$

$$\therefore \varepsilon_s = 0.00508 \quad \textit{(Tensile reinforcement)}$$

$$\sigma_s = \varepsilon_s E_s = 0.00508\times200000 = 1015\ MPa \quad \text{(C.18)}$$

$v_3 = \frac{x}{d\prime_s} = \frac{85.1}{38} = 2.24$ (C.19)

$\varepsilon'_s = \varepsilon_{cu}\left(1 - \frac{1}{v_3}\right) = 0.0035\left(1 - \frac{1}{2.24}\right) = 0.00194$ *(Compression reinforcement)* (C.20)

$\sigma'_s = \varepsilon'_s E_s = 0.00194 \times 200000 = 387.5MPa$ (C.21)

$\varepsilon_f = \left(\frac{h}{d\prime_s v_3} - 1\right)\varepsilon_{cu} - \varepsilon_{u0} = \left(\frac{1}{38 \times 2.24} - 1\right)0.0035 = 0.006944$ (C.22)

$\sigma_f = \varepsilon_f E_f = 0.006944 \times 165000 = 1145\ MPa$ *(FRP)* (C.23)

C.4. Deflection assessment of strengthened RC beam:

1. *Allowable deflection:*

$\frac{l}{d} = \frac{1800}{208.5} = 8.63$ (C.24)

→ *support conditions: truly simply supported* ∴ *ratio = 16*

$f_s = \frac{2}{3} f_y \frac{A_{s,req}}{A_{s,prov}} = \frac{2}{3} \times 450 \times \frac{787.7}{982} = 240{,}64$ (C.25)

$m_{ft} = 0.55 + \frac{477 - f_s}{120\left(0.9 + \frac{M}{bd^2}\right)} = 0.55 + \frac{477 - 240.64}{120\left(0.9 + \frac{49150000}{155 \times 208.5^2}\right)} = 0.79$ (C.26)

$\frac{100A_s'}{bd} = \frac{100 \times 157}{155 \times 208.5} = 0.486$ (C.27)

∴$m_{fc} = 1.136$ *(from Table 12, SANS10100-1, 4.3.6.3.2)*

$\frac{l}{d} = 8.63 < 14 = 16 m_{ft} m_{fc} = 16 \times 0.7 \times 1.136$ ∴ *Deflection acceptable* (C.28)

2. *Actual deflection:*

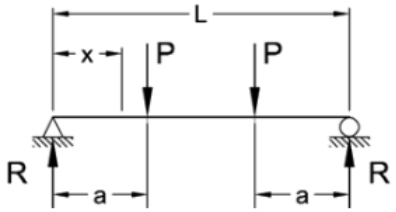

Figure C.2 Four-point configuration free body diagram

$$\alpha_s = \frac{E_s}{E_c} = \frac{200000}{39600} = 5.05 \quad \text{(C.29)}$$

$$\alpha_f = \frac{E_f}{E_c} = \frac{165000}{39600} = 4.17 \quad \text{(C.30)}$$

→ *The horizontal equilibrium equation for this cross-section was used to determine the neutral axis position* $\boldsymbol{x}$

$$\frac{bx^2}{2} + (\alpha_s - 1)A'_s(x - d'_s) = \alpha_s A_s(d_s - x) + \alpha_f A_f(h - x) \quad \text{(C.31)}$$

$$\frac{155x^2}{2} + (5.05 - 1)157(x - 38) = 982 \times 5.05(216 - x) + 4.17 \times 120(254 - 38)$$

→*Solving for x gives quadratic equation:*

$77.5x^2 + 5651.9x - 1215095.8 = 0$

$\therefore x = 93.95mm$

→ *Neutral axis position used to check revised stiffness of cracked strengthened section:*

$$I_2 = \frac{bx^3}{12} + bx\left(\frac{x}{2}\right)^2 + (\alpha_s - 1)A'_s(x - d'_s)^2 + \alpha_s A_s(d_s - x)^2 \quad \text{(C.32)}$$

$$= \frac{b \times 93.95^3}{12} + 155 \times 93.95\left(\frac{93.95}{2}\right)^2 + (5.05 - 1)157(93.95 - 38)^2 + 5.05 \times 982(216 - 132.48)^2$$

$= 119463265.5mm^4$

For the four point configuration shown in **Figure C.2**, **Equation C.34** can be used to calculate actual beam deflection.

$$\alpha = \frac{a}{l} = \frac{675}{1800} = 0.375 \quad \text{(C.33)}$$

→*Actual deflection (40%stress range)*

$$\delta_{actual} = \frac{Pl^3(3\alpha - 4\alpha^3)}{24E_cI} = \frac{54800 \times 1800^3(3 \times 0.375 - 4 \times 0.375^3)}{24 \times 39600 \times 119463265.5} = 2.57mm < 8.6 = \frac{1800}{208.5} \quad \text{(C.34)}$$

∴ *Deflection acceptable*

→*Actual deflection (60%stress range)*

$$\delta_{actual} = \frac{Pl^3(3\alpha - 4\alpha^3)}{24E_cI} = \frac{82200 \times 1800^3(3 \times 0.375 - 4 \times 0.375^3)}{24 \times 39600 \times 119463265.5} = 3.86mm < 8.6 = \frac{1800}{208.5} \quad \text{(C.35)}$$

∴ *Deflection acceptable*

D. Research programme

This appendix contains a detailed research programme that was used during the theoretical and experimental investigation. As shown in **Figure D.1**, a reasonable amount of time was allocated for each task and adjustments were made where unforeseen delays arose. The initial thesis submition was scheduled for 31 July 2018. This initial submission date allowed for additional time to make changes to the final submission where required.

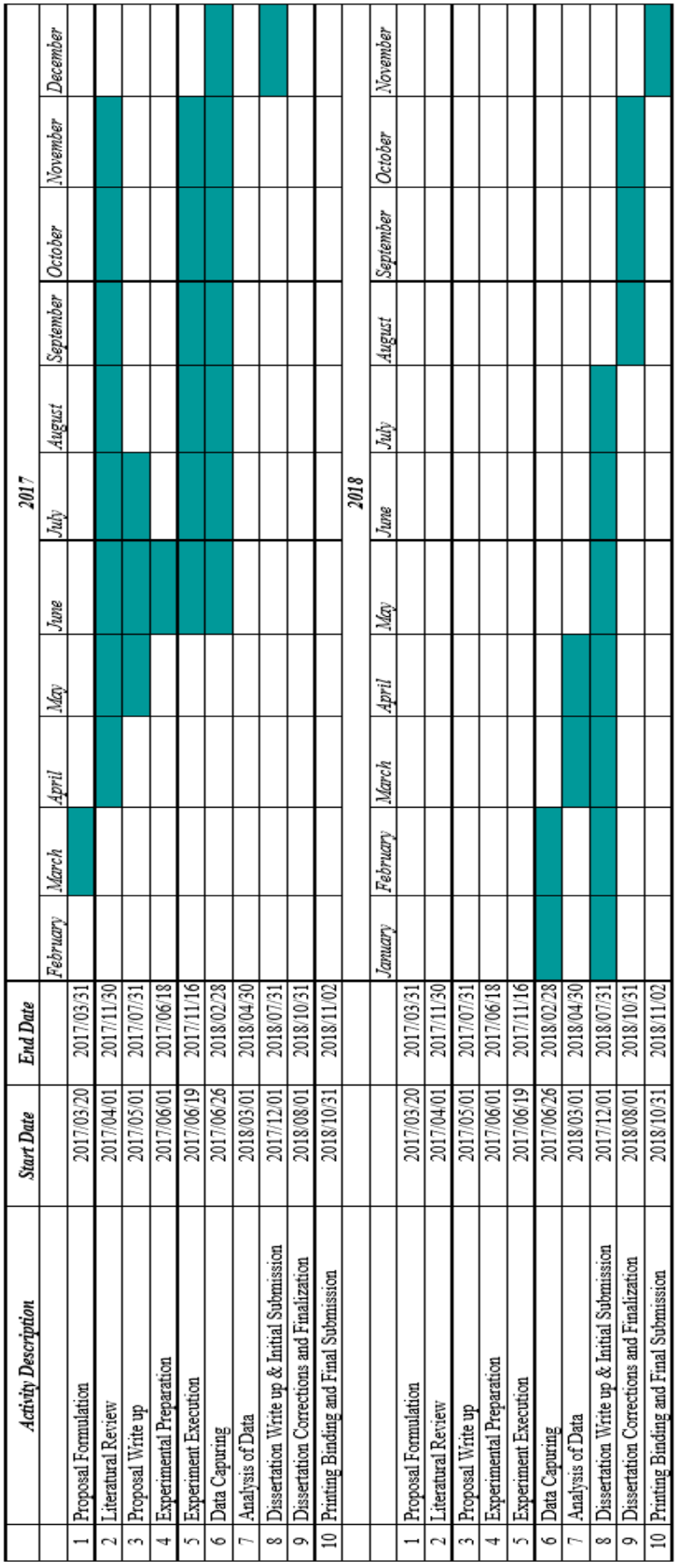

	Activity Description	Start Date	End Date	2017												
				February	March	April	May	June	July	August	September	October	November	December		
1	Proposal Formulation	2017/03/20	2017/03/31													
2	Literatural Review	2017/04/01	2017/11/30													
3	Proposal Write up	2017/05/01	2017/07/31													
4	Experimental Preparation	2017/06/01	2017/06/18													
5	Experiment Execution	2017/06/19	2017/11/16													
6	Data Capuring	2017/06/26	2018/02/28													
7	Analysis of Data	2018/03/01	2018/04/30													
8	Dissertation Write up & Initial Submission	2017/12/01	2018/07/31													
9	Dissertation Corrections and Finalization	2018/08/01	2018/10/31													
10	Printing Binding and Final Submission	2018/10/31	2018/11/02													
				2018												
				January	February	March	April	May	June	July	August	September	October	November		
1	Proposal Formulation	2017/03/20	2017/03/31													
2	Literatural Review	2017/04/01	2017/11/30													
3	Proposal Write up	2017/05/01	2017/07/31													
4	Experimental Preparation	2017/06/01	2017/06/18													
5	Experiment Execution	2017/06/19	2017/11/16													
6	Data Capuring	2017/06/26	2018/02/28													
7	Analysis of Data	2018/03/01	2018/04/30													
8	Dissertation Write up & Initial Submission	2017/12/01	2018/07/31													
9	Dissertation Corrections and Finalization	2018/08/01	2018/10/31													
10	Printing Binding and Final Submission	2018/10/31	2018/11/02													

Figure D.1 Research experiment programme

E. Ethics clearance form

Application for Approval of Ethics in Research (EiR) Projects
Faculty of Engineering and the Built Environment, University of Cape Town

APPLICATION FORM

Please Note:
Any person planning to undertake research in the Faculty of Engineering and the Built Environment (EBE) at the University of Cape Town is required to complete this form before collecting or analysing data. The objective of submitting this application *prior* to embarking on research is to ensure that the highest ethical standards in research, conducted under the auspices of the EBE Faculty, are met. Please ensure that you have read, and understood the EBE Ethics in Research Handbook (available from the UCT EBE. Research Ethics website) prior to completing this application form: http://www.ebe.uct.ac.za/usr/ebe/research/ethics.pdf

APPLICANT'S DETAILS		
Name of principal researcher, student or external applicant		Valentino James
Department		Civil Engineering
Preferred email address of applicant:		Valentinojames@gmail.com
If a Student	Your Degree: e.g., MSc, PhD, etc.,	MSc
	Name of Supervisor (if supervised):	Professor Phiata Moyo
If this is a research contract, indicate the source of funding/sponsorship		
Project Title		Carbon Fibre and Finite Element Analysis

I hereby undertake to carry out my research in such a way that:

- there is no apparent legal objection to the nature or the method of research; and
- the research will not compromise staff or students or the other responsibilities of the University;
- the stated objective will be achieved, and the findings will have a high degree of validity;
- limitations and alternative interpretations will be considered;
- the findings could be subject to peer review and publicly available; and
- I will comply with the conventions of copyright and avoid any practice that would constitute plagiarism.

SIGNED BY	Full name	Signature	Date
Principal Researcher/ Student/External applicant	Valentino R James	signature removed	13 Feb 2017

APPLICATION APPROVED BY	Full name	Signature	Date
Supervisor (where applicable)	Professor Phiata Moyo	signature removed	17/3/2017
HOD (or delegated nominee) Final authority for all applicants who have answered NO to all questions in Section1; and for all Undergraduate research (Including Honours).	Dyllon Randall	signature removed	25 Nov 2019
Chair : Faculty EIR Committee For applicants other than undergraduate students who have answered YES to any of the above questions.			